Formation of Amphitheater-Headed Canyons

by

Michael Patrick Lamb

B.S. (University of Minnesota, Minneapolis) 2001
M.S. (University of Washington, Seattle) 2003

A dissertation submitted in partial satisfaction of the
requirements for the degree of

Doctor of Philosophy

in

Earth & Planetary Science

in the

GRADUATE DIVISION

of the

UNIVERSITY OF CALIFORNIA, BERKELEY

Committee in charge:

Professor William E. Dietrich, Chair
Professor Michael M. Manga
Professor Mark Stacey

Spring 2008

Formation of Amphitheater-Headed Canyons

Abstract

Formation of Amphitheater-Headed Canyons

by

Michael Patrick Lamb

Doctor of Philosophy in Earth & Planetary Sciences

University of California, Berkeley

Professor William E. Dietrich, Chair

The amphitheater headwalls of some bedrock canyons have been used to infer the environmental conditions and erosion processes responsible for shaping the surfaces of Earth and Mars. Morphologic identification of process is hampered, however, because we lack basic field observations and quantitative models of erosion and sediment-transport in bedrock canyons. Herein I describe five related efforts to identify erosion and transport processes through field observations and measurements of canyons on Earth, and to develop quantitative models for some of these processes. First, I present a compilation of new observations and those of others, and conclude that, despite assertions that amphitheater form is due to groundwater-seepage erosion, the evidence to support this hypothesis is ambiguous or nonexistent for most bedrock canyons. A detailed examination of two prominent examples, the Kohala valleys in Hawai‘i and Box Canyon in Idaho, has revealed no evidence for seepage erosion. Instead, field observations and topographic analyses of the Kohala valleys suggest that they likely

formed by waterfall plunge-pool erosion following large-scale slumping of Kohala Volcano. In addition, sediment transport measurements and dating indicate that Box Canyon owes its origin to large-scale flooding that occurred about 45 thousand years ago. To better quantify erosion and transport processes, a mechanistic model is presented to predict the conditions under which coarse sediment is mobilized in rivers and streams over a wide range of channel-bed slopes. Lastly, I present a model for abrasion of bedrock riverbeds by impacting particles carried in bedload and suspended load.

_____

Professor William E. Dietrich
Dissertation Committee Chair

Contents

Acknowledgements

As a collaborator and advisor on all of the research presented herein, I first and foremost thank Bill Dietrich. Throughout the course of my dissertation, Bill has encouraged and challenged me to be a better scientist. I can only hope that a bit of his brilliance, curiosity, and knack for asking the right questions at the right times has rubbed off on me during my graduate studies at Berkeley.

This dissertation could not have been completed without the benefit of many collaborators. Alan Howard inspired me to ponder the significance and mystery of amphitheater-headed canyons. As a pioneer on this topic (and many others), he humbly guided me through the fascinating landscapes of the American Southwest, Hawai‘i and Mars, and was instrumental in the research presented in Chapters 2 and 3. Michael Manga and Mark Stacey served on my dissertation committee and provided helpful advice and discussion. I am fortunate to have found a fine friend and colleague in Taylor Perron, who helped with the field research and analysis in Chapters 2 - 4. Joel Johnson and Kelin Whipple kindly contributed to Chapter 2. Many thanks to Sarah Aciego and Don DePaolo whose collaborative dating results in Idaho were invaluable to the research presented in Chapter 4. Warm thanks to Christine May, Jim McKean, Russ Thurow and Thijs van Soest for field assistance. I have enjoyed conversations with Jeremy Venditti and Leonard Sklar, who helped with the research presented in Chapters 5 and 6, respectively. Some parts of this dissertation have been submitted for journal

publication and have benefited from the reviews of Darryll Pederson, Tom Dunne, Lewis Owen, Dieter Rickenmann, John Buffington, Ben Crosby, and Jens Turowski.

Several teachers and colleagues deserve mention for helping me in my collegiate life. At the University of Wisconsin, Lou Maher sparked my interest in geosciences. I am indebted to Chris Paola and Gary Parker for introducing me to geomorphology and sedimentology, and encouraging me to conduct my first research project and pursue graduate studies. Jeff Parsons, Jim Kirchner, Kurt Cuffey, Russ McDuff, Chuck Nittrouer, Christian Teyssier, Dino Bellugi, Ionut Iordache, and David Yuen have provided valuable advice and assistance. Graduate-school life would not have been the same without the community of Christian Braudrick, Peter Nelson, David Finlayson, Kathy Presto, Chris Belnap, Erik Oerter, Joel Rowland, Elowyn Yager, Ken Ferrier, Leslie Hsu, Brent Grocholski and Stewart McWilliams.

On a personal level, I cannot begin to articulate my thanks to my family and friends for their love and support. My parents, Linda and Patrick Lamb, have always pushed me to follow my interests, regardless of financial gain or time spent in college (11 years). My wife Anna has endured moves from Minnesota to Washington, California, and now Texas, all while I have provided a standard of living far below what she deserves. I am thankful for her continued love and support. Thanks to Andy Kriss, Jason Schulz, Peter Lamb, Ben Lamb, Brianna Lamb, Colleen Lamb, Diana Lamb, Bill Knoff, Dan Rudolf and Matt Gove for making an effort over long distances. Ed Meehan, Natalie Moore, Sarah Heilbrun and Dave Gross showed me the wonders of Catan.

Funding for this work was provided by a NASA Astrobiology Institute grant to the BioMars Center led by Jill Banfield at U.C. Berkeley. Topographic data of Box Canyon, Idaho, was provided by the National Center for Airborne Laser Mapping and the National Center for Earth Surface Dynamics. Additional funding for my time came from the George D. Louderback Fund, the National Defense and Engineering Graduate Fellowship, and the Academic Rewards for College Scientists Fellowship.

Chapter 1

Introduction

1.1. Why Study Amphitheater-Headed Canyons?

A central theme in geomorphology and planetary science is to decipher the environmental history of a planet's surface by observing and interpreting landscape form. A prominent example is the formation of amphitheater-headed canyons (e.g., Fig. 1). The processes responsible for creating these spectacular landforms, with steep stubby headwalls and little landscape dissection upstream, have long intrigued geomorphologists (Hinds, 1925; Stearns, 1936; Laity and Malin, 1985). Can the morphology of amphitheater-headed canyons be used to decipher the erosional processes active on a planet's surface? This question is not only important for unraveling Earth history, but is also at the forefront of Martian exploration, where the discovery of bedrock canyons (e.g., Fig. 2) has sparked debate about the possibility of rainfall, groundwater, and life on Mars (Sharp and Malin, 1975; Pieri, 1976; Carr and Clow, 1981; Baker, 1990; Malin and Carr, 1999; Harrison and Grimm, 2005).

The leading hypothesis for formation of amphitheater-headed canyons is erosion by emerging spring water (i.e. seepage erosion or groundwater sapping) (Dunne, 1980;

Figure 1. Aerial photograph of Box Canyon, Idaho. Box Canyon is a short (~ 2 km) amphitheater-headed tributary of the Snake River Canyon, near Hagerman Idaho. See Chapter 4 for more detail.

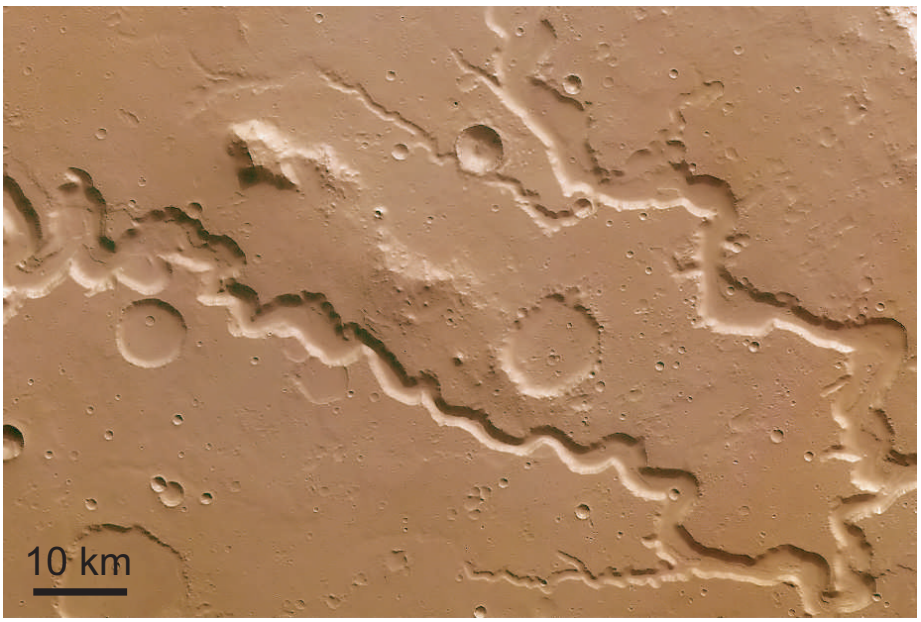

Figure 2. Nanedi Valles, Mars. Note the tributaries of the larger canyons often end abruptly as stubby amphitheater-headed canyons. Credit: European Space Agency.

Higgins, 1984; Baker, 1990; Dunne, 1990). In this model, canyon headwalls are undermined and collapse due to seepage induced weathering (Fig. 3). This results in upstream headwall retreat and eventually formation of a canyon. Despite the popularity of this hypothesis, fundamental questions about the amount and duration of water discharge responsible for carving amphitheater-headed canyons remain unanswered because we lack both robust morphologic criteria to identify erosion processes in bedrock and quantitative models that describe those processes. Basic observations and measurements of bedrock erosion and sediment transport processes are needed to test and quantify models for canyon formation.

The original goal of my dissertation was to fill this knowledge gap using field measurements and model development of bedrock erosion and canyon formation by seepage flow. Three field sites were selected that contain amphitheater-headed canyons in bedrock: the canyons of the Colorado Plateau, the Kohala valleys of Hawaii, and Box Canyon of Idaho. The first two sites are often cited as *classic* examples of canyons formed by seepage erosion, and subsequently are commonly used as Martian analogs (Laity and Malin, 1985; Kochel and Piper, 1986). Despite previous work, at all sites investigated I found the evidence for seepage erosion to be ambiguous or non-existent. This surprising result led to a reanalysis of the evidence for seepage erosion in bedrock, presented in Chapter 2. In Chapter 3, I reinterpret the Kohala valleys of Hawaii as a product of large-scale slumping and waterfall plunge-pool erosion. In Chapter 4, I show strong evidence against the seepage-erosion hypothesis at Box Canyon, Idaho, and demonstrate that this canyon was carved by a megaflood ca. 45 ka.

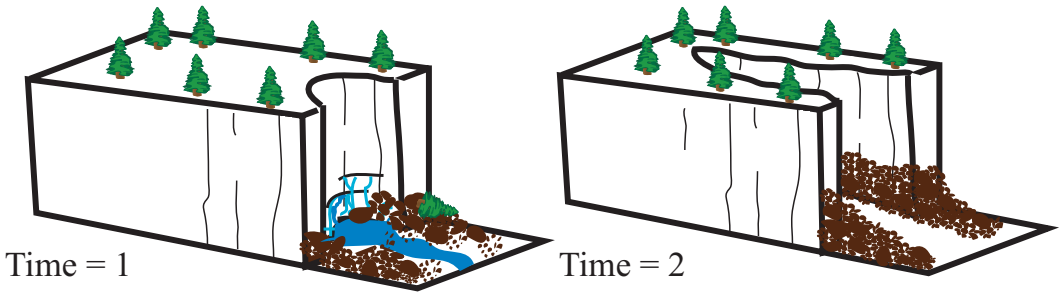

Figure 3. Cartoon illustrating the seepage-erosion hypothesis for creating amphitheater canyons with steep headwalls. Time 1) Emerging spring water from a cliff face erodes and undermines the cliff. Time 2) Focused erosion and removal of sediment leads to an amphitheater-headed canyon.

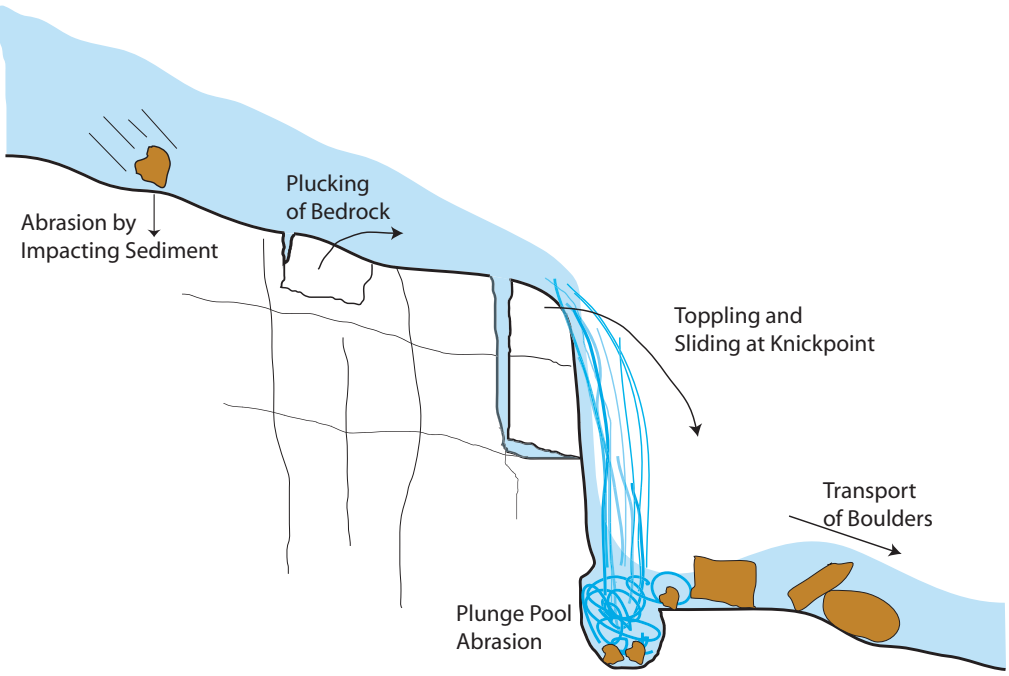

Figure 4. Cartoon illustrating the erosion and transport processes at a canyon headwall. Bedrock is worn from abrasion by impacting sediment and plucking of rock. Headwall retreat can occur due to plunge-pool erosion and toppling. Boulders and other sediment must be transported away to allow continued headwall retreat.

Since seepage erosion appears to be much less important for amphitheater-canyon formation than previously thought, it is important to give careful consideration to alternative erosion mechanisms. I have identified two basic and necessary processes for formation of amphitheater-headed canyons in bedrock: 1) erosion of the canyon headwall, and 2) transport of collapsed sediment out of the canyon (Fig. 3). Erosion processes at a particular site might include fluvial abrasion, plucking, plunge pool erosion or block toppling (Fig. 4). The latter chapters are devoted to developing quantitative models to describe some of these processes. A portion of Chapter 3 presents a quantitative model for plunge pool erosion applied to the case of Hawaiian amphitheater-headed valleys. Chapter 5 presents a model to predict the conditions for sediment entrainment in steep mountain streams. Finally, Channel 6 discusses a model for abrasion of a bedrock river-channel by suspended and bedload sediment. A more detailed summary of each chapter is given below.

1.2. Summary of Chapters 2 - 6

In Chapter 2, I review the evidence for seepage erosion in bedrock to address whether amphitheater morphology can be used as a diagnostic indicator of seepage erosion. Seepage erosion is shown to be an important process in loose sediment where hydraulic forces cause grain detachment, often resulting in amphitheater-headed valleys. However, the extension of these processes to resistant rock is uncertain. In sedimentary rocks, groundwater might control the shape and rate of valley formation. It is possible, however, that seepage plays only a secondary role to runoff processes. This seems likely in basaltic valleys on Earth, where little evidence exists for seepage

erosion. Since the ability of seepage to erode bedrock valleys remains unclear and because many amphitheater-headed valleys were probably carved by other processes, I conclude that seepage erosion should not be inferred based solely on valley form.

In Chapter 3, a detailed case study is presented of the spectacular canyons of Kohala, Hawai‘i, one of the most widely cited terrestrial analogs for Martian amphitheater-headed valleys in basalt (e.g., Kochel and Piper, 1986). New field observations and topographic analyses of the amphitheater-headed Kohala valleys reveal no evidence for intensively weathered rocks or alcoves around springs at valley headwalls. Instead, valley-head erosion appears to be dominated by waterfall plunge pools. Stream flow from peak-annual precipitation events exceeds spring discharge by more than an order of magnitude and such flow is responsible for evacuation of the coarse sediment that lines the streams. Bathymetry along the Kohala coast has revealed a large submarine landslide, the Pololū Slump, directly offshore of the Kohala valleys. The headscarp of this massive landslide is proposed to be expressed as the present day ~ 400 m Kohala sea cliffs. I propose that as dominant streams poured over this headscarp as waterfalls, vertical plunge-pool erosion and undercutting caused upstream propagation of knickpoints, eventually producing amphitheater-headed valleys. Island subsidence following valley formation has resulted in alluviation of the valley floors creating the observed U-shaped valley cross sections. The average rate of valley headwall advance is found to be as high as 60 mm/yr using island subsidence rates and the ages of volcanic eruptions and submarine terraces. After the slump, many streams did not form upslope propagating waterfalls because they had smaller discharges due to smaller drainage areas caused by a radial drainage pattern and fault-bounded drainage

divides, which prevented runoff from the wetter summit of the volcano. In addition to the field analysis, a simple model is proposed for upslope headwall propagation by vertical waterfall erosion based on abrasion by impacting sediment particles in plunge pools. This model indicates that headwall propagation depends non-linearly on the sediment flux passing over the waterfall and linearly on the ratio of kinetic versus potential energy of sediment impacts. A threshold for headwall propagation due to sediment supply or sediment-transport capacity is consistent with the model.

In Chapter 4, I present observations from Box Canyon, Idaho, which was originally thought to have been carved by seepage erosion owing to the ~10 m^3/s spring that emanates from the base of its ~35-m high vertical headwall, and because of the lack of drainage-network development upstream (Stearns, 1936). I found, however, that weathering is not enhanced near the spring, and flows larger than 220 m^3/s are required to move the boulders that line the canyon floor. Moreover, plunge pools and a broad shallow channel with scour marks upstream of the canyon head indicate overflow of a large-magnitude flood (> 800 m^3/s) in the past. U-Th/He eruption ages, ^3He cosmogenic ages of scoured bedrock and boulders, and ^{14}C dates from shells within a backwater deposit support canyon formation between ca. 86 ka and 50 ka, with little activity since except talus production. I propose that a large flood, possibly related to a glacial-lake outburst from the Wood or Lost drainages to the northeast, poured over the wall of the Snake River Canyon ca. 50 ka, causing headward erosion for a time-period of weeks to months, resulting in Box Canyon. These results add to a growing recognition of Quaternary catastrophic flooding in the American northwest, and may imply that similar features on Mars also formed by floods rather than seepage erosion.

Because excavation of sediment is one of the necessary conditions for canyon formation (Fig. 4), Chapter 5 is devoted to assessing the mobility of boulders in mountain streams. Data from laboratory flumes and natural streams are presented to show that the critical Shields stress for initial sediment motion increases with channel slope, which indicates that particles of the same size are more stable on steeper slopes. This observation is contrary to standard models that predict reduced stability with increasing slope due to the added downstream gravitational force. Processes that might explain this discrepancy are explored using a force-balance model, including increased drag from channel walls and bed morphology, variable friction angles, grain emergence, flow aeration, and changes to the local flow velocity and turbulent fluctuations. I found that increased drag due to changes in bed morphology does not appear to be the cause of the slope dependency because both the magnitude and trend of the critical Shields stress are similar for flume experiments and natural streams, and significant variations in bed morphology in flumes is unlikely. Instead, grain emergence and changes in local flow velocity and turbulent fluctuations seem to be responsible for the slope dependency due to the coincident increase in the ratio of bed-roughness scale to flow depth (i.e., relative roughness). A model for the local velocity within the grain-roughness layer is proposed based on a 1-D eddy viscosity with wake mixing. In addition, the magnitude of near-bed turbulent fluctuations is shown to depend on the depth-averaged flow velocity and the relative roughness. Extension of the model to mixed grain sizes indicates that the coarser fraction becomes increasingly difficult to transport on steeper slopes.

In Chapter 6, a mechanistic model is derived for the rate of fluvial erosion into bedrock by abrasion from impacting particles transported in bed and suspended load.

The model is an extension of recent work that considers only impacts from bedload sediment (Sklar and Dietrich, 2004). The erosion rate is equated to the product of the impact rate, the mass loss per particle impact, and a bed-coverage term. Unlike previous work, the impact rate is not assumed to tend to zero as the shear velocity approaches the threshold for suspension. Instead, a given sediment supply is distributed between the bed and suspended load by utilizing common formulas for the bedload-layer height, bedload velocity, logarithmic fluid-velocity profile, and Rouse sediment-concentration profile. I propose that the impact rate scales linearly with the product of the near-bed sediment concentration and the impact velocity. Particles are considered to impact the bed due to gravitational settling and advection by turbulent eddies. Results imply, unlike models that consider only bedload, that the erosion rate increases with increasing transport stage (for a given relative sediment supply), even for transport stages that exceed the onset of suspension. In addition, erosion can occur when the sediment supply exceeds the bedload capacity because a portion of the sediment load is transported in suspension.

Extracts from some chapters have been published elsewhere and are reproduced here with permission. Chapter 2 has been published in the *Journal of Geophysical Research – Planets* (Lamb et al., 2006), Chapter 3 has been published in the *Geological Society of America Bulletin* (Lamb et al., 2007), Chapter 4 has been accepted for publication in *Science* (Lamb et al., 2008a), Chapter 5 has been published in, and Chapter 6 has been submitted to the J*ournal of Geophysical Research – Earth Surface* (Lamb et al., 2008b).

1.3. References

Baker, V. R., 1990, Spring sapping and valley network development, with case studies by R.C. Kochel, V.R. Baker, J.E. Laity, and A.D. Howard, *in* Higgins, C. G., and Coates, D. R., eds., Groundwater Geomorphology, The Role of Subsurface Water in Earth-Surface Processes and Landforms: Boulder, Colorado, Geological Society of America Special Paper 252, p. 235-265.

Carr, M. H., and Clow, G. D., 1981, Martian channels and valleys - their characteristics, distribution, and age: Icarus, v. 48, no. 1, p. 91-117.

Dunne, T., 1980, Formation and controls of channel networks: Progress in Physical Geography, v. 4, p. 211-239.

Dunne, T., 1990, Hydrology, mechanics, and geomorphic implications of erosion by subsurface flow, *in* Higgins, C. G., and Coates, D. R., eds., Groundwater Geomorphology; The Role of Subsurface Water in Earth-Surface Processes and Landforms: Boulder, Geological Society of America Special Paper 252, p. 1-28.

Harrison, K. P., and Grimm, R. E., 2005, Groundwater-controlled valley networks and the decline of surface runoff on early Mars: Journal of Geophysical Research-Planets, v. 110, no. E12.

Higgins, C. G., 1984, Piping and sapping; development of landforms by groundwater flow, *in* LaFleur, R. G., ed., Groundwater as a geomorphic agent: Boston, Allen and Unwin, p. 18-58.

Hinds, N. E. A., 1925, Amphitheatre valley heads: Journal of Geology, v. 33, no. 816-818.

Kochel, R. C., and Piper, J. F., 1986, Morphology of large valleys on Hawaii - evidence for groundwater sapping and comparisons with Martian valleys: Journal of Geophysical Research-Solid Earth and Planets, v. 91, no. B13, E175-E192.

Laity, J. E., and Malin, M. C., 1985, Sapping processes and the development of theater-headed valley networks on the Colorado Plateau: Geological Society of America Bulletin, v. 96, p. 203-217.

Lamb, M.P., Dietrich, W.E., Aciego, S.M., DePaolo, S.M., Manga, M., 2008a, Formation of Box Canyon Idaho by megaflood: Implications for seepage erosion on Earth and Mars. *Science* (in press).

Lamb, M. P., Dietrich, W. E., and Venditti, J., 2008b, Is the critical Shields stress for incipient sediment motion dependent on channel-bed slope?: Journal of Geophysical Research (in press).

Lamb, M. P., Howard, A. D., Dietrich, W. E., and Perron, J. T., 2007, Formation of amphitheater-headed valleys by waterfall erosion after large-scale slumping on Hawaii: Geological Society of America Bulletin, v. 119, p. 805-822. doi:10.1130/B25986.1.

Lamb, M. P., Howard, A. D., Johnson, J., Whipple, K., Dietrich, W. E., and Perron, J. T., 2006, Can springs cut valleys into rock?: Journal of Geophysical Research, v. 111, no. E07002, doi:10.1029/2005JE002663.

Malin, M. C., and Carr, M. H., 1999, Groundwater formation of Martian valleys: Nature, v. 397, no. 6720, p. 589-591.

Pieri, D., 1976, Distribution of Small Channels on Martian Surface: Icarus, v. 27, no. 1, p. 25-50.

Sharp, R. P., and Malin, M. C., 1975, Channels on Mars: Geological Society of America Bulletin, v. 86, no. 5, p. 593-609.

Sklar, L. S., and Dietrich, W. E., 2004, A mechanistic model for river incision into bedrock by saltating bed load: Water Resources Research, v. 40, no. 6.

Stearns, H. T., 1936, Origin of the large springs and their alcoves along the Snake River in southern Idaho: Journal of Geology, v. 44, p. 429-450.

Chapter 2

Can Springs Cut Canyons into Rock?

2.1. Introduction

The common expression of river incision into irregular uplands is a network of roughly V-shaped valleys and intervening ridges, the amplitude of which diminishes towards the drainage divide. Deep amphitheater-headed valleys cut into relatively undissected uplands are strikingly different, and, where a full network develops, the form is distinctly stubby in appearance (Figure 1). Such channel networks would seem to require different processes than simply fluvial or debris flow incision. For over 100 years [e.g., *Russel*, 1902; *Hinds*, 1925; *Wentworth*, 1928; *Higgins*, 1984; *Baker*, 1990], it has been argued that the amphitheater shaped heads arise from the effects of groundwater exfiltrating along the base of a headwall, leading to mechanical and chemical breakdown and eventual collapse of the valley head front. Such channel networks are relatively uncommon, albeit spectacular where they occur, and had received little attention until early photographic images of Mars revealed numerous occurrences there [*Sharp and Malin*, 1975; *Pieri*, 1976; *Carr and Clow*, 1981]. Since then it has become generally accepted that the amphitheater shape is a reliable indicator

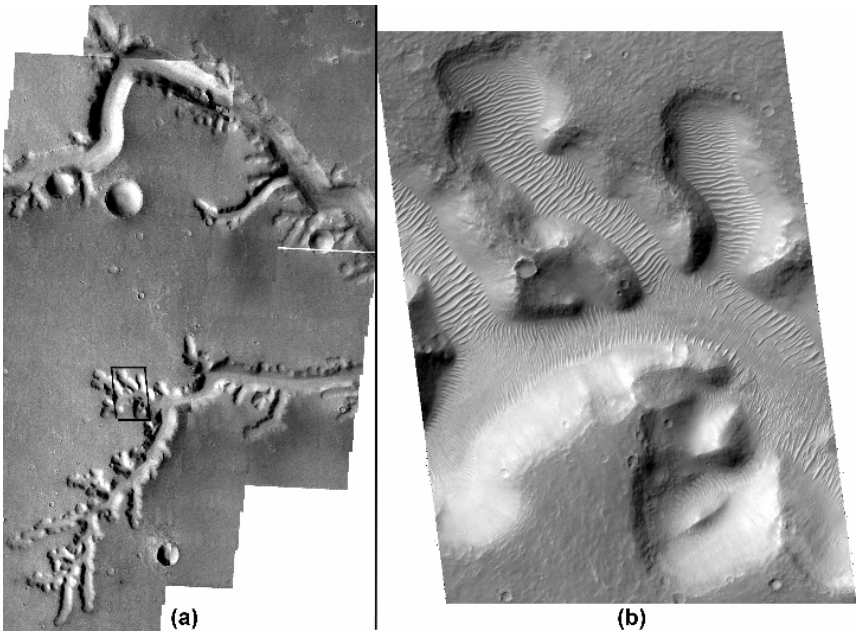

Figure 1. Nirgal Valles on Mars. (a) Nirgal Valles main channel (top) and stubby, branching tributaries (bottom). Mosaic of THEMIS VIS images V07929005, V01962005, and V1600005. Image width about 27.6 km. North to top of image. Mosaic centered at about -27.2ºS and 317.0ºE. (b) Detail of tributary headwalls from MOC NA image E02-02651, image width 2.89 km. Location of image shown by box in (a). Ridges along channel floor are eolian megaripples. Eolian infilling, mass wasting and impact cratering have infilled the valley floors and reduced the steepness of the valley walls, so that no definitive inferences can be made about the processes forming the valley network.

of groundwater outflow driven erosion, with important consequences for interpreting the hydrologic cycle and potential for life on Mars [*Baker*, 1982; *Tanaka*, 1986; *Squyres*, 1989; *Squyres and Kasting*, 1994; *Malin and Carr*, 1999; *Gulick*, 2001; *Aharonson et al.*, 2002; *Jaumann and Reiss*, 2002]. Inspired by Mars observations, studies have been conducted on what appear to be terrestrial analogs, especially in the American Southwest [*Laity*, 1983; *Laity and Malin*, 1985; *Howard and Kochel*, 1988] and Hawaii [*Kochel and Piper*, 1986; *Kochel and Baker*, 1990]. It has become commonplace in terrestrial studies to assume spring-driven erosion processes ("seepage erosion" *sensu* Dunne [1990]) based largely on valley topographic form [*Mars channel working group*, 1983; *Higgins*, 1984; *Baker*, 1990; *Uchupi and Oldale*, 1994; *Hoke et al.*, 2004].

Caution has been proposed regarding this morphometry-based inference. Howard [1988] and Howard and Kochel [1988] review terrestrial field studies and Mars observations and conclude that morphometric features may not be uniquely associated with seepage erosion. They emphasize that, due to bedrock strength (which demands seepage weathering precede seepage erosion) and the large size of amphitheater-shaped canyons on Mars, enormous discharges of water (requiring repeated recharge of upslope drainage areas) would be necessary to create these canyons by seepage erosion (if it in fact occurs). Here we further question the reliability of morphometric features as indicators of seepage erosion. We develop this proposal by first reviewing where seepage erosion unambiguously leads to amphitheater shaped valley heads—in loose sediment. We then summarize numerous studies that have proposed seepage erosion in bedrock, emphasizing ones since 1988, and conclude that the evidence is most often

ambiguous. This leads to a reanalysis of the two most cited terrestrial analog sites: the Colorado Plateau and Hawaii. While some seepage weathering due to salt precipitation clearly takes place in the Colorado Plateau, spring flow is not able to remove boulders and gravel that tumble onto the canyon floor. Moreover, high-magnitude flash floods capable of transporting boulders and incising into coherent rock are a common occurrence in this landscape and must have contributed significantly to the long-term evolution of these canyons. In Hawaiian basalts, we have found no direct evidence of seepage erosion. Instead, waterfalls appear to dominate erosion at the valley heads and runoff is necessary to transport collapsed material. Finally, we review the evidence for seepage erosion on Mars. We conclude that unreliability of morphologic criteria, coupled with the lack of local evidence of erosion processes (e.g., alcoves, seepage faces, boulder beds) due to post canyon formation modifications by mass wasting, eolian deposition and impact effects, makes the case for seepage on Mars equivocal.

2.2. Seepage Erosion Definitions

In this paper we follow the terminology proposed by Dunne [1990]. *Seepage* is groundwater that emerges from rock or sediment. Weathering processes that are facilitated by seepage (e.g. salt precipitation, chemical dissolution or frost growth) are collectively referred to as *seepage weathering*. The removal of mass from a seepage face is termed *seepage erosion*. In unconsolidated sediments, seepage erosion can occur in the absence of seepage weathering if the discharge of seepage water is sufficient to detach and mobilize the sediment. However, in rock, seepage weathering is needed to render the rock cohesionless before seepage erosion can occur. *Sapping*

describes processes that undercut or undermine a scarp leading to an overhang. A variety of processes cause sapping (e.g. cut bank erosion by a meandering river, wave erosion of a sea cliff, seepage erosion at the base of a scarp or headwall, plunge pool erosion at the base of a waterfall). The term *groundwater sapping* then refers to sapping induced by seepage erosion.

2.3. Seepage Erosion in Sediment

By far the most conclusive studies connecting seepage erosion to valley morphology have been in sediments with little to no cohesion. Here, we briefly summarize studies on seepage erosion in sediments to motivate our discussion of seepage erosion processes in rock. For earlier, more encompassing reviews of seepage erosion in sediments the reader is referred to Higgins [1984] and Dunne [1990]. Seepage can carve valleys in sand by undermining the seepage face and evacuating collapsed sediment [*Kochel et al.*, 1985; *Howard and McLane*, 1988; *Owoputi and Stolte*, 2001; *Schorghofer et al.*, 2004]. The eroding headwall lowers the local hydraulic head focusing groundwater flow to the seepage face, which in turn accelerates erosion of the seepage face. This feedback, first envisioned by Dunne [1980], has been shown to produce valleys with amphitheater heads in sand boxes [*Howard and McLane*, 1988], sandy beaches [*Higgins*, 1982], and in numerical simulations [*Howard*, 1995]. The rate of headward erosion is primarily limited by the capacity of the seepage water to transport sediment from the seepage face, which scales with seepage discharge [*Howard and McLane*, 1988]. If a valley becomes choked with colluvium it will

transmit the water through the colluvium (as groundwater) and thus shut off seepage erosion [*Dunne*, 1990].

Larger amphitheater-headed valleys carved into loose sediments have also been attributed to seepage erosion. For example, headcut erosion in gullies or headwater hollows are often attributed to seepage erosion [*Higgins et al.*, 1990; *Dietrich and Dunne*, 1993]. A relict seepage erosion origin has been postulated for the flat-floored amphitheater-headed valleys formed in glacial outwash sediments of Cape Cod and Martha's Vineyard and Nantucket Islands, Massachusetts [*Uchupi and Oldale*, 1994]. Similarly, large amphitheater-headed valleys cut into Quaternary shallow marine and terrestrial sands and gravels in South Taranaki, New Zealand, have been attributed to seepage erosion [*Pillans*, 1985]. In the Canterbury Plain, New Zealand, Schumm and Phillips [1986] described similar seepage erosion valleys carved into fluvial deposits from Pleistocene drainage of the Southern Alps. However, they concluded that the valleys were originally formed from runoff processes and were later widened by seepage erosion resulting in amphitheater-headed morphologies. They postulated that valley growth is limited by the competence of the flow to transport the coarser gravels that form a lag on the valley floor and that precipitation-induced runoff is probably necessary to remove these gravels.

Schumm et al. [1995] proposed that valleys in the Florida panhandle in essentially unconsolidated sediments of the Pleistocene Citronelle formation were formed by seepage erosion. The valleys typically have vegetated angle-of-repose walls, symmetric amphitheater heads (locally known as "steepheads"), flat bottoms, short first order streams, and springs emerging from sands and sandy clays at the bottom of the

valley headwalls. Very high infiltration rates into the unconsolidated sediment and dense vegetation are consistent with a lack of channels upslope of the amphitheater heads. Amphitheater-headed valleys are found in non-marine quartz sands with discontinuous layers of clay, indurated "hardpans", and gravel [*Schumm et al.*, 1995], as well as unconsolidated beach sands [*Lobkovsky et al.*, 2005] suggesting that lithologic strength or permeability contrasts are unimportant in setting the first-order morphology of these valleys.

In sediments finer than sands, erosion at the seepage face is typically limited by detachment of the grains, rather than the ability of the water to transport sediment. In silts and clays the permeability is low such that the groundwater discharge is often less than that required to overcome the cohesive forces of the grains [*Dunne*, 1990] and channelized runoff, sometimes aided by moisure-induced disaggregation of the sediment, is the dominant erosive agent. Feedback processes in cohesive sediment often cause tunneling or piping [*Jones*, 1981; *Higgins*, 1984; *Dunne*, 1990].

2.4. Seepage Erosion in Rock

Dunne [1980] proposed that seepage erosion processes similar to those observed in sediments could occur in rock. Before rock can be eroded by seepage, however, it must first be rendered cohesionless by seepage weathering [*Dunne*, 1980; *Dietrich and Dunne*, 1993]. Dunne [1980] envisioned seepage weathering occurring as emerging groundwater weakens the bedrock while increasing its porosity and hydraulic conductivity through chemical weathering. For example, in Vermont, Dunne [1980] described siliceous and calcareous granulite bedrock that was friable and stained brown

where springs emerged along joints. Once weakened to the point of cohesionless sediment, the material can be removed through drag forces induced by the flowing seepage water in the manner described above for seepage erosion in sediment. Seepage erosion at the base of a headwall might then lead to undermining (i.e., sapping), collapse of the rock above, and retreat of the headwall. Similar to seepage in sediments, Dunne [1980] proposed that focusing of groundwater discharge at the channel head and seepage weathering form a positive feedback leading to the formation of channels through the retreat of the headwall. Thus, channels could be initiated and extended creating channel networks without the aid of surface runoff.

Howard [1995] showed numerically that amphitheater-headed valleys can form from seepage erosion in rock if the erosion rate of the valley head scales with groundwater discharge. Such a relationship has been used in models of landscape evolution [*Willgoose et al.*, 1991; *Stark*, 1994; *Howard*, 1995; *Hovius et al.*, 1998]. However, potential seepage weathering mechanisms (e.g. chemical weathering, wetting and drying, freeze-thaw, salt wedging, root wedging, and ice needle growth [*Higgins*, 1984]), have yet to be investigated quantitatively. It is possible that for some of these mechanisms, weathering rate is inversely related to seepage discharge. For example, weathering due to salt precipitation facilitated by seepage evaporation [e.g. *Laity*, 1983] could be less effective if seepage discharge exceeds the evaporation rate [*Mason and Pederson*, 2004]. Freeze-thaw processes might be less effective for large springs with a greater thermal inertia. For these cases, the feedback between headwall retreat and seepage erosion, described above, could be negative. Focusing of groundwater flow

towards the migrating headwall [*Dunne*, 1980] would then cause a decrease in seepage weathering and an eventual demise of the canyon.

It is difficult to observe seepage erosion in bedrock because, if it occurs, it requires long timescales. Therefore, valleys formed by seepage erosion are often identified based largely on their form [e.g. *Baker*, 1982; *Mars channel working group*, 1983; *Higgins*, 1984; *Kochel and Piper*, 1986; *Baker*, 1990; *Luo*, 2000; *Hoke et al.*, 2004]. These studies typically assume that seepage erosion valleys in rock have amphitheater heads, drawing on the studies of seepage erosion in sediments.

Instead of a morphometric analysis, we focus here on mechanistic evidence for seepage erosion. In order for seepage to erode a bedrock canyon it must be able to 1) weather the seepage face and 2) transport collapsed material. Similarly, if a case is to be made for surface runoff, it must be able to do the same - erode bedrock and transport sediment. Physical erosion of bedrock by surface runoff is known to occur by a variety of mechanisms (e.g. abrasion, plucking and cavitation [*Whipple*, 2004]) and some process-based rate laws for quantifying geomorphic change due to these processes have been developed [e.g. *Whipple et al*., 2000; *Sklar and Dietrich*, 2004]. Unfortunately, seepage weathering and erosion in rock have not been quantified nor have mechanistic rate laws been proposed. In fact, in most studies the mechanism by which seepage erosion occurs has not been identified. Thus, deciphering the processes responsible for weathering or eroding a bedrock headwall is necessarily qualitative. For seepage weathering and erosion, we expect weathered and mechanically weakened rock, secondary porosity, and alcoves around the seepage face. For runoff processes, we expect scoured bedrock, plucked blocks and plunge pools. A spring does not

necessarily indicate seepage erosion, just as a waterfall does not necessarily indicate plunge pool erosion. Many large springs exist that are not associated with amphitheater-headed valleys [e.g. *Whiting and Stamn*, 1995]. It should be noted that this qualitative description of erosion processes does not prove process dominance for valley formation. Rather, these observations provide the first step towards mechanistic hypotheses for amphitheater valley formation, which will then require further exploration through the development and testing of quantitative geomorphic rate laws [e.g. *Dietrich et al.*, 2003].

In addition to bedrock erosion and weathering, evacuation of collapsed material from the valley headwall also provides a necessary constraint for valley formation, which fortunately can be assessed quantitatively with sediment transport theory. The talus of collapsed rock from above the seepage face is not likely to be weathered by seepage, at least initially. If the talus cannot be removed, it will eliminate the exposed seepage face [*Dunne,* 1990] and buttress the headwall, preventing further retreat and leading to the demise of the canyon. As talus accumulates on the valley floor, it might reach a slope in which sediment transport can occur. However, if this slope is greater than the regional topographic slope updip of the retreating headwall, the headwall will decrease in height as it migrates upstream, again leading to the eventual demise of the canyon (Figure 2). Thus, large discharges of water or steep regional slopes are required to maintain an upslope propagating headwall, or substantial time is required to weather the talus to transportable sizes.

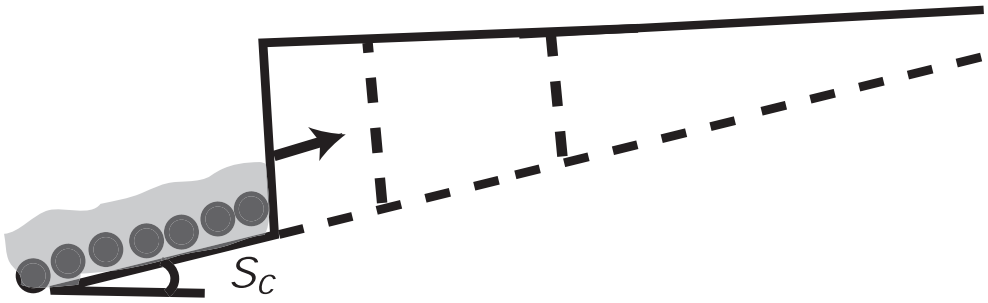

Figure 2. Schematic of upslope headwall propagation due to seepage erosion, illustrating the necessary condition of debris removal. If the discharge is not sufficient to transport collapsed debris at a given slope, the bed will aggrade until the slope surpasses the critical slope necessary for transport. If this critical slope S_c is greater than the regional topographic slope, then the headwall will diminish in height as it propagates upslope, eventually leading to the demise of the canyon.

2.4.1. Case Studies

Mastronuzzi and Sanso [2002] examined valley networks developed in the permeable limestone and calcarenite in the Apulia region of southern Italy. These valleys are currently dry, but Mastronuzzi and Sanso reason that high water tables during sea level high stands might have promoted seepage erosion at the valley heads. They suggested that the low relief of the region caused a lack of overland flow and high infiltration rates. Besides the morphometric evidence, they mentioned notches, tafoni, and caves along the valley walls. These erosional forms likely indicate some seepage or groundwater erosion. Due to the calcareous substrate, erosion might have occurred by dissolution.

In Yorkshire, England, a plateau consisting of lower Jurassic calcareous grit and upper Oxford Clay is cut by amphitheater-headed valleys [*Nash*, 1996]. The upper portion of the lower calcareous grit sandstone has more silica cementation and defines that plateau. The lower calcareous grit provides a permeable aquifer bounded roughly on the bottom by the upper Oxford Clay. Groundwater emerges along bedding planes in a 20-30 cm thick zone. Rock above the seepage zone shows little evidence for weathering while rock below the seepage zone shows substantial weathering with material broken down into centimeter-sized angular pieces. There is an increase in jointing and fracturing along the bedding planes in the seepage zone. Like the Apulia valleys, dissolution might be important particularly because of the calcareous substrate. Alternatively, the calcareous grit is weakly consolidated and hydraulic forces might be sufficient to mobilize grains with little or no seepage weathering. Nash [1996] proposed that seepage erosion was responsible for headward development of the

valleys. However, he stressed that there also has been significant contribution from surface runoff with channels evident upstream of the valley headwalls and that much of the drainage network was originally formed by surface flow from glacial meltwater.

Some soil or sediment mantled bedrock valleys have been proposed to have a seepage origin. Here it is unclear if seepage erosion is occurring in the soil, bedrock, or both. For example, Onda [1994] reports on amphitheater-headed valleys in Obara, Japan where a thick soil covers granodiorite bedrock. Seepage erosion was observed in the soil. The deep amphitheater-heads of the valleys, however, suggest that the form of the valleys is expressed in the bedrock, not just in the soil cover. It is unclear how the erosional processes in the soils affect the bedrock. Onda [1994] proposed simultaneous seepage erosion in rock at the soil-rock interface through enhanced chemical weathering and in soil at the soil-air interface where visual observations of seepage erosion were made. Another possible explanation might be that in reducing the soil thickness, seepage erosion indirectly increased the erosion of bedrock at the valley head by increasing the rate of local soil production [e.g. *Heimsath et al.* 1997]. It also remains possible that the soil is a thick as the valley relief and the valleys is not cut into the underlying bedrock. In this case, the amphitheater form is a result of seepage erosion in the soil only. For example, in his Vermont study site, Dunne [1980] noted seepage erosion in the sediment, but did not document erosion of the underlying substrate.

Two studies in areas underlain by basalt deserve mention here due to the potential of a similar lithology on Mars [*Scott and Tanaka,* 1986]. Based on overhangs near plunge pools, Pederson [2001] interpreted seepage erosion to be an important erosional process at Akaka and Rainbow Falls that spill over basaltic bedrock on the

island of Hawaii. We observed in August 2004 that the alcoves near the base of these waterfalls seem to be associated, at least spatially, with the waterfall plunge pools. Although the alcove at Rainbow Falls is almost cave-like and extends on the order of 10 m behind the waterfall, we found semi-circular lines of twigs and debris deep within the alcove indicative of plunge pool spray. Macdonald et al. [1983] interpreted the alcove at Rainbow Falls to be the result of a weaker lava bed overlain by a more resistant waterfall-forming bed. Bedrock scours and potholes upstream of Rainbow Falls indicate that surface flow can cause substantial erosion of the more resistant bedrock. Thus, headwall retreat via plunge-pool undercutting of the weaker bed seems plausible.

Several large amphitheater-headed valleys exist as tributaries to the Snake River near Hagerman, Idaho. These valleys were first proposed to have a seepage erosion origin by Russel [1902] and later by Stearns [1936] because of their amphitheater heads and because some of the largest springs in North America emanate from their heads. In addition, there is no overland flow currently entering the canyons and there is little development of a drainage network upslope of the canyons (Figure 3). We have begun to study one of these canyons, Box Canyon, which has the 11th largest spring in the United States (~ 10 m^3/s, [*Meinzer*, 1927, USGS gauge 13095500]) emanating from the base of its headwall (Figure 4). Box Canyon was carved into near-horizontal layered flood basalts, named Sand Springs Basalt [*Stearns*, 1936], with an age of ~ 95 ka [*Tauxe et al.*, 2004]. Stearns [1936] postulated that Box Canyon was formed by rock dissolution and that the absence of talus at the head of the canyon in comparison to its side walls is evidence of continued dissolution where most of the seepage occurs (Figure 4). Our qualitative observations at the head of the canyon, however, indicate

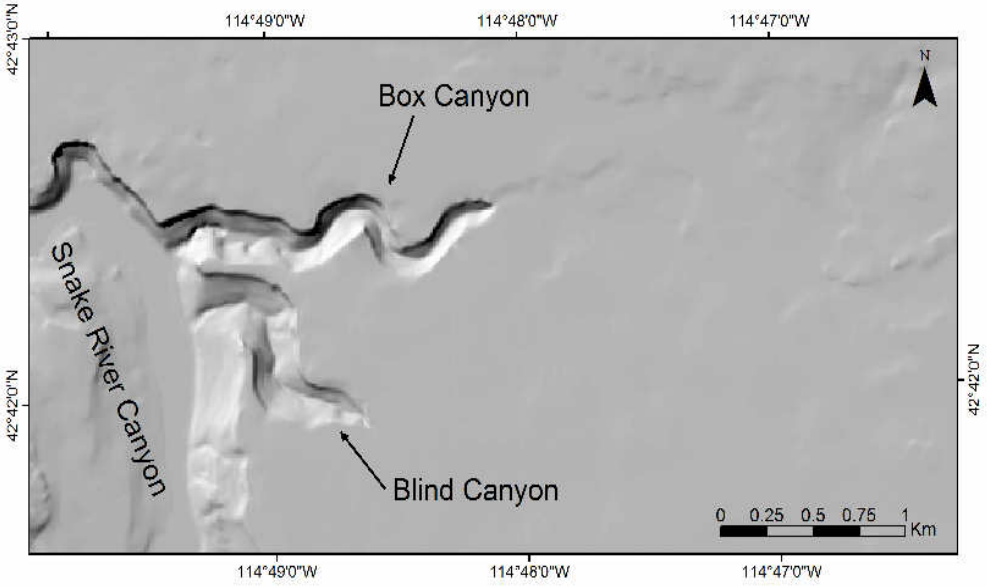

Figure 3. Shaded relief map of 10 m topographic data (USGS NED) of Box and Blind Canyons, Idaho. Although the regional topographic slope dips towards the canyon, the landscape is largely undissected upslope of the canyons, which end in near vertical headwalls.

that the rock does not appear mechanically weaker or more weathered than rock found elsewhere in the region. In fact, the most weathered boulders are found well downstream from the channel head. The water that feeds Box Canyon is from the Snake River Plain aquifer, which extends over much of southern Idaho and is composed almost entirely of flood basalts. Water samples taken by the U.S. Geological Survey from Box Canyon creek and neighboring wells indicate silica concentrations typically ranging from 32-35 mg/L, which bracket the saturation value of approximately 33 mg/L [*Faure*, 1998] (for dissolved Quartz and amorphous silica at 14 degrees Celsius and pH = 8, conditions typical of Box Canyon [USGS gauge]). Thus, enhanced chemical weathering does not appear to be occurring at the seepage face. Further, there are numerous large springs in close proximity to Box Canyon that are fed by the same basaltic aquifer and do not have canyons associated with them. For example, Thousand Springs is located along the wall of the Snake River canyon about 2 km from Box Canyon and emits ~ 34 m^3/s, which is more than three times that of Box Canyon, and does not have an alcove. The basalt in Box Canyon breaks down into large (~ 1 m) boulders that, without weathering, must be transported away from the canyon head to allow canyon growth. Despite the great discharge of the spring, no measurable amount of sediment is currently being transported through Box Canyon. We have begun to document evidence for a large flood that would have been capable of moving the boulders [*Lamb et al.*, 2004]. This hypothesis is supported by bedrock scours at the rim of the headwall and semi-circular talus-free regions at the head of the canyon indicative of plunge pools (Figure 4). The origin of Box Canyon is the topic of our future

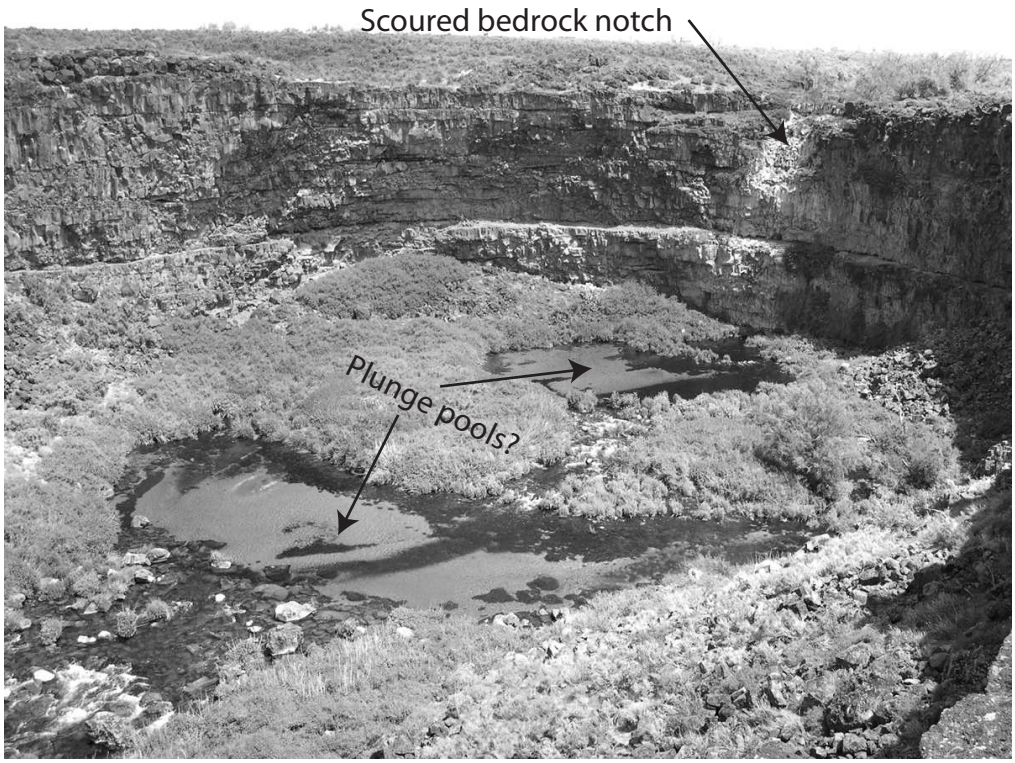

Figure 4. Photograph of the headwall of Box Canyon. Spring water is discharged from the base of the headwall below the water line. Note the absence of talus near the headwall and the semi-circular boulder-free regions possibly indicating plunge pools. A scoured notch at the rim of the canyon indicates some overflow in the past. Headwall relief is approximately 40 m.

research, but at this preliminary stage we can conclude that a waterfall origin seems at least as likely as a seepage-erosion origin.

2.4.2. The Colorado Plateau

Perhaps the most studied bedrock valleys attributed to seepage erosion are amphitheater-headed canyon tributaries to the Colorado, San Juan, and Escalante Rivers [*Laity,* 1983; *Laity and Malin,* 1985; *Howard and Kochel,* 1988]. These canyons are developed primarily at the lithologic contact where the permeable eolian Navajo sandstone overlies impermeable mudstones and sandstones of the fluvial Kayenta Formation (Figure 5). The case for formation of these valleys by seepage erosion was most strongly argued by Laity and Malin [1985]. In their conceptual model, groundwater flows out along the contact between these two formations because of the contrast in permeability. Weathering and erosion are accelerated where seepage occurs, primarily through salt weathering in which salt crystal growth, associated with groundwater exfiltration and evaporation, causes breakup of the bedrock, leading to focused undermining and alcove development [*Laity,* 1983]. Some amphitheater heads are near drainage divides suggesting that minor groundwater flow can be effective in advancing canyon headwalls. Navajo sandstone blocks appear to break down easily to sand once dislodged from cliffs, given the limited amount of coarse debris on canyon floors. This absence of coarse load might allow spring flows or possibly wind to carry away residual sand.

Although we agree that direct evidence for groundwater seepage and seepage weathering at the Navajo-Kayenta contact is clear, the relative importance of seepage

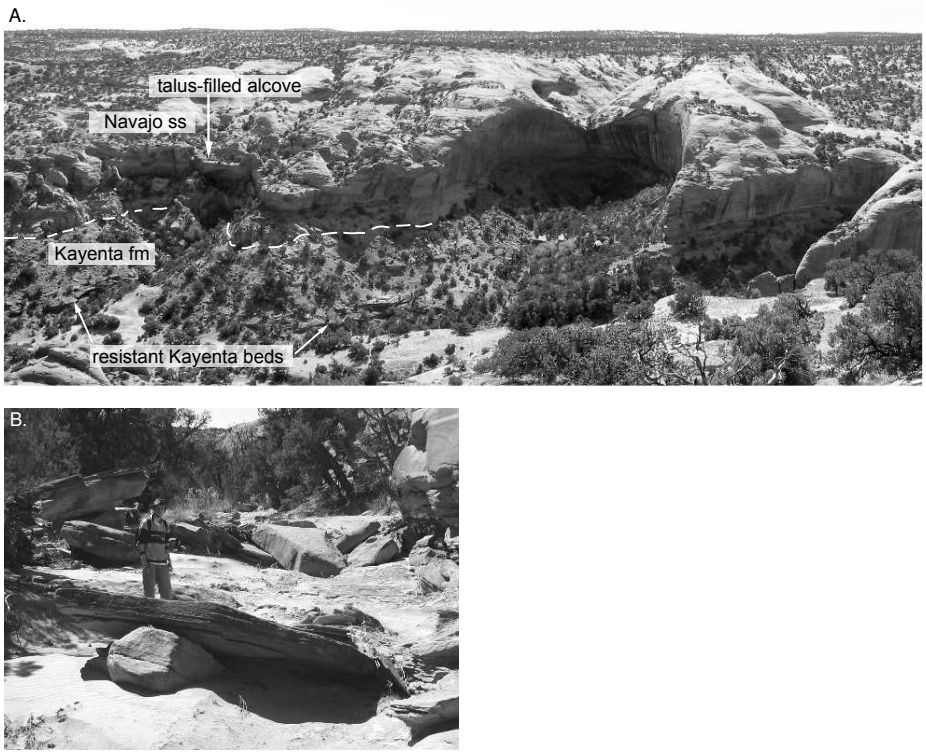

Figure 5. (a) Panoramic view into a large alcove ~400 m east of Wildcat Seep in Horseshoe Canyon (Head Spur Quadrangle, Utah). The contact between the eolian Navajo sandstone above and the fluvial Kayenta formation below is marked; note that the valley bottoms downstream of the alcoves are significantly inset into the Kayenta formation due to fluvial channel incision into both weak mudstones and resistant fluvial sandstones that form ledges. These resistant Kayenta beds form large boulders that the fluvial channels transport in large flash floods, as indicated in 8b. Also note that the fluvial channel above the well-developed alcove has incised significantly into the Navajo sandstone (making a "v" shaped notch), and that the headwall with little drainage area to the left is filled in with collapsed talus that has not been excavated. (b) Large, primarily Kayenta boulders in the fluvial channel a short distance downstream of the alcove at Wildcat Seep. Note the imbricated stacking of the slabs, indicating fluvial transport.

processes versus surface flow processes in setting both valley morphology and headwall retreat rate is ambiguous. Howard [1988; 1994] and Howard and Kochel [1988] provide detailed reviews of evidence for and against a dominant role of seepage erosion in the formation of these valleys. Here, based on our field observations, we further demonstrate the importance of overland flow in transporting sediment and eroding bedrock in this arid environment, and the role of lithologic controls in canyon formation.

Flash flood discharges caused by rapid surface flow across the bedrock uplands greatly exceed spring flows. For example, in three years of monitoring, Dick et al. [1997] measured a flash flood discharge of ~0.9 m^3/s from ~1 km^2 drainage area in this region. Spring discharges from the Navajo sandstone are nearly three orders of magnitude smaller, with maximum measured flows from about 0.001 m^3/s [*Gregory*, 1916] to 0.003 m^3/s [*Laity and Malin*, 1985]. The strong role of precipitation runoff in transporting sediment is illustrated by the dramatic headcut advance of an interior channel (i.e. arroyo) that occurred in a tributary of Toenlushushe Canyon, Arizona between 1985 and 2004 (Figure 6). The arroyo incised into primarily fine alluvial sediment that was probably deposited during the aggradational epoch of the present arroyo cycle that ended by about 1880 [*Cooke and Reeves*, 1976]. This aggradation was followed throughout much of the Southwest by deep incision. Based upon measurements we made from aerial photographs and topographic maps, the ~ 18 m high headcut progressed about 400 m over the 19 years between pictures (Figure 6). Simple hydraulic calculations suggest that a 0.003 m^3/s spring flow would only fill the arroyo with approximately 1 mm of water (neglecting infiltration and evaporation and using

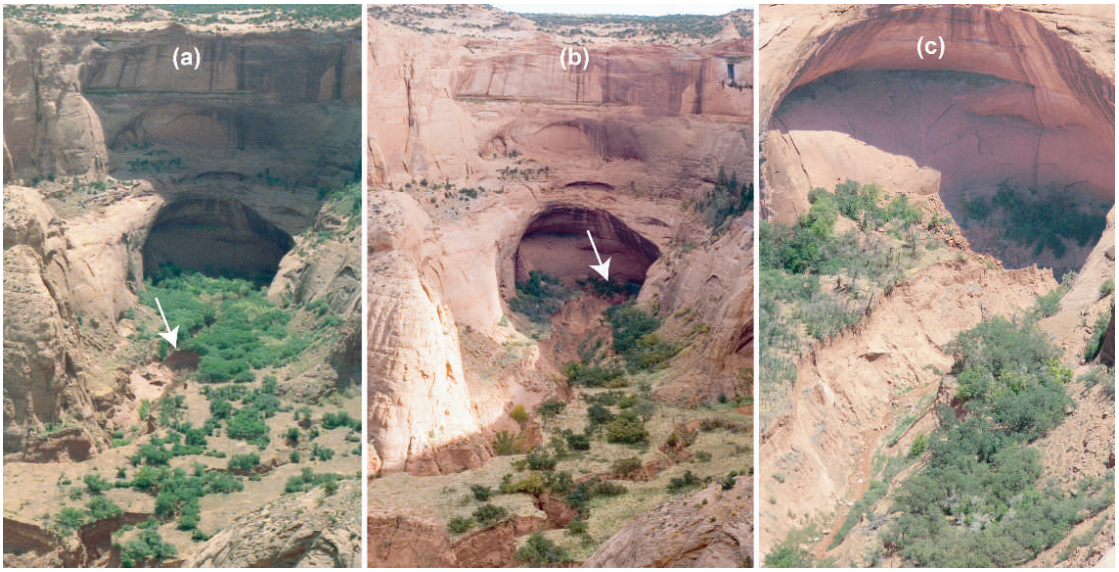

Figure 6. Erosion of alluvial fill in a tributary to Toenleshushe Canyon, Navajo Indian Reservation, Arizona. (a) View of valley and alcove headwall in 1985. Note the densely vegetated and nearly undissected alluvial fill near the headwall. (b) View in 2004, showing extensive removal of alluvial fill and vegetation near the headwall. Note that viewpoints are slightly different. (c) Detail of alcove headwall in 2004. Talus has been reexposed in the headwall, and meter-scale boulders occur within the entrenched channel. The headwall is centered at 36.669ºN and 110.776ºW on the 7.5' Inscription House Quadrangle.

Manning's equation with n = 0.03, slope of 0.02, and arroyo width of 48 m measured from U.S. Geological Survey quadrangle). Such a flow could not transport even the fine sand (~ 0.25 mm) found on the valley floor [*Buffington and Montgomery,* 1997]. In order for seepage flow with a constant discharge to transport the required sediment flux, the flow depth must exceed ~ 6.5 cm (based on Meyer-Peter and Muller [1948] equation for bedload transport, recently revised by Wong and Parker [*in press*], assuming a rectangular channel cross section, and a minimum average transport rate of 3.7×10^{-4} m^3/s calculated from the total volume of sediment, 2.2×10^5 m^3, eroded over a maximum time of 19 years. The volume of eroded sediment was calculated from the arroyo dimensions (18 m x 400 m x 48 m) assuming a porosity of 0.35.). The required sediment flux could only be achieved by the observed seepage discharge if the channel width was less than 9.8 cm. A channel with this aspect ratio, however, is unreasonable based on our observations of typical spring-fed channels which have width-to-depth ratios much larger than 2. Furthermore, meter-scale boulders in multi-boulder groupings are observed on the bed of the gully (Figure 6c), suggesting flows capable of transporting clasts of this size. The arroyo has a contributing drainage area of about 0.8 km^2 from two washes upslope of the canyon headwall. The inability of spring flow to transport significant amounts of fine sand, in contrast to the inferred transport of meter-scale boulders, suggests that flash floods from summer thunderstorms are responsible for most of the observed sediment excavation.

Amphitheater heads that drain moderate to large surface areas (where significant quantities of surface runoff can occur) typically have plunge pools associated with waterfalls. Figure 7 shows a survey of a typical alcove in Horseshoe Canyon, Utah,

with nearly 30 m of overhang. The slope from the point of maximum overhang down to the basal plunge pool is talus covered and at the angle of repose for non-cohesive material. Although the plunge pools are significantly smaller in diameter than the overall amphitheaters, their incision may enable retreat of the much wider canyon headwall by removing the surrounding sediment and talus. Figure 8 illustrates conceptually how vertical plunge pool incision will undermine the angle of repose apron on the seepage face, removing sediment and perhaps leading to deeper undermining of the overlying bedrock and its eventual collapse. This model still requires the formation of an angle of repose slope, which could come about from seepage weathering and collapse of material from above. However, undermining could also occur simply because of recessive weathering of Kayenta mudstone layers. In this way it is at least plausible that the amphitheater width is significantly wider than the plunge pool due to undermining unrelated to seepage.

Ultimately, to move sediment out of the channel, the downstream channel must remain steep enough to transport the sediment; this requires that alcove retreat be tied to incision on the downstream channel [*Howard and McLane*, 1988]. If seepage erosion alone were driving headwall retreat, the zone of maximum seepage and recession would be at the valley floor, which is rarely the case (e.g., Figure 7). Many of the fluvial channels just downstream of alcoves have incised into resistant beds of the Kayenta formation (Figure 5). These channels are commonly steep, such that boulders that fall onto the canyon floor or are excavated from the channel bed can be effectively removed by flash floods.

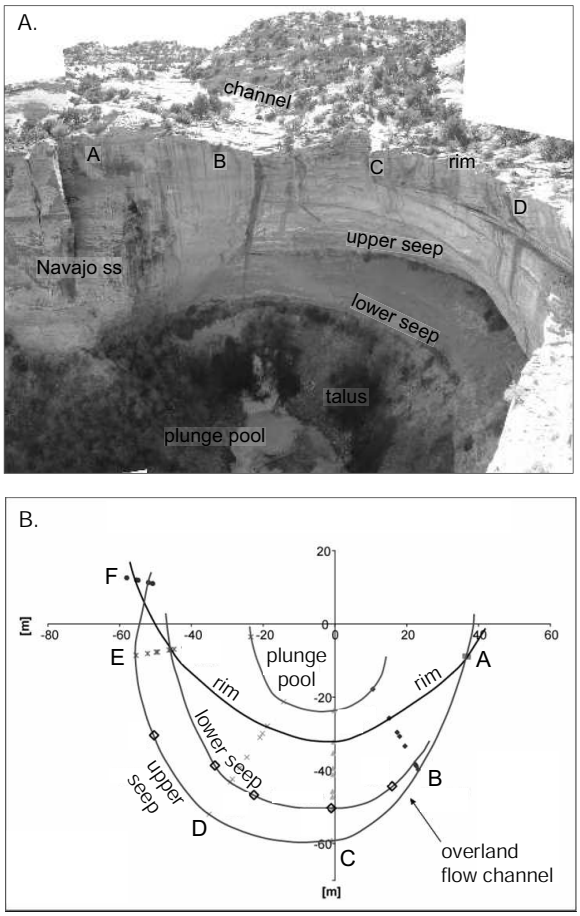

Figure 7. (a) Panoramic photograph of Burro Seep alcove of Horseshoe Canyon (Head Spur Quadrangle, Utah), just east of Canyonlands National Park. The contact between the eolian Navajo Sandstone above and the fluvial Kayenta formation below occurs at the lower seep level, significantly above the valley bottom. The plunge pool is ice-covered due to active seepage in this March 2002 photograph. Field observations verify that the talus-covered ramp is at the angle of repose for non-cohesive material, and is symmetric around the plunge pool. Drainage area above the alcove is 1.2 km^2. (b) Surveyed morphology of the alcove, shown in planview. Lines A-E correspond to surveyed cross sections in 7c. Measurements made by Simon Brocklehurst. (c) Surveyed cross section profiles of the alcove, showing vertical valley walls on the sides (profiles A, F) and nearly 30m of overhang in the center (D). The overhang is greatest in the center of the alcove and is notably offset from the entrance point of the main overland flow channel, although the current zone of most active seepage, indicated by ice on the talus ramp, occurs directly under the channel.

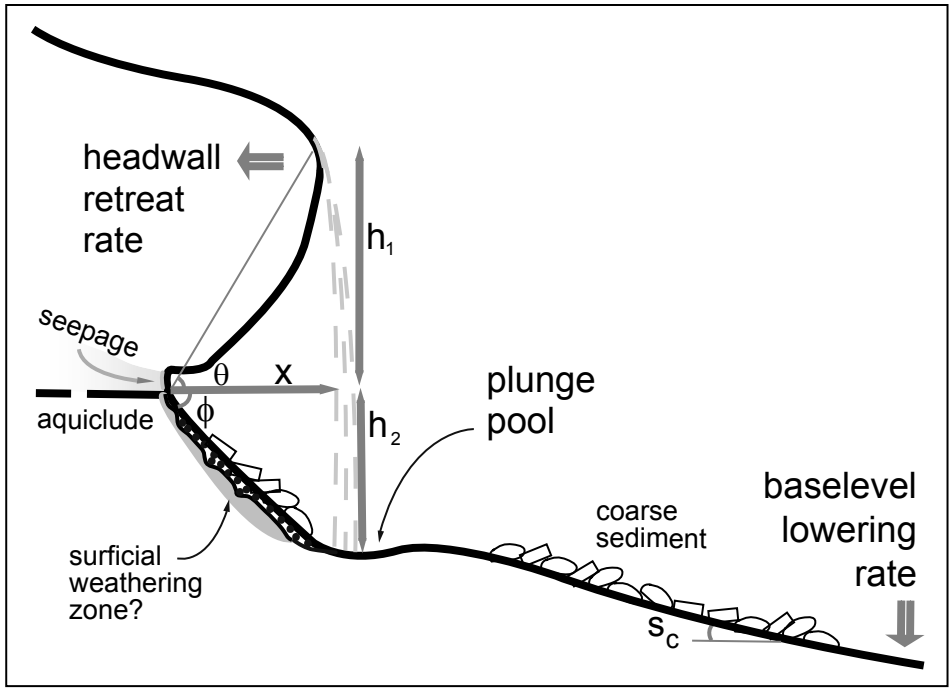

Figure 8. Conceptual model of some likely controls on alcove morphology and headwall retreat rate at the Navajo/Kayenta contact. Headwall morphology is dictated by: caprock strength (maximum θ) and thickness (h_1), which sets the critical overhang distance (x), plus the maximum stable angle of the weathered, typically sediment-covered zone (ϕ), in turn is set by the angle of repose for sediment or the residual strength of the weathered rock. The combination of overhang required for failure (x) and the critical slope (ϕ) of the seepage zone dictate the depth of incision below the upper seep required for headwall retreat (h_2), which is likely accomplished by plunge-pool scour and fluvial erosion. Ultimately, plunge pool downcutting may be limited by the baselevel lowering rate of the downstream fluvial channel because the channel must maintain a critical slope (S_c) that enables the transport of coarse sediment derived from incremental headwall collapse and downstream channel erosion.

The particular stratigraphy of nearly horizontal, permeable, and relatively unjointed (hence relatively strong to slope collapse) but easily weathered sandstone (Navajo formation) overlying an impermeable, mechanically weak strata (Kayenta formation) are essential to the emergence of the distinct canyons. Laity and Malin [1985] suggested that tributaries on the east side of the Escalante do not have amphitheater heads (in comparison to valleys on the west side) because, due to the dip of the Kayenta-Navajo contact, little groundwater flow is directed to the valley heads. Given the sensitivity of canyon morphology to exposure of Kayenta-Navajo contact, this comparison is incomplete because the east-side tributaries expose the recessive and impermeable upper Kayenta formation, while the west-side tributaries do not.

These observations suggest that the morphology of these canyons likely does not depend uniquely on seepage erosion processes. There are amphitheater valleys with little upland runoff and with groundwater seepage, where salt weathering forms local alcoves and mostly likely contributes to headwall retreat. However, in many instances, if not all, runoff in channels from overland flow is a contributor and in some cases may dominate the channel incision through plunge pool erosion and transport of collapsed debris. The particular geologic framework and the possibility of significant contributions from both surface runoff and seepage suggest that these canyons are at present an ambiguous analog for interpreting valley forming processes elsewhere.

2.4.3. Hawaiian Islands

The most cited examples of amphitheater-headed valleys in basalt are on the windward, wet sides of the Hawaiian Islands [*Hinds*, 1925; *Stearns and Macdonald*,

1946; *Macdonald et al.*, 1983; *Kochel et al.*, 1985; *Baker*, 1990; *Howard et al.*, 1994; *Craddock and Howard*, 2002; *Lamb et al.*, in review]. Some of the most spectacular are the Kohala valleys on the island of Hawaii (Figure 9). These valleys have U-shaped cross-sections in their lower reaches, and most of the headwalls are steep and semicircular in planform. In contrast, smaller valleys that run along side of and often drain into the larger canyons have more V-shaped heads in planform and lack steep headwalls.

The similarity of the Kohala amphitheater-headed valleys with those in the Colorado Plateau and in sand boxes (mainly the flat floors and steep headwalls) led Kochel and Piper [1986] and Kochel and Baker [1990] to argue that seepage eroded the Kohala canyons. Building upon earlier suggestions by Wentworth [1928] and Stearns and Macdonald [1946], they proposed that rapid chemical weathering induced by seepage at the intersection between dike-impounded water tables and streambeds caused the formation and subsequent undercutting of knickpoints. These knickpoints carved the valleys by propagating upslope, eventually forming the steep valley headwalls. The smaller valleys were not able to tap groundwater and therefore remained small.

If seepage erosion carved the Hawaiian valleys, springs must have been able to weather and erode the seepage face, as well as transport collapsed talus and boulders out of the valleys. The evidence for such processes is lacking. Well-developed alcoves, secondary porosity, or obviously weathered rocks are rare at valley heads [*Howard et al.*, 1994]. Furthermore, springs have not been found in some valley heads (e.g., Pololu valley [*Stearns and Macdonald*, 1946]). Where springs occur, the discharges are small and the flows are unable to transport the large (~ 1 m) basalt boulders that accumulate

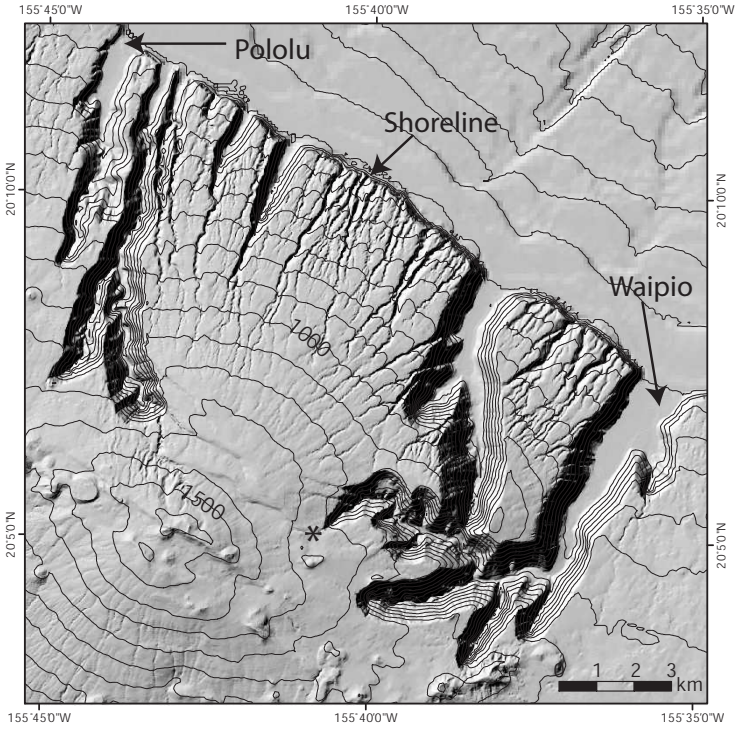

Figure 9. Shaded relief map of 10 m resolution topographic data and 90 m resolution bathymetric data of the Kohala region of Hawaii. 100 m contour interval. The 1000 m and 15000 m contours are labeled. Data from U.S. Geological Survey, Monterey Bay Aquarium Research Institute, and U.S. Army Corps of Engineers.

Figure 10. Photographs showing waterfall plunge pools at the head Waipio valley (indicated with "*" on Figure 9). Headwall relief is approximately 600 m. Note multiple waterfalls that appear to be vertically eroding plunge pools.

in the channels. For example, Waipio valley (Figure 9) has the greatest number and discharge of springs which range from 0.35- 0.96 m^3/s, with a cumulative discharge of 2.76 m^3/s [*Stearns and Macdonald*, 1946]. These springs, however, are dwarfed by Wailoa stream, which flows through the main section of Waipio valley with a mean annual-peak discharge of 120 m^3/s and a maximum recorded peak discharge of 241 m^3/s (USGS gauge 1632200).

Hawaiian amphitheater-headed valleys typically have waterfalls at their headwalls [*Stearns and Vaksvik*, 1935; *MacDonald et al.*, 1983]. These waterfalls are commonly stepped and appear to cause substantial erosion as indicated by the deep plunge pools interrupting the cascading falls (Figure 10) [*Howard et al.*, 1994]. Multiple active waterfalls along with mass wasting at the headwall could allow for the retreat of a headwall that is much wider than any individual waterfall [*Stearns*, 1985]. The retreat of a wide headwall, mass wasting of valley side walls, and the radial drainage pattern are all potentially important in capturing neighboring streams [*MacDonald et al.*, 1983]. The flat floors near the valley mouths, while previously argued to indicate groundwater sapping [*Kochel and Piper*, 1986; *Kochel and Baker*, 1990], are the result of alluviation of valley floors following island subsidence [*Stearns*, 1985; *Moore and Clague*, 1992]. Lamb et al. [2005; in review] combined these observations and proposed that the Kohala valleys formed from upstream propagation of huge knickpoints due to waterfall erosion, rather than seepage erosion. These knickpoints were most likely initiated by the headscarp of a huge flank collapse of Kohala volcano, the Pololu Slump [*Moore et al.*, 1994; *Smith et al.*, 2002], expressed as the present-day ~400 m sea cliffs. Smaller valleys might not have developed into

amphitheater-headed valleys because they have smaller drainage areas contributing to surface runoff [*Lamb et al.*, 2005; in review].

2.5. Amphitheater-Headed Bedrock Canyons: Alternative Interpretations

Amphitheater-headed valleys can arise from other processes in the absence of seepage, such as upstream advancing waterfalls where plunge pool erosion and mass wasting drive headwall retreat. Plunge pool processes in layered sediments are known to result in knickpoints [e.g. *Holland and Pickup*, 1976; *Robinson and Hanson*, 1996; *Hanson et al.*, 1997; *Bennett et al.*, 2000; *Bennett and Casali*, 2001]. These knickpoints can develop an amphitheater form as they advance upstream. For example, in the welded ash of the Ka'u desert, Hawaii, amphitheater-headed canyons have formed exclusively from plunge pool undermining by surface runoff [*Craddock et al.*, 2005] (Figure 11). Headwall propagation by waterfall erosion also occurs in more resistant rock [*Rosenblum and Anderson*, 1994; *Seidl et al.*, 1994; *Yoshida and Ikeda*, 1999; *Bollaert and Schleiss*, 2003; *Hayakawa and Matsukura*, 2003; *Bishop et al.*, 2005; *Crosby and Whipple*, in press]. For example, Niagara falls retreats upstream as the resistant limestone caprock fails due to plunge pool undercutting of the underlying mudstone [*Gilbert*, 1907], leading to an amphitheater-headed valley (Figure 12). An example in basalt are the series of amphitheater-headed tributaries of the Snake River, Idaho, (e.g. Blue Lakes Canyon) formed by the Eden Channel of the gigantic Bonneville Flood spilling over the walls of the Snake River Canyon [*Malde*, 1968; *O'Connor*, 1993].

Figure 11. Photograph of small amphitheatre-headed canyons eroded into layers of welded ash in the Ka'u desert on the island of Hawaii.

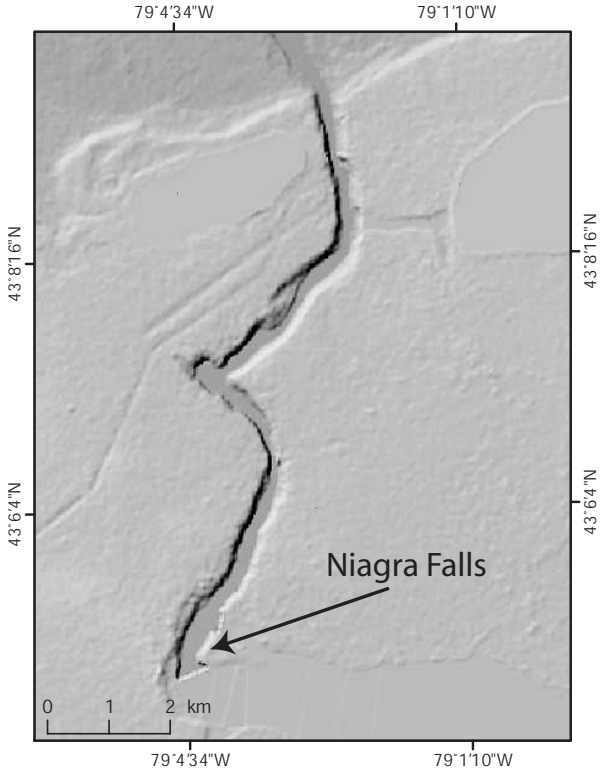

Figure 12. Shaded relief map of 30 m SRTM topographic data (US Geological Survey) of Niagara Falls. Lake Erie is to the north. Note that at this resolution the channel upstream of the waterfall is relatively indecipherable, such that the falls could be taken as the headwall of an amphitheatre-headed canyon.

In the aforementioned examples of amphitheater-headed valleys, an initial near-vertical face was imposed on the valleys by some external source, and therefore might be a necessary condition for the formation of amphitheater-headed valleys. For example, Box Canyon, as well as the canyons of the Colorado Plateau, grew outward from the deeply incised river canyons of the Snake River and the Colorado and San Juan Rivers, respectively. The Kohala valleys of Hawaii likely evolved from the steep headwall of the Pololu Slump [*Lamb et al.*, in review]. A near vertical headwall was typically used as the lower boundary condition in seepage-erosion sand box experiments [*Kochel et al.*, 1985; *Howard and McLane*, 1988]. On Mars, such knickpoints might be induced by the wall of a deeply incised river canyon or impact crater.

Perhaps a more important factor leading to an amphitheater head is the stability of the headwall relative to the resistance of the material to incision, rather than any particular erosion process, be it seepage or plunge pool erosion. One of the most obvious similarities between all of the amphitheater-headed valleys cited, whether carved in basalt or sediments, by seepage or waterfall, is that they have been eroded into a material consisting of relatively horizontal beds of varying strength. This configuration is relatively resistant to vertical incision, in that eventually a strong bed will need to be cut through. On the other hand, such materials are relatively susceptible to lateral retreat by backwasting of a near vertical face because a vertical face exposes weaker beds, which can then be undercut. The near horizontal layering also promotes stability of a vertical face, which leads to a more amphitheater-like shape [*Dunne*, 1990]. Vertical variations in rock strength are well illustrated in the layered sandstones

and mudstones of the Colorado Plateau. In the layered volcanic rocks of Hawaii and Box Canyon there might be subtle differences in rock strength for the different lava flows, but this is less obvious. However, basalts have an inherent anisotropy in their resistance to erosion because of fracturing. While basalt is relatively resistant to vertical incision by fluvial processes [*Sklar and Dietrich*, 2001], erosion by lateral back-wasting might be more effective because vertical columnar fractures allow the face to easily collapse (e.g. Figure 4). Stearns [1985] also suggested that vertical jointing and horizontal bedding in basalt makes it more prone to stand as a vertical headwall in Hawaii. In weak sedimentary rocks or sediments, subtle changes in grain size, such as a cohesive layer or a gravel lag, or vegetation cover might favor lateral retreat over vertical incision, and tend to produce a steep headwall. Even in seepage erosion experiments that used a homogeneous sand substrate [e.g., *Howard and McLane*, 1988], there was likely a vertical variation in the resistance to erosion because surface tension of pore water acted to provide cohesion above the seepage zone, allowing a near vertical headwall.

In some cases the rate of headwall retreat might be governed by the loss of strength and failure of the vertical face rather than any particular hydraulic process. Such a mechanism has been proposed for the formation of amphitheater-headed canyons along the Australian escarpment [*Young*, 1985; *Seidl et al.*, 1996; *Weissel and Seidl*, 1997]. Seepage or surface flow might then only play a role in evacuating collapsed material that would otherwise form a talus slope and buttress the headwall from further collapse.

2.6. Seepage Erosion on Mars?

Involvement of groundwater seepage in excavation of valley networks on the cratered highlands of Mars has been postulated in numerous studies [e.g. *Pieri*, 1980; *Carr and Clow*, 1981; *Baker and Partridge*, 1986; *Goldspiel and Squyres*, 2000; *Grant*, 2000; *Gulick*, 2001]. Difficulties in finding mechanisms for producing an atmosphere early in Martian history capable of supporting precipitation and runoff led to early suggestions that valley network erosion could be due to mobilization of water originally stored in the regolith. Erosion of valleys, however, requires volumes of water at least 100 times the volume of sediment removed in cutting the valley, even in the case of cohesionless sands [*Howard and McLane*, 1988]. For cohesive soils or indurated rock cumulative discharges greater than 10^5 times valley volume is required in terrestrial valley networks to accomplish weathering, bed erosion, and transport of sediment through the valley network [*Howard*, 1988; *Goldspiel and Squyres*, 1991]. This large water demand led others to suggest that flows through the valley networks might have been supplied by hydrothermally-driven flows from volcanic intrusions [*Gulick*, 1998; *Gulick*, 2001] or from crater impacts [*Tanaka et al.*, 1998]. Basal melting of the south polar cap has also been proposed as a source of water for groundwater seepage to cut valley networks [*Clifford and Parker*, 2001]. *Carr* [2002] notes, however, that many valley networks occur at elevations too high for this to have been a contributing source of water. Some valley networks with amphitheater headwalls originate high on the outer rims of crater basins, so that, if they were formed by seepage erosion, water sources had to be very local and derived from precipitation [*Grant*, 2000]. Indeed, recent acquisition of high resolution images suggests that flow magnitudes and drainage

patterns most likely required precipitation [*Craddock and Howard*, 2002; *Malin and Edgett*, 2003; *Moore et al.*, 2003; *Mangold et al.*, 2004; *Irwin et al.*, 2005; *Moore and Howard*, 2005].

Low Martian drainage densities have also been suggested to be indicative of seepage erosion. The assumption is that a large drainage area per unit length of channel (the inverse of drainage density) implies a large discharge is required for channel cutting, and this would be consistent with the relative weak process of spring driven incision. Measurements of drainage density based upon Viking and Mariner 9 images with resolutions ~200 m/pixel resulted in estimated drainage densities of ~0.02 km^{-1} [*Carr and Chuang*, 1997]. Recent measurements based upon higher resolution images from the Narrow Angle Mars Observer Camera (MOC NA) and the Mars Observer Laser Altimeter (MOLA) have increased maximum estimated drainage densities to ~0.1 km^{-1}, which approaches the range of terrestrial drainage densities [*Irwin and Howard*, 2002; *Hynek and Phillips*, 2003]. Rather than being indicative of seepage, the relatively low drainage densities might arise from high permeability of the impact-generated regolith on early Mars, abundant small depressions from impacts [*Hartmann et al.*, 2001] that encourage infiltration, and modification of the valleys by eolian infilling, mass-wasting, and impact gardening subsequent to the time period of active flows [*Williams and Phillips*, 2001; *Craddock and Howard*, 2002; *Irwin and Howard*, 2002].

Even if one assumes that amphitheater-headed valleys are indicators of seepage erosion, a morphologic analysis is hampered on Mars by image resolution and post-incision degradation by mass wasting. Images of the Martian surface from missions

through the Viking Orbiters produced near-global coverage at resolutions generally between 200-300 m/pixel. At such resolution many valley networks appeared to terminate at abrupt headwalls. In more recent higher resolution images from Mars Global Surveyor, Mars Odyssey, and Mars Express, small tributaries are generally seen to gradually shallow headwards, merging progressively with their contributing uplands (Figure 13).

Once channel incision ceased on Mars, mass wasting, eolian deposition and erosion, and impact cratering continued to erode and deposit mass, destroying diagnostic features of smaller tributaries. The Nirgal Valles system, long considered to be the type example for a groundwater sapping network on Mars, has been deeply infilled by eolian sediments, as evidenced by the shallow valley headwalls and the abundant megaripples on the valley floor (Figure 1). The valley walls show little evidence of bedrock layering, despite the probable excavation of the valley into layered basaltic flows [*Scott and Tanaka*, 1986]. Mass wasting processes and impact gardening have apparently relaxed the valley walls until they average about 19 degrees in steepness. Slope angles less than typical angle of repose slopes (>30 degrees) may have been produced by ice-driven creep [*Perron et al.*, 2003]. As a result of these modifications, many of the local features in terrestrial drainage networks that suggest a seepage-erosion origin cannot be found, including seepage faces and undercut valley headwalls.

Simulations by *Howard* [1995] of scarp planform evolution showed that valleys formed initially in layered rocks by fluvial erosion (producing scarps with headward canyon terminations that are pointed in planform) can develop rounded amphitheater

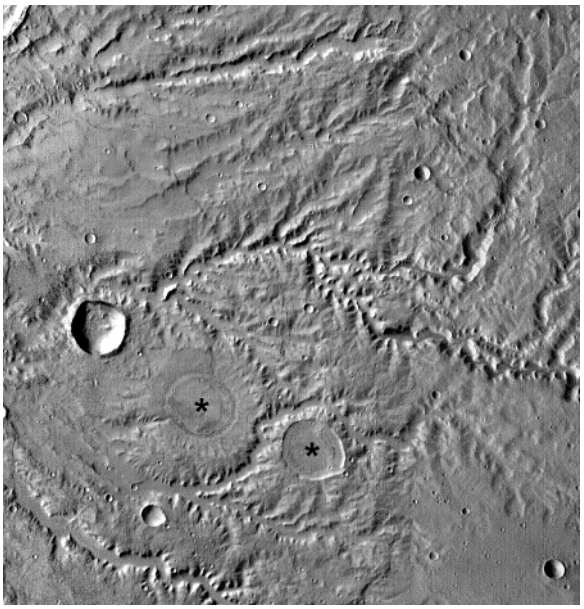

Figure 13. A portion of the Parana Valles Martian valley network. Image width is 63.7 km. Image centered at about 21.5ºS and 349.5ºE. Although the larger valleys are deeply incised with steep valley walls, smaller tributaries generally shallow gradually towards their headward end, often merging insensibly with the source upland. Note the two impact craters marked with "*" that have been eroded to the point that their rims are nearly obliterated. North to top of image. Mosaic of portions of THEMIS IR images I01886002, I00825004, I04495002, and I06717002.

headwalls if they are subsequently modified by uniform scarp retreat driven by weathering and mass wasting**.** Hence, not only are channel features obscured, but valley morphology can take on a form that appears to be due to seepage erosion, even when it doesn't occur. This suggests a simple test. Figures 14 and 15 show shaded relief images of a portion of the Grand Canyon showing steep tributaries to the Colorado River and the towering cliffs in sandstones and limestones bordering these valleys. Although seepage erosion may play a minor role in valley extension within the Kaibab and Redwall Limestones, the main processes of canyon erosion and extension are runoff erosion and debris flow incision [*Webb et al.*, 1989; *Griffiths et al.*, 2004]. The tributaries on the north side of the Colorado River have eroded farther due to extensive drainage from the highlands north of the Grand Canyon passing over the canyon rim. This asymmetry is due to the gentle southward dip of the Paleozoic sedimentary layers exposed in the upper portions of the canyon. To explore the morphologic effects of mass wasting, we have iteratively modified the digital elevation model (DEM) of this landscape by assuming that the steep rocky slopes greater than 20 degrees gradually weather, yielding debris that is transported by mass wasting, with the produced debris accumulating at the base of the slope (conserving total rock volume) until no slope is steeper than 20 degrees. Slopes less than 20 degrees are unmodified. This modeling is a numerical implementation of the geometrical mass wasting model of *Bakker and Le Heux* [1952]. The result is that canyon-wall tributaries exhibit broad rounded headwalls and narrow infilled valleys. The fine-scale fluvial network on the steep slopes is eradicated (Figure 15). This morphology is very similar to stubby tributaries of Valles Marineris (Figure 16), which have long been attributed to a

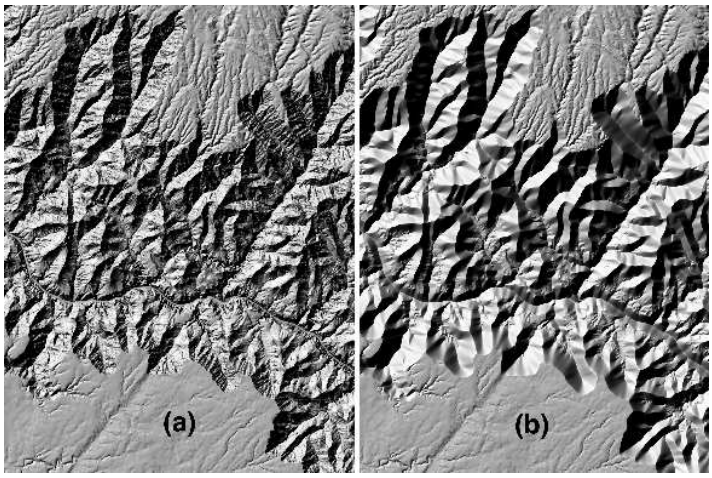

Figure 14. Shaded relief image of portions of the Phantom Ranch, Shiva Temple, Grand Canyon, Bright Angel Point, Kanabounits Spring , and Little Park Lake 7.5' digital 10m DEM, before (a) and after (b) simulated relaxation of slopes steeper than 20 degrees.

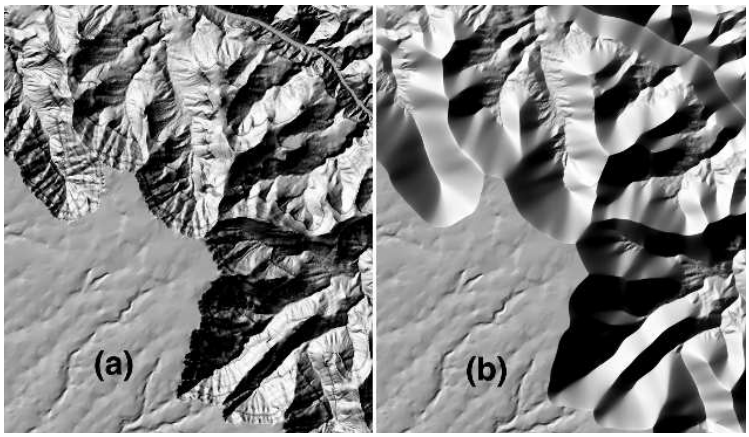

Figure 15. Detail of the lower right corner of Figure 14, showing (a) a shaded relief image of the existing topography (based upon the Phandom Ranch 7.5' 10 m DEM). (b) The same region after simulated relaxation of steep valley walls to 20 degrees. Note the stubby tributaries, the rounded valley headwalls, and the eradication of the fine scale drainage network on the steep slopes. Compare (b) with the Martian valley topography shown in Figure 16.

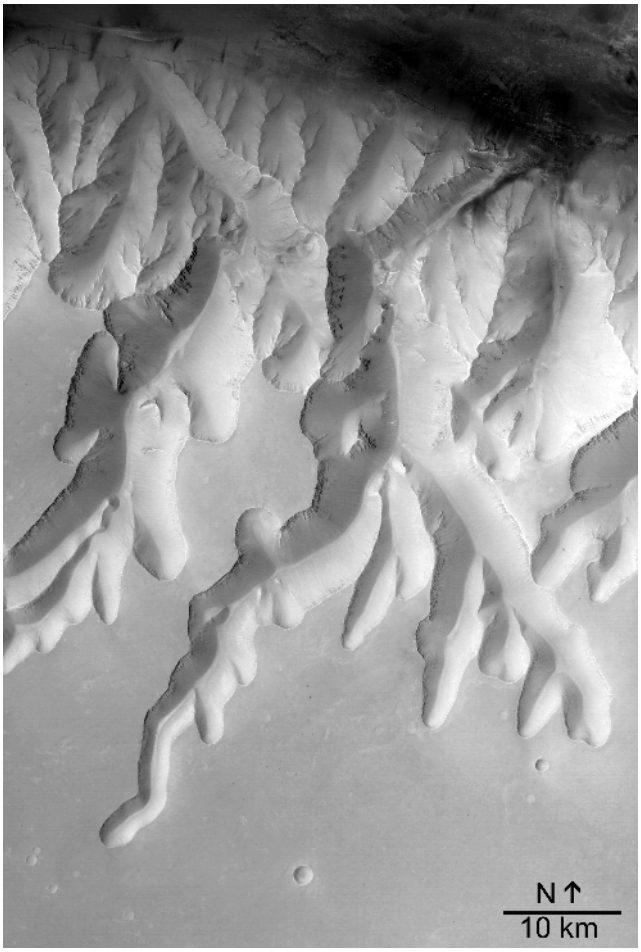

Figure 16. Deeply incised valleys on the south wall of Ius Chasma on Mars, at the western end of Valles Marineris. These valleys are part of Louros Valles. The floor of Ius Chasma is at the north end of the image. Relief from the plateau surface to the chasma floor is about 7 km. Image located at about 8.5ºS and 278.8ºE. Image from Mars Express High Resolution Stereo Camera, orbit H0097, courtesy of the European Space Agency Multimedia Gallery.

groundwater-sapping origin. Side slopes of these valleys average about 26 degrees. Similar modifications might have produced the rounded headwalls of the Nirgal Valles system (Figure 1). This simple analysis suggests that subsequent mass wasting has modified the valleys to the extent that any inferences about the formative erosion processes must be speculative.

The proposed groundwater-sapping origin for Martian valley networks is based primarily on the assumption that seepage erosion creates a distinctive morphology, an assumption we have challenged throughout this paper. The surface lithology of Mars consists of volcanic and sedimentary rocks [*Malin et al.*, 1998; *Bandfield et al.*, 2000; *Hamilton and Christensen*, 2005; *Malin and Edgett*, 2000]. The evidence for seepage alone carving valleys into volcanic and sedimentary rocks on Earth is ambiguous. A major process limitation in resistant rock is the apparent inability of springs on Earth to transport coarse talus that collapses into the channels. This, however, does not rule out a seepage origin for Martian valleys. For example, if the valleys were carved into sedimentary rock with easily dissolved cement that weathers to fine-grained transportable sediment, or if the bedrock has been pulverized through repeated bolide impacts, creating a cohesionless, relatively fine-grained detrital waste, then a seepage-erosion origin is possible.

2.7. Seepage Erosion on Titan?

The recent discovery of branching valley networks on Titan, some of which appear to have short, stubby tributaries, has led to suggestions that seepage processes played a role in their formation [*Tomasko et al.*, 2005]. The stubby appearance of the

valleys on Titan is based mainly on albedo contrasts in images, however; the available topographic data are not sufficiently detailed to determine whether the valleys have amphitheater heads. Some of these valley networks have morphologic characteristics that are inconsistent with spring-fed fluid discharge, including radial drainage patterns formed on isolated peaks in the topography and tributaries that extend to within 200 m of one another on opposite sides of a topographic divide [*Perron et al.*, in review].

Erosion mechanisms on Titan involve combinations of materials that are unfamiliar on Earth and Mars: Titan's water-ice crust [*Schubert et al.*, 1986] at the surface temperature of 94 K has strength [*Durham et al.*, 1983; *Cuda and Ash*, 1984] comparable to terrestrial bedrock [*Goodman*, 1989]. The volatile in Titan's "hydrologic" cycle is probably methane, which comprises several percent of Titan's thick atmosphere and is stable in liquid form at its surface. Springs on Titan probably do not cause significant chemical erosion because the solubility of water ice in liquid methane is extremely small [*Rest et al.*, 1990; *Lorenz and Lunine*, 1996]. Chemical weathering rates on Titan could be higher if the surface material contains a significant fraction of hydrated ammonia compounds [*Lorenz and Lunine*, 1996], but no signature of these compounds has yet been identified in surface spectra.

Recent ground-based [e.g., *Griffith et al.*, 2000; *Brown et al.*, 2002] and spacecraft [e.g., *Porco et al.*, 2005; *Griffith et al.*, 2005] observations of Titan have documented the development and rapid dissipation of tropospheric clouds, which suggests an active methane cycle involving rainfall. Seepage erosion may have contributed to the formation of the valley networks on Titan if the surface material is poorly consolidated, but it seems likely that surface runoff associated with methane

precipitation has also played a role, perhaps eroding water-ice bedrock [*Collins*, 2005] and transporting sediment [*Perron et al.*, in review] by processes similar to those on Earth.

2.8. Conclusions

Mechanistic evidence for springs eroding valleys with distinctive morphologies into rock is sparse and inconclusive. Lithology has been shown to be a first-order control on whether and how seepage erosion might occur. In unconsolidated, permeable sediments groundwater seepage can be sufficient to both erode the valley head and remove the eroded material, sometimes (but not always) resulting in valleys with amphitheater heads. In weakly consolidated sedimentary rocks, groundwater might control the shape and perhaps the rate of valley formation. But, it is also possible that seepage erosion plays a secondary role to runoff processes such as plunge pool erosion, or to mechanical processes such as loss of strength and mass failure. Sediment must be evacuated from the valley in order for retreat of the headwall to continue, which seems to require surface runoff for most cases on Earth. In basaltic valleys, there is no clear evidence that seepage causes significant erosion. Instead, plunge pools and large boulders that line the valley bottoms support erosion and excavation by surface runoff. While we know of no unambiguous case of seepage eroding an amphitheater-headed valley in resistant rock, several examples exist of valley formation by runoff and mass wasting processes in the absence of seepage erosion. Instead of a particular hydraulic process, amphitheater heads might instead be indicative of a substrate that, because of rock strength and fracture orientation, is relatively unstable to headwall

retreat, but resistant to incision at the rim of the headwall. Amphitheater valley heads should not be used as a diagnostic indicator of seepage erosion on Earth, Mars or elsewhere because of the present uncertainty in the ability of seepage to independently erode bedrock valleys and the fact that mass wasting and runoff processes can (also) carve amphitheater-headed valleys.

Our analysis, however, does not prove or disprove the ability of seepage to erode amphitheater-headed valleys in rock. The lack of processes-based observations of seepage erosion and the overlapping evidence for other processes makes it difficult to quantitatively assess the relative importance of seepage. Clearly more work is needed. On Earth, mechanistic studies are needed to identify the actual erosion mechanisms responsible for seepage erosion for a variety of lithologies and to determine their rate dependence, if any, with groundwater discharge. In addition, studies are needed to explore other processes that can produce amphitheater-headed valleys in bedrock landscapes. On Mars, more information on lithology (or some measure of rock strength) and sediment size is needed to begin to decipher the role of seepage erosion in valley formation and to constrain the magnitude of the flows responsible for eroding the valleys.

2.9. References

Aharonson, O., M.T. Zuber, D.H. Rothman, N. Schorghofer, and K.X. Whipple (2002), Drainage basins and channel incision on Mars, Proc. Natl. Acad. Sci. U. S. A., 99 (4), 1780-1783.

Baker, V.R. (1982), The Channels of Mars, University of Texas Press, Austin.

Baker, V.R. (1990), Spring sapping and valley network development, with case studies by R.C. Kochel, V.R. Baker, J.E. Laity, and A.D. Howard, in Groundwater Geomorphology; The Role of Subsurface Water in Earth-Surface Processes and Landforms, edited by C.G. Higgins, and D.R. Coates, Geol. Soc. Am. Spec. Paper 252, pp. 235-265, Boulder.

Baker, V.R., and J.B. Partridge (1986), Small martian valleys: Pristine and degraded morphology, *J. Geophys. Res., 91*, 3561-3572.

Bakker, J.P., and J.W.N. Le Heux (1952), A remarkable new geomorphological law, *Koninklijke Nederlandsche Academie van Wetenschappen, B55*, 399-410, 554-571.

Bandfield, J.L., V.E. Hamilton, and P.R. Christensen (2000), A global view of Martian surface compositions from MGS-TES, *Science, 287* (5458), 1626-1630.

Bennett, S.J., C.V. Alonso, S.N. Prasad, and M.J.M. Romkens (2000), Experiments on headcut growth and migration in concentrated flows typical of upland areas, *Water Resour. Res., 36* (7), 1911-1922.

Bennett, S.J., and J. Casali (2001), Effect of initial step height on headcut development in upland concentrated flows, *Water Resour. Res., 37* (5), 1475-1484.

Bishop, P., T.B. Hoey, J.D. Jansen, and I.L. Artza, (2005), Knickpoint recession rate and catchment area: the case of uplifted rivers in Eastern Scotland, *Earth Surface Processes and Landforms, 30* (6), 767-778.

Bollaert, E., and A. Schleiss (2003), Scour of rock due to the impact of plunging high velocity jets Part I: A state-of-the-art review, *J. Hydraul. Res., 41* (5), 451-464.

Brown, M.E., A.H. Bouchez, and C.A. Griffith (2002), Direct detection of variable tropospheric clouds near Titan's south pole, *Nature, 420* (6917), 795-797.

Buffington, J.M., and D.R. Montgomery (1997), A systematic study of eight decades of incipient motion studies, with special reference to gravel-bedded rivers, *Water Resour. Res., 33* (8), 1993-2029.

Carr, M.H. (2002), Elevations of water-worn features on Mars: Implications for circulation of groundwater, *J. Geophys. Res.*, *107* (E12), DOI:10.1029/2002JE001845.

Carr, M.H., and F.C. Chuang (1997), Martian drainage densities, *J. Geophys. Res.*, *102*, 9145-9152.

Carr, M.H., and G.D. Clow (1981), Martian channels and valleys - their characteristics, distribution, and age, *Icarus*, *48* (1), 91-117.

Clifford, S.M., and T.J. Parker (2001), The evolution of the Martian hydrosphere: Implications for the fate of a primordial ocean and the current state of the northern plains, *Icarus*, *154* (1), 40-79.

Collins, G.C. (2005), Relative rates of fluvial bedrock incision on Titan and Earth, *Geophys. Res. Lett.*, *32* (22).

Cooke, R.U., and W.R. Reeves (1976), *Arroyos and Environmental Change in the American South-West*, Clarendon Press, Oxford.

Craddock, R.A., and A.D. Howard (2002), The case for rainfall on a warm, wet early Mars, *J. Geophys. Res.*, *107* (E11), doi:10.1029/2001JE001505.

Craddock, R.A., R.P. Irwin, R. Williams, D. Swanson, A.D. Howard, C. Quantin, R. Kuzmin, J.R. Zimbelman (2005), The Geology of the Ka'u Desert, Hawaii as a Mars Analog, *Eos Trans. AGU 86*(52), Fall Meet. Suppl., Abstract H33C-1402.

Crosby, B.T., and K.X. Whipple, (in press), Knickpoint initiation and distribution within fluvial networks in the Waipaoa River, North Island, New Zealand, *Geomorphology*.

Cuda, V., and R. L. Ash (1984), Development of a uniaxial ice tensile specimen for low temperature testing, *Cold Regions Sci. Tech.*, 9, 47-52.

Dick, G.S., R.S. Anderson, and D.E. Sampson (1997), Controls on flash flood magnitude and hydrograph shape, Upper Blue Hills badlands, Utah, *Geology*, *25* (1), 45-48.

Dietrich, W.E., D. Bellugi, L. Sklar, J.D. Stock, A.M. Heimsath, and J.J. Roering (2003), Geomorphic transport laws for predicting landscape form and dynamics, in *Prediction in Geomorphology*, edited by P. Wilcock, and R. Iverson, pp. 1-30, DOI: 10.1029/135GM09.

Dietrich, W.E., and T. Dunne (1993), The channel head, in *Channel Network Hydrology*, edited by K. Beven, and M.J. Kirkby, pp. 175-219, John Wiley & Sons.

Dunne, T. (1980), Formation and controls of channel networks, *Prog. Phys. Geog.*, *4*, 211-239.

Dunne, T. (1990), Hydrology, mechanics, and geomorphic implications of erosion by subsurface flow, in *Groundwater Geomorphology; The Role of Subsurface Water in Earth-Surface Processes and Landforms*, edited by C.G. Higgins, and D.R. Coates, Geol. Soc. Am. Spec. Paper 252, pp. 1-28, Boulder.

Durham, W. B., H. C. Heard, and S. H. Kirby (1983), Experimental deformation of polycrystalline H2O ice at high pressure and low temperature: Preliminary results, *J. Geophys. Res.*, 88, B377-B392.

Faure, G. (1998), *Principles and Applications of Geochemstry*, 600 pp., Prentice Hall, Upper Sadle River.

Gilbert, G.K. (1907), The rate of recession of Niagara Falls, *U. S. Geol. Surv. Bull.*, *306*, 1-31.

Goldspiel, J.M., and S.W. Squyres (1991), Ancient aqueous sedimentation on Mars, *Icarus*, *89*, 392-410.

Goldspiel, J.M., and S.W. Squyres (2000), Groundwater sapping and valley formation on Mars, *Icarus*, *148* (1), 176-192.

Goodman, R. E. (1989), *Introduction to Rock Mechanics*, 562 pp., Wiley, New York.

Grant, J.A. (2000), Valley formation in Margaritifer Sinus, Mars, by precipitaiton-recharged ground-water sapping, *Geology*, *28* (3), 223-226.

Gregory, H.E. (1916), The Navajo country; a geography and hydrographic reconnaissance of parts of Arizona, New Mexico, and Utah, *U. S. Geol. Surv. Water Supply Paper*, *W0380*, 219.

Griffith, C.A., J.L. Hall, and T.R. Geballe (2000), Detection of daily clouds on Titan, *Science*, *290* (5491), 509-513.

Griffith, C.A., P. Penteado, K. Baines, P. Drossart, J. Barnes, G. Bellucci, J. Bibring, R. Brown, B. Buratti, F. Capaccioni, P. Cerroni, R. Clark, M. Combes, A. Coradini, D. Cruikshank, V. Formisano, R. Jaumann, Y. Langevin, D. Matson, T. McCord, V. Mennella, R. Nelson, P. Nicholson, B. Sicardy, C. Sotin, L.A. Soderblom, and R. Kursinski (2005), The evolution of Titan's mid-latitude clouds, *Science*, *310* (5747), 474-477.

Griffiths, P.G., R.H. Webb, and T.S. Melis (2004), Frequency and initiation of debris flows in Grand Canyon, Arizona, *J. Geophys. Res.*, *109*, F04002, doi:10.1029/2003JF000077.

Gulick, V.C. (1998), Magmatic intrusions and a hydrothermal origin for fluvial valleys on Mars, *J. Geophys. Res.*, *103*, 19365-19388.

Gulick, V.C. (2001), Origin of the valley networks on Mars: a hydrological perspective, *Geomorphology*, *37* (3-4), 241-268.

Hamilton, V.E., and P.R. Christensen (2005), Evidence for extensive, olivine-rich bedrock on Mars, *Geology*, *33* (6), 433-436.

Hanson, G.J., K.M. Robinson, and K.R. Cook (1997), Headcut migration analysis of a compacted soil, *Trans. A.S.A.E.*, *40* (2), 355-361.

Hartmann, W.K., Anguita, J., de La Casa, M. A., Berman, D. C., and Ryan, E. V. (2001), Martian cratering 7: The role of impact gardening, Icarus, 149, 37-53.

Hayakawa, Y., and Y. Matsukura, (2003), Recession rates of waterfalls in Boso Peninsula, Japan, and a predictive equation, *Earth Surface Processes and Landforms*, *28* (6), 675-684.

Heimsath, A.M., W.E. Dietrich, K. Nishiizumi, and R.C. Finkel (1997), The soil production function and landscape equilibrium, *Nature*, *388* (6640), 358-361.

Higgins, C.G. (1982), Drainage systems developed by sapping on Earth and Mars, *Geology*, *10*, 147-152.

Higgins, C.G. (1984), Piping and sapping; development of landforms by groundwater flow, in *Groundwater as a Geomorphic Agent*, edited by R.G. LaFleur, pp. 18-58, Allen and Unwin, Boston.

Higgins, C.G., B.R. Hill, and A.K. Lehre (1990), Gully development, in *Groundwater Geomorphology; The Role of Subsurface Water in Earth-Surface Processes and Landforms*, edited by C.G. Higgins, and D.R. Coates, Geol. Soc. Am. Spec. Paper 2521, pp. 139 – 156, Boulder.

Hinds, N.E.A. (1925), Amphitheater valley heads, *J. Geol.*, *33*, 816-818.

Hoke, G.D., B.L. Isacks, T.E. Jordan, and J.S. Yu (2004), Groundwater-sapping origin for the giant quebradas of northern Chile, *Geology*, *32* (7), 605-608.

Holland, W.N., and G. Pickup (1976), Flume study of knickpoint development in stratified sediment, *Geol. Soc. Am. Bull.*, *87* (1), 76-82.

Hovius, N., C.P. Stark, M.A. Tutton, and L.D. Abbott (1998), Landslide-driven drainage network evolution in a pre-steady-state mountain belt: Finisterre Mountains, Papua New Guinea, *Geology*, *26* (12), 1071-1074.

Howard, A.D. (1988), Groundwater sapping on Earth and Mars, in *Sapping Features of the Colorado Plateau*, edited by A.D. Howard, R.C. Kochel, and H.R. Holt, pp. 1-4, NASA, Washington, D.C.

Howard, A.D. (1994), Rockslopes, in *Geomorphology of Desert Environments*, edited by A.D. Abrahams, and A.J. Parsons, pp. 123-172, Chapman & Hall, London.

Howard, A.D. (1995), Simulation modeling and statistical classsification of escarpment planforms, *Geomorphology*, *12*, 187-214.

Howard, A.D., W.E. Dietrich, and M.A. Seidl (1994), Modelling fluvial erosion on regional and continental scales, *J. Geophys. Res.*, *99*, 13971-13986.

Howard, A.D., and R.C. Kochel (1988), Introduction to cuesta landforms and sapping processes on the Colorado Plateau, in *Sapping Features of the Colorado Plateau: A Comparitive Planetary Geology Field Guide*, edited by A.D. Howard, R.C. Kochel, and H. Holt, pp. 6-56, NASA Special Publication, Washington D.C.

Howard, A.D., and C.F. McLane (1988), Erosion of cohesionless sediment by groundwater seepage, *Water Resour. Res.*, *24* (10), 1659-1674.

Hynek, B.M., and R.J. Phillips (2003), New data reveal mature, integrated drainage systems on Mars indicative of past precipitation, *Geology*, *31* (9), 757-760.

Irwin, R.P., R.A. Craddock, and A.D. Howard (2005), Interior channels in Martian valley networks: Discharge and runoff production, *Geology*, *33* (6), 489-492.

Irwin, R.P., and A.D. Howard (2002), Drainage basin evolution in Noachian Terra Cimmeria, Mars, *J. Geophys. Res.*, *107* (E7), 10.1029/2001JE001818.

Jaumann, R., and D. Reiss (2002), Nirgal Valles: Evidence for extensive sapping, *Lunar and Planetary Science XXXIII*, abstract 1579.

Jones, J.A.A. (1981), *The Nature of Soil Piping; A Review*, 301 pp., GeoBooks, Norwich.

Kochel, R.C., and V.R. Baker (1990), Groundwater sapping and the geomorphic development of large Hawaiian valleys, in in *Groundwater Geomorphology*; *The Role of Subsurface Water in Earth-Surface Processes and Landforms*, edited by C.G. Higgins, and D.R. Coates, Geol. Soc. Am. Spec. Paper 252, pp. 235-265, Boulder.

Kochel, R.C., A.D. Howard, and C.F. McLane (1985), Channel networks developed by groundwater sapping in fine-grained sediments; Analogs to some Martian

valleys, in *Models in Geomorpholgy*, edited by M. Woldenberg, pp. 313-341, Allen and Unwin, London.

Kochel, R.C., and J.F. Piper (1986), Morphology of large valleys on Hawaii - Evidence for groundwater sapping and comparisons with Martian valleys, *J. Geophys. Res., 91* (B13), E175-E192.

Laity, J.E. (1983), Diagenetic controls on groundwater sapping and valley formation, Colorado Plateau, revealed by optical and electron microscopy, *Phys. Geog., 4* (2), 103-125.

Laity, J.E., and M.C. Malin (1985), Sapping processes and the development of theatre-headed valley networks on the Colorado Plateau, *Geol. Soc. Am. Bull., 96*, 203-217.

Lamb, M.P., W.E. Dietrich, and A.D. Howard (2004), Can springs cut valleys into bedrock?, *Eos Trans. AGU, 85(47)*, Abstract H53C-1258.

Lamb, M.P., A.D. Howard, W.E. Dietrich, J.T. Perron (2005), Hawaiian analog for Martian amphitheater-headed valleys, *Eos Trans. AGU 86*(52), Fall Meet. Suppl., Abstract H33C-1404.

Lamb, M.P., A.D. Howard, W.E. Dietrich, J.T. Perron (in review), Formation of amphitheater-headed valleys by waterfall erosion after large-scale slumping on Hawaii, *Geol. Soc. Am. Bull.*

Lobkovsky, A., B. Smith, D. Mohrig, A. Kudrolli, and D. Rothman (2005), Dynamical evolution of channels driven by subsurface flow, *Eos Trans. AGU 86*(52), Fall Meet. Suppl., Abstract H31A-1276.

Lorenz, R.D., and J.I. Lunine (1996), Erosion on Titan: past and present, *Icarus, 122*, 79-91.

Luo, W. (2000), Quantifying groundwater-sapping landforms with a hypsometric technique, *J. Geophys. Res., 105* (E1), 1685-1694.

Macdonald, G.A., A.T. Abbott, and F.L. Peterson (1983), *Volcanoes in the Sea, the Geology of Hawaii*, 517 pp., University of Hawaii Press, Honolulu.

Malde, H.E. (1968), The catastrophioc late Pleistocene Bonneville Flood in the Snake River Plain, Idaho, *U. S. Geol. Surv. Prof. Paper, 596*, 1-52.

Malin, M.C., and M.H. Carr (1999), Groundwater formation of Martian valleys, *Nature, 397* (6720), 589-591.

Malin, M.C., M.H. Carr, G.E. Danielson, M.E. Davies, W.K. Hartmann, A.P. Ingersoll, P.B. James, H. Masursky, A.S. McEwen, L.A. Soderblom, P. Thomas, J. Veverka, M.A. Caplinger, M.A. Ravine, and T.A. Soulanille (1998), Early views of the Martian surface from the Mars orbiter camera of Mars global surveyor, *Science, 279* (5357), 1681-1685.

Malin, M.C., and K.S. Edgett (2000), Sedimentary rocks of early Mars, *Science*, *290*, 1927-1937.

Malin, M.C., and K.S. Edgett (2003), Evidence for persistent flow and aqueous sedimentation on early Mars, *Science*, *302* (5652), 1931-1934.

Mangold, N., C. Quantin, V. Ansan, C. Delacourt, and P. Allemand (2004), Evidence for precipitation on Mars from dendritic valleys in the Valles Marineris Area, *Science, 305*, 78-81.

Mars channel working group (1983), Channels and valleys on Mars, *Geol. Soc. Am. Bull.*, *94*, 1035-1054.

Mason, L.J. and D.T. Pederson (2004), Salt weathering of waterfall escarpments along the Niobrara River near Valentine, NE, *Abstracts with Programs – Geol. Soc. Am., 36* (5), 231.

Mastronuzzi, G., and P. Sanso (2002), Pleistocene sea-level changes, sapping processes and development of valley networks in the Apulia region (southern Italy), *Geomorphology*, *46* (1-2), 19-34.

Meinzer, O.E. (1927), Large springs in the United States, *U. S. Geol.l Surv. Water Supply Paper 557*, 42-51.

Meyer-Peter, E. and Müller, R. (1948), Formulas for bed-load transport, *Proceedings*, 2nd Congress, International Association of Hydraulic Research, Stockholm: 39-64.

Moore, J.G., W.R. Normark, and R.T. Holcomb (1994), Giant Hawaiian landslides, *Ann. Rev. Earth Plan. Sci., 22*, 119-144.

Moore, J.G., and D.A. Clague (1992), Volcano growth and evolution of the island of Hawaii, *Geol. Soc. Am. Bull., 104* (11), 1471-1484.

Moore, J.M., and A.D. Howard (2005), Large alluvial fans on Mars, *J. Geophys. Res., 110* (E4), Art. No. E04005.

Moore, J.M., A.D. Howard, W.E. Dietrich, and P.M. Schenk (2003), Martian layered fluvial deposits: implications for Noachian climate scenarios, *Geophys. Res. Lett., 30* (24), Art. No. 2292.

Nash, D.J. (1996), Groundwater sapping and valley development in the Hackness hills, north Yorkshire, England, *Earth Surf. Proc. Land.*, *21* (9), 781-795.

O'Connor, J.E. (1993), *Hydrology, Hydraulics and Geomorphology of the Bonneville Flood*, Geol. Soc. Am. Spec. Paper 274, 83 pp., Boulder.

Onda, Y. (1994), Seepage erosion and its implication to the formation of amphitheater valley heads – A case-study at Obara, Japan, *Earth Surface Processes and Landforms*, *19* (7), 627-640.

Owoputi, L.O., and W.J. Stolte (2001), The role of seepage in erodibility, *Hydrol. Proc.*, *15* (1), 13-22.

Pederson, D.T. (2001), Stream piracy revisited: a groundwater sapping solution, *GSA Today*, *11* (9), 4-10.

Perron, J.T., W.E. Dietrich, A.D. Howard, J.A. McKean, and J.R. Pettinga (2003), Ice-driven creep on Martian debris slopes, *Geophys. Res. Lett.*, *30* (14), 1747, doi: 10.1029/2003GL017603.

Perron, J.T., M.P. Lamb, C.D. Koven, I. Fung, and M. Adamkovics (in review), Rainfall and sediment transport on Titan, *J. Geophys. Res.*

Pieri, D. (1976), Distribution of small channels on Martian surface, *Icarus*, *27* (1), 25-50.

Pieri, D.C. (1980), Martian valleys: Morphology, distribution, age, and origin, *Science*, *210*, 895-897.

Pillans, B. (1985), Drainage initiation by subsurface flow in South Taranaki, New Zealand, *Geology*, *13*, 262-265.

Porco, C.C., E. Baker, J. Barbara, K. Beurle, A. Brahic, J.A. Burns, S. Charnoz, N. Cooper, D.D. Dawson, A.D. Del Genio, T. Denk, L. Dones, U. Dyudina, M.W. Evans, S. Fussner, B. Giese, K. Grazier, P. Helfenstein, A.P. Ingersoll, R.A. Jacobson, T.V. Johnson, A. McEwen, C.D. Murray, G. Neukum, W.M. Owen, J. Perry, T. Roatsch, J. Spitale, S. Squyres, P. Thomas, M. Tiscareno, E.P. Turtle, A.R. Vasavada, J. Veverka, R. Wagner, and R. West (2005), Imaging of Titan from the Cassini spacecraft, *Nature*, *434* (7030), 159-168.

Rest, R.J., R.G. Scurlock, and M.F. Wu (1990), The solubilities of nitrous oxide, carbon dioxide, aliphatic ethers and alcohols, and water in cryogenic liquids, *Chem. Eng. J. and Biochem. Eng. J.*, *43*, 25-31.

Robinson, K.M., and G.J. Hanson (1996), Gully headcut advance, *Trans. A.S.A.E.*, *39* (1), 33-38.

Rosenblum, N.A., and R.S. Anderson, (1994), Hillslope and channel evolution in a marine terraced landscape, Santa Cruz, California, *J. Geophys. Res.*, *99* (7), 14013-14029.

Russel, I.C. (1902), Geology and water resources of the Snake River Plains of Idaho, *U. S. Geol. Surv. Bull. 199*, 1-192.

Schorghofer, N., B. Jensen, A. Kudrolli, and D.H. Rothman (2004), Spontaneous channelization in permeable ground: theory, experiment, and observation, *J. Fluid Mech.*, *503*, 357-374.

Schubert, G. S., T. Spohn, and R. T. Reynolds (1986), Thermal histories, compositions and internal structures of the moons of the solar system, in *Satellites*, edited by J. A. Burns and M. S. Matthews, Univ. of Arizona Press, Tucson, pp. 224-292.

Schumm, S.A., K.F. Boyd, C.G. Wolff, and W.J. Spitz (1995), A groundwater sapping landscape in the Florida panhandle, *Geomorphology*, *12* (4), 281-297.

Schumm, S.A., and L. Phillips (1986), Composite channels of the Canterbury Plain, New Zealand: a Martian analog?, *Geology*, *14*, 326-329.

Scott, D. H., and Tanaka, K. L., (1986) Geologic map of the western equatorial region of Mars, U.S. Geol. Surv. Misc. Investigations Map, I-1802-A.

Seidl, M.A., W.E. Dietrich, and J.W. Kirchner, (1994), Longitudinal profile development into bedrock: an analysis of Hawaiian channels, *Journal of Geology*, *102*, 457–474.

Seidl, M.A., J.K. Weissel, and L.F. Pratson (1996), The kinematics and pattern of escarpment retreat across the rifted continental margin of SE Australia, *Basin Research*, *8* (3), 301-316.

Sharp, R.P., and M.C. Malin (1975), Channels on Mars, *Geol. Soc. Am. Bull.*, *86* (5), 593-609.

Sklar, L.S., and W.E. Dietrich (2001), Sediment and rock strength controls on river incision into bedrock, *Geology*, *29* (12), 1087-1090.

Sklar, L.S., and W.E. Dietrich, (2004), A mechanistic model for river incision into bedrock by saltating bed load, *Water Resources Research*, *40* (6), Art. No. W06301.

Smith, J.R., K. Satake, J.K. Morgan, and P.W. Lipman (2002), Submarine landslides and volcanic features on Kohala and Mauna Kea Volcanoes and the Hana Ridge,

Hawaii, in *Hawaiian Volcanoes: Deep Underwater Perspectives, Geophysical Monograph 128*, American Geophysical Union.

Squyres, S.W. (1989), Urey Prize Lecture - Water on Mars, *Icarus*, *79* (2), 229-288.

Squyres, S.W., and J.F. Kasting (1994), Early Mars - How warm and how wet, *Science*, *265* (5173), 744-749.

Stark, C.P. (1994), Cluster growth modeling of plateau erosion, *J. Geophys. Res.*, *99* (B7), 13957-13969.

Stearns, H.T. (1936), Origin of the large springs and their alcoves along the Snake River in southern Idaho, *J. Geol.*, *44*, 429-450.

Stearns, H.T. (1985), *Geology of the State of Hawaii*, 266 pp., Pacific Books, Palo Alto, California.

Stearns, H.T., and G.A. Macdonald (1946), Geology and ground-water resources of the island of Hawaii, *Hawii Division of Hydrography*, *Bulletin 9*, 363 pp.

Stearns, H.T., and K.N. Vaksvik, (1935), Geology and ground-water resources of the island of Oahu, Hawaii, *Hawii Division of Hydrography Bulletin*, *1*.

Tanaka, K.L. (1986), The stratigraphy of Mars, *J. Geophys. Res.*, *91* (B13), E139-E158.

Tanaka, K.L., J.M. Dohm, J.H. Lias, and T.M. Hare (1998), Erosional valleys in the Thaumasia region of Mars: Hydrothermal and seismic origins, *J. Geophys. Res.*, *103*, 31407-31420.

Tauxe, L., C. Luskin, P. Selkin, P. Gans, and A. Calvert (2004), Paleomagnetic results from the Snake River Plain: Contribution to the time-averaged field global database, *Geochem. Geophys. Geosyst.*, *5*, doi:10.1029/2003GC000661.

Tomasko, M.G., B. Archinal, T. Becker, M. Bushroe, M. Combes, D. Cook, A. Coustenis, C. de Bergh, L.E. Dafoe, L. Doose, A. Eibl, S. Engel, F. Gliem, B. Grieger, K. Holso, E. Howington-Kraus, E. Karkoschka, H.U. Keller, R. Kirk, R. Kramm, M. Kuppers, P. Lanagan, E. Lellouch, M. Lemmon, J. Lunine, E. McFarlane, J. Moores, G.M. Prout, B. Rizk, M. Rosiek, P. Rueffer, S.E. Schroder, B. Schmitt, C. See, P. Smith, L. Soderblom, N. Thomas, and R. West (2005), Rain, wind and haze during the Huygens probe's decent to Titan's surface, *Nature*, *438*, doi:10.1038/nature04126.

Uchupi, E., and R.N. Oldale (1994), Spring sapping origin of the enigmatic relict valleys of Cape-Cod and Marthas-Vineyard and Nantucket Islands, Massachusetts, *Geomorphology*, *9* (2), 83-95.

Webb, R.H., P.T. Pringle, and G.R. Rink (1989), Debris flows from the tributaries of the Colorado River, Grand Canyon National Park, Arizona, *U. S. Geol. Surv. Prof. Paper, 1492*, 1-39.

Weissel, J.K., and M.A. Seidl (1997), Influence of rock strength properties on escarpment retreat across passive continental margins, *Geology, 25* (7), 631-634.

Wentworth, C.K. (1928), Principles of stream erosion in Hawaii, *J. Geol., 36*, 385-410.

Whiting, P.J., and J. Stamn (1995), The hydrology of spring-dominated channels, *Geomorphology, 12*, 233-240.

Whipple, K.X., (2004), Bedrock rivers and the geomorphology of active orogens, *Annual Review of Earth and Planetary Sciences, 32*, 151-185.

Whipple, K.X., G.S. Hancock, and R.S. Anderson, (2000), River incision into bedrock: Mechanics and relative efficacy of plucking, abrasion, and cavitation, *Geological Society of America Bulletin, 112* (3), 490-503.

Willgoose, G., R.L. Bras, and I. Rodrigueziturbe (1991), A coupled channel network growth and hillslope evolution model: 1. Theory, *Water Resour. Res., 27* (7), 1671-1684.

Williams, R.M.E., and R.J. Phillips (2001), Morphometric measurements of martian valley networks from Mars Orbiter Laser Altimeter (MOLA) data, *J. Geophys. Res., 106* (E10), 23737-23751.

Wong, M., and G. Parker, (in press) The bedload transport relation of Meyer-Peter and Müller overpredicts by a factor of two. *J. Hydraul. Eng.*

Yoshida, M., and H. Ikeda, (1999), The origin of the Ryumon Falls in Karasuyama Town, Tochigi Prefecture, *Bulletin of the Environmental Research Center, the University of Tsukuba, 24*, 73-79.

Young, R. (1985), Waterfalls: form and process, *Ziet Geomorphologie, NF Suppl Bd 55*, 81-95.

Chapter 3

Formation of Amphitheater-Headed Valleys by Waterfall Erosion after Large-Scale Slumping on Hawai‘i

3.1. Introduction

Spectacular amphitheater-headed valleys line the coastlines of Kaua‘i, O‘ahu, Moloka‘i, Maui, and Hawai‘i (Fig. 1). The origin of the steep, stubby (i.e. box-shaped planform geometry) headwalls and flat floors of these valleys has been debated for more than 80 years (Hinds, 1925; Davis, 1928; Wentworth, 1928; Stearns and Vaksvik, 1935; Cotton, 1943; Stearns and Macdonald, 1946; White, 1949; Macdonald et al., 1983; Stearns, 1985; Kochel and Piper, 1986; Kochel and Baker, 1990; Howard et al., 1994; Craddock and Howard, 2002; Lamb et al., 2006). The leading hypothesis has been that seepage-induced chemical weathering at the intersection between the water table and streambed leads to development of a knickpoint (Wentworth, 1928; Stearns and Macdonald, 1946; White, 1949; Kochel and Piper, 1986; Kochel and Baker, 1990). Seepage erosion at the base of the knickpoint is proposed to cause undercutting (i.e. sapping), collapse, and subsequent upstream propagation of the knickpoint, eventually

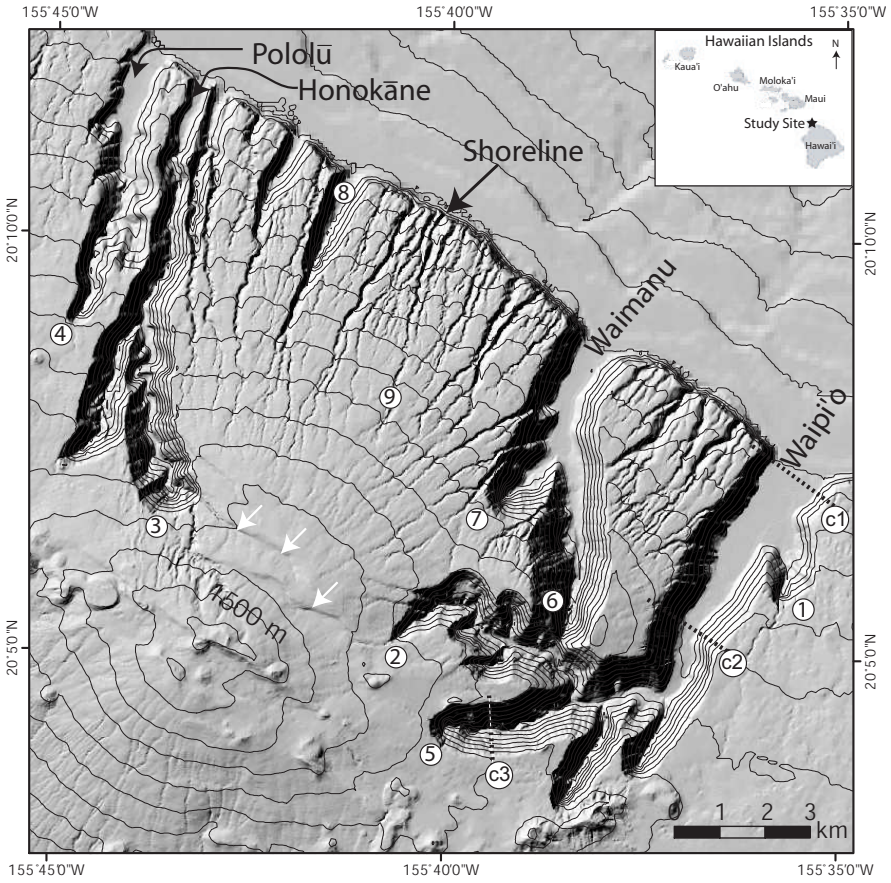

Figure 1. 10-m shaded relief and topographic contour map of northeast side of Kohala Volcano. Contour interval is 100 m. The 1500 m contour is labeled. Present-day sea level is at 0 m. The four large Kohala amphitheatre-headed valleys are named on the figure. Longitudinal profiles for valleys numbered 1-9 are given in Figure 6 and associated data is given in Table 1. Dotted lines across Waipi‘o Valley are cross sections (c1-c3) given in Figure 7. Faults that funnel high elevation drainage to the amphitheatre-headed valleys near the volcano summit are indicated by white arrows. Data from U.S. Geological Survey (7.5 min. Quadrangles), Monterey Bay Aquarium Research Institute, and US Army Corps of Engineers LIDAR. (datum: NAD 83, projection: UTM zone 5). The inset figure in the upper right corner shows the location of the study site in the Hawaiian Islands.

forming the steep valley headwall. Since the 1980's much attention has been given to the Hawaiian valleys because of their apparent similarity to Martian amphitheater-headed valleys in morphology and potentially in lithology (i.e. basalt). Small physical experiments have shown that amphitheater-headed valleys with flat floors can result from seepage erosion in loose sand (e.g. Howard and McLane, 1988). Similarity in form has been used to infer process, such that the connection between seepage erosion and amphitheater-headed valleys in sand has been used to argue for seepage erosion on Hawai'i and, by analogy, Mars (Kochel and Piper, 1986; Kochel and Baker, 1990; Gulick, 2001). A seepage origin of Martian valleys would be significant because it could indicate an early Mars that did not support rainfall (Pieri, 1976; Carr and Clow, 1981; Squyres, 1989; Malin and Carr, 1999) or that precipitation infiltrated to cause seeps without appreciable direct runoff (e.g. Grant, 2000).

The seepage erosion hypothesis for Hawai'i has not been without criticism. While springs have been found in some Hawaiian valleys, they are often high up the valley walls where they seem to drain perched aquifers associated with less permeable ash layers (Stearns and Macdonald, 1946). To our knowledge, there are no published field observations documenting weathering or erosion associated with Hawaiian springs. Indeed, well-developed alcoves, secondary porosity, or obviously weathered rocks are rare (Howard et al., 1994). Furthermore, several springs issue from the sea cliffs along the present-day shoreline and do not have canyons or alcoves associated with them (Stearns and Macdonald, 1946). In loose sediment (e.g. Howard and McLane, 1988; Uchupi and Oldale, 1994; Schumm et al., 1995) or weakly cemented sedimentary rocks (e.g. Laity and Malin, 1985; Howard et al., 1988; Nash, 1996)

seepage erosion is a plausible hypothesis for canyon formation (Lamb et al., 2006). In resistant rock like basalt, however, seepage must first weather the rock to transportable-sized particles before erosion can occur (Dunne, 1990; Dietrich and Dunne, 1993). If seepage flow cannot transport collapsed debris away from the valley headwall, then talus will buttress the headwall and prevent retreat.

Here we present an alternative model for the formation of the Hawaiian amphitheater-headed valleys. The Hawaiian amphitheater-headed valleys typically form on the wet sides of the islands and often have spectacular waterfalls at their headwalls. Based on observations of well-developed plunge pools, we propose that waterfalls have been the dominant erosive agent causing headwall retreat, rather than seepage erosion. This idea is not new; many workers have suggested that waterfall processes are important for headwall erosion in Hawai‘i (Stearns and Vaksvik, 1935; Macdonald et al., 1983; Howard et al., 1994; Craddock and Howard, 2002). We expand on previous work using new field observations and topographic analyses to hypothesize the origin of large knickpoints from massive landslides. The rates of knickpoint propagation are found using recently acquired bathymetric maps coupled with age determinations of Hawaiian basalts and marine terraces. Lastly, a simple mechanistic rule is proposed for waterfall plunge-pool erosion and headwall propagation following recent developments in bedrock-erosion theory (e.g. Sklar and Dietrich, 2004). Our study is focused on the largest, youngest and perhaps most impressive set of these valleys: Waipi‘o, Waimanu, Honokāne, and Pololū Valleys on the northeast side of Kohala Volcano on the island of Hawai‘i (Fig. 1).

3.2. Construction and Subsidence of Kohala Volcano

Kohala Volcano, on the island of Hawai‘i, began erupting subaerially the basaltic Pololū volcanics at approximately 700 ka and this continued to about 250 ka (Dalrymple, 1971; McDougal and Swanson, 1972; Wolfe and Morris, 1996). During this period of volcanism, the Kohala shield was constructed and a distinct break in slope was formed at paleo-sea-level because subaqueously chilled lava solidifies at a steeper slope than subaerial lava (Moore and Clague, 1992). This break in slope will be referred to as a *volcanic terrace* following Moore and Clague (1992). Near the end of the shield building stage, the volcano experienced a relative sea-level rise due to isostatic subsidence as indicated by several drowned coral reefs off the west flank of Kohala (Fig. 2). The volcanic terrace is now ~1000 m below present-day sea level (Moore and Clague, 1992) (Fig. 2), indicating 1000 m of relative-sea level rise since the terrace was formed. Subsidence has occurred at roughly a steady rate of 2.6 mm/yr based on radiometric ages of drowned coral reefs (Fig. 2) (Moore and Fornari, 1984; Szabo and Moore, 1986; Ludwig et al., 1991). We estimate the volcanic terrace to have formed ~ 385 ka by dividing the subsidence distance of 1000 m by the mean subsidence rate of 2.6 mm/yr. A drowned reef at 950 m below present-day sea level yielded radiometric ages of 248-314 ka (Ludwig et al., 1991; Jones, 1995), which is consistent with this estimate. It should be noted that scatter about the mean subsidence rate exists and might be due to erosion of the reefs, differential subsidence, landsliding, or diagenetic effects that alter the dating technique (Moore and Clague, 1992; Ludwig et al., 1991). After the shield building stage, the Hawi volcanic series erupted and

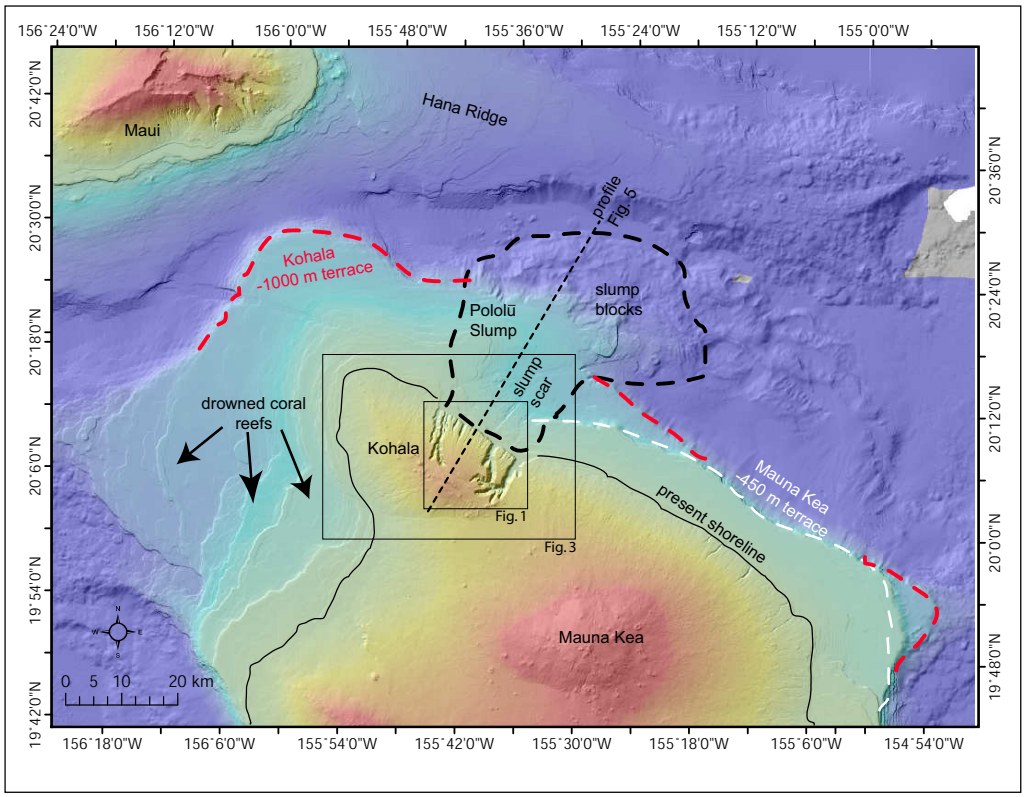

Figure 2. Shaded relief map of the northern half of Hawai‘i and the associated bathymetry. Data resolution varies between different data sets. Hot and cold colors correspond to high and low elevations, respectively. The following interpretations are following Smith et al. (2002): the Pololū Slump is outlined with a black dashed line; Mauna Kea terrace at -450 m (shoreline at the end of the shield building stage) is marked by a white dashed line; the Kohala terrace at -1000 m is marked by a red dashed line. The present shoreline is outlined with a thin solid black line. See text for details. The thin black dashed line is the location of the slump profile shown in Figure 5. The two black boxes indicate the locations of the maps shown in Figures 1 and 3. Data sources include U.S. Geological Survey, Monterey Bay Aquarium Research Institute, US Army Corps of Engineers LIDAR, National Geophysical Data Center (NOAA), and Japan Marine Science and Technology Center.

unconformably overlies the Pololū volcanics. The Hawi volcanics range in age from 230 to 120 ka (McDougal and Swanson, 1972; Wolfe and Morris, 1996) (Fig. 3).

During subsidence of Kohala Volcano, a second large volcanic terrace from the younger Mauna Kea Volcano developed along the northeast shoreline of Kohala and has since subsided ~ 450 m below present-day sea level (Fig. 2). The age of this terrace must be within the range in ages of Mauna Kea volcanics of 250 ka to 65 ka (Wolfe and Morris, 1996). The terrace must also be older than a drowned coral reef at -360 m that has a radiometric age of ~120 ka (Moore and Fornari, 1984; Szabo and Moore, 1986; Ludwig et al., 1991). We estimate that the Mauna Kea terrace formed ~173 ka (and therefore records the location of the paleo-shoreline at this time) using the mean subsidence rate of 2.6 mm/yr (i.e. 450 m / 2.6 mm/yr = 173 ka).

Gravel terraces on Kohala Volcano at altitudes as high as 300 m above present-day sea level indicated to Stearns and MacDonald (1946) that the island has undergone partial emergence, not continuous submergence. These deposits, however, have been reinterpreted as tsunami deposits associated with one of the many huge landslides of the Hawaiian Islands (McMurtry et al., 2004).

3.3. Pololū Slump and Kohala Sea Cliffs

A massive landslide, the Pololū Slump, occurred directly offshore of the Kohala amphitheater-headed valleys on the northeast flank of Kohala Volcano (Fig. 2). This landslide was ~20 km wide and traveled 130 km (Moore et al., 1989; Moore and Clague, 1992). The most obvious features of the slump are huge disorganized blocks

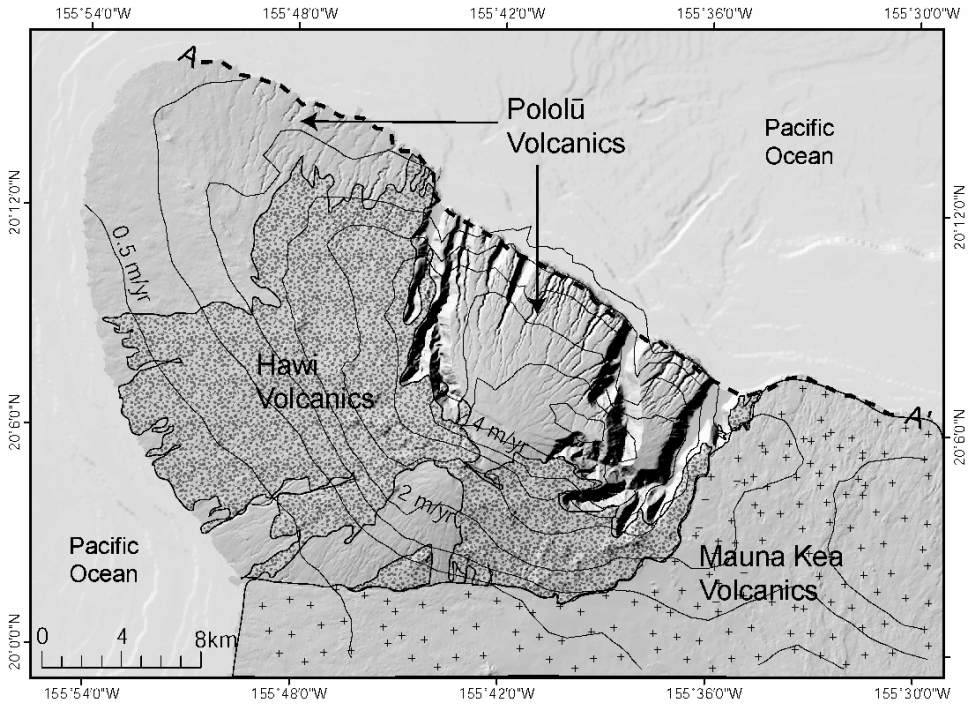

Figure 3. Shaded relief map of Kohala Volcano with volcanic units outlined following Wolf et al. (1996). Note that the Pololū volcanics are not patterned. Coastal profile A-A' is shown in Figure 4. Contour map of average annual precipitation (1961-1990) is shown, with a contour interval of 0.5 m/yr, from PRISM climate model (Spatial Climate Analysis Service, Oregon State University, http://www.ocs.oregonstate.edu/prism/, created 4 Feb 2004). Note that orographic effects cause rainfall to exceed 4 m/yr near the heads of the amphitheatre-headed valleys. See Figure 2 for topographic data sources.

below the 1000 m isobath (Fig. 2). Upslope of the blocks is a broad ~400 m bathymetric depression, which likely represents the slump scar or a down-dropped block related to the slump (Smith et al., 2002). It is difficult to reconstruct the dimensions of the slump scar due to post-slumping carbonate and siliciclastic sedimentation. Further complicating the bathymetry are several submarine canyons, which cut through the bathymetric depression (Figs. 1 & 3). These canyons have the greatest relief near their heads and shallow downstream, becoming indistinct at a depth of ~ 900 m. The canyons are cut into a carbonate platform (Clague et al., 1998), and likely formed from submarine processes, such as turbidity currents. Several of the canyons end abruptly in amphitheater heads, which led to the interpretation that they were formed by dissolution of the carbonate platform by freshwater seepage (Clague et al., 1998).

Directly upslope of the slump scar are the prominent (up to 450 m high) Kohala sea cliffs (Fig. 4). The Kohala cliffs are anomalous in that neighboring sea cliffs are consistently only 20-50 m high (Fig. 4). The shoreline of Hawai‘i generally follows the topographic contours of the volcanoes, and at the scale of 10s – 100s of meters is relatively jagged in planform. In the region of the high cliffs, the shoreline is remarkably straight in planform. Since the volcano is dome shaped, the straight shoreline cuts across topographic contours resulting in the greatest relief in the middle of the cliffs (Fig. 4). The Kohala cliffs are abruptly inset ~ 2.5 km from the adjacent sections of the Hawaiian shoreline (Fig. 3). These observations suggest that the Kohala sea cliffs are the bounding headwall of the Pololū Slump (Wolfe and Morris, 1996). The near vertical failure plane would explain why the cliffs are anomalously high, straight in

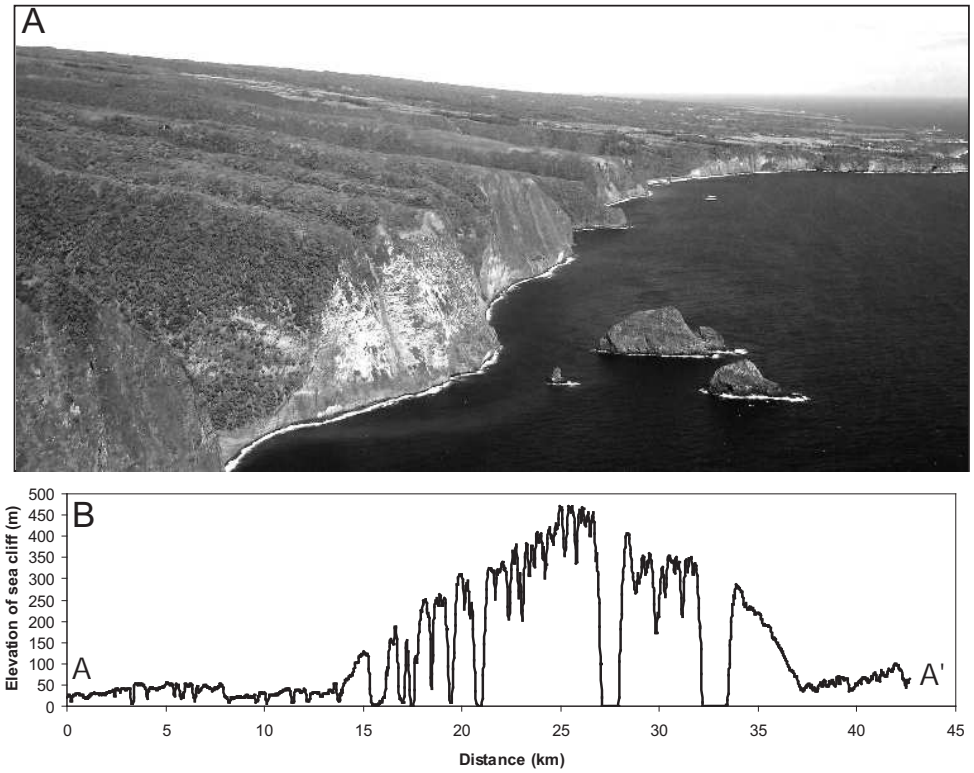

Figure 4. Kohala sea cliffs. (a) Photograph of Kohala sea cliffs. (b) Topographic profile of sea cliff elevation above present-day sea level extracted from 10-m DEM (U.S. Geological Survey). Location of profile is shown as A-A' on Figure 3. Note that in the region of the amphitheatre-headed valleys the sea cliffs are approximately an order of magnitude greater in elevation than neighboring cliffs. The mouth of Waimanu and Waipi‘o Valleys are at approximately 28 and 33 km, respectively.

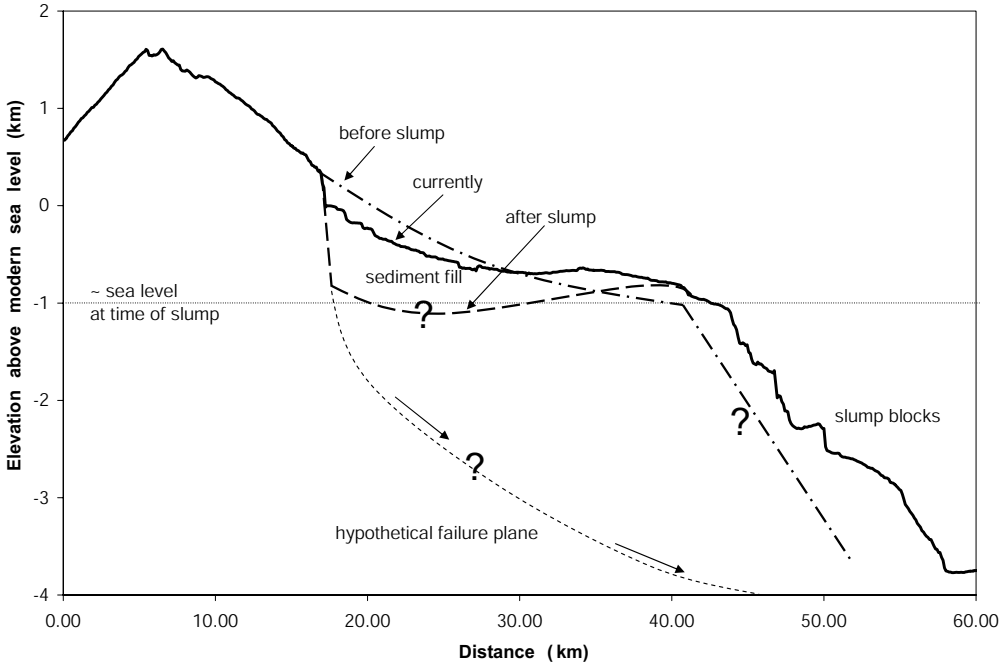

Figure 5. Topographic profile from Kohala Volcano over the Pololū Slump. Profile location is shown in Figure 2. All dashed lines are untested interpretations of the topography before and immediately after the Pololū Slump. Note that sea level at the time of the slump was probably about 1000 m lower than at present. The headscarp of the slump (expressed as the present-day sea cliffs) might have had 600-700 m of additional relief at the time of the slump as indicated by the submergence of the valleys. Since that time hundreds of meters of sediment have been deposited within the slump scar.

planform, inset significantly from the rest of the shoreline, and cut across topographic contours. Figure 5 shows a longitudinal profile from the summit of Kohala Volcano through the Pololū Slump with a hypothetical illustration of a failure plane.

Stearns and Macdonald (1946) argued that the Kohala sea cliffs are anomalously high because they are composed of older and weaker basalt and therefore have experienced greater wave erosion. It is true that southeast of Waipiʻo Valley the shoreline is composed of younger Mauna Kea flows. However, most of the shoreline northwest of Pololū Valley is composed of the same Pololū volcanics as the Kohala cliffs (Fig. 3). Wave erosion might still explain the Kohala cliffs if wave attack was somehow focused in this region. This, however, seems unlikely because the Kohala cliffs are of roughly the same trend as the neighboring cliffs. Furthermore, wave erosion cannot easily account for the abruptly straight coastline that cross-cuts topographic contours.

Moore et al. (1989) suggested that the headwall of the Pololū Slump is near the summit of Kohala Volcano where several extensional faults, akin to pull-apart basins, have been mapped (Stearns and Macdonald, 1946) (indicated by white arrows on Fig. 1). In such a scenario, Waipiʻo and Pololū Valleys might follow faults that laterally bound the slump. Waipiʻo and Honokāne Valleys do appear to follow these faults near their heads (Fig. 1). Smith et al. (2002) argued, however, that the surface of the volcano laterally bounded by Waipiʻo and Pololū Valleys is continuous with the rest of the volcano summit, indicating little displacement. The volcano flank is actually slightly steeper in this region as compared to the neighboring slopes, which is not consistent with slumping. The faults near the summit of Kohala probably resulted from an ancient

caldera (Stearns and Macdonald, 1946), or radial rift arms that accommodated hanging displacement as the Kohala rift zone extended (Smith et al., 2002). A few of these faults cross cut both the Pololū and Hawi volcanics. The majority of Hawi flows, however, appear to have been diverted to the northwest and southeast by the graben, which suggests that most of the displacement predates the Hawi volcanics (Stearns, 1985).

The Pololū Slump, like other large Hawaiian landslides, likely occurred when the volcano was close to its maximum size (~385 ka) and seismic and volcanic activity was high (Moore et al., 1989; Moore and Clague, 1992; Moore et al., 1994). Since the -1000 m terrace is only slightly disturbed in the region of the Pololū Slump (Fig. 2), Moore et al. (1989) hypothesized that the slump occurred prior to or during the formation of the -1000 m terrace. An alternate explanation is that the slump postdates the formation of the terrace and that the -1000 m isobath was not significantly disturbed because there was little displacement in this region, e.g. if the slump was rotational (Fig. 5). The latter interpretation is also consistent with the observation that the 1000 m isobath is pushed ~ 5 km seaward in the region of the Pololū Slump as compared to the surrounding area (Figs. 2 & 5). Furthermore, the slump is composed of Pololū volcanics and therefore is probably younger than 250 ka. In either scenario, the slump scar is overlain by the -450 m Mauna Kea terrace (Fig. 2), restricting the slump to be older than ~173 ka. If the faults near Kohala summit were caused by the slump, then the slump must be older than the eruption of Hawi volcanics about 230 ka. These observations suggest that the slump occurred between 385 ka and 173 ka, and perhaps between 250 ka and 230 ka.

3.4. Kohala Amphitheater-Headed Valleys

While streams have barely cut into the drier western slopes of Kohala Volcano, the amphitheater-headed valleys to the east are typically 300-750 meters deep and terminate abruptly in steep headwalls (Fig. 1). These valleys have stubby heads (U-shaped in planform), which led to the *amphitheater* designation (Hinds, 1925). In order to analyze the Kohala valleys, we have constructed longitudinal profiles for nine valleys that are typical of the range of valley morphologies in the region (Fig. 6). Valley numbers (1-9) are shown on Figure 1 and valley and stream characteristics are given in Table 1. Valleys 1-7 are *amphitheater-headed valleys*. Amphitheater-headed valleys have cut through the Kohala sea cliffs and have steep headwalls located several kilometers inland from the cliffs. The abrupt termination of valleys at steep headwalls and the greater steepness of headwalls as compared to valley sidewalls suggest valley erosion by headwall propagation. This interpretation is further supported by stream piracy inferred from valley cross-cutting relationships, as discussed below.

In contrast to the amphitheater-headed valleys, there are smaller valleys with acutely pointed heads (i.e. gradually narrowing in planform) and longitudinal profiles that grade smoothly with the regional topographic slope (e.g. valley 9). These smaller valleys run along side of and often drain into the larger canyons or pour over the Kohala sea cliffs (Figure 4a), and will therefore be referred to as *hanging valleys*. There are a few valleys intermediate in size between the smaller hanging valleys and the larger amphitheater-headed valleys (e.g. valley 8). *Intermediate valleys* have pointed heads in

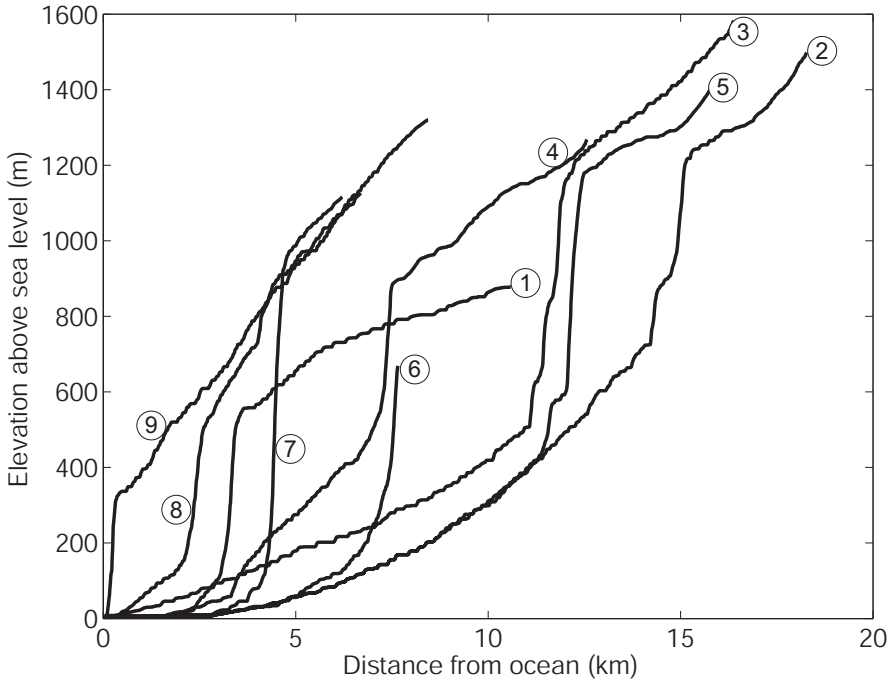

Figure 6. Longitudinal profiles from amphitheatre-headed valleys (1-7), an intermediate valleys (8) and a hanging valley (9). Profile 9 is representative of many valleys that are hanging at the sea cliffs, which are not shown here to avoid redundancy. The geographic locations of the valleys are shown in Figure 1. Profiles were generated following the steepest slope (D8) using a 10-m digital elevation model (U.S. Geological Survey). Much of the fine scale variation is an artifact of resolution of the grid. Depressions were artificially filled to generate the profiles. Profiles were chosen to represent the entire length of the drainage area from source to valley mouth. Note that lower portions of many of the amphitheatre-headed valleys have subsided below present-day sea level and are filled with sediment.

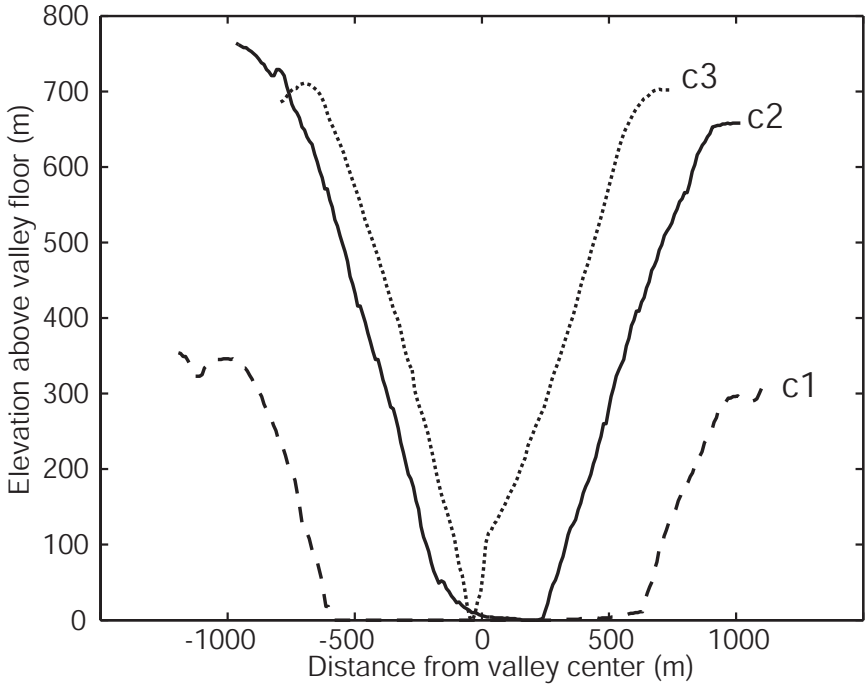

Figure 7. Cross sections of Waipi‘o Valley. Profiles were generated from a 10-m digital elevation model (U.S. Geological Survey). Profile locations are shown as dotted lines on Figure 1. These cross sections are typical of the other amphitheatre-headed valleys in that near their heads the valleys are V-shaped, while near their mouths valleys are U-shaped due to relative sea level rise and sedimentation. The true bedrock valley bottom at c1 might extend 600 - 700 m below present-day sea level based on extrapolation of the valley wall slopes.

planform like the hanging valleys, but they widen and deepen significantly near their mouths similar to the amphitheater-headed valleys.

Most of the upstream portions of the amphitheater-headed valleys are V-shaped in cross-section (Figs. 7, 8A & C), in contrast to the U-shape called for in the seepage-erosion model (Kochel and Piper, 1986; Kochel and Baker, 1990). As an example, Figure 7 shows three topographic cross sections of Waipi‘o Valley, the locations of which are shown on Figure 1. We have found that most valley sidewalls have slopes of approximately 50 degrees, despite being different sized valleys with varying drainage areas. Soil production, vegetation growth, and shallow landsliding are active processes and are likely important in maintaining the relatively constant valley-wall slopes (Wentworth, 1943; White, 1949; Scott and Street, 1976; Stearns, 1985). While V-shaped in cross-section near their headwalls, amphitheater-headed valleys are flat-floored near their mouths (Figs. 7, 8B). This is not a result of seepage erosion, but rather of sedimentation concurrent with island subsidence (Stearns and Macdonald, 1946). The depth to which the valleys have been carved below present-day sea level is not known, but estimates range from 100 m (Macdonald et al., 1983) to more than 400 m (Stearns, 1985). Extrapolation of the side slopes of Waipi‘o Valley (Fig. 7) results in a bedrock valley floor about 600 - 700 m below present day sea level. This, however, is an upper estimate because the valley walls have probably retreated laterally following subsidence.

The amphitheater valley headwalls often have several plunge pools interrupting cascading waterfalls, which appear to dominate erosion of valley headwalls (Figs. 8C-E). These plunge pools. Howard et al. (1994) inferred that stepped waterfalls are

vertically *drilling* into the rock through the impact of falling water and sediment. Figure 8D shows coarse sediment deposited within and next to plunge pools, which must have been delivered by the waterfalls. In some cases, plunge pool erosion also appears to be undercutting the headwall (Fig. 8E), possibly exploiting weaker beds in the layered volcanic rock. The locations of the plunge pools do not seem to correlate with any major discontinuities in rock strength (unlike classic models of waterfall erosion, e.g. Niagara Falls (Gilbert, 1907)). Instead, plunge pools are at a variety of different elevations and often in a series of steps along a single flow path. During high precipitation events, tens of waterfalls can be active at a single valley head (personal communication with local residents, 2004; Figs. 8C-E).

Springs do exist in the Kohala valleys, as one would expect in any deeply incised canyon that intersects water tables. However, we have not observed weathered rock or overhangs associated with springs, which are expected indicators of seepage erosion (Lamb et al., 2006). Peak annual surface flows exceed spring discharges by nearly two orders of magnitude (Table 1). Coarse debris that lines the streambeds must be transported away from valley headwalls for headwall propagation to occur. Spring discharges are presently incapable of transporting this material.

If valley formation occurred from upstream propagation of valley headwalls due to waterfall erosion, then one might expect there to be a correlation between headwall migration distance and stream discharge (e.g. Whipple and Tucker, 1999; Hayakawa and Matsukura, 2003; Bishop et al., 2005; Crosby and Whipple, in press). Using the digital elevation data shown in Figure 1, we have calculated the contributing drainage area to the dominant knickpoints in the valley profiles (i.e. the headwalls for the

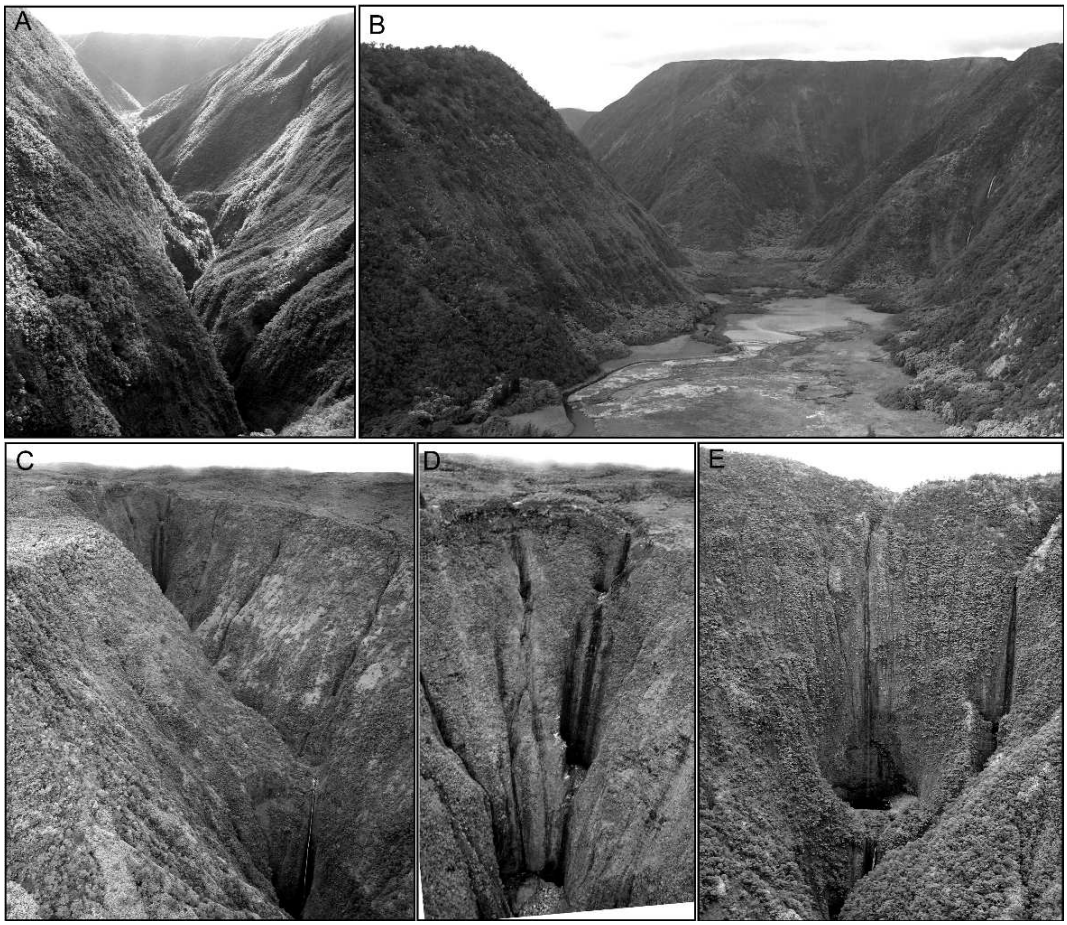

Figure 8. Photographs of Kohala amphitheatre-headed canyons. (A) Upslope portion of Waipiʻo Valley showing V-shaped cross section (near c3 in Figs. 1 & 7). (B) Mouth of Waipiʻo Valley showing U-shaped cross section (near c1 in Figs. 1 & 7). (C) Headwall of Waipiʻo Valley (valley 2). (D) Close-up of headwall of Waipiʻo Valley (valley 2) showing multiple plunge pools vertically drilling into the rock. (E) Headwall of East Honokāne (valley 3) showing plunge pool drilling as well as undercutting.

Valley #	Stream/Valley Name	Morphology	Average annual peak discharge (m^3/s)	Spring flow (m^3/s)	Migration distance (km)	Drainage area (km^2)
1	Hiilawe / Waipiʻo	Amphitheater	?	0.35	3.33	16.46
2	Kawainui & Kawaiki / Waipiʻo	Amphitheater	41.40	0.35-0.96	15.06	8.51
3	East Honokāne	Amphitheater	?	0.46-0.59	11.85	8.38
4	Pololū	Amphitheater	?	0	7.46	4.31
5	Alkahi / Waipiʻo	Amphitheater	12.47	?	12.15	3.92
6	Waimanu / Waimanu	Amphitheater	?	0.22 - 0.52	7.56	0.58
7	Waihilau / Waimanu	Amphitheater	?	0.22 - 0.52	4.41	1.54
8	Honopue	Intermediate	?	?	2.47	4.49
9	Waikaloa	Hanging	?	?	0.26	4.15

Table 1. Characteristics of Kohala valleys. Locations of valleys are shown on Figure 1 and longitudinal profiles are shown on Figure 6. Annual peak discharge is from U.S. Geological Survey (gauge # 16720000, 16720300, 16725000) averaged over a 40 year period. Spring flow measurements are from Stearns and MacDonald (1946) and Kochel and Piper (1986). Knickpoint migration distance was measured from the longitudinal profiles (Figure 6) as the distance from the present day shoreline to the location of maximum slope, which typically corresponds to midway up the headwall for the amphitheatre and intermediate valleys, and midway up the sea cliffs for the hanging valley (which is why valley 9 has a nonzero migration distance). Drainage area is the contributing area to the valley heads (waterfalls) for the amphitheatre and intermediate valleys, and to the sea cliffs for the hanging valley. Note that the drainage areas to the valleys have changed in time due to upslope propagation of knickpoints and stream capture.

amphitheater and intermediate valleys, and the Kohala sea cliffs for the hanging valleys). Drainage area is used as a proxy for stream discharge because historic stream records are only available for two sites (Table 1). All of the intermediate and hanging valleys in the Kohala region have drainage areas less than 5 km^2. For example, valleys 8 and 9, which are two of the largest intermediate and hanging-type valleys, have drainage areas of 4.49 and 4.15 km^2, respectively. In contrast, the amphitheater-headed Waipi‘o Valley (valley 2) and West Honokāne Valley (valley 3) have two of the largest drainage areas contributing to their headwalls of ~ 8 km^2 each (Table 1). Valleys 2 and 3 also drain the very wet Kohala summit (Fig. 3), have what visually appears to be the most active plunge pools (Figs. 8C-E), and have two of the longest headwall-propagation distances from the present-day sea cliffs of ~ 15 and 12 km, respectively (Table 1).

Several of the amphitheater-headed valleys, however, do not appear to follow a trend of increasing headwall migration distance with increasing drainage area. For example, Hiilawe Valley (valley 1) has the largest drainage area of any of the amphitheater valley heads of about 16 km^2, but its headwall is only ~ 3 km from the sea cliffs (Fig. 1). Part of the reason for this is probably because Hiilawe Stream drains the relatively dry southeast side of Kohala Volcano, where average annual rainfall is about half that of the wet Kohala summit (Fig. 3). Also important is that the headwall of Hiilawe Valley is presently located at the contact between Pololū and Mauna Kea basalts (Fig. 3). Headwall retreat might have stalled at this geologic contact because Mauna Kea basalt is younger and possibly less weathered and more resistant to erosion than Kohala basalt.

In contrast to Hiilawe Valley (valley 1), amphitheater-headed valleys 4-7 (Fig. 1) have headwalls located many kilometers from the present-day sea cliffs, but have drainage areas feeding their waterfalls that are less than 5 km^2 – values typical of the hanging and intermediate valleys. We speculate that these valleys are inactive and that headwall migration occurred in the past when drainage areas were larger. The drainage areas to these valley headwalls have declined in time because 1) the headwalls have cut into their own contributing areas as they have migrated upstream, and 2) dominant streams (particularly valleys 2 and 3) have pirated the drainage that once flowed to valleys 4-7. As an example of the later point, the headwall of Waimanu Valley (valley 6) is about 4 km inland from the sea cliffs, although its present-day drainage area is only 0.58 km^2. It does not appear to have an actively eroding headwall because it is mantled with talus (Kochel and Piper, 1986) and plunge pools are not well developed. Examination of the topography clearly shows that Waipi‘o Valley (valley 2) has cut across the headwall of Wiamanu Valley and captured its drainage (Fig. 1). This suggests that Waimanu Valley formed before it was truncated by Waipi‘o Valley. After truncation, the contributing drainage to Waimanu Valley has been insufficient to transport the coarse debris at its headwall and further headwall propagation (despite active seepage flow of 0.22 – 0.52 m^3/s, Table 1). While the piracy of Waimanu (valley 6) by Waipi‘o (valley 2) is visually the clearest example in Figure 1, it is possible that all of the eastern amphitheater-valley heads (e.g., valleys 5 – 7) have lost some drainage to Waipi‘o (valley 2), and that Pololū Valley (valley 4) and West Honokāne Valley have lost drainage to the eastern head of Honokāne (valley 3). This can be seen by analyzing current drainage paths (perpendicular to contours) on Figure 1.

In order to quantitatively test whether there is a correlation between drainage area and knickpoint propagation rate, it would be ideal to have a record of drainage area to the knickpoints before significant headwall retreat and stream piracy. Unfortunately, this is not possible since headwall propagation has changed drainage patterns through time. This notwithstanding, it is encouraging for the plunge-pool-erosion hypothesis that the two valleys (valleys 2 and 3) that appear to have the most actively eroding plunge pools, also have two of the largest drainage areas and headwall propagation distances, and the drainage areas to these valley heads are about twice as large as those to the hanging and intermediate valleys. If valleys 2 and 3 are truly the only active amphitheater-headed valleys, then a threshold drainage area of about 5-8 km^2 might be necessary for knickpoint propagation on Kohala.

The dominance of valleys 2 and 3 over the hanging and intermediate valleys (and perhaps over the other amphitheater-headed valleys) is at least partially due to the faults near the Kohala summit (Fig. 1). While argued above not to represent the headscarp of the Pololū Slump, these faults clearly have influenced drainage to the Kohala valleys. The faults cut off the headwaters of the hanging valleys and funnel this drainage laterally to the amphitheater-headed valleys. The fact that the amphitheater-headed valleys are developed only on the edge of this fault scarp, combined with the observation that the hanging valleys are bordered upslope by the fault scarp, suggests that this drainage divide encouraged the amphitheater-headed valleys to grow at the expense of the hanging valleys.

The Kohala amphitheater-headed valleys cut through the Pololū volcanics and therefore must be younger than ~ 250 ka. Some of the valleys formed before the

cessation of Hawi volcanics (~ 130 ka) and Mauna Kea volcanics (~ 65 ka) because Hawi flows poured into the heads of Pololū Valley (and were later incised through (Macdonald et al., 1983)) and East Honokāne (valley 3) (Wolfe and Morris, 1996), and Mauna Kea volcanics filled the head of Hiilawe valley (valley 1) (Fig. 3). If the estimated fill of 600-700 m in Waipiʻo Valley is correct, then such incision implies that the valley headwall must have propagated upstream on the order of several kilometers or more when sea level was lower than presently by 600-700 m (Fig. 1). This suggests that headward erosion of Waipiʻo Valley began shortly after the cessation of Pololū volcanics (~ 250 ka) when Kohala Volcano was an additional 650 m above sea level (i.e. 250 ka x 2.6 mm/yr = 650 m). This would place the valley initiation time appropriately close to the age of Pololū Slump.

3.5. Conceptual Model

The large Kohala amphitheater-headed valleys are directly upslope from and are laterally bounded at their outlets by the Pololū Slump and the Kohala sea cliffs (Fig. 2). Based on this spatial correlation and the coincident timing discussed above, we propose that the Pololū Slump (rather than seepage erosion) created large knickpoints in pre-existing stream profiles. Further, we suggest, based on our field observations of plunge pool erosion, that waterfall erosion (rather than seepage erosion) has caused upstream migration of these knickpoints to form the amphitheater-headed valleys.

Before the Pololū Slump, several factors might have led to the development of dominant streams (Fig. 9A). In any drainage network, non-uniform topography, lithology, and precipitation cause some streams to capture more drainage area than

others. Fault scarps near the summit of Kohala force high elevation drainage to flow laterally, diverting runoff toward valleys at the northwest and southeast edges of the slump zone. Orographic variation in rainfall across the volcano is presently significant (Fig. 3) and was likely even greater when the volcano was an additional 1000 m above sea level. Due to the fault scarp and the radial drainage pattern, only a few streams receive high elevation runoff, and due to orographic effects, precipitation is greater at high elevations, leading to the dominance of streams with their source regions near the summit.

Approximately 250 ka, the Pololū Slump imposed giant knickpoints on the streams (Fig. 9B). We propose that waterfalls in dominant streams had sufficient sediment and water discharge that, through waterfall erosion, the knickpoints propagated upstream (Fig. 9C). As discussed above, observations of the valley headwalls suggest that vertical drilling into the rock by the falling water and sediment is a dominant headwall erosion process. Mass failures likely also contribute to headwall propagation and probably result from plunge-pool undercutting and failure of the narrow ridges in between plunge pools (Stearns, 1985). Despite failures, horizontal bedding and vertical fracturing of the basalt promote a relatively stable headwall and thus preserve the amphitheater shape of the propagating valley heads (Stearns, 1985; Dunne, 1990). Storm-induced runoff events are probably necessary to evacuate collapsed material and allow headwall propagation to continue.

Bedrock can be eroded within a plunge pool through plucking of fractured blocks due to cavitation or differential fluid pressure, and abrasion due to impacting sediment (Whipple et al., 2000). Plucking might be particularly important if the

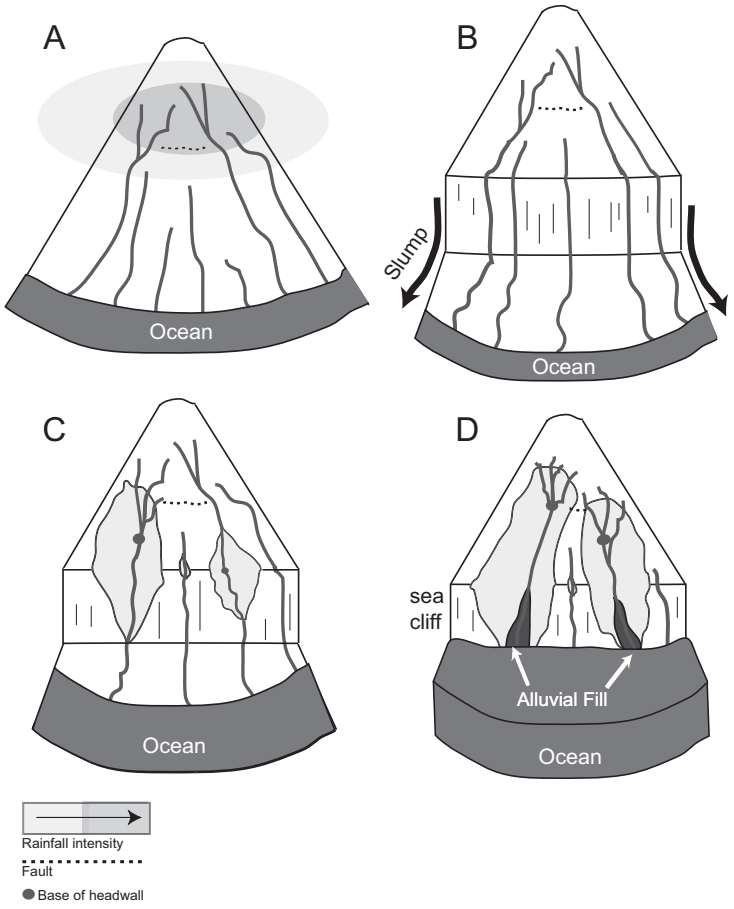

Figure 9. Conceptual model for the formation of the Kohala amphitheatre-headed canyons. (A) Variable topography, lithology, orographic precipitation, fault-induced drainage divides, and a radial drainage pattern leads to dominant streams. (B) The Pololū Slump imposes giant knickpoints on the streams. (C) Knickpoints propagate in dominant streams and through plunge pool erosion and mass wasting capture the headwaters of neighboring streams. Smaller streams remain hanging at the slump headscarp. (D) Rising sea level floods the lower portions of the valley floors causing sedimentation and U-shaped valley cross sections.

bedrock is well fractured (e.g. Bollaert and Schleiss, 2003). If the rock is massive, then abrasion is expected to dominate erosion (Whipple et al., 2000). Sediment might abrade the bedrock within a plunge pool due to the initial impact and later impacts as the turbid water is churned within the pool.

As a waterfall drills into a plunge pool, erosion must eventually cease when the plunge pool is approximately level with the valley floor. At this point the valley floor slope is too gentle to transport sediment away from the headwall and the plunge pool becomes armored with sediment. In order for retreat of the headwall to continue via vertical plunge-pool incision, a new plunge pool must be initiated. Thus, the creation of steps that lead to plunge pools might be a rate limiting process for headwall retreat. We speculate that steps on the face of the headwalls form as weaker beds (e.g. inter-bedded ash layers) are weathered and attacked by surface runoff. Many small sub-horizontal steps of protruding basalt beds can be seen at a variety of elevations at valley headwalls (Fig. 8). Prominent steps might eventually form plunge pools as they are bombarded by falling water and sediment. The abundance of protruding beds and plunge pools at different elevations at a single valley headwall (e.g. Figure 8D) suggests that plunge-pool form frequently.

As a headwall propagates upstream, the radial drainage pattern induced by the dome shape of the volcano allows the capture of the headwaters of other streams. Multiple waterfalls and mass wasting of narrow ridges in between plunge pools cause propagation of a headwall that is much wider than any individual stream (e.g. Fig. 8D). Mass wasting along valley sidewalls also captures neighboring drainage (e.g. Hovius et al., 1998). Valley-wall slopes are reduced to a near constant 50 degrees, where

presumably vegetation growth aids stability (Scott and Street, 1976). Cross cutting of smaller valleys by amphitheater-headed valleys has been used as evidence for seepage erosion in Hawai‘i (Kochel and Piper, 1986; Kochel and Baker, 1990) and elsewhere (e.g. Hoke et al., 2004). This need not be the case because such cross cutting relationships are expected to result from headwall propagation due to waterfall erosion and mass wasting (Macdonald et al., 1983). As discussed above, the Kohala drainage is strongly influenced by faults, which appear to control the orientation of the heads of Waipi‘o and Honokāne Valleys. It is possible that some of the cross-cutting relationships (e.g., Waipi‘o crossing Waimanu Valley) were caused by rerouting of drainage due to these faults.

Shortly after failure of the Pololū Slump, the headwalls might have been more pointed or V-shaped in planform than currently because the streams upslope of the headwalls would have had larger drainage areas and higher erosion rates (Fig. 9C). For example, the intermediate Honopue Valley (valley 8) has a pointed headwall in planform because of substantial incision upslope of the knickpoint (Fig. 1). As the headwalls propagate upstream, they progressively cut into their own drainage areas, eventually resulting in reduced water and sediment discharge. When a headwall approaches the volcano summit, valleys upstream of the headwalls are not significantly incised, and therefore headwalls are more U-shaped in planform. At this point, sediment generated from mass failures at the headwall itself might become more important than previously for providing tools to abrade within plunge pools. Eventually, as drainage area diminishes, headwall propagation by waterfall erosion will cease. Weathering and mass wasting then become dominant processes for headwall

erosion (e.g. Young, 1985; Weissel and Seidl, 1997), likely resulting in talus deposition at the base of the headwall. If hillslope processes cause the headwall slope to relax at the same rate as the valley walls, then the amphitheater shape will maintain even if the headwall is no longer actively retreating (e.g. Howard, 1995).

Long profiles of the Kohala valley floors are generally concave up downstream of valley headwalls (Fig. 6) indicating an increasing channel slope with decreasing drainage area. The slope of the streambeds is probably set by the flows ability to transport coarse sediment (Sklar and Dietrich, in press). If sediment cannot be removed from the base of the headwall, deposition will occur and the streambed slope will increase until sediment transport can occur. Transport of sediment away from the headwall, therefore, is a fundamental control on the height of the headwall as it propagates upstream. As relative sea-level rises, however, the valley floor becomes graded to sea level, transitioning to an alluvial-mantled reach. Subsidence eventually submerges the lower reaches of the valleys, which forces deposition and U-shaped valley cross sections (Fig. 9D).

Most of the Kohala valleys are widest near their mouths and narrow slightly headward. This, however, is not true of Honokāne Valley, which widens headward (Fig. 1). Headward widening is significant because it is thought to be a characteristic of seepage erosion (e.g. Higgins, 1984). Since the Kohala valleys are V-shaped in cross section and have near uniform sidewall slopes, geometry requires that valleys with more relief must also be wider. This appears to be the case for Honokāne Valley. Headward widening of Honokāne correlates with a headward increase in relief because the volcano surface is steeper than the valley floor (Fig. 6). As discussed above, a streams ability to

transport sediment governs the valley-floor slope, which in turn sets valley relief. Thus, headward widening of Honokāne valley might simply be a result of a headward increase in valley relief and does not necessarily indicate seepage erosion.

Smaller streams have not produced migrating knickpoints because they have smaller drainage areas (< 5 km^2) and therefore insufficient water and sediment discharge to cause knickpoint retreat. The threshold might come about because the waterfalls are not able to initiate the step-forming process, pluck blocks from the plunge pools, transport deposited sediment out of plunge pools, or transport sediment to the plunge pools. These mechanisms are discussed in more detail below.

If the knickpoints were initiated by the Pololū Slump about 250 ka at the approximate location of the present-day sea cliffs, than an average knickpoint migration rate can be calculated. Here, we make this calculation for valleys 2 and 3 since they are arguably the most active valley heads. Dividing migration distance (Table 1) by 250 ka yields average headwall migration rates of 60 and 47 mm/yr for valleys 2 and 3, respectively. These rates are large, but are not unreasonable. For example, average waterfall retreat rates in excess of 1 m/yr have been documented for Niagara falls, U.S. (Gilbert, 1907; Philbric, 1974), Ryumon Falls, Japan (Yoshida and Ikeda, 1999), and various waterfalls in Scotland (Bishop et al., 2005).

3.6. Scaling of Plunge Pool Erosion

Waterfall propagation is typically thought to occur in layered material through undercutting of a weak layer and the subsequent collapse of an overlying strong layer (e.g. Gilbert, 1907; Holland and Pickup, 1976). Many bedrock waterfalls, however, are

not undercut, which sheds doubt on the universality of this model (Young, 1985). In fact, the validity the waterfall-undercut model has even been questioned for its most prominent field example, Niagara Falls, USA (Philbric, 1974). Instead, it has been proposed that waterfalls retreat by fatigue and mass failure, and that the water only sweeps material away that would otherwise buttress the headwall (e.g. Young, 1985; Seidl et al., 1996; Weissel and Seidl, 1997). Nonetheless, most quantitative models treat waterfall propagation as a fluvial incision process using drainage area (Hayakawa and Matsukura, 2003; Crosby and Whipple, in press) or stream power (Howard et al., 1994; Rosenblum and Anderson, 1994; Seidl et al., 1994; Whipple and Tucker, 1999; Bishop et al., 2005) as the driver for knickpoint propagation. While these models might simulate an upstream propagating wave in the landscape, they do not explicitly include the processes that we observe at the Kohala waterfalls, mainly vertical plunge pool erosion and mass wasting.

Herein we propose a simple quantitative expression for headwall propagation. Our current level of knowledge does not permit a complete model of headwall retreat involving mass failures due to plunge-pool undercutting, drilling and weathering. We instead focus solely on developing scaling relationships for vertical plunge-pool incision. While this paints an incomplete picture, it is a useful exercise because vertical-plunge-pool erosion might be the driver for headwall propagation in Hawai‘i and, to our knowledge, it has not been described in detail. For simplicity, we only consider abrasion due to the initial impact of particles falling over a waterfall. We neglect possible contributions of plunge pool wear due to plucking of fractured bedrock

or abrasion by secondary impacts of particles as they are circulated within a turbulent pool.

Sklar and Dietrich (2004) developed a model for the abrasion of a bedrock river bottom by impacting particles, which we adopt here for the case of a plunge pool. The rate of vertical bedrock erosion E (Lt^{-1}) can be written as

$$E = \frac{q_s}{VL}\frac{\varepsilon}{\kappa}\left[1-\frac{q_s}{q_t}\right]. \qquad (1)$$

The first ratio on the right-hand side (RHS) of equation (1) represents the rate of particle impacts per unit bedrock area, where q_s is the volumetric flux of sediment that impacts the bed per unit width, V is the volume of an impacting particle and L is the bedrock area per unit width over which impacts occur. The second ratio on the RHS of equation (1) represents the volume of bedrock eroded per particle impact, where ε is the kinetic energy of a particle impact and κ is the energy required to detach a unit volume of bedrock (energy / volume). κ is a measure of the capacity of the bedrock to store energy elastically and depends on the tensile yield strength of the rock and Young's modulus of elasticity (Sklar and Dietrich, 2004). Equation (1) assumes that there is not a threshold kinetic energy to cause abrasion, which has been verified experimentally (Sklar and Dietrich, 2001). The last ratio on the RHS of equation (1) accounts for alluvial coverage that protects the bedrock from erosion, where q_t is the volumetric sediment-transport capacity of the flow per unit width. For the case of a plunge pool, q_t is the maximum sediment flux, per unit width, that the waterfall is able

to transport out of the pool. Bedrock erosion is zero when the sediment supply exceeds the flow's capacity to transport sediment (i.e. deposition occurs).

The kinetic energy of a falling particle is given by

$$\varepsilon = \frac{1}{2}\rho_s V w_f^2 \qquad (2)$$

where w_f is the vertical velocity of a particle when it collides with the bedrock and ρ_s is the particle density. If we define d as the surface area of the floor of the plunge pool per unit width, then equations (1) and (2) can be written for the case of a plunge pool as

$$E = \frac{q_s}{2d}\frac{\rho_s w_f^2}{\kappa}\left[1 - \frac{q_s}{q_t}\right]. \qquad (3)$$

The volumetric flux of material eroded from the bedrock (per unit width) at a valley headwall due to plunge-pool erosion can be written mEd, where m is the number of successive plunge pools stacked vertically above one another for an average contributing stream (Fig. 10). This implicitly assumes that E is an average or characteristic vertical erosion rate for m successive plunge pools. m does not include the plunge pool at the base of the headwall, since presumably this pool is not vertically incising and therefore does not contributing to headwall retreat. For the purpose of formulating an average headwall propagation rate, this vertical flux of material can be written as a horizontal flux of material averaged over the entire surface area the headwall (per unit width) by continuity as

$$mEd = HP \tag{4}$$

where H is the height of the propagating headwall and P is the inferred average headwall retreat rate due solely to vertical plunge-pool erosion (Fig. 10).

Equations (3) and (4) now can be combined for the rate of headwall propagation due to vertical plunge-pool erosion,

$$P = \frac{mq_s}{2H}\frac{\rho_s w_f^2}{\kappa}\left[1-\frac{q_s}{q_t}\right]. \tag{5}$$

In order to better illustrate the dependencies of headwall propagation it is useful to use the fact that the product of the total number of waterfalls in series (i.e., m+1, which is one more than the total number of plunge pool contributing to erosion m) and their average fall distance h is equal to the total height of the headwall (i.e., $H = (m+1)h$) (Fig. 10). In addition, if it is assumed that the average plunge pool depth η is much smaller than the waterfall height (i.e. $h >> \eta$), then $h \approx h + \eta$ and equation (5) can be written as

$$P = \frac{\rho_s g q_s}{\kappa}\left[1-\frac{q_s}{q_t}\right]\left[\frac{m}{m+1}\right]\left[\frac{w_f^2}{2g(h+\eta)}\right] \tag{6}$$

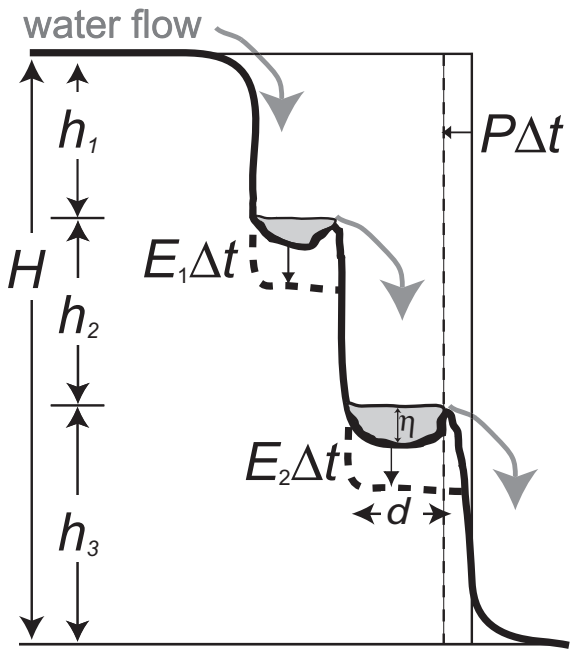

Figure 10. Schematic diagram of vertical plunge pool erosion resulting in net upslope headwall retreat as given by equation (4). There are two plunge pools (m = 2) for the particular case shown. Vertical erosion in each plunge pool acts over an area, per unit width, d assuming the plunge pools are of roughly the same diameter. After a time Δt (shown by dashed lines) a net volume of eroded material per unit width is given by (E_1 + E_2)$d\Delta t$, or equivalently $mEd\Delta t$, where E is the average plunge pool erosion rate. As shown by the thin lines, this eroded volume is equivalent to a headwall propagation rate P acting over the total area of the propagating headwall, per unit width, H in time Δt. Note that the sum of the heights of the waterfalls is equal to the total height of the headwall, or equivalently the product of the average waterfall height h and the total number of waterfalls (i.e. $h_1 + h_2 + h_3 = H = (m+1)h$).

Equation (6) is preferred over equation (5) because it illustrates that, in addition to sediment supply q_s, sediment density ρ_s and rock erodibility κ, headwall propagation is a function of three non-dimensional ratios, with values between zero and unity, shown in brackets: 1) the sediment supply versus transport capacity of the plunge pools, 2) the existence and relative number of plunge pools, and 3) the kinetic versus potential energy of sediment impacts. Note that headwall propagation given by equations (5) and (6) is predicted to be independent of the surface area of the plunge pools *d*.

Equations (3) and (6) predict that the rates of vertical plunge pool erosion and headwall propagation depend (non-linearly) on the flux of sediment that passes over the waterfall. Sediment flux is positively correlated with the rate of conversion of rock to sediment from the valley walls and channel bed upslope of the waterfall, and the drainage area of the basin that contributes to the waterfall. Sediment flux also depends inversely on the recurrence interval of sediment-transporting events in the stream upslope of the waterfall (e.g. Sklar and Dietrich, in press). Given that the production of sediment and the recurrence interval of storm events are probably similar for different Kohala amphitheater-headed valleys because of similar bedrock lithology and climate (except for valley 1), equations (3) and (6) are in qualitative agreement with our Kohala observations that valley headwalls with relatively large contributing drainage areas appear to have better developed plunge-pools and faster headwall retreat rates.

While sediment can abrade rock, it can also protect bedrock from erosion if the sediment supply exceeds the waterfalls ability to transport sediment out of the plunge pools causing deposition (e.g. Sklar and Dietrich, 2001). As shown in the first bracketed ratio on the RHS of equation (6), the headwall propagation rate is predicted to

tend to zero as sediment supply approaches the transport capacity. To our knowledge, the sediment transport capacity of a plunge pool has yet to be assessed. It is likely to be different than the simpler and better studied unidirectional case due to complex 3D flow of the impinging jet. For example, as a plunge pool grows in depth, the ponded water slows the impact velocity of the falling particles and dissipates energy of the plunging water. If deposition occurs, the downstream lip of the plunge pool must be incised into so that sediment can be transported out of the pool and erosion can continue.

Critical to erosion by vertical plunge-pool drilling is the formation of plunge pools, i.e. the functional form of m. The second bracketed ratio on the RHS of equation (6) shows that headwall propagation is only weakly dependent on the number of plunge pools m for large m. m must be greater than zero, however, for headwall propagation by waterfall drilling to occur. As discussed in the Conceptual Model section, m is a function of step formation, which in turn probably depends on heterogeneity of rock strength at the headwall, the magnitude of differential weathering, and the discharge of water and sediment pouring down the face of the headwall. The mechanics of step formation, however, remain unclear. In order for equation (6) to be a valid representation of headwall retreat, we must assume that the formation of steps is not a rate limiting process, so that $m > 0$ at all times. This appears to be a reasonable assumption in Hawai‘i since most headwalls have several active plunge pools and many protruding beds that could become plunge pools (Fig. 8D). Typical values of m for the Kohala valleys are between 1 and 10. Implicit in equation (6) is the assumption that steps are generated at the top of the headwall. This also seems reasonable, as there are many steps that occur near the top of the headwalls (e.g. Fig. 8D) and there does not

appear to be a critical fall distance necessary to generate steps. In reality, however, steps can develop below the top of the headwall if the overlying rock is removed by weathering and mass wasting, processes neglected in this scaling analysis.

The third bracketed ratio on the RHS of equation (6) represents the ratio of kinetic versus potential energy of a particle impact, which is a function of the amount of energy lost to drag. The impact velocity increases as the height of the waterfall increases until drag on the particle causes it to approach terminal velocity. In Appendix 1, we derive an expression (equation A9) for the fall velocity of a particle considering the effects of air drag and drag induced on the particle within the ponded water of a plunge pool. The solution to equation (A9), shown in Figure 11, indicates that drag is important for small particle diameters D, large waterfall heights h, and large plunge pool depths η (Fig. 11). For waterfall heights typical of the Kohala valleys (h ~ 100 m), air drag has only a minor effect on particle fall velocity for $D \geq$ 10 cm and reduces the fall velocity by approximately a factor of two for $D \approx 1$ cm (Fig. 11A). Drag within the plunge pool, however, is much more significant than air drag and must be taken into account for $D <$ ~ 1 m when $\eta >$ ~ 1 m (Fig. 11B). For D < 10 cm and $\eta >$ ~ 1 m, particles approach terminal velocity within the plunge pool, and Equation (A9) can be reduced to

$$w_f = \sqrt{\frac{4(\rho_s - \rho_w)}{3\rho_w}\frac{gD}{C_d}} \qquad (7)$$

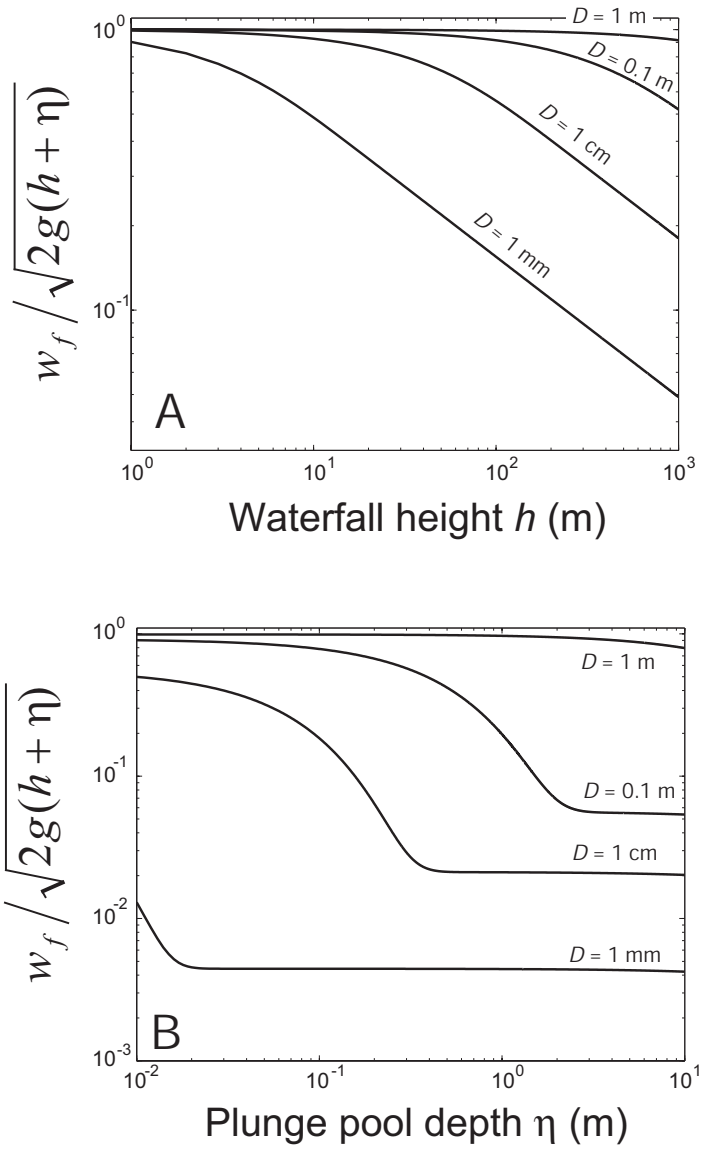

Figure 11. Plot of particle impact velocity as given by equation (A9) normalized by the impact velocity assuming no drag (equation 8) for different particle diameters *D*. Equation (A9) is evaluated for the conditions of (A) different waterfall heights and zero plunge pool depth and (B) a constant waterfall height of 100 m and variable plunge pool depths. The calculation assumes that the density of sediment = 2800 kg/m^3, the density of water = 1000 kg/m^3 and the density of air = 1.275 kg/m^3. The particles are assumed spherical, so that $V/A = 2D/3$. The drag coefficient C_d was calculated for natural spherical particles at terminal settling velocity using the formula of Dietrich (1982). See Appendix 1 for more detail.

where g is the acceleration due to gravity and ρ_w is the density of water. C_d is a drag coefficient and it depends on the particle Reynolds number (e.g. Dietrich, 1982). Inserting equation (7) into equation (6) reveals that headwall propagation is linearly dependent on the particle size and inversely dependent on the waterfall height for drag-dominated particles.

On the other hand, both air drag and plunge-pool drag are predicted to be negligible for large particle sizes (D > 10 cm) and small plunge pool depths (η < 10 cm) (Fig. 11). Drag might be further reduced in air due to downdrafts caused by the falls (Young, 1985) and in plunge pools due to the vertical velocity of the impinging waterfall and aeration of the pool. If drag can be neglected, then the impact velocity can be approximated by assuming full conversion of potential energy to kinetic energy,

$$w_f = \sqrt{2g(h+\eta)} \tag{8}$$

and therefore the third bracketed ratio in equation (6) is unity. Interestingly, for this case headwall propagation is predicated to be independent of the particle size, the waterfall height and the total headwall height. This is because the energy of the sediment impacts depends linearly on waterfall height and so does the volume of rock that must be eroded for the headwall to propagate a unit distance. Note, however, that a single larger particle is still expected to erode more bedrock than a single smaller particle because the larger particle constitutes a greater sediment flux.

3.7. Prediction of Headwall Propagation Rate

It is not yet possible to use equation (6) in a landscape evolution model because there are several terms whose functional dependencies are not known, most notably m and q_t. We can, however, estimate a maximum headwall propagation rate by assuming that 1) plunge pools are abundant and their formation is not rate limiting (i.e. $m >> 0$), 2) particle fall velocities are unaffected by drag (i.e., equation (8)), and 3) that sediment supply is much less than the sediment-transport capacity of the plunge pools (i.e. no coverage of bedrock, $q_s << q_t$). With these assumptions, the three bracketed ratios on the RHS of equation (6) are all unity, and equation (6) reduces to a maximum propagation rate

$$P_{\max} = \rho_s g q_s / \kappa \qquad (9)$$

The maximum headwall-propagation rate predicted by equation (9) can now be compared with the average propagation rate found for Waipi‘o and Honokāne Valleys (i.e. valleys 2 and 3) of ~ 55 mm/yr to see if the model yields a reasonable prediction.

Unfortunately, there is much uncertainty in determining both the average sediment flux passing over the waterfall q_s and the erosion parameter κ. If the valley dimensions upstream of the headwalls were known, than the average sediment flux over a waterfall could be estimated by neglecting dissolution and erosion of interfluves and assuming that all valley erosion upstream of an amphitheater head produced sediment that was transported over the waterfall, i.e.

$$q_s w = A_v L_v / \Delta t \qquad (10)$$

where A_v is the average cross-sectional area of a valley upstream of a headwall, L_v is the cumulative valley length upstream of the headwall (averaged in time), Δt is the change in time over which valley incision occurred, and w is the width of the channel at the waterfall. It is not possible to quantify the valley dimensions upstream of the Kohala amphitheater headwalls because the valleys have been erased as the headwalls have propagated upstream, effectively reducing L_v in time. For valleys 2 and 3, we estimate L_v now to be approximately 4 km and at the time of the Pololū Slump to have been on the order of 20 km from Figure 6, assuming no contribution from tributaries. These end-member values are used to calculate an average or effective L_v of ~ 8 km (i.e. (20 km – 4 km)/2). To make an order-of-magnitude estimate of sediment flux, we assume a valley cross-sectional area (averaged in space and time) to be triangular with a width of ~300 m and a depth of ~100 m, yielding A_v = 15000 m^2. These dimensions seem reasonable based on a rough survey of some of the larger hanging valleys. We set Δt to be the approximate age of the Pololū Slump (i.e. Δt = 250 ka), estimate the stream channel width w = 5 m, and calculate q_s = 96 m^2/yr from equation (10). While these estimates are rough, they are unlikely to be off by more than a factor of two or three. There is significantly more uncertainty in the estimate of κ.

Sklar and Dietrich (2004) define $\kappa = k\sigma_T^2 / 2Y$, where σ_T is the rock tensile strength, Y is Young's Modulus of elasticity (~ 10^5 MPa (Selby, 1993)), and k is an

empirical non-dimensional constant ($k \approx 10^6$ based on laboratory experiments of Sklar and Dietrich (2001), which, to our knowledge, has not yet been tested at field scale). σ_T varies from about 1 – 20 MPa for most rock types (Selby, 1993). At the laboratory scale, intact basalt might have a tensile strength around 10 MPa, although weathering and fracturing in the field could lower this estimate by an order of magnitude or more.

Given this uncertainty, we solve equations (9) and (10) for the values specified above, and $\rho_s = 2800$ kg/m^3, for a range in rock tensile strengths. The result of this calculation yields $P_{\max}$ = 5.3 - 530 mm/yr for σ_T = 1 – 10 MPa. These values bracket the inferred average propagation rate of ~ 55 mm/yr for valleys 2 and 3. While there is much uncertainty in this calculation, it is encouraging that the model yields feasible headwall propagation rates that compare well with observed rates, despite the fact that mass wasting, plucking, and erosion from churning of sediment within a plunge have been neglected.

3.8. Thresholds for Headwall Propagation

We hypothesized in the Conceptual Model section that some valleys have remained hanging at the Kohala sea cliffs because they have had insufficient water or sediment discharge to cause headwall propagation. Here we elaborate on possible mechanisms that might explain the possible drainage area threshold for headwall propagation of 5-8 km^2. First is the formation of plunge pools. If m = 0, then headwall propagation will not occur. It is difficult to assess this possibility given our ignorance of the step-formation process. Nonetheless, it seems reasonable that the hanging valleys

might experience insufficient discharge of water or sediment to initiate and renew plunge pools. A second possible threshold is through the sediment capacity term q_t. If the waterfall is unable to transport the supplied sediment out of the plunge pools and away from the valley head, then deposition will occur and erosion will cease (i.e. $q_s > q_t$ in equation (6)). Thus, it is possible that the hanging valleys have not had sufficient discharge to evacuate the sediment delivered by mass failures or from upstream.

The third possible threshold is through the sediment flux term q_s. The sediment flux at a waterfall during a particular flow event depends not only on the production rate of sediment (as discussed above), but also on the ability of the flow upslope of the waterfall to mobilize that sediment. Sediment mobility is typically expressed through a non-dimensional Shields number (e.g. Buffington and Montgomery, 1997). For coarse grains of similar density, the median particle size that can be transported depends linearly on the flow depth and the bed slope. Given the similar slopes of the Kohala valleys upslope of the knickpoints, it is possible that the hanging valleys have remained hanging because they have had insufficient discharge or flow depth to mobilize the coarse sediment found on their beds, effectively setting $q_s = 0$ in equation (6). Unfortunately, we do not yet have exposure ages or sediment transport data to test whether sediment is immobile in the Kohala hanging valleys. The possibility of relatively immobile sediment in the hanging valleys, however, seems reasonable. For example, Seidl et al. (1994; 1997) showed that large boulders that line streams on Kaua‘i (of similar slope and lithology as the Kohala valleys) have been immobile for as long as 180 ka based on cosmogenic exposure dating.

If sediment is presently immobile in the hanging valleys, this must not have always been the case. The hanging valleys are topographic depressions and were at one time carved by flows capable of transporting sediment. How did such flows carve the valleys without causing headward retreat at the knickpoint? It is possible that fluvial erosion in the hanging valleys only occurs as boulders and bedrock in the channels weather to small transportable pieces that do not cause appreciable plunge pool erosion because of small impact velocities due to drag (*cf.* equation (7)) or viscous damping (e.g. Schmeeckle et al., 2001). Another possibility is that the hanging valleys were carved before knickpoints were imposed on the streams by the Pololū Slump. Before the slump occurred, the hanging valleys would have had greater discharges because of higher precipitation rates (because the volcano was an additional 1000 m above sea level) and larger drainage areas (because there might not have been fault-induced drainage divides near the Kohala summit).

Lastly, it is possible that knickpoint propagation has occurred for the hanging valleys, but that it has not kept pace with coastal cliff retreat from wave erosion. Wave erosion is an active process as evidenced by sea stacks and 20 – 50 m sea cliffs along the entire northeast shoreline of Hawai‘i. Dividing the sea cliff relief (20 – 50 m) by the regional volcano slope (~ 0.1) indicates at least 200 - 500 m of horizontal sea cliff retreat. This retreat distance is a minimum because some portion of the sea cliffs might now be submerged due to island subsidence. Valleys will therefore remain hanging at the coast if headwall retreat rates are less than ~ 500 m / 250 ka, or ~ 2 mm/yr. A similar mechanism was proposed for the difference between hanging and amphitheater-headed valleys on the coast of New Zealand (Pillans, 1985).

3.9. Other Hawaiian Valleys

Large submarine landslides are found offshore of Kauaʻi, Oʻahu, Molokaʻi, Maui, and Hawaiʻi, and when they occur on the windward wet sides of the islands, are often associated spatially with amphitheater-headed valleys (Moore et al., 1989; Moore and Clague, 1992). Clague and Moore (2002) suggested that this might be a coincidence as both landslides and deep valleys likely require high precipitation rates. Landslides might be triggered by groundwater-induced pressurization caused by magma intrusion or phreatomagmatic eruptions (Clague and Moore, 2002) and amphitheater-headed valleys are generally found in areas where annual precipitation exceeds 2.5 m (Scott and Street, 1976). Moore et al. (1989), however, suggested that the amphitheater-headed valleys might be genetically linked to the landslides, as the landslides could have caused "oversteepening" or removed vegetation. Like our interpretation for Kohala, Seidl et al. (1994) argued that valleys on the Na Pali coast of Kauaʻi were carved by upstream-migrating landslide-induced knickpoints.

Amphitheater-headed valleys on the north coast of Molokaʻi, most notably Pelekunu and Wailau Valleys (Stearns, 1985), were interpreted by Kochel and Piper (1986) to have resulted from seepage erosion. Like Kohala, these valleys have incised through large sea cliffs that have ~ 1000 m of relief in the region of the valleys and taper to less than ~ 100 m to the east and west (Clague and Moore, 2002). Directly off the north shore of Molokaʻi is the huge Wailau Landslide (Moore et al., 1989). Similar to Kohala, the origin of the sea cliffs were originally attributed to wave backcutting (Wentworth, 1927; Macdonald et al., 1983), but were later interpreted to be the headwall of the Wailau Landslide when bathymetric surveys revealed the slide (Moore

et al., 1989; Satake and Smith, 2000). More recently, Clague and Moore (2002) have suggested, based on comparison with a similar feature on Kilauea Volcano, that the sea cliffs are a result of normal or listric faulting independent of the landslide.

On Molokaʻi and the other Hawaiian Islands, the spatial correlation between landslides, sea cliffs and amphitheater-headed valleys are generally not as clear as on Kohala, making interpretations more difficult. This might be because the other islands are older and have experienced a more complicated relative sea-level history (e.g. Dickenson, 2001). Erosion of some amphitheater-headed valleys has progressed to the point that they have coalesced, making it difficult to distinguish where valleys once were (e.g. on Kauaʻi (Stearns, 1985)). It does seem plausible, however, that large sea cliffs were formed by giant mass failures at least on Molokaʻi and Kohala. Even if the sea cliffs on these islands were created by faulting unrelated to mass failures, the spatial correlation between amphitheater-headed valleys and large sea cliffs on the windward, wet sides of many of the Hawaiian Islands suggests a causal relationship consistent with the knickpoint-retreat model presented herein.

3.10. Conclusions

The Kohala amphitheater-headed valleys have steep, stubby headwalls that are dominated by waterfall plunge pools. These headwalls appear to be at odds with classic models of waterfall retreat because plunge pools do not coincide with significant changes in bedrock strength and headwalls are not significantly undercut. Instead, the falling water and sediment appears to be vertically drilling into the headwall in a series of steps that interrupt the cascading falls. Springs do exist in the Kohala valleys, as one

would expect in any deeply incised canyon that intersects water tables. We, however, have not observed weathered rock or overhangs associated with springs. Peak annual surface flows exceed spring discharges by nearly two orders of magnitude and are likely necessary to excavate collapsed talus. The amphitheater-headed valleys have approximately uniform valley-wall slopes and are V-shaped in cross-section in their upstream portions, but flat floored near the valley mouths. The valleys occur directly upslope of anomalously high sea cliffs, which in turn are upslope from the Pololū Sump. Faults located near the volcano summit cause lateral (cross-slope) surface flow of high elevation (orographically enhanced) precipitation to the amphitheater-headed valleys at the expense of smaller valleys that remain hanging at the sea cliffs.

To explain these observations, we propose that the Kohala amphitheater-headed valleys formed by upstream propagation of huge knickpoints induced by the Pololū Slump. Approximately 250 ka, the Pololū Slump created an immense headscarp that is recorded presently as the > 400 m sea cliffs that laterally bound the slump. As dominant streams cascaded over the cliffs they developed waterfalls which, through plunge pool erosion and mass wasting, induced upstream propagation of knickpoints at rates up to 60 mm/yr, eventually forming deep amphitheater-headed valleys. Upstream propagation of valley headwalls resulted in cross-cutting of drainage networks and stream piracy. Smaller streams did not develop into amphitheater-headed valleys because they had smaller discharges due to orographic precipitation, a radial drainage pattern, and fault-induced drainage divides near the summit of the volcano. Topographic analysis suggests a potential drainage area threshold of ~ 5-8 km^2 between the arguably active amphitheater-headed valleys and the inactive amphitheater-headed,

intermediate, and hanging valleys. Subsidence drowned the lower portions of the amphitheater-headed valleys resulting in alluviation, flat floors and U-shaped cross sections.

We propose a simple expression to describe headwall retreat by vertical plunge-pool erosion due to impacting sediment. This model suggests that headwall propagation and plunge-pool erosion scale with drainage area through the sediment flux term, which is partially supported by our field observations and drainage area analysis. The rate of headwall propagation is predicted to be dependent on the kinetic versus potential energy of sediment impacts, which is a function of sediment size, plunge-pool depth, and waterfall height. Surprisingly, for large particles and small plunge pool depths, drag can be neglected and headwall propagation is not a function of sediment size, waterfall height or total headwall height. Headwall propagation is only weakly dependent on the number of plunge pools and is independent of the surface area of the plunge pools. The derived expression is consistent with the notion of a threshold for headwall propagation through either the development of plunge pools, the sediment-transport competency of the streams feeding the plunge pools, or the sediment-transport capacity of plunge pools themselves. The model does not include other potential thresholds such as a waterfall's inability to pluck fractured rock from plunge pools or keep pace with coastal cliff retreat. While the model is an oversimplification, it is encouraging that it yields feasible headwall propagation rates that compare favorably with those inferred.

The interpretation that the Kohala valleys formed by waterfall processes is significant as it implies that amphitheater-form is not a diagnostic indicator of seepage erosion. The process of knickpoint formation and retreat following large-scale

landsliding described for Kohala might also explain the origin of amphitheater-headed valleys on other Hawaiian Islands. Moreover, amphitheater-headed valleys (e.g. on oceanic islands of Vanuatu, Tahiti and La Réunion (Karátson, et al., 1999)) and stepped waterfalls (e.g., Skógar River, Iceland; Cascade River, Minnesota, USA) are a relatively common occurrence on Earth, especially in basaltic landscapes. Knickpoint retreat is thought to be one of the main mechanisms for valley incision (e.g. Whipple, 2004) and the process of vertical drilling proposed herein might be found relevant for landscape evolution outside of the Hawaiian Islands. Mars in particular has abundant amphitheater-headed valleys, which should be reevaluated with attention to waterfall processes in addition to seepage erosion.

3.11. Appendix 1 – Particle Fall Velocity

The acceleration of a falling particle can be calculated from the difference between the gravitational acceleration of the particle and deceleration due to drag

$$\frac{dw}{dt} = C_1 - C_2 w^2 \qquad \text{(A1)}$$

where w is velocity in the vertical dimension, g is the acceleration due to gravity and C_1 and C_2 are given by

$$C_1 = \frac{(\rho_s - \rho_f)}{\rho_s} g \qquad \text{(A2)}$$

$$C_2 = \frac{1}{2} C_d \frac{\rho_f}{\rho_s} \frac{A}{V} \qquad \text{(A3)}$$

where C_d is a drag coefficient, ρ_f is the density of the fluid that the particle is falling through, ρ_s is the particle density, A is the cross sectional area of the particle perpendicular to fall velocity, and V is the volume of the particle. We are interested in the acceleration over a certain fall distance rather than over a certain fall time. Equation (A1) can be written in terms of vertical distance z (positive downward) by substituting $dt = dz / w$, which yields

$$w\frac{dw}{dz} + C_2 w^2 = C_1 \tag{A4}$$

In order to solve equation (A4) analytically, we assume that C_2, and therefore C_d, is a not a function of *z*. In reality C_d should vary as particles accelerate and the particle Reynolds number increases. Using a simple numerical integration, we found that accounting for a variable drag coefficient typically had less than a 10%-effect on settling velocity. We, therefore, assume that C_d is a constant for a given particle size and solve the non-linear ordinary differential equation given by equation (A4) analytically as

$$w = \sqrt{\frac{C_1}{C_2} + C_3 \exp\left(-2C_2 z\right)}. \tag{A5}$$

C_3 is a constant of integration that must be specified using a boundary condition. Neglecting the influence of the surrounding falling water, a particle falling down a waterfall will first fall through air for a distance *h* and then through water within the pool for a distance η before impacting the bedrock. We first specify equation (A5) for the case of a particle falling through air. We then use this solution as the boundary condition for a particle falling through water. For the particle falling through air, we define $C_1 = C_{1a}$ and $C_2 = C_{2a}$ for the case when $\rho_f = \rho_a$ in equations (A2) and (A3), where ρ_a is the density of air. Solving equation (A5) for C_3 and assuming that the vertical velocity of the particle at the top of the waterfall (*z* = 0) is zero, yields

$C_3 = -C_{1a} / C_{2a}$. Thus, the velocity of a particle when it impacts the water in a plunge pool ($z = h$), denoted by w_a, can be written following equation (A5) as

$$w_a = \sqrt{\frac{C_{1a}}{C_{2a}}\left(1 - \exp\left(-2C_{2a}h\right)\right)} \tag{A6}$$

Now, we solve equation (A5) for the particle-bedrock impact velocity at the bottom of the plunge pool. For the case of a particle falling through water, we define $C_1 = C_{1w}$ and $C_2 = C_{2w}$ for the case when $\rho_f = \rho_w$ in equations (A2) and (A3), where ρ_w is the density of water. At the top of the pool of water ($z = 0$), the velocity of the particle is w_a given by equation (A6). This assumes that no energy is dissipated at the air-water interface. Given this boundary condition, C_3 is found from equation (A5) to be

$$C_3 = w_a^2 - \frac{C_{1w}}{C_{2w}} \tag{A7}$$

Combining equations (A5) and (A7) yields the impact velocity of a particle w_f after passing through a plunge pool of depth η

$$w_f = \sqrt{\frac{C_{1w}}{C_{2w}} + \left(w_a^2 - \frac{C_{1w}}{C_{2w}}\right)\exp\left(-2C_{2w}\eta\right)}\,. \tag{A8}$$

The final expression for impact velocity of a particle after falling over a waterfall of height h and through a plunge pool of depth η is found by combining equations (A6) and (A8),

$$w_f = \sqrt{\frac{C_{1w}}{C_{2w}} + \left(\frac{C_{1a}}{C_{2a}} \left(1 - \exp\left(-2C_{2a}h\right)\right) - \frac{C_{1w}}{C_{2w}} \right) \exp\left(-2C_{2w}\eta\right)} \qquad \text{(A9)}$$

3.12. Appendix 2 - Notation

A Cross-sectional area of a sediment particle (L^2)

A_v Average cross-sectional area of a valley upstream of a headwall (L^2)

C_d Drag coefficient (dimensionless)

d Surface area of a plunge pool per unit width (L)

D Sediment diameter (L)

E Vertical erosion rate (LT^{-1})

g Acceleration of gravity (LT^{-2})

h Average waterfall height for m+1 waterfalls in series at a headwall (L)

k Empirical rock erodibility coefficient (dimensionless)

L_v Average length of a valley upstream of a headwall (L)

m number of plunge pools in series at a headwall (not including bottom of headwall)

P Headwall propagation rate (LT^{-1})

P_{max} Estimate of maximum headwall propagation rate (LT^{-1})

q_s Volumetric sediment flux or supply per unit width (L^2T^{-1})

q_t Volumetric sediment-transport capacity per unit width (L^2T^{-1})

t Time (T)

V Volume of a sediment particle (L^3)

w Vertical velocity of a falling particle (LT^{-1})

w_f Impact velocity of a particle at the bedrock interface (LT^{-1})

Y Young's modulus of elasticity ($ML^{-1}T^{-2}$)

z Vertical coordinate (L)

η Plunge pool depth (L)

κ Rock erodibility parameter ($ML^{-1}T^{-2}$)

ρ_s Density of sediment (ML^{-3})

ρ_f Density of fluid (ML^{-3})

ρ_w Density of water (ML^{-3})

ρ_a Density of air (ML^{-3})

σ_T Rock tensile strength ($ML^{-1}T^{-2}$)

3.13. References

Bishop, P., Hoey, T. B., Jansen, J. D., and Artza, I. L., 2005, Knickpoint recession rate and catchment area: the case of uplifted rivers in Eastern Scotland: Earth Surface Processes and Landforms, v. 30, no. 6, p. 767-778.

Bollaert, E., and Schleiss, A., 2003, Scour of rock due to the impact of plunging high velocity jets Part II: Experimental results of dynamic pressures at pool bottoms and in one- and two-dimensional closed end rock joints: Journal of Hydraulic Research, v. 41, no. 5, p. 465-480.

Buffington, J. M., and Montgomery, D. R., 1997, A systematic study of eight decades of incipient motion studies, with special reference to gravel-bedded rivers: Water Resources Research, v. 33, no. 8, p. 1993-2029.

Carr, M. H., and Clow, G. D., 1981, Martian channels and valleys - their characteristics, distribution, and age: Icarus, v. 48, no. 1, p. 91-117.

Clague, D. A., and Moore, J. G., 2002, The proximal part of the giant submarine Wailau landslide, Molokai, Hawai‘i: Journal of Volcanology and Geothermal Research, v. 113, no. 1-2, p. 259-287.

Clague, D. A., Reynolds, J. R., Maher, N., Hatcher, G., Danforth, W., and Gardner, J. V., 1998, High-resolution Simrad EM300 multibeam surveys near the Hawaiian islands: Canyons, reefs, and landslides: EOS, Transactions of the American Geophysical Union, v. 79, p. F826.

Cotton, C. A., 1943, Oahu valley sculpture: a composite review: Geology Magazine, v. 80, p. 237-243.

Craddock, R. A., and Howard, A. D., 2002, The case for rainfall on a warm, wet early Mars: Journal of Geophysical Research-Planets, v. 107, no. E11.

Crosby, B. T., and Whipple, K. X., in press, Knickpoint initiation and distribution within fluvial networks in the Waipaoa River, North Island, New Zealand: Geomorphology.

Dalrymple, G. B., 1971, Potassium-Agron ages from Pololū volcanic series, Kohala Volcano, Hawai‘i: Geological Society of America Bulletin, v. 82, no. 7, p. 1997-2000.

Davis, W. M., 1928, The Coral Reef Problem, American Geographical Society Special Publication 9, 596 p.

Dickenson, W. R., 2001, Paleoshoreline record of relative Holocene sea levels on Pacific islands: Earth Science Reviews, v. 55, p. 191-234.

Dietrich, W. E., 1982, Settling velocity of natural particles: Water Resources Research, v. 18, no. 6, p. 1615-1626.

Dietrich, W. E., and Dunne, T., 1993, The channel head, *in* Beven, K., and Kirkby, M. J., eds., Channel Network Hydrology, John Wiley & Sons, p. 175-219.

Dunne, T., 1990, Hydrology, mechanics, and geomorphic implications of erosion by subsurface flow, *in* Higgins, C. G., and Coates, D. R., eds., Groundwater geomorphology; The role of subsurfacce water in Earth-surface processes and landforms: Boulder, Geological Society of America Special Paper.

Gilbert, G. K., 1907, The rate of recession of Niagara Falls: U.S. Geological Survey Bulletin, v. 306, p. 1-31.

Grant, J. A., 2000, Valley formation in Margaritifer Sinus, Mars, by precipitation-recharged ground-water sapping: Geology, v. 28, no. 3, p. 223-226.

Gulick, V. C., 2001, Origin of the valley networks on Mars: a hydrological perspective: Geomorphology, v. 37, no. 3-4, p. 241-268.

Hayakawa, Y., and Matsukura, Y., 2003, Recession rates of waterfalls in Boso Peninsula, Japan, and a predictive equation: Earth Surface Processes and Landforms, v. 28, no. 6, p. 675-684.

Higgins, C. G., 1984, Piping and sapping; development of landforms by groundwater flow, *in* LaFleur, R. G., ed., Groundwater as a geomorphic agent: Boston, Allen and Unwin, p. 18-58.

Hinds, N. E. A., 1925, Amphitheater valley heads: Journal of Geology, v. 33, no. 816-818.

Hoke, G. D., Isacks, B. L., Jordan, T. E., and Yu, J. S., 2004, Groundwater-sapping origin for the giant quebradas of northern Chile: Geology, v. 32, no. 7, p. 605-608.

Holland, W. N., and Pickup, G., 1976, Flume study of knickpoint development in stratified sediment: Geological Society of America Bulletin, v. 87, no. 1, p. 76-82.

Hovius, N., Stark, C. P., Tutton, M. A., and Abbott, L. D., 1998, Landslide-driven drainage network evolution in a pre-steady-state mountain belt: Finisterre Mountains, Papua New Guinea: Geology, v. 26, no. 12, p. 1071-1074.

Howard, A. D., 1995, Simulation modeling and statistical classification of escarpment planforms: Geomorphology, v. 12, p. 187-214.

Howard, A. D., Dietrich, W. E., and Seidl, M. A., 1994, Modeling fluvial erosion on regional and continental scales: Journal of Geophysical Research-Solid Earth, v. 99, p. 13971-13986.

Howard, A. D., Kochel, R. C., and Holt, H., 1988, Sapping Features of the Colorado Plateau: A Comparitive Planetary Geology Field Guide, NASA Special Publication, 71-83 p.

Howard, A. D., and McLane, C. F., 1988, Erosion of cohesionless sediment by groundwater seepage: Water Resources Research, v. 24, no. 10, p. 1659-1674.

Jones, A. T., 1995, Geochronology of Drowned Hawaiian Coral-Reefs: Sedimentary Geology, v. 99, no. 3-4, p. 233-242.

Karátson, D., Thouret, J.C., Moriya, I., and Lomoschitz, A., 1999, Erosion calderas: origins, processes, structural and climatic control: Bull. Volcanol., v. 61, [. 174-193.

Kochel, R. C., and Baker, V. R., 1990, Groundwater sapping and the geomorphic development of large Hawaiian valleys., *in* Higgins, C. G., and Coates, D. R., eds., Groundwater Geomorphology, The Role of Subsurface Water in Earth-Surface Processes and Landforms: Boulder, Colorado, Geological Society of America Special Paper 252, p. 245-257.

Kochel, R. C., and Piper, J. F., 1986, Morphology of large valleys on Hawai‘i - Evidence for groundwater sapping and comparisons with Martian valleys: Journal of Geophysical Research-Solid Earth and Planets, v. 91, no. B13, p. E175-E192.

Laity, J. E., and Malin, M. C., 1985, Sapping processes and the development of theater-headed valley networks on the Colorado Plateau: Geological Society of America Bulletin, v. 96, p. 203-217.

Lamb, M. P., Howard, A. D., Johnson, J., Whipple, K. X., Dietrich, W. E., and Perron, J. T., 2006, Can springs cut canyons into rock?: Journal of Geophysical Research. V. 111, no. E07002, doi:10.101029/2005JE002663.

Ludwig, K., Szabo, B., Moore, J., and Simmons, K., 1991, Crustal subsidence rates off Hawai‘i determined from 234U/238U ages of drowned coral reefs: Geology, v. 19, p. 171-174.

Macdonald, G. A., Abbott, A. T., and Peterson, F. L., 1983, Volcanoes in the Sea, the Geology of Hawai‘i: Honolulu, University of Hawai‘i Press, 517 p.

Malin, M. C., and Carr, M. H., 1999, Groundwater formation of Martian valleys: Nature, v. 397, no. 6720, p. 589-591.

McDougal, I., and Swanson, D. A., 1972, Potassium-Argon ages of lavas from Hawi and Pololū volcanic series, Kohala Volcano, Hawai‘i: Geological Society of America Bulletin, v. 83, no. 12, p. 3731-3737.

McMurtry, G. M., Fryer, G. J., Tappin, D. R., Wilkinson, I. P., Williams, M., Fietzke, J., Garbe-Schoenberg, D., and Watts, P., 2004, Megatsunami deposits on Kohala Volcano, Hawai‘i, from flank, collapse of Mauna Loa: Geology, v. 32, no. 9, p. 741-744.

Moore, J. G., and Clague, D. A., 1992, Volcano growth and evolution of the island of Hawai‘i: Geological Society of America Bulletin, v. 104, no. 11, p. 1471-1484.

Moore, J. G., Clague, D. A., Holcomb, R. T., Lipman, P. W., Normark, W. R., and Torresan, M. E., 1989, Prodigious submarine landslides on the Hawaiian ridge: Journal of Geophysical Research-Solid Earth and Planets, v. 94, no. B12, p. 17465-17484.

Moore, J. G., and Fornari, D. J., 1984, Drowned reefs as indicators of the rate of subsidence of the island of Hawai‘i: Journal of Geology, v. 92, p. 752-759.

Moore, J. G., Normark, W. R., and Holcomb, R. T., 1994, Giant Hawaiian landslides: Annual Review or Earth and Planetary Science, v. 22, p. 119-144.

Nash, D. J., 1996, Groundwater sapping and valley development in the Hackness hills, north Yorkshire, England: Earth Surface Processes and Landforms, v. 21, no. 9, p. 781-795.

Philbric, S. S., 1974, What future for Niagara falls?: Geological Society of America Bulletin, v. 85, no. 1, p. 91-98.

Pieri, D., 1976, Distribution of small channels on Martian surface: Icarus, v. 27, no. 1, p. 25-50.

Pillans, B., 1985, Drainage initiation by subsurface flow in South Taranaki, New Zealand: Geology, v. 13, p. 262-265.

Rosenblum, N. A., and Anderson, R. S., 1994, Hillslope and channel evolution in a marine terraced landscape, Santa Cruz, California: Journal of Geophysical Research, v. 99, no. 7, p. 14013-14029.

Satake, K. and Smith, J.R., 2000, Tsunami modeling from Hawaiian submarine landslides. EOS, Trans. Am. Geophys. Union, 81, WP251.

Schmeeckle, M. W., Nelson, J. M., Pitlick, J., and Bennett, J. P., 2001, Interparticle collision of natural sediment grains in water: Water Resources Research, v. 37, no. 9, p. 2377-2391.

Schumm, S. A., Boyd, K. F., Wolff, C. G., and Spitz, W. J., 1995, A ground-water sapping landscape in the Florida Panhandle: Geomorphology, v. 12, no. 4, p. 281-297.

Scott, G. A. J., and Street, J. M., 1976, The role of chemical weathering in the formation of Hawaiian amphitheater-headed valleys: Zeit. Geomorph., v. 20, p. 171-189.

Selby, 1993, Hillslope Materials and Processes, Oxford University Press, 451 p.

Seidl, M. A., Dietrich, W. E., and Kirchner, J. W., 1994, Longitudinal profile development into bedrock: an analysis of Hawaiian channels: Journal of Geology, v. 102, p. 457–474.

Seidl, M. A., Finkel, R. C., Caffee, M. W., Hudson, G. B., and Dietrich, W. E., 1997, Cosmogenic isotope analysis applied to river longitudinal profile evolution: problems and interpretations: Earth Surface Processes and Landforms, v. 22, p. 195-209.

Seidl, M. A., Weissel, J. K., and Pratson, L. F., 1996, The kinematics and pattern of escarpment retreat across the rifted continental margin of SE Australia: Basin Research, v. 8, no. 3, p. 301-316.

Sklar, L. S., and Dietrich, W. E., 2001, Sediment and rock strength controls on river incision into bedrock: Geology, v. 29, no. 12, p. 1087-1090.

Sklar, L. S., and Dietrich, W. E., 2004, A mechanistic model for river incision into bedrock by saltating bed load: Water Resources Research, v. 40, no. 6, p. Art. No. W06301.

Sklar, L. S., and Dietrich, W. E., in press, The role of sediment in controlling steady-state bedrock channel slope: implications of the saltation-abrasion incision model: Geomorphology.

Smith, J. R., Satake, K., Morgan, J. K., and Lipman, P. W., 2002, Submarine landslides and volcanic features on Kohala and Mauna Kea Volcanoes and the Hana Ridge, Hawai‘i, Hawaiian Volcanoes: Deep Underwater Perspectives, Geophysical Monograph 128, American Geophysical Union, p. 11-28.

Squyres, S. W., 1989, Urey Prize Lecture - Water on Mars: Icarus, v. 79, no. 2, p. 229-288.

Stearns, H. T., 1985, Geology of the State of Hawai‘i: Palo Alto, California, Pacific Books, 266 p.

Stearns, H. T., and Macdonald, G. A., 1946, Geology and ground-water resources of the island of Hawai‘i, Hawai‘i Division of Hydrography Bulletin: Honolulu, Advertiser Publishing Co., 430 p.

Stearns, H. T., and Vaksvik, K. N., 1935, Geology and ground-water resources of the island of Oahu, Hawai‘i, Hawai‘i Division of Hydrography Bulletin: Wailuku, Maui Publishing Company, 536 p.

Szabo, B., and Moore, J. G., 1986, Age of -360 m reef terrace, Hawai‘i, and the rate of late Pleistocene subsidence of the island: Geology, v. 14, p. 967-968.

Uchupi, E., and Oldale, R. N., 1994, Spring sapping origin of the enigmatic relict valleys of Cape-Cod and Marthas-Vineyard and Nantucket Islands, Massachusetts: Geomorphology, v. 9, no. 2, p. 83-95.

Weissel, J. K., and Seidl, M. A., 1997, Influence of rock strength properties on escarpment retreat across passive continental margins: Geology, v. 25, no. 7, p. 631-634.

Wentworth, C. K., 1928, Principles of stream erosion in Hawai‘i: Journal of Geology, v. 36, p. 385-410.

Wentworth, C. K., 1943, Soil avalanches on Oahu, Hawai‘i: Geological Society of America Bulletin, v. 54, p. 53-64.

Whipple, K. X., 2004, Bedrock rivers and the geomorphology of active orogens: Annu. Rev. Earth Planet. Sci., v. 32, p. 151-185.

Whipple, K. X., Hancock, G. S., and Anderson, R. S., 2000, River incision into bedrock: Mechanics and relative efficacy of plucking, abrasion, and cavitation: Geological Society of America Bulletin, v. 112, no. 3, p. 490-503.

Whipple, K. X., and Tucker, G. E., 1999, Dynamics of the stream-power river incision model: Implications for height limits of mountain ranges, landscape response timescales, and research needs: Journal of Geophysical Research-Solid Earth, v. 104, no. B8, p. 17661-17674.

White, S. F., 1949, Process of erosion on steep slopes of Oahu, Hawai‘i: American Journal of Science, v. 247, p. 168-186.

Wolfe, E. W., and Morris, J., 1996, Geologic map of the island of Hawai‘i: U. S. Geological Survey Geologic Investigations Series, Map I-2534-A.

Yoshida, M., and Ikeda, H., 1999, The origin of the Ryumon Falls in Karasuyama Town, Tochigi Prefecture: Bulletin of the Environmental Research Center, the University of Tsukuba, v. 24, p. 73-79.

Young, R., 1985, Waterfalls: form and process: Zeit. Geomorph., v. NF Suppl Bd 55, p. 81-95.

Chapter 4

Formation of Box Canyon, Idaho, by Megaflood: Implications for Seepage Erosion on Earth and Mars

4.1. Introduction

A central thrust in geomorphology and planetary science is to link diagnostic landscape morphologies to formation processes. A prominent example is the formation of amphitheater-headed canyons, in which the stubby appearance of valley heads, steep headwalls, and little landscape dissection upstream have long been interpreted to result from seepage erosion (i.e., groundwater sapping) on Earth (*1-4*), Mars (*5*, *6*) and now Titan (*7*). Theory (*8*), experiments (*9*), and field studies (*10*) have validated this hypothesis in unconsolidated sand, showing that valley heads are undermined and propagate upstream from seepage-induced erosion. This means that valleys can grow without precipitation-fed overland flow, which has profound implications for landscape evolution on Earth, and the hydrologic cycle and habitability of Mars.

Despite widespread acceptance of the seepage-erosion hypothesis, and its validation in sand, we lack an unambiguous example of amphitheater-headed canyon

formation by seepage erosion in bedrock, owing to overlapping features generated by rainfall runoff for most sites on Earth (*11*). Even the amphitheater-headed valleys of the Colorado Plateau and Hawai‘i, which are most often cited as classic examples of groundwater sapping in bedrock (*2, 3*), have been questioned due to evidence for flashfloods and plunge-pool erosion (*11-13*). To better evaluate the seepage-erosion hypothesis, we set out to study the erosion and transport processes within a bedrock canyon, Box Canyon, Idaho U.S.A, that exhibits all of the morphologic and hydrologic traits attributed to seepage erosion (i.e., steep amphitheater-shaped headwall, lack of landscape dissection and runoff contribution upstream, and contains the 11th largest spring in the U.S.), without the overlapping indicators of rainfall runoff that have made other sites controversial (Fig. 1A). Moreover, Box Canyon exhibits remarkable similarity in morphology and potentially lithology (i.e., basalt) with many Martian canyons (Fig. 1B) that have been attributed to seepage-erosion (*5, 6*).

4.2. Box Canyon

Box Canyon is located within the Snake River Plain, a broad and relatively flat basin in southern Idaho filled by volcanic flows that erupted ca. 15 Ma to 2 ka and sediments (*14*). Several tributaries of the Snake River Canyon appear as stubby valleys that end abruptly in amphitheater heads, including Malade Gorge, Blind Canyon and Box Canyon (Fig. 2), all of which have been attributed to seepage erosion (*1, 4*). Box Canyon is cut into the Sand Springs Basalt (also named the Basalt of Rocky Butte (*15*)) with an Ar-Ar eruption age of 95 $\pm$ 10 ka (*16*) and U-Th/He eruption ages that range from 86 $\pm$

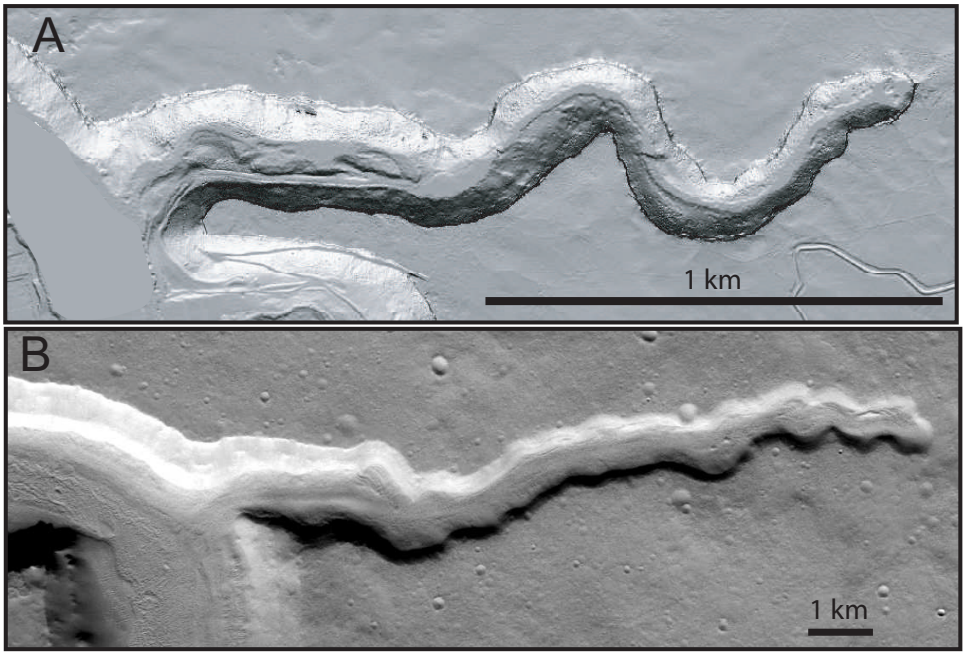

Figure 1. A) Shaded relief map of Box Canyon, Idaho. Airborne Laser Detection and Ranging (LiDAR) data was collected by the National Center for Airborne Laser Mapping. The data have been filtered to remove vegetation that exists along the creek banks. UTM zone 11 projection, NAD83 datum, 1-m resolution. B) THEMIS (*32*) infrared daytime image of Mamers Vallis, Mars. Image V19470014, 19 m resolution.

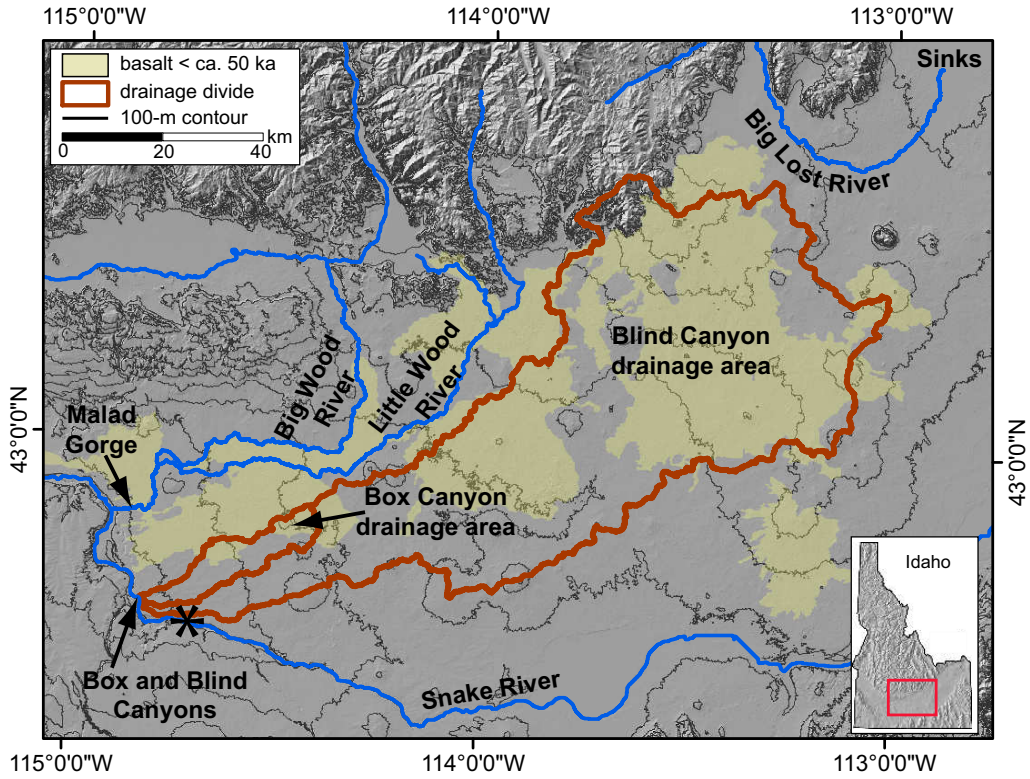

Figure 2. Topographic map of the eastern Snake River Plain, the location of which is shown on the inset map of Idaho, USA. The drainage areas feeding Box Canyon (228 km^2) and Blind Canyon (4713 km^2) are outlined following the path of steepest decent. The yellow shaded regions mark the locations of volcanism younger than ca. 50 ka (*15*). The asterisk (*) illustrates a location where a dam of the Snake River Canyon could cause overflow into the Box and Blind Canyon drainage areas, although no lava dams have been discovered there. The thin black lines are 100-m topographic contours. Topographic data is from the U.S. Geological Survey. UTM zone 11 projection, NAD83 datum, 25-m resolution.

12 ka to 130 $\pm$ 12 ka (*17*), and this flow was inferred to fill an ancestral canyon of the Snake River (*18*).

The permeable lava flows of the Snake River Plain form an extensive aquifer with recharge entering in the east (e.g., Big Lost River sinks, Fig. 2) and flowing westward. Large springs emanate from the east wall of the Snake River Canyon between Box Canyon and Malade Gorge, where the river jogs north – perpendicular to the regional topographic slope and the groundwater-flow direction. These springs constitute a cumulative discharge of ~ 170 m^3/s, and one of the largest (~ 10 m^3/s) emanates from the head of Box Canyon creating Box Canyon Creek (*19*).

Box Canyon is sinuous (Fig. 3A), and the longitudinal profile is approximately 2.68 km in length with an average channel-bed slope of 2.18% (Fig. 3B). The canyon is ~ 35-m deep and 120-m wide at its head, and about twice as deep and wide at its mouth. The columnar basalt walls of the canyon have collapsed creating steep (~ 20^o - 35^o) talus slopes that often abut Box Canyon creek. Talus accumulation lessens upstream and is absent at the canyon head (Fig. 4A). Several terrace-like platforms are elevated 2 to 7 m above the current stream level, and separate the steep talus slopes from the creek (Fig. 3). These contain large boulders (> 1 m) and some appear imbricated in the downstream direction indicating past fluvial transport.

4.3. Seepage or Megaflood?

Stearns (*4*) postulated that Box Canyon was formed by rock dissolution from seepage, and that the lack of talus at the head of the canyon is evidence of continued dissolution. We have found, however, that bedrock composing the headwall and

surrounding talus are blocky and hard, and show no visual evidence for enhanced weathering. Indeed, water samples taken from Box Canyon creek and neighboring wells indicate silica concentrations ranging from 32-35 mg/L, which bracket the saturation value (*20*), suggesting that the groundwater is in equilibrium with the basaltic aquifer and significant dissolution is not occurring at Box Canyon spring.

Despite no modern overland flow contribution to Box Canyon creek, three features at the canyon head indicate overflow of water into the canyon in the past. First, three concentric semicircles of boulders within the canyon head appear to be waterfall plunge pools with ~ 2 m of relief (Fig. 4A). Second, a small notch (~ 300 m^3) in the center of the headwall rim (Fig. 4A) has linear flute-like abrasion marks, millimeters in width and several centimeters long, that follow the local curvature of the notch indicating past overspill. The scours appear as divots on the inferred upstream end that gradually fan outward and diminish in relief downstream (Fig. 4B). Third, this scoured rock extends ~ 1 km upstream of the canyon head and delineates flow towards the canyon (Fig. 3). Unfortunately, the scoured path cannot be followed further upstream due to loess deposition, which commenced ca. 40 ka and ceased ca. 10 ka, i.e., coincident with the Pinedale glaciation (*21*).

The basalt in Box Canyon breaks down into large boulders (~ 1 m) that without dissolution must be transported downstream to allow canyon growth. Despite the great discharge of the spring, no measurable amount of sediment is currently transported. A minimum estimate of flow needed to carve the canyon can be found by calculating the discharge necessary to initiate sediment transport on the creek bed. Channel cross sections, longitudinal channel-bed profiles, and grain-size distributions (D_{84} = 0.6 m,

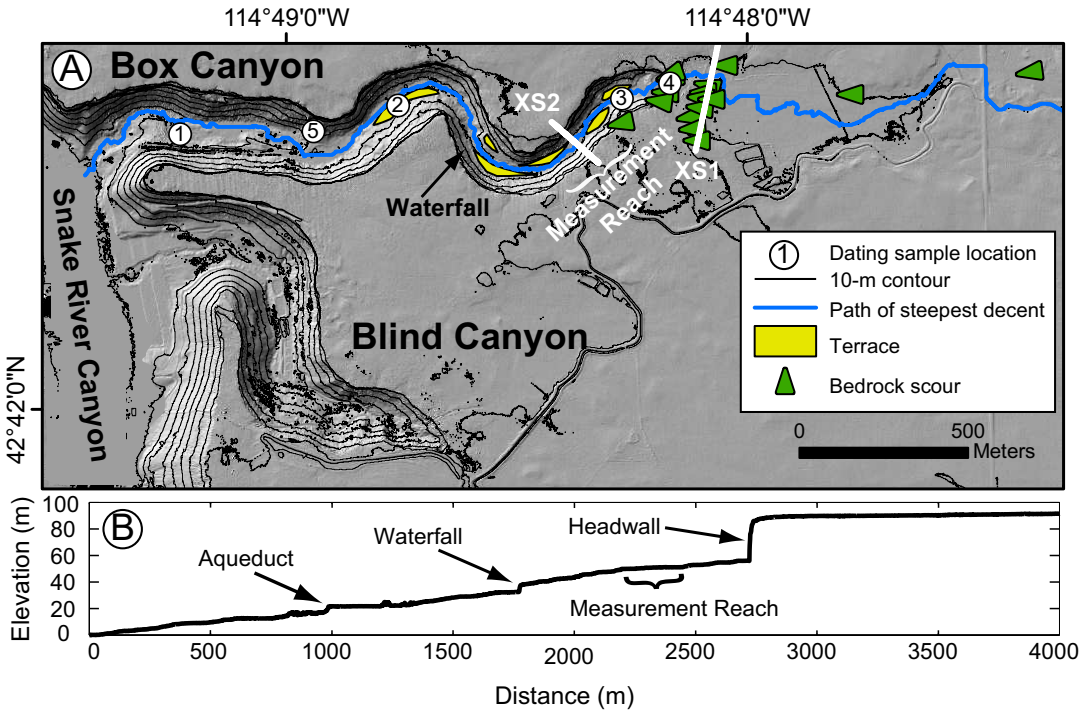

Figure 3. A) High resolution topographic map of Box and Blind Canyons. The yellow shaded regions mark potential fluvial terraces, which range from 2-7 m above current stream level. Detailed measurements of flow depth, water surface slope, bed slope, channel width, and bed particle size were made within the region marked *measurement reach* (*24*). Discharge calculations were made using cross-sectional areas measured at XS1 and XS2. Mapped scours on bedrock (e.g., Fig. 4B) are shown as green arrows. The white circles are sample locations used for dating. The thin black lines are 10-m topographic contours. The blue line is the calculated path of steepest descent, but does not indicate modern-day flow paths since no flow on record has spilled over the canyon headwall. See Fig. 1 for data source and projection. B) Longitudinal profile of Box Canyon extracted from the LiDAR data (Fig. 3A) following the path of steepest descent. Major breaks in slope correspond to the canyon headwall, waterfall, and a disturbed region near the canyon mouth due to an aqueduct.

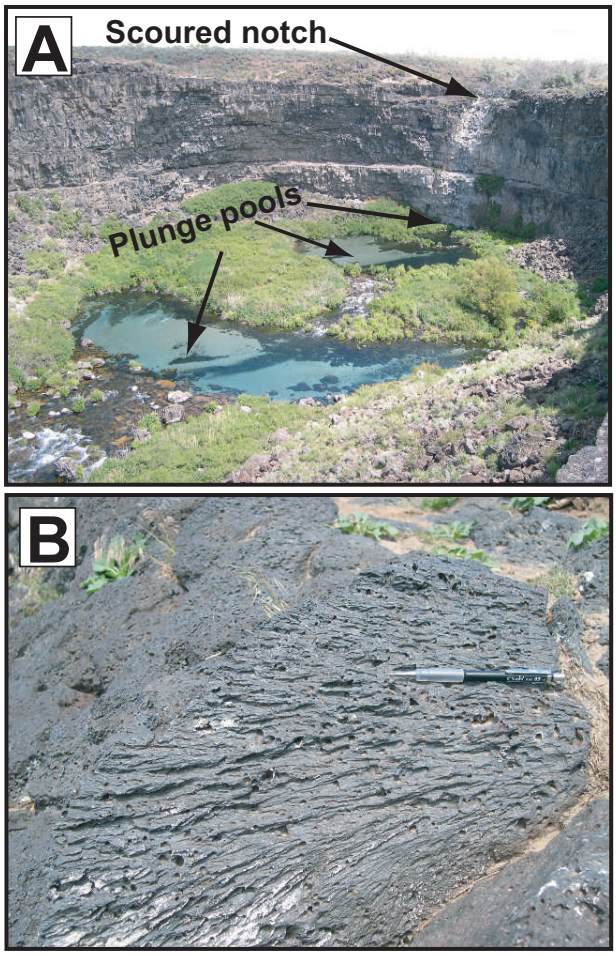

Figure 4. A) Photograph of the head of Box Canyon. The three concentric circles that lack boulders are interpreted to be plunge pools. The headwall relief is ~ 35 m. B) Photograph of scours within the notch of the Box Canyon headwall. The pencil for scale is ~ 14 cm and points in the inferred flow direction.

D_{50} = 0.29 m, and D_{16} = 0.13 m) were measured at a relatively straight 125-m reach within the canyon (Fig. 3A). A critical Shields stress formula for incipient motion (*26*) combined with our measured channel cross section (XS2, Fig. 3A), average bed slope (S = 1.85%, Fig. 3B), and a flow resistance equation (*23*) yields a flow discharge of $Q >$ 220 m^3/s (corresponding to an average flow depth of $h > 1.7$ m) that is necessary to move the sediment bed and continue canyon erosion (*20*). This is a factor of 22 larger than the modern spring discharge ($Q \sim 10$ m^3/s) and is consistent with our observations that no sediment is presently moving within the canyon.

The scoured rock upstream of the canyon head occurs within a broad channel-like depression ~250-m wide and 3-m deep (XS1, Fig. 3A). The scours extend over the southern bank of XS1 indicating that flow was deeper than and only partially bounded by this channel. A discharge estimate can be made for the flood event that spilled over the canyon rim by assuming the flow was contained within this channel. Using the measured cross-sectional area at the threshold of overspill of XS1 (475 m^2), the regional bedrock slope parallel to scour marks (S = 0.74%), a flow resistance formula (*23*), and a wide range in bed roughness-length scales $0.1 \leq k_s \leq 1$ m (since this is the least constrained parameter), we calculate a minimum flow discharge ranging from 800 – 2800 m^3/s (*20*), which would have filled the canyon to a depth of 3.7 – 5.8 m within our measurement reach, and (unlike seepage) would have exceeded the competency threshold to transport the bouldery bed. These estimated discharges are large, but are still smaller than the peak discharge of other catastrophic floods in the region (e.g., Bonneville flood, 10^6 m^3/s (*24*); Big Lost River Flood: 60,000 m^3/s (*25*)).

We do not yet have mechanistic theories for the rate of headwall retreat in bedrock during large-scale flooding. The verticality of the headwall suggests that it migrated upstream as a knickpoint, and the vertical joints inherent to flood basalt probably promoted toppling of basalt columns. The lack of gravel upstream of the canyon head also limited abrasion of the canyon rim. If sediment transport was the rate limiting step for canyon erosion, a duration of flow needed to carve the canyon can be estimated by dividing the total volume of the canyon (~ 1.53×10^7 m^3) by a volumetric transport rate of sediment (*26*) for our estimates of flood discharge (i.e., 800 – 2800 m^3/s). This suggests that flow was sustained for 35 - 160 days to transport the required load out of the canyon (*20*), which is similar to the duration of the Bonneville flood (~100 days, (*24*)). Excavation of Box Canyon could have taken less time, however, since the flood was only partially contained within the channel at XS1.

Four samples, distributed in the streamwise direction within the canyon (Fig. 3), were chosen for ^{3}He cosmogenic exposure age dating to further constrain the duration of canyon formation. Scoured bedrock exposed at the canyon-head rim was sampled (location 4), and the remaining three samples were taken from boulders due to poor bedrock exposure elsewhere. Large boulders that appeared separated from the active talus slopes were selected since they are most likely to have been stable since canyon formation. Active talus production from canyon walls, as well as weathering, constrains boulder surfaces to be minimum bounds for the age of canyon formation.

Of the boulders sampled, only location 2 was on a terrace among other large imbricated boulders indicating past fluvial transport (Fig. 3). This sample yielded an exposure age of 48 $\pm$ 3 ka (1-sigma error) and the other two boulders were nearly half

as old (location 1: 21 ± 1 ka; location 3: 19 ± 3 ka) (*17*, *20*). The scoured notch (location 4) yielded the same age as the imbricated boulder at location 2: 45 ± 5 ka.

Another constraint on the age of canyon formation comes from a ~ 20-cm thick, finely laminated bed containing clay, silt and sand, that is exposed in a small road-cut within the talus slope (location 5, Fig. 3). Two shells found within the layer yielded ^{14}C radiocarbon ages of 22.4 ± 1 ka (*20*), which is equivalent to ca. 26 ka calibrated age (*27*).

Together, these observations, hydraulic calculations and dates eliminate the seepage-erosion hypothesis for the formation of Box Canyon. Here, seepage is not significantly enhancing weathering of the headwall, and contemporary seepage flow is deficient by a factor of ~22 to evacuate sediment from the canyon. Moreover, erosion of the canyon headwall ceased ca. 45 ka owing to age of the scoured bedrock notch. The observations of scoured bedrock and plunge pools point towards a flood or floods competent to transport boulders and carve the canyon in weeks or months – illustrating the power of rare, catastrophic events in shaping the landscape. This hypothesis is supported by the similarity in surface exposure ages of the terrace-bound boulder at location 2 and the scoured notch. We interpret the younger boulders to have rolled to the canyon floor after the canyon was formed, which is consistent with the shell deposit sandwiched between several meters of talus, indicating canyon formation occurred well before 22 ka, and wall collapse has been active since. While a single flood event is the simplest interpretation, it is not possible to rule out multiple events occurring after 86 ± 12 ka (the eruption age of the basalt: (*17*)) with the last resetting the exposure ages ca. 45 ka.

4.4. Flood Source

The regional geology and topography, as well as our dates and hydraulic calculations place constraint on the origin of the paleoflood(s). Our dating results indicate that the canyon is much older than the Bonneville flood that occurred within the Snake River Canyon ca. 14.5 ka. Given the drainage area of Box Canyon (228 km^2) and Blind Canyon (4713 km^2) (Fig. 2), and our flood duration and discharge estimates, a sufficient meteorological flood would require more than 1.7 m of runoff lasting for several weeks or longer, which is highly unlikely as modern annual precipitation averages only 0.22 m over the eastern Snake River Plain, infiltration is extremely high, and conditions were likely dryer ca. 45 ka (*28*). Another possibility is that the Snake River was dammed by volcanism upstream of Box Canyon, causing overflow into the Box-Canyon drainage area. Modern peak flows on the Snake River near Box Canyon are as high as 1300 m^3/s (*19*), which is similar to our estimated range of flood discharges. The Snake River Canyon and the Box and Blind drainages are separated topographically, however, except for one location (marked with an asterisk on Fig. 2) and no volcanic dams with an age of ca. 45 ka have been discovered there.

The remaining flood sources include 1) the Little and Big Wood River drainage basins to the north, or 2) the Big Lost River drainage basin to the northeast (Fig. 2). Although the largest recorded modern discharges (Wood Rivers = 250 m^3/s; Big Lost River = 120 m^3/s (*23*)) are smaller than our estimate of the Box Canyon flood, both of these drainages have produced large magnitude paleofloods that cut canyons in Quaternary basalt, scoured bedrock, and transported large (~ 1 m) boulders (i.e., Malade Gorge, (*15*); Big-Lost-River flood, (*25*)). For example, the paleo-megaflood of the Big

Lost River, which occurred sometime between ca. 19 ka and 95 ka (*29*), was probably an outburst from Pleistocene Glacial-Lake East Fork and had a peak flow of 60,000 m^3/s (*25*) – more than 20 times our estimated discharge at Box Canyon. Such an event would have easily surpassed drainage divides since the volcanic plain separating Box Canyon from the Wood and Lost River drainages is relatively flat (Fig. 1). Moreover, the divides themselves have shifted since the formation of Box Canyon due to volcanism that postdates the Box-Canyon flood (Fig. 2).

4.5. Conclusions

Our analysis of Box Canyon forces us to abandon the seepage-erosion hypothesis for formation of amphitheater-headed canyons. Instead, we propose that such amphitheater morphology might be expected in basaltic plains where vertical fractures in basalt promote a steep face, and where catastrophic flooding is competent to topple basalt columns and transport boulders. Thus, Box Canyon and other amphitheater-headed canyons produced by catastrophic outburst floods in volcanic terrains (e.g., Dry Falls, Washington State, U.S.A. (*30*); Asbyrgi Canyon, Iceland (*31*)) might be better analogs of Martian canyons than seepage channels in sand. Deciphering the history of the Martian surface, however, will require higher resolution imagery at canyon heads, as scour marks and even boulder sizes at Box Canyon are small relative to the resolution of contemporary Martian orbiter cameras (e.g., Mars Orbiter Camera, High Resolution Imaging Science Experiment).

4.6. Appendix 1 - Methods

Discharge at incipient motion

We estimated the flow needed to carve Box Canyon from the dimensionless bed-shear stress or Shields stress at incipient sediment motion τ_{*c}:

$$\tau_{*c} = \frac{\tau_b}{(\rho_s - \rho) g D_{50}} \qquad (1)$$

where τ_b is the bed shear-stress, ρ_s and ρ are the densities of sediment and fluid, respectively, g is the acceleration due to gravity, and D_{50} is the median grain diameter (*S1*, *S2*). We assume steady and uniform flow, i.e. $\tau_b = \rho g R S$, where *R* is the hydraulic radius and *S* is the water-surface slope.

To evaluate equation (1), we made measurements within a 125-m reach (Fig. S1A) along the canyon floor (marked "Measurement Reach" in Fig. 3), which was chosen because it was relatively straight in planform and wadeable. The bed is bouldery throughout the canyon and is probably best described as plane-bed morphology (*S3*), although there are local clusters of boulders and pools. The grain size distribution was measured within this reach (Fig. S2) and the particle-size statistics are D_{84} = 0.60 m, D_{50} = 0.29 m, and D_{16} = 0.13 m, where the subscripts denote the percentage of grains finer than. We measured the intermediate axes of 100 grains by counting particles every 1 m along the channel and conducting four transects spaced ~10 m apart (Fig. S1A). Owing to the large size of particles, measurements were made

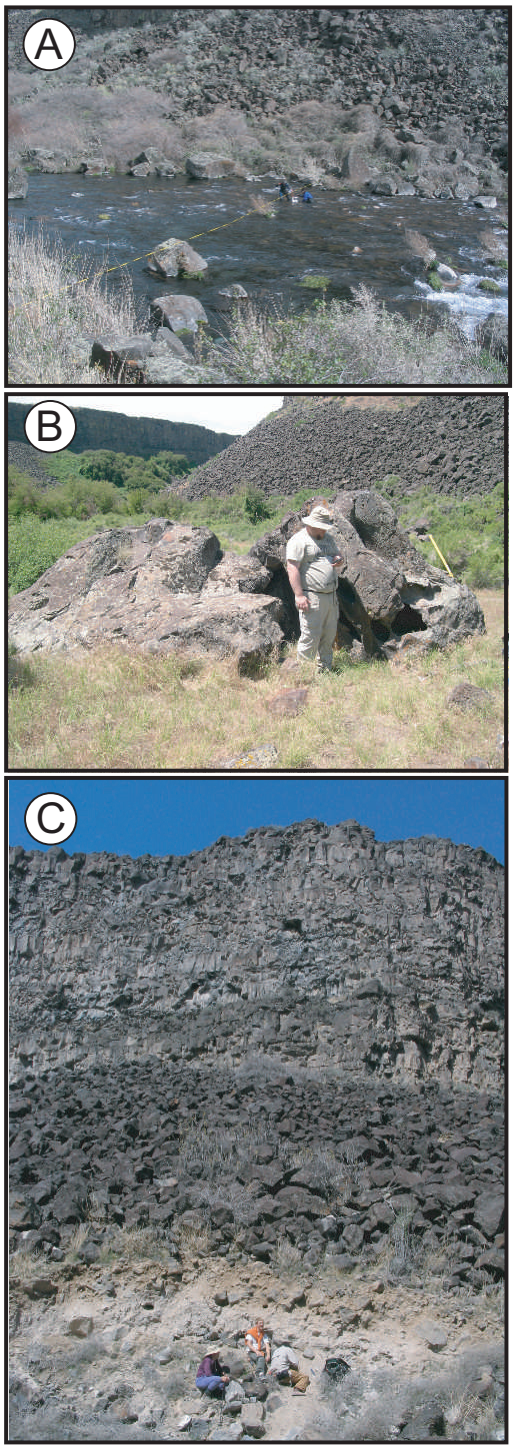

Fig. S1. **(**A) Photograph of the measurement reach and cross section XS2 within Box Canyon (the stream is ~ 35 m wide for scale). (B) Photograph of the boulder at location 2 (Fig. 3) sampled for ^{4}He cosmogenic exposure dating. (C) Photograph of a sediment deposit exposed within the talus slope (location 5, Fig. 3) containing shell fragments that were used for ^{14}C dating.

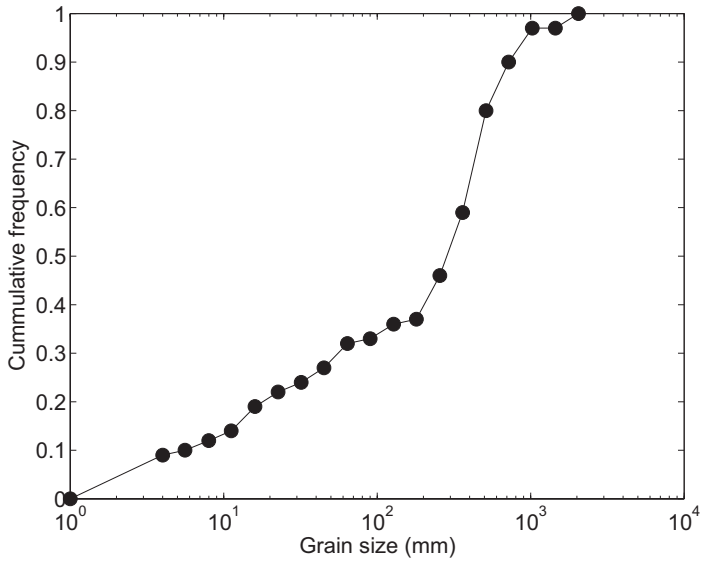

Fig. S2. Cumulative frequency distribution of particle sizes along the stream bed of Box Canyon within the measurement reach.

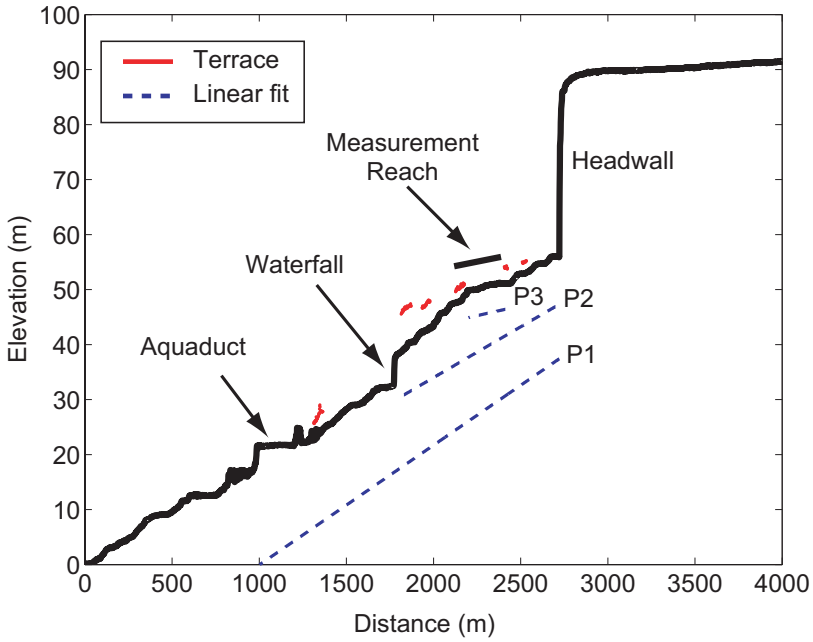

Fig. S3. Longitudinal profile of Box Canyon calculated as the path of steepest descent from the 1-m resolution DEM. Three linear, least-squares fits to the data, used to calculate channel-bed slope, are shown as dashed lines (displayed offset from the data) for P1: the entire length of the canyon (S = 2.18%), P2: a 900-m reach bounded by the waterfall and the canyon head (S = 1.85%), and P3: the measurement reach (S = 0.9%). The elevations of mapped terraces (Fig. 3) are shown in red.

in situ using a tape measure and snorkel gear. A few grains were larger than 1 m across and these were counted twice in the distribution. The particle sizes were binned following the phi scale.

The longitudinal profile of the water surface was measured from 1-m resolution airborne Light Detection and Ranging (LiDAR) data collected by the National Center for Airborne Laser Mapping (Fig. S3). The profile was extracted from a digital elevation model (DEM) following the path of steepest descent, and this profile was verified to be accurate by comparison with a field survey within the measurement reach conducted with a self-leveling level and stadia rod. During floods, bed irregularities will be drowned out and the water surface-slope will tend to be more uniform over a length scale of many times the channel width. To account for this, we estimated the water-surface slope during flood as the average water-surface slope over a 900-m reach bounded by the waterfall downstream and the canyon headwall upstream (Profile P2, Fig. S3). Using a linear least-squares fit, the slope was found to be S = 1.85%, and for this channel slope τ_{*_c} = 0.055 (*S4*). Using these values, the necessary bed shear-stress to move the bouldery bed was calculated from equation (1) to be 290 N/m^2 assuming $(\rho_s - \rho)$ = 1800 kg/m^3 for basalt.

From these calculations and measurements, the discharge needed to move sediment within the canyon can be calculated from the empirical formula of Bathurst (*S5*):

$$Q = UA = a(gRS)^{1/2}\left(\frac{h}{k_s}\right)^b A, \qquad (2)$$

where U is the average flow velocity across a channel cross section, A is the cross sectional area of flow, h is the average flow depth, and k_s is the roughness length scale of the bed. a and b were found empirically from measurements in mountain streams to be $a = 3.84$ and $b = 0.547$ for $S < 0.8\%$, and $a = 3.1$ and $b = 0.93$ for $S > 0.8\%$ (*S5*).

Bathurst (*S5*) suggested $k_s \approx D_{84}$, although this likely depends on the site-specific substrate (e.g., bed forms, particle-size distribution, particle angularity). Others have shown that k_s can be two or three times D_{84} (e.g., *S6*). Instead of assuming k_s, we calculated it from equation (2) for conditions in Box Canyon creek using our surveyed cross section, water surface profile, and the USGS measured discharge ($Q = 9.15$ m^3/s) from March 2004 (*S7*). A cross section (XS2, Fig. 3) within the measurement reach was surveyed using a self leveling level and stadia rod (Fig. S4A). At the time of the measurements, the maximum flow depth was 1.08 m and the average depth over the cross section was $h = 0.58$ m, which is equivalent to a hydraulic radius of $R = 0.57$ m. Within the measurement reach, the water surface slope at the time of our measurements was approximately uniform and equal to 0.9% (Profile P3, Fig. S3). Inserting these values into equation (2) results in $k_s = 0.81$ m, which is about one-third larger than our measured D_{84} within the reach. In the following calculations we use $k_s = 0.81$ m rather than D_{84} making our discharge estimates conservative.

At incipient motion, the hydraulic radius was calculated from equation (1) to be $R = 1.6$ m. Such a flow would fill the canyon at XS2 to an average depth of $h = 1.7$ m and a maximum depth of 2.5 m (Fig. S4A). Using these values and $S = 1.85\%$, equation

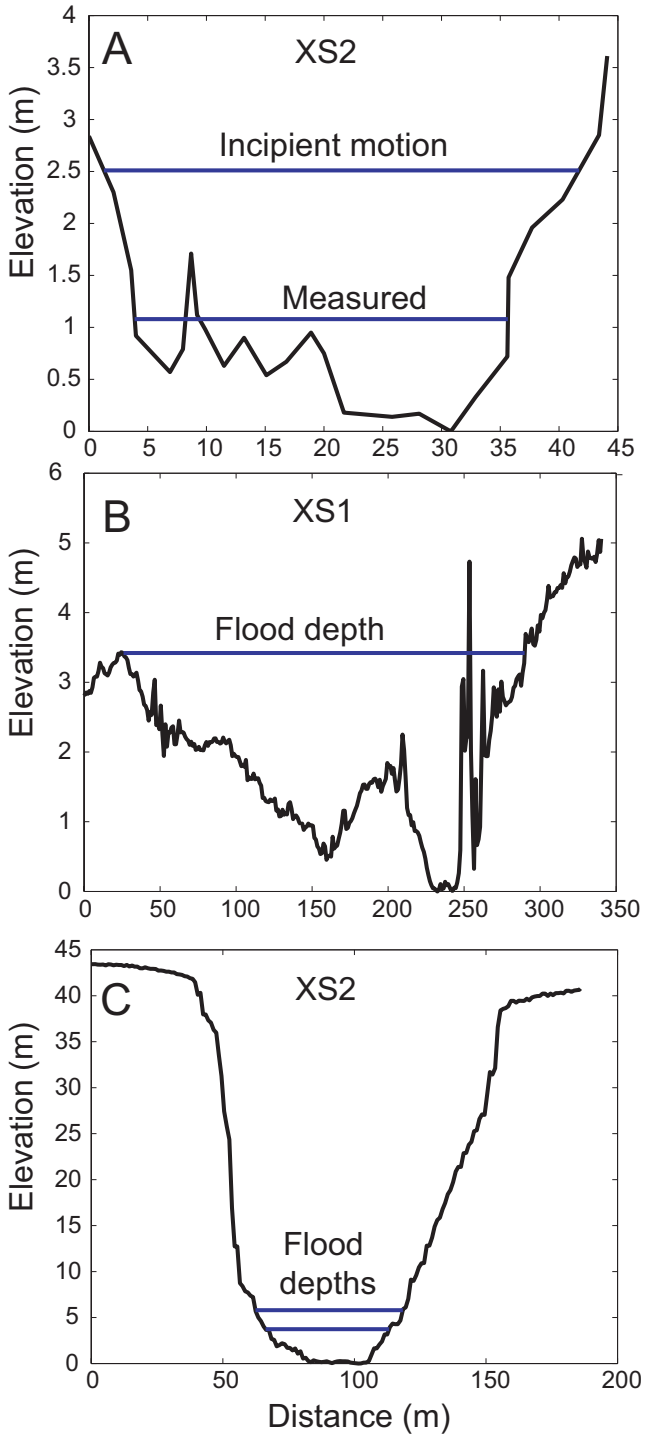

Fig. S4. Cross sections of Box Canyon. (A) XS2 (Fig. 3) along the stream bed showing the bed and water surface topography surveyed in the field, as well as the calculated depth for incipient motion. (B) XS1 (Fig. 3) extracted from the DEM showing the depth used to constrain the flood discharge. (C) XS2 extracted from the DEM showing a range in depths that correspond to the range in calculated flood discharges.

(2) was solved to find that a discharge $Q > 220$ m^3/s is needed to begin to move the sediment bed and continue canyon erosion.

Discharge of the flood event

The scoured channel upstream of the canyon head was used to estimate the discharge of the flood event. Aside from scour marks and a few plucked blocks along bedding planes, most of the bedrock surface within the channel is continuous with the neighboring land surface and appears to be the original volcanic surface. This suggests that the broad channel was not created by the flood event, but rather was inherited topography that likely focused flow towards the canyon.

A cross section (XS1, Fig. 3) was extracted from the LiDAR DEM (Fig. S4B), and at the threshold of overspill of the southern bank (which corresponds to a distance of ~ 25 m on Fig. S4B) was found have an area of 475 m^2. The water-surface slope during the flood was assumed to be similar to the regional bedrock slope in the direction parallel to the scour marks (S = 0.74%), which was also extracted from the DEM. These measurements were used, along with a spectrum of roughness-length scales ($0.1 \le k_s \le 1$ m) to solve equation (2), resulting in a flow discharge ranging from 800 to 2800 m^3/s. Using the same parameters for the incipient-motion calculation above (i.e., S = 1.85% and k_s = 0.81 m), we found that this flood event would have filled the canyon to a depth ranging from 3.7 m to 5.8 m within our measurement reach (Fig. S4C).

Time to excavate the canyon

If sediment transport was the rate limiting step for canyon erosion, a duration of flow needed to carve the canyon can be estimated by dividing the total volume of the canyon (*V*) by a volumetric transport rate of sediment (Q_s). The total volume of the canyon (V = 1.53 x 10^7 m^3) was found using the DEM and differencing a surface interpolated from the topography surrounding the canyon and the topography of the canyon itself. For our estimated range of flood discharge (i.e., 800 - 2800 m^3/s) and the corresponding range in hydraulic radii (2.5 – 3.9 m), the volumetric transport rate was calculated as

$$Q_s = 5.7W\left(rgD_{50}^3\right)^{1/2}\left(\frac{\tau_b}{r\rho gD_{50}} - \tau_{*c}\right)^{3/2} \quad (3)$$

where $r = (\rho_s - \rho)/\rho$ = 1.8 and *W* is the average bed-width of flow (*S8*), which at XS2 was found to be 47 m and 56 m for the two discharge estimates (Fig. S4C). This calculation (i.e., V/Q_s) suggests that flow was sustained for 35 - 160 days to transport the required load out of the canyon.

^{4}He Cosmogenic exposure ages

The original up-direction and, if present, original lava-flow surface of the sampled boulders (e.g., Fig. S1B) was identified by basalt density (extent of vesicularity) and vesicle orientation. Samples were taken at least 1-m below volcanic-flow surfaces to avoid inherited exposure that resulted during hiatuses between basalt

eruptions. In addition, the sample from the eroded notch was taken from ~2 m below the original flow surface as inferred by tracing bedding surfaces laterally. Helium exposure ages were measured on olivine separates from several kilograms of basalt taken from the upper 4 cm of the exposed surfaces. After extracting any magmatic helium from the olivine, cosmogenic ^{3}He was released from the samples by heating *in vacuo* and measured. Exposure ages were then calculated using an average production rate scaled for latitude, altitude and surface slope. The correction for shielding from canyon walls was found to be less than 4% for all samples and was folded into the error for each age determination. Measurements and calculations are further detailed in *(S9)*.

^{14}C Radiocarbon ages

The shells were extracted from a ~ 20-cm thick, finely laminated bed containing clay, silt and sand, which is exposed in a small road-cut within the talus slope (Fig. S1C). This bed is probably a backwater deposit from an unknown flood of the Snake River, and appears younger than the Yahoo Clay deposited throughout the region following damming of the river by McKinny basalt flows (*S10*) ca. 52 $\pm$ 24 ka (*S11*), and older than the Bonneville flood (*S12*). Three dates from two shells within the layer yielded ^{14}C radiocarbon ages of 22.51 $\pm$ 0.07 ka, 22.55 $\pm$ 0.07 ka, and 22.34 $\pm$ 0.07 ka. The error bars represent two standard deviations. The first two dates are gas splits from acidification of the same shell. The measurements were made at the Keck Carbon Cycle AMS Facility, Earth System Science Department, University of California - Irvine, U.S.A, following the conventions of (*S13*). Sample preparation backgrounds were subtracted based on measurements of ^{14}C-free calcite.

4.7. Appendix 2 - Supporting Text

Geologic setting

Recently Gillerman et al. (*S14*) reinterpreted the basalt that composes Box Canyon as the Thousand Springs Basalt (also called Basalt of Flat Top Butte; ~ 395 ± 20 ka, (*S11*)), and the inferred the relatively young appearance of bedrock and the origin of Box Canyon to be from scour by the catastrophic Bonneville flood, which drained glacial lake Bonneville ca. 14.5 ka (*S12*). In his autobiography (*S15*), Stearns also admits the possibility that his seepage-erosion hypothesis (*S16*) was incorrect and that the Bonneville flood carved Box Canyon and scoured the neighboring landscape. Hydraulic modeling by O'Conner (*S17*), however, showed that the Bonneville flood did not overspill the Snake River Canyon in this region, which is consistent with our dating and analysis that Box Canyon was carved by an older event(s). U-Th/He eruption ages (*S9*) confirm that the basalt of Box Canyon is 86 ± 12 ka to 130 ± 12 ka and this is consistent with the earlier designation of Sand Springs Basalt (*S18*, *S19*) (also named the Basalt of Rocky Butte (*S14*)) with an Ar-Ar eruption age of ~ 95 ± 10 ka (*S11*).

Near the mouth of Box Canyon, the Quaternary basalt overlies a ~ 5-m thick Pliocene or Miocene stratified volcaniclastic unit (*S14*, *S20*), which appears older and more weathered than the basalt. This unit is only exposed near the canyon mouth, where the talus slope was excavated recently for an aqueduct. Most of the canyon floor is composed of basalt boulders so the underlying bedrock cannot be determined. Quaternary basalt is exposed, however, at a ~5-m high waterfall (Fig. S5A) approximately 730 m downstream of the canyon head (Figs. 3 and S3). The log from the nearest well, about 0.5 km southeast of the canyon head, extends to a depth of 43

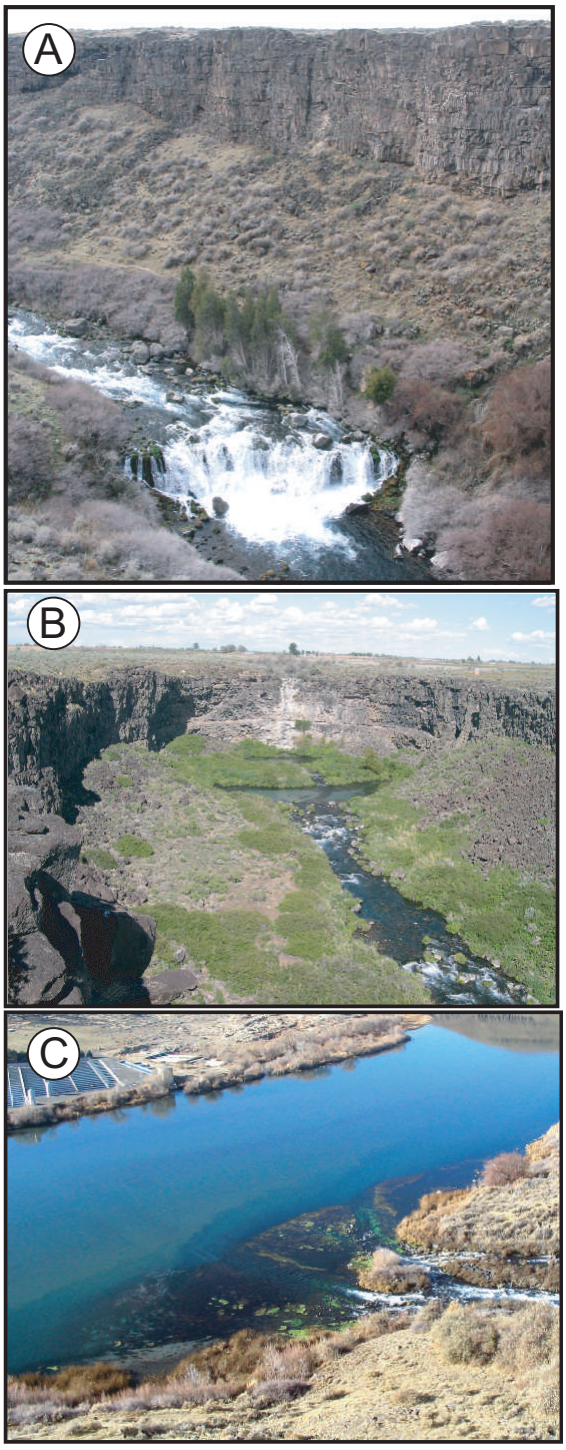

Fig. S5. Photographs of Box Canyon showing the (A) ~ 5-m high waterfall, (B) ~ 35-m high canyon headwall, and (C) small delta at the confluence with the Snake River (the Snake River is ~ 200 m wide for scale).

meters, or ~ 7 m below the canyon floor near the headwall, and indicates intact basalt to this depth (*S21*). Thus, if the underlying older unit is laterally extensive, it does not appear to have played a role in formation of the canyon, at least upstream of the waterfall.

Spring discharge and chemistry

Fig. S6 shows the daily average discharge and the dissolved silica concentration for Box Canyon creek as recorded by the U.S. Geological Survey (*S7*). The saturation value of 33 mg/L was calculated for dissolved quartz and amorphous silica at 14^{o} C and pH = 8 (*S22*), conditions typical of Box Canyon creek. Seasonal variations in discharge are less than 10 to 20% and trends over the 58-year duration of record are thought to record changes in farm irrigation across the plain, rather than natural forcing.

Talus at the canyon head

It is puzzling that there is almost no talus at the canyon head (Fig. S5B), while talus slopes are well developed elsewhere in the canyon. Our date of the notch at the canyon head suggests that wall collapse has not occurred there since ca. 45 ka. Perhaps, the basalt columns are more interlocked at the headwall, which might also explain why the headwall stalled at this location during canyon formation. Alternatively, maybe the spring flow prevents rock breakdown at the headwall, e.g. by preventing freeze-thaw (*S23*).

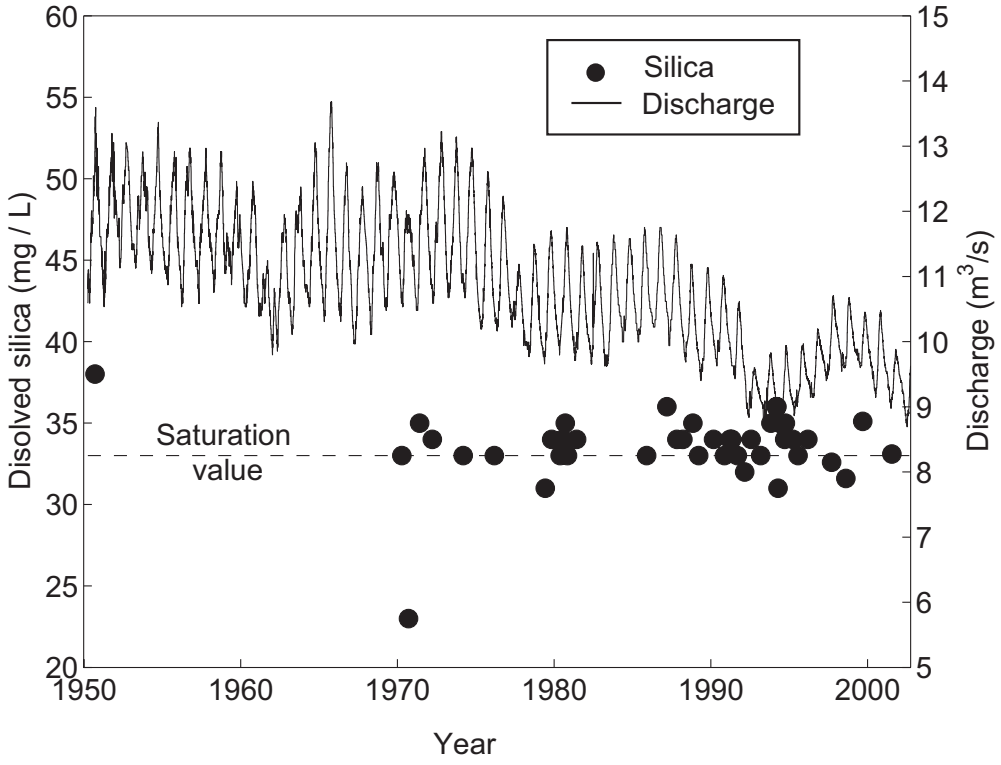

Fig. S6. Discharge and dissolved silica records for Box Canyon creek from the U.S. Geological Survey gauge 13095500.

Table S1 – Inferred wind abrasion marks.

Location	Longitude	Latitude	Scour orientation
Box Canyon	42.70566˚	-114.81971˚	113˚
Box Canyon	42.70902˚	-114.81895˚	115˚
Box Canyon	42.70874˚	-114.82214˚	115˚
~ 10 km East	42.7163˚	-114.70708˚	110˚

Delta at the canyon mouth

There appears to be a small delta (<<1% of the total canyon volume) at the mouth of Box Canyon (Fig. S5C). This might imply that there has been active transport of sediment since ca. 14.5 ka when the Bonneville flood swept through the Snake River Canyon (*S17*), or perhaps sediment transport occurred within Box Canyon because of withdrawal of the Bonneville floodwater.

Bedrock scour directions

Bedrock scours near the canyon head indicate flow towards the canyon headwall (Fig. 3). We identified three locations near the canyon mouth, however, with bedrock scours that appear to display an opposite flow direction with orientations ranging from 113 ^{o} to 115 ^{o} (Table S1). The consistency of these directions, all aligned with the prevailing westerly wind direction, suggests that these outliers resulted from wind abrasion. A high knob of bedrock ~ 7.8 km to the east of Box Canyon also shows scours orientated 110 ^{o} consistent with this hypothesis.

4.8. References and Notes

1. I. C. Russel, *United States Geological Survey Bulletin 199* (1902).

2. J. E. Laity, M. C. Malin, *Geological Society of America Bulletin* **96**, 203 (1985).

3. R. C. Kochel, J. F. Piper, *Journal of Geophysical Research-Solid Earth and Planets* **91**, E175 (Nov 30, 1986).

4. H. T. Stearns, *Journal of Geology* **44**, 429 (1936).

5. M. C. Malin, M. H. Carr, *Nature* **397**, 589 (1999).

6. K. P. Harrison, R. E. Grimm, *Journal of Geophysical Research-Planets* **110** (2005).

7. M. G. Tomasko *et al.*, *Nature* **438**, doi:10.1038/nature04126 (2005).

8. T. Dunne, *Progress in Physical Geography* **4**, 211 (1980).

9. A. D. Howard, C. F. McLane, *Water Resources Research* **24**, 1659 (1988).

10. S. A. Schumm, K. F. Boyd, C. G. Wolff, W. J. Spitz, *Geomorphology* **12**, 281 (1995).

11. M. P. Lamb *et al.*, *Journal of Geophysical Research* **111**, doi:10.1029/2005JE002663 (2006).

12. M. P. Lamb, A. D. Howard, W. E. Dietrich, J. T. Perron, *Geological Society of America Bulletin* **119**, 805 (2007).

13. A. D. Howard, W. E. Dietrich, M. A. Seidl, *Journal of Geophysical Research-Solid Earth* **99**, 13971 (1994).

14. H. E. Malde, in *Quaternary Nonglacial Geology; Conterminous U.S.* R. B. Morrison, Ed. (Geological Society of America, Boulder, Colorado, 1991), vol. K-2.

15. J. D. Kauffman, K. L. Otherberg, V. S. Gillerman, D. L. Garwood, *Geologic map of the Twin Falls 30 x 60 minute quadrangle, Idaho* (Idaho Geological Survey, Moscow, Idaho, 2005).

16. L. Tauxe, C. Luskin, P. Selkin, P. Gans, A. Calvert, *Geochemistry Geophysics Geosystems* **5**, doi:10.1029/2003GC000661 (2004).

17. S. M. Aciego *et al.*, *Earth and Planetary Science Letters*, doi:10.1016/j.epsl.2006.11.039 (2007).

18. H. E. Malde, *U.S. Geological Survey Professional Paper*, 20 (1971).

19. U.S. Geological Survey: Box Canyon Creek, gauge 13095500; Big Lost River, gauge 13120500; Big Wood River, gauge 13139510; Snake River, gauge 13154500.

20. See the Supporting Materials (Sections 4.8 – 4.

21. S. L. Forman, R. P. Smith, W. R. Hackett, J. A. Tullis, P. A. McDaniel, *Quaternary Research* **40**, 30 (1993).

22. M. P. Lamb, W. E. Dietrich, J. Venditti, *Journal of Geophysical Research* (in press).

23. J. C. Bathurst, *Journal of Hydrology* **269**, 11 (2002).

24. J. E. O'Connor, *Hydrology, Hydraulics and Geomorphology of the Bonneville Flood*, GSA Special Paper 274 (Geological Society of America, Boulder, CO, 1993), pp. 90.

25. S. L. Rathburn, *Geomorphology* **8**, 305 (1993).

26. R. Fernandez Luque, R. van Beek, *J. Hydraul. Res.* **14**, 127 (1976).

27. P. J. Reimer *et al.*, *Radiocarbon* **46**, 1029 (2004).

28. D. B. Madsen *et al.*, *Palaeogeography Palaeoclimatology Palaeoecology* **167**, 243 (Mar 15, 2001).

29. T. E. Cerling, R. J. Poreda, S. L. Rathburn, *Geology* **22**, 227 (1994).

30. J. H. Bretz, *Journal of Geology* **31**, 617 (1923).

31. H. Tomasson, *Natturufraeoingurinn* **43**, 12 (1973).

32. P. R. Christensen *et al.*, *Space Science Reviews* **110**, 85 (2004).

4.9. Supporting References and Notes

S1. A. Shields, *Mitt. Preuss. Versuchsanst. Wasserbau Schiffbau* **26**, 26 (1936).

S2. J. M. Buffington, D. R. Montgomery, *Water Resources Research* **33**, 1993 (1997).

S3. D. R. Montgomery, J. M. Buffington, *Geological Society of America Bulletin* **109**, 596 (1997).

S4. M. P. Lamb, W. E. Dietrich, J. Venditti, *Journal of Geophysical Research* in press, (available at http://www.agu.org/journals/pip/jf/2007JF000831-pip.pdf).

S5. J. C. Bathurst, *Journal of Hydrology* **269**, 11 (2002).

S6. J. W. Kamphuis, *Journal of Hydraulic Research* **12**, 193 (1974).

S7. U.S. Geological Survey, gauge 13095500, Box Canyon Creek, Idaho

S8. R. Fernandez Luque, R. van Beek, *J. Hydraul. Res.* **14**, 127 (1976).

S9. S. M. Aciego *et al.*, *Earth and Planetary Science Letters* **254**, 288, doi:10.1016/j.epsl.2006.11.039 (2007).

S10. H. E. Malde, in *Cenozoic Geology of Idaho* B. Bonnichsen, R. M. Breckenridge, Eds. (1982), vol. 26, pp. 617-628.

S11. L. Tauxe, C. Luskin, P. Selkin, P. Gans, A. Calvert, *Geochemistry Geophysics Geosystems* **5**, doi:10.1029/2003GC000661 (2004).

S12. W. E. Scott, K. L. Pierce, J. P. Bradbury, R. M. Forester, in *Cenezoic Geology of Idaho: Idaho Bureau of Mines and Geology Bulletin* G. Bonnichsen, R. M. Breckenridge, Eds. (1982), vol. 26, pp. 581-595.

S13. M. Stuiver, H. A. Polach, *Radiocarbon* **19**, 355 (1977).

S14. V. S. Gillerman, J. D. Kauffman, K. L. Otherberg, *Geologic map of the Thousand Springs Quadrangle, Gooding and Twin Falls counties, Idaho* (Idaho Geological Survey, Moscow, Idaho, 2004).

S15. H. T. Stearns, *Journal of Geology* **44**, 429 (1936).

S16. H. T. Stearns, *Memoirs of a Geologist: From Poverty Peak to Piggery Gulch* (Hawaii Institute of Geophysics, Honolulu, Hawaii, 1983).

S17. J. E. O'Connor, *Hydrology, Hydraulics and Geomorphology of the Bonneville Flood*, GSA Special Paper 274 (Geological Society of America, Boulder, CO, 1993), pp. 90.

S18. H. E. Malde, *U.S. Geological Survey Professional Paper*, 20 (1971).

S19. H. R. Covington, J. N. Weaver, *Geologic map and profiles of the north wall of the Snake River Canyon, Thousand Springs and Niagara Springs quadrangles, Idaho*, U.S. Geological Survey Miscellaneous Investigations I-1947C (1991).

S20. H. E. Malde, H. A. Powers, *Geological Society of America Bulletin* **73**, 1197 (1962).

S21. Elsing Well Drilling, Well Log # 40916, Department of Water Resources, Idaho (1975).

S22. G. Faure, *Principles and Applications of Geochemstry* (Prentice Hall, Upper Sadle River, ed. 2nd, 1998), pp. 600.

S23. L. J. Mason, D. T. Pederson, R. J. Goble, *Eos Trans. AGU Fall Meet. Suppl.* **85**, Abstract H51C (2004).

Chapter 5

Is the Critical Shields Stress for Incipient Sediment Motion Dependent on Channel-Bed Slope?

5.1. Introduction

Predicting initial sediment motion is one of the most fundamental and practical problems in sedimentology and geomorphology. Sediment transport predictions are needed to route sediment through river networks [*Cui and Parker*, 2005; *Cui et al.*, 2006; *Wiele et al.*, 2007], model river incision into bedrock [*Sklar and Dietrich*, 2004; *Lamb et al.*, 2007], restore river functionality and habitat [*Rosgen*, 1996; *Buffington et al.*, 2004], and mitigate debris flows initiated from channel-beds [*Papa et al.*, 2004]. Sediment transport predictions also are crucial for understanding surface processes on planets and satellites like Mars and Titan, as they provide a straightforward and quantitatively robust method for constraining the amount of fluid that is flowing or once flowed across these planetary surfaces [*Komar*, 1979; *Burr et al.*, 2006; *Lamb et al.*, 2006; *Perron et al.*, 2007].

Many widely used bedload sediment-transport models are based on the concept that sediment transport either begins at, or can be scaled by, a constant value of the non-dimensional bed-shear stress or the critical Shields stress τ_{*_c} [*Meyer-Peter and Müller*, 1948; *Engelund and Fredsoe*, 1976; *Luque and van Beek*, 1976; *Parker*, 1990; *Wilcock and Crowe*, 2003]. The Shields stress is defined as

$$\tau_{*cg} \equiv \frac{\tau_g}{(\rho_s - \rho)gD} = \frac{u_*^2}{rgD} \qquad (1)$$

where τ_g is the shear stress at the bed, and the shear velocity $u_* \equiv \sqrt{\tau_g / \rho}$. D is the diameter of a particle, g is the acceleration due to gravity, and r is the submerged specific density of the sediment, $r = (\rho_s - \rho)/\rho$, where ρ_s and ρ are the densities of sediment and fluid, respectively. The subscript g in equation (1) is used to denote the portion of the total bed stress that is borne by sediment grains on the bed (discussed below). τ_{*_c} without further subscripts is used to describe the critical Shields criterion generically, without regard to stress partitioning.

The concept of a constant Shields-stress criterion for incipient motion is based on the pioneering experimental work of *Shields* [1936], which showed that the Shields stress at incipient motion τ_{*_c} varies with the particle Reynolds number Re_p, but is roughly constant (i.e., $\tau_{*_c} \approx 0.045$ [*Miller et al.*, 1977; *Yalin and Karahan*, 1979]) for $\mathrm{Re}_p > 10^2$ (corresponding to about $D > 3$ mm for rivers on Earth), where

$$\mathrm{Re}_p = \frac{u_* D}{\nu} \qquad (2)$$

and ν is the kinematic viscosity of the fluid. This result has been reproduced by many others (e.g., see review by *Buffington and Montgomery* [1997]), although significant scatter in the data exists. Theoretical models based on balancing forces on particles also have reproduced these experimental findings [e.g., *Wiberg and Smith*, 1987a; *Bridge and Bennett*, 1992].

Considerable attention has been placed on sediment mixtures, in which grain shape, orientation, exposure, protrusion, and variable pocket geometry can influence the critical Shields stress [e.g., *Wiberg and Smith*, 1987a; *Kirchner et al.*, 1990; *Komar and Carling*, 1991; *Johnston et al.*, 1998]. If τ_{*c} is a constant, then equation (1) indicates that smaller particles are more mobile, as they require less shear stress to move (Note that the term "mobility" is used herein to describe the boundary shear stress necessary to initiate sediment motion, and does not refer to the rate of bedload transport). Most studies have shown, however, that sediment is more equally mobile than that predicted by equation (1) because the differences in exposure and friction angles tend to offset differences in particle weight [*Parker et al.*, 1982; *Wiberg and Smith*, 1987a; *Parker*, 1990]. Incipient motion for mixtures then can be reasonably determined from a single function of τ_{*c} for the bulk mixture with the representative grain diameter in equations (1) and (2) set to $D = D_{50}$, where D_{50} is the median grain size. Nevertheless, finer particles are generally considered to move at slightly lower shear stresses than coarser

particles [e.g., *Parker*, 1990; *Ferguson*, 2003], and this difference can be more profound in steep mountain streams [e.g., *Andrews*, 1983; *Lenzi et al.*, 2006].

While experimental studies on incipient particle motion have explored a wide range of parameter space, they often have been limited to moderate channel slopes and consequently the empirically determined τ_{*c} might not be applicable to steep mountain streams or lowland rivers (Slope is defined here as $S = \tan\beta$, where β is the bed-slope angle from horizontal). Shields himself recognized a potential slope dependency of τ_{*c} [*Shields*, 1936], but it was over 30 years before *Neill* [1967] showed that τ_{*c} increases with increasing channel slope. Neill later retracted his results and stated that criticism from colleagues caused him to re-examine his data, which revealed measurement bias [*Neill*, 1968]. The original slope-dependent findings of Neill, however, have been reproduced subsequently for steep slopes in experimental [*Ashida and Bayazit*, 1973; *Aguirre-Pe*, 1975; *Bathurst et al.*, 1984; *Olivero*, 1984; *Graf and Suszka*, 1987; *Torri and Poesen*, 1988; *Aguirre-Pe and Fuentes*, 1991; *Picon*, 1991] and field studies [*Bartnick*, 1991; *Mueller et al.*, 2005; *Lenzi et al.*, 2006]. Detailed experiments by *Shvidchenko and Pender* [2000] and *Shvidchenko et al.* [2001] indicate that incipient motion is slope dependent even on low slopes ($S < 0.01$) and for small particles ($\mathrm{Re}_p < 10^2$), which suggests that a slope-dependent Shields stress is applicable for lowland rivers as well as steep mountain streams.

The reasons for an increase in critical Shields stress with increasing channel slope remain largely unexplored. Consequently τ_{*c} is typically assumed to be independent of slope in bedload transport models (see *Shvidchenko et al.* [2001], *Papanicolaou et al.* [2004], and *Mueller and Pitlick* [2005] for notable exceptions).

Theoretical models actually suggest an opposite trend to that observed; sediment should become more mobile as slope increases due to the increased component of gravity in the downstream direction [e.g., *Wiberg and Smith*, 1987a].

The reduced mobility on steep slopes has been attributed to increased relative roughness of the flow (i.e., k_s / h where h is the total flow depth and k_s is the roughness length-scale of the bed) [e.g., *Shields*, 1936; *Ashida and Bayazit*, 1973; *Buffington and Montgomery*, 1997; *Buffington and Montgomery*, 1999; *Shvidchenko and Pender*, 2000; *Mueller et al.*, 2005], since for a given total bed stress, the flow depth varies inversely with bed slope for steady uniform flow. It is true that the total flow resistance (i.e., the depth-averaged flow velocity normalized by the shear velocity, as in Manning-Strickler or Darcy-Weisbach friction relations) is a function of k_s / h for flow over hydraulically rough beds [*Nikuradse*, 1933]. It is the local near-bed velocity, however, that induces sediment motion [e.g., *Wiberg and Smith*, 1987b]. Both standard formulations for the local velocity (e.g., the log-layer profile [*Nikuradse*, 1933; *Schlichting*, 1979]) and velocity profiles corrected for particle-induced form drag [e.g., *Wiberg and Smith*, 1987b; *Wiberg and Smith*, 1991; *Nelson et al.*, 1991] predict a local near-bed flow velocity that is a function of z / k_s (where z is the height above the bed), but is independent of the total flow depth h and relative roughness k_s / h.

Some have formulated models based on a critical mean flow velocity (e.g., a critical discharge [e.g., *Schoklitsch*, 1962; *Bathurst*, 1987] or a critical densimetric Froude number [e.g., *Aguirre-Pe et al.*, 2003]) for incipient motion, rather than τ_{*c}, and claimed to find a better collapse of the data with relative roughness. As pointed out by *Gessler* [1971] and *Bettes* [1984], however, these models necessarily trend with relative

roughness because the mean flow velocity is a function of the relative roughness [*Nikuradse*, 1933], and therefore are not an improvement over the Shields approach.

The goal of this chapter is to present a mechanistic model and a compilation of data, which indicate that the critical Shields stress for incipient motion is a function of channel slope. First we present a comprehensive collection of flume and field data for coarse particles that indicates that sediment is less mobile (larger τ_{*c}) on steeper slopes. Second, a simple force-balance model is formulated that allows for predictions of τ_{*c} for single-sized sediment. Third, we hypothesize several effects that might explain the variation in τ_{*c} with channel slope and incorporate them into the force-balance model to assess quantitatively their influence on incipient motion. The effects considered are wall drag, drag due to morphologic structures on the bed, variable friction angles, grain emergence, flow aeration, and slope-dependent variations in the structure of flow velocity and turbulent fluctuations. The results suggest that the slope dependent critical Shields stress is fundamentally due to the coincident change in k_s / h with slope for a given bed stress and roughness. Surprisingly, it is the eddy viscosity and turbulent fluctuations that appear to depend most strongly on k_s / h, not form drag from particles or morphologic structures as is often assumed. Last, we extend the model to sediment mixtures and discuss implications for natural streams.

5.2. Data Compilation

A large set of experimental and field data from incipient motion studies in unidirectional flows is presented in Figure 1. The data have been filtered so that only

measurements with $\mathrm{Re}_p > 10^2$ are shown. By neglecting studies with $\mathrm{Re}_p \leq 10^2$ the flow is hydraulically rough and potential false relations with *S* have been avoided since, for small Re_p, τ_{*c} is a function of Re_p which in turn is a function of *S* (see *Buffington and Montgomery* [1997] for discussion). Thus, the data in Figure 1 represent the regime where τ_{*c} is thought to be a constant ranging from 0.03 to 0.06 [*Buffington and Montgomery*, 1997]. *Yalin and Karahan* [1979] and *Wilcock* [1993], for example, suggested a constant τ_{*c} value of 0.047 for mixed size gravel, which is widely used. It is clear from Figure 1 that much of the data does not fall within $0.03 < \tau_{*c} < 0.06$. Moreover, despite data scatter, there is a trend of increasing critical Shields stress with channel slope. A best-fit line to all data (in a least-squared sense) is shown in Figure 1 and is given by

$$\tau_{*c} = 0.15 S^{0.25} \qquad (3)$$

The data are separated according to the environment where they were collected: laboratory flumes or natural streams (field). Both data sets appear to have a similar magnitude and trend of τ_{*c} with channel slope. There is an obvious lack of data for $S < 10^{-3}$ and $S > 10^{-1}$, the former is likely due to the bed being sand covered in natural rivers (i.e., $\mathrm{Re}_p \leq 10^2$).

The scatter in the data probably is due to differences in friction angles, drag from channel walls and morphologic structures on the bed, sediment shapes, and size distributions. In addition, there is variability in the criteria for defining incipient motion

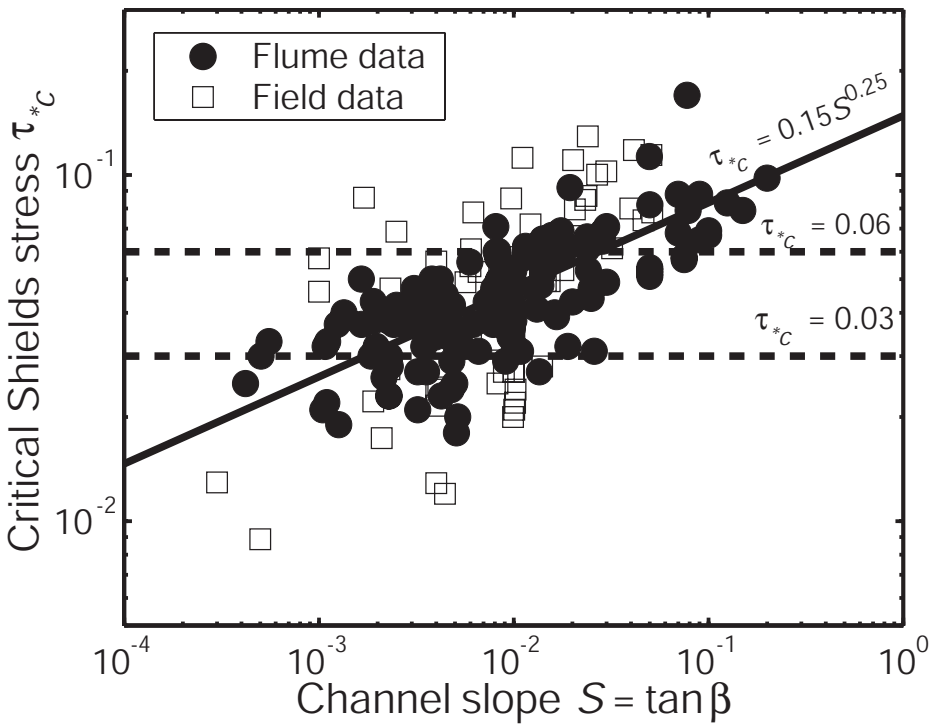

Figure 1. Compilation of previously published data showing the slope dependency of the critical Shields stress. τ_{*c} is used here generically, where in actuality most of the data are based on the total stress (i.e., τ_{*cT}) and some of these are corrected for wall drag (i.e., τ_{*cTR}). The best-fit line in a least square sense is given by $\tau_{*c} = 0.15S^{0.25}$ with an r-square value of 0.41. Also shown are the typical upper $\tau_{*c} = 0.06$ and lower values $\tau_{*c} = 0.03$ assumed for a gravel bed. The data have been filtered so that $Re_p > 10^2$. Data sources include *Buffington and Montgomery* [1997], *Shvidchenko and Pender* [2000], and *Mueller et al.* [2005]. Data sources previously compiled by *Buffington and Montgomery* [1997] include: *Gilbert* [1914], *Liu* [1935], *USWES* [1935], *Ho* [1939], *Meter-Peter and Mueller* [1948], *Neill* [1967], *Paintal* [1971], *Everts* [1973], *Ashida and Bayazit* [1973], *Fernandez Luque and van Beek* [1976], *Mizuyama* [1977], *Bathurst et al.* [1979], *Day* [1980], *Dhamotharah et al.* [1980], *Parker and Klingeman* [1982], *Ikeda* [1982], *Carling* [1983], *Bathurst et al.* [1984], *Bathurst et al.* [1987], *Diplas* [1987], *Graf and Suszka* [1987], *Hammond et al.* [1987], *Wilcock* [1987], *Ashworth and Ferguson* [1989], *Parker* [1990], *Komar and Carling* [1991], *Ashworth et al.* [1992], *Wilcock and McArdell* [1993], *Ferguson* [1994] and *Wathen et al.* [1995]. In addition, the data set includes the data of *Milhous* [1973] previously compiled and analyzed by *Komar* [1987], *Wilcock and Southard* [1988], *Komar and Carling* [1991] and *Wilcock* [1993], as well as the data of *Hammond et al.* [1984] previously compiled by *Komar* [1987].

[*Buffington and Montgomery*, 1997]. This notwithstanding, the trend of increasing τ_{*c} with *S* is significant despite the fact that the data have not been corrected to account for these effects. The remainder of the chapter is devoted to explaining the overall trend in the data by balancing forces about a particle.

5.3. Force Balance Model

In stream flow, the buoyancy force F_B, lift force F_L, and drag force F_D act to mobilize particles, while the force due to gravity F_G holds particles in place (Figure 2) [e.g., *Wiberg and Smith*, 1987a]. Initial particle motion occurs when these forces are balanced (in the coordinate system parallel to the stream bed), i.e.,

$$F_D + (F_G - F_B)\sin\beta = [(F_G - F_B)\cos\beta - F_L]\tan\phi_0 \qquad (4)$$

where ϕ_0 is the friction angle between grains and β is the bed-slope angle ($S \equiv \tan\beta$). In this model, we neglect the possibility that particles might move due to undermining. In equation (4), F_B is taken to be in the vertical direction, rather than perpendicular to the water surface as is sometimes assumed [*Mizuyama*, 1977; *Christensen*, 1995], based on the discussion of *Chiew and Parker* [1995]. We define the forces acting on a particle as follows:

$$F_D = \frac{1}{2} C_D \rho \langle u^2 \rangle A_{xs} \qquad (5)$$

$$F_L = \frac{1}{2} C_L \rho \left\langle u^2 \right\rangle A_{xs} \tag{6}$$

$$F_B = \rho g V_{ps} \tag{7}$$

$$F_G = \rho_s g V_p \tag{8}$$

where C_D and C_L are the drag and lift coefficients, respectively. V_p is the total volume of the particle. In this derivation, we allow for the fact that a portion of the particle might be emergent from the flow at incipient motion. Thus, A_{xs} is the cross-sectional area of the particle that is perpendicular to and exposed to the flow. A_{xs} does not include any portion of the particle that is emergent from the flow or within the zero-velocity region near the bed [*Kirchner et al.*, 1990]. Likewise, V_{ps} is the submerged volume of the particle and equals V_p only if the particle is fully submerged. $\left\langle u^2 \right\rangle$ is local velocity squared and spatially averaged over A_{xs}. Equations (5) – (8) can be combined and rearranged in terms of a critical Shields stress as,

$$\tau_{*cg} = \frac{u_*^2}{rgD} = \frac{2}{C_D} \frac{u_*^2}{\left\langle u^2 \right\rangle} \cos\beta \left(\frac{\tan\varphi_0 - \tan\beta}{1 + (F_L / F_D)\tan\phi_0} \right) \left[\frac{V_p}{A_{xs} D} \frac{1}{r} \left(\frac{\rho_s}{\rho} - \frac{V_{ps}}{V_p} \right) \right]. \tag{9}$$

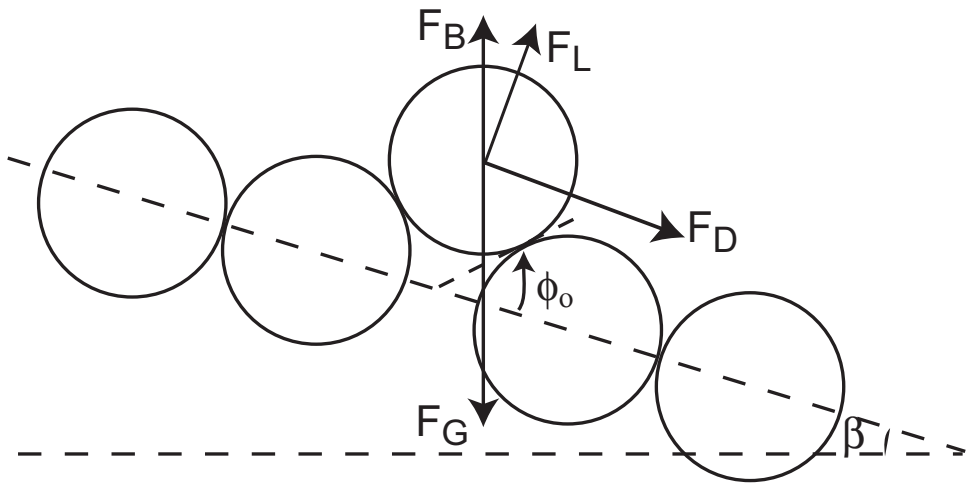

Figure 2. Force balance on a grain (modified from *Wiberg and Smith* [1987a]). F_B, F_L, F_D and F_G are the forces due to buoyancy, lift, drag and gravity, respectively. ϕ_0 is the friction angle and β is the bed-slope angle.

Equation (9) is identical to the formula derived by *Wiberg and Smith* [1987a] except for the term in the brackets, which accounts for grain emergence and is equal to a constant (i.e., a grain-shape factor) for a fully submerged particle.

Equation (9) has been written in terms of the portion of shear stress that acts on the sediment grains τ_g. In practice, the Shields stress more often is calculated from laboratory or field measurements of the total driving stress at the bed τ_T, which is a sum of the stress spent on the channel walls τ_w, bed morphology τ_m, and the particles of interest on the bed τ_g [e.g., *Einstein and Barbarossa*, 1952; *Vanoni and Brooks*, 1957; *Smith and McLean*, 1977], i.e.

$$\tau_T = \tau_g + \tau_m + \tau_w . \tag{10}$$

Note that we use the term *morphologic drag* (i.e., τ_m) to describe the portion of the total stress spent on collections of particles and other bed morphologic structures that are larger than the individual grain scale. *Morphologic drag* is used instead of the more common term *form drag* because each individual component of stress in equation (10) (i.e., τ_g, τ_m and τ_w) can result from a combination of viscous skin-friction stresses and form-drag stresses [e.g., *McLean and Nikora*, 2006], although form drag dominates for high roughness Reynolds numbers. For steady and uniform flow conditions, the total stress at the bed can be calculated from

$$\tau_T = \rho g h \sin\beta . \tag{11}$$

In practice, the low-slope approximation of $\sin\beta \approx \tan\beta \equiv S$ is often employed. By combining equations (1) and (9)-(11), we formulate a version of the critical Shields stress τ_{*cT} that incorporates both the total stress and the low-slope approximation as

$$\tau_{*cT} = \frac{hS}{rD} = \frac{2}{C_D}\frac{u_*^2}{\langle u^2 \rangle}\left(\frac{\tau_T}{\tau_T - \tau_m - \tau_w}\right)\left(\frac{\tan\phi_0 - \tan\beta}{1 + (F_L / F_D)\tan\phi_0}\right)\left[\frac{V_p}{A_{xs}D}\frac{1}{r}\left(\frac{\rho_s}{\rho} - \frac{V_{ps}}{V_p}\right)\right] \quad (12)$$

As can be seen by inspection of equation (12), the term $\tan\beta$ will cause τ_{*cT} to decrease with increasing channel slope, which is counter to the observations (Figure 1). This indicates that, for a given particle size *D*, at least one of the other variables in equation (12) must depend on channel slope or flow depth *h* in such a way that produces increasing τ_{*cT} with increasing channel slope. Below, several of the terms in equation (12) are considered.

5.4. Potential Slope Dependent Effects

In this section wall drag, drag from morphologic structures on the bed, variable friction angles, grain emergence, air entrainment, variable drag and lift coefficients, the local vertical-velocity profile, and the structure of turbulent velocity fluctuations are considered as potential causes for the slope dependency of τ_{*cT}. In Section 5.5, these effects are quantified and incorporated into the force balance (equation 12) to assess their importance on incipient motion.

5.4.1. Wall Drag

Wall drag (τ_w) is the portion of the driving stress that is spent on the channel banks. In rectangular channels where the channel bed and walls are equally rough, the wall drag can be calculated from $\tau_w = (2h/w)\tau_g$ [*Vanoni and Brooks,* 1957]. Thus, wall drag becomes important for channels with small width-to-depth ratios. For this case, a critical Shields number that incorporates wall drag τ_{*cTR} can be written by substituting $\tau_w = (2h/w)\tau_g$ and equation (10) into equation (12) and rearranging, as

$$\tau_{*cTR} = \frac{RS}{rD} = \frac{2}{C_D}\frac{u_*^2}{\langle u^2 \rangle}\left(\frac{\tau_T}{\tau_T - \tau_m}\right)\left(\frac{\tan\phi_0 - \tan\beta}{1 + (F_L/F_D)\tan\phi_0}\right)\left[\frac{V_p}{A_{xs}D}\frac{1}{r}\left(\frac{\rho_s}{\rho} - \frac{V_{ps}}{V_p}\right)\right] \quad (13)$$

where the hydraulic radius is $R = wh/(w+2h)$. Note that this formulation for the wall drag should not be used when the wall roughness is substantially different than that on the bed. For example, in flume experiments with smooth walls, τ_w will be much smaller [*Johnson*, 1942; *Houjou et al.*, 1990].

Neglecting wall corrections could result in a slope-dependent critical Shields stress if the width-to-depth ratios of flows at incipient motion decrease or the roughness of the channel walls relative to the bed increase with channel slope. The former is likely true in natural channels where the bank-full width-to-depth ratio tends to be inversely related to channel slope [e.g., *Parker et al.*, in press]. This notwithstanding, a partial or full wall correction (see *Buffington and Montgomery* [1997] for discussion) has been applied to the much of the data presented in Figure 1 (e.g., *Gilbert* [1914], *Liu* [1935], *USWES* [1935], *Meter-Peter and Mueller* [1948], *Neill* [1967], *Paintal* [1971],

Everts [1973], *Ashida and Bayazit* [1973], *Fernandez Luque and van Beek* [1976], *Ikeda* [1982], *Mizuyama* [1977], *Bathurst et al.* [1987], *Graf and Suszka* [1987], *Wilcock* [1987], *Ashworth and Ferguson* [1989], *Ashworth et al.* [1992], *Wilcock* [1993], *Wilcock and McArdell* [1993], *Shvidchenko and Pender* [2000]). Moreover, many of these individual studies show a slope-dependent critical Shields stress (e.g., *Ashida and Bayazit* [1973], *Mizuyama* [1977], *Bathurst et al.* [1987], *Graf and Suszka* [1987], *Shvidchenko and Pender* [2000]). Therefore, other factors besides wall drag must be responsible for the slope-dependent critical Shields stress.

5.4.2. Bed Morphology and Friction Angles

Changes to the bed morphology with channel slope might affect the incipient motion criteria given by equation (12) through variations in the stress borne on morphologic structures (τ_m), friction angles (ϕ_0), or both. It is common to assume that the trend of increasing critical Shields stress with slope is due to an increase in drag caused by morphologic structures on the bed (τ_m) [*Buffington and Montgomery*, 1997; *Mueller et al.*, 2005; *Lenzi et al.*, 2006; *Parker et al.*, in press]. The stress spent on morphologic structures usually is dominated by form drag due to flow separation, wakes, and secondary currents caused by particle clusters [*Brayshaw et al.*, 1983; *Hassan and Reid*, 1990], stone cells [*Church et al.*, 1998; *Hassan and Church*, 2000], bars [*Parker and Peterson*, 1980; *Millar*, 1999], woody debris [*Braudrick and Grant*, 2000; *Manga and Kirchner*, 2000], immobile or protruding particles [*Wiberg and Smith*, 1991; *Nelson et al.*, 1991; *Millar*, 1999; *Yager et al.*, 2007] or step-pools [*Bathurst*, 1985; *Aberle and Smart*, 2003; *Wilcox et al.*, 2006].

The magnitude of form drag due to flow separation in turbulent flow is proportional to the size and concentration of the roughness elements, and the square of the local flow velocity about the elements [e.g., *Batchelor*, 1967; *Smith and McLean*, 1979]. Thus, the hypothesized increase in morphologic drag on steeper slopes could be due to changes in the bed morphology that increase roughness. For example, if the size or concentration of morphologic structures on the channel bed increase with increasing channel slope, then this could cause greater morphologic drag (τ_m) and larger τ_{*cT} on steeper slopes (equation 12). These effects are undoubtedly important in natural streams [*Millar*, 1999; *Buffington et al.*, 2004], but are not important in flume experiments where the same sediment of near-uniform size was used on different slopes, and the sediment beds were leveled before each experiment.

In addition to morphologic drag, systematic changes in the friction angle ϕ_0 with increasing channel slope also might be responsible for the trend in τ_{*c} with slope. Variations in friction angles can occur in natural streams because of differences in shapes, orientations, and sorting of the supplied sediment [*Kirchner et al.*, 1990; *Buffington et al.*, 1992; *Johnston et al.*, 1998; *Armanini and Gregoretti*, 2005]. The morphologic structures described above could cause larger ϕ_0 if grains form more stable patterns [*Brayshaw et al.*, 1983; *Hassan and Church*, 2000; *Church and Hassan*, 2002]. In addition, bimodal size distributions (e.g., sand and gravel) can have a smoothing effect by reducing friction angles and consequently τ_{*cT} [*Wilcock*, 1998; *Wilcock and Crowe*, 2003], and sand might be more prevalent in lower sloping rivers. Nonetheless, like morphologic drag, a systematic increase in friction angles with

channel slope is an unlikely result for flume experiments where the sediment mixture was held constant at different channel slopes.

Since variations in morphologic structures and friction angles with channel slope are deemed unimportant in flume experiments, a comparison between flume and field data allows for the assessment of these effects in natural streams. Surprisingly, there is no distinct difference in either the magnitude of τ_{*c} or the trend with channel slope between field and flume data (Figure 1). It is possible that there is some effect of increasing morphologic drag or friction angles for $S > 0.02$ as much of the field data plot above the regression line for these slopes. The field data, however, are also more scattered than the flume data, which could be due to more variable morphologic drag in the field (or other effects discussed above). Nonetheless, like the flume data, it seems reasonable to conclude that morphologic drag and variable friction angles are not primarily responsible for the observed slope dependency in the field.

5.4.3. Grain Emergence

One obvious effect that would cause reduced mobility with increasing slope is grain emergence [*Graf*, 1979]. As a particle emerges from the flow, both the area of the particle that is exposed to the flow A_{xs} and the buoyancy force on the particle are reduced, which results in reduced mobility with increasing slope. This can be seen in the term $\left[\frac{V_p}{A_{xs}D}\frac{1}{r}\left(\frac{\rho_s}{\rho}-\frac{V_{ps}}{V_p}\right)\right]$ in equation (12), which becomes large with particle emergence. This, however, cannot fully explain the observed trend because a slope-dependent Shields criterion has been documented for $S < 10^{-2}$ when grains were well

submerged (Figure 1) [*Shvidchenko and Pender*, 2000]. At incipient motion, particles typically are not emergent from the flow for $S < \sim 10^{-1}$ [*Ashida and Bayazit*, 1973].

5.4.4. Air Entrainment

To our knowledge, *Wittler and Abt* [1995] were the first to suggest that aeration would result in reduced mobility with increasing channel slope due to a reduction in the density of the water-air mixture. Aeration also can affect the mean flow velocity and the corresponding bulk friction factor [*Straub et al.*, 1954; *Straub and Lamb*, 1956; *Chanson*, 2004]. The mean flow velocity increases with increased aeration because of reduced drag, so it is probable that these two effects offset one another when assessing the drag force on a particle. Due to the lack of data, only reduced fluid density with aeration is considered here.

From continuity, the density of the air-water mixture ρ can be written as

$$\rho = \rho_w (1 - c_a) \tag{14}$$

where ρ_w is the density of water, c_a is the volumetric concentration of air, and the mass of air is assumed negligible. The equilibrium concentration of air in open-channel flow has been shown to be a strong function of channel slope. *Chanson* [1994] fit the relationship

$$c_a = 0.9 \sin \beta \tag{15}$$

to experimental data [*Straub and Anderson*, 1958; *Aivazyan*, 1987] and suggested that the relationship is independent of flow discharge, velocity, and channel roughness. Nonetheless, equation (15) probably underestimates the air concentration in natural streams because it does not take into account large roughness elements that can enhance mixing. For example, air concentrations of 0.1 to 0.4 have been measured in the wake of a hydraulic jump in a natural stream with a reach-averaged bed slope of about 0.04 [*Valle and Pasternack*, 2006]. Equation (15) only predicts an air concentration of 0.036 for the same slope.

Stream aeration appears to be a plausible mechanism for an increase in τ_{*c} with increasing channel slope. Equations (14) and (15) indicate that the fluid density would decrease with increasing channel slope due to aeration. A reduction in fluid density decreases the drag on the particles and the buoyancy force, which both increase particle stability (equation 12). As will be shown in Section 5.5, however, aeration cannot fully explain the observed slope dependence of the critical Shields criterion because significant aeration only occurs for steep slopes.

5.4.5. Drag and Lift Coefficients

The drag coefficient C_D is typically thought to be independent of channel slope, with a constant value of about 0.4 to 0.5 for large particle Reynolds numbers based on the settling velocity of spheres [*Schlichting*, 1979]. Direct measurements using a force transducer suggest that this is an underestimate and that $C_D \cong 0.9$ [*Nelson et al.*, 2001; *Schmeeckle et al.*, 2007]. Very few studies have measured C_D under shallow flows or on steep slopes. One notable exception is the study of *Flammer et al.* [1970], which

showed that drag can increase by an order of magnitude for shallow flows due to back-water effects and an associated pressure differential across a particle referred to as *wave-drag*. Later experiments have confirmed this trend [*Lawrence*, 2000; *Carling et al.*, 2002]. Unfortunately, these relationships are difficult to incorporate into a force balance because C_D was measured as a function of the depth-averaged velocity rather than the local velocity around the grain. Because the depth-averaged velocity is a function of the relative roughness k_s / h and the local velocity about the grains is not (as discussed in Section 5.1), these measurements might falsely indicate increasing C_D with increasing relative roughness. Caution also should be used when applying these results to natural settings because the measurements were often made on isolated particles in an otherwise flat flume bed. Particles, when isolated, provide a more significant obstacle to the flow than for a packed sediment bed, and therefore might produce a larger pressure differential. If the wave-drag hypothesis is correct, incorporating the additional pressure differential would produce deceasing τ_{*c} with increasing slope, which is opposite of the observed trend (Figure 1). Therefore, this cannot be the mechanism for increasing τ_{*c} with channel slope.

Several studies have pointed to the fact that C_D might have a particle Reynolds number dependence even for large $\mathrm{Re_p}$ where τ_{*c} is thought to be Reynolds-number independent. For isolated spheres with $\mathrm{Re_p} > 10^5$, C_D is known to decrease from 0.5 to about 0.2, which is deemed the *drag crisis* [*Schlichting*, 1979; *Shen and Wang*, 1985]. *Shvidchenko and Pender* [2000] showed that τ_{*c} decreased with increasing $\mathrm{Re_p}$ (for constant *S*) even for $10^2 < \mathrm{Re_p} < 10^5$. Figure 3 shows the incipient motion data

stratified according to Re_p. There might be a slight trend of increasing τ_{*_c} with increasing Re_p, but this is due to the dependence of Re_p on S and should not be considered important. Looking at the variation in τ_{*_c} along lines of equal slope, there does not appear to be a significant Reynolds number dependence. There are no data for $Re_p > 10^5$, such that the effect of the drag crises cannot be determined.

Little work has been done on measuring the lift coefficient, especially in steep streams with low particle submergence. Recent direct measurements indicate that lift does not scale with the velocity difference across a grain [*Nelson et al.*, 2001; *Schmeeckle et al.*, 2007], which is inconsistent with expectations of flow according to the Bernoulli principle. It seems possible that lift forces might become less important when grains emerge from the flow, although pressure fluctuations within a porous bed can still cause lift on emergent particles [*Smart*, 2005; *Vollmer and Kleinhans*, 2007]. The lack of data and theory make it difficult to incorporate lift into a force balance at present [*Nelson et al.*, 2001; *Schmeeckle and Nelson*, 2003; *Schmeeckle et al.*, 2007].

5.4.6. Structure of Average Flow Velocity

The remaining process that could be responsible for the decrease in mobility with increasing slope is the structure of the local flow velocity, i.e. u/u_* in equation (12). The double-averaged component of the flow velocity $\bar{u}$ (i.e., averaged in time and space [e.g., *McLean and Nikora*, 2006]) is considered here and turbulent fluctuations are discussed in Section 5.4.7. The flow velocity $\bar{u}$ is typically described as varying logarithmically near the bed [*Schlichting*, 1979],

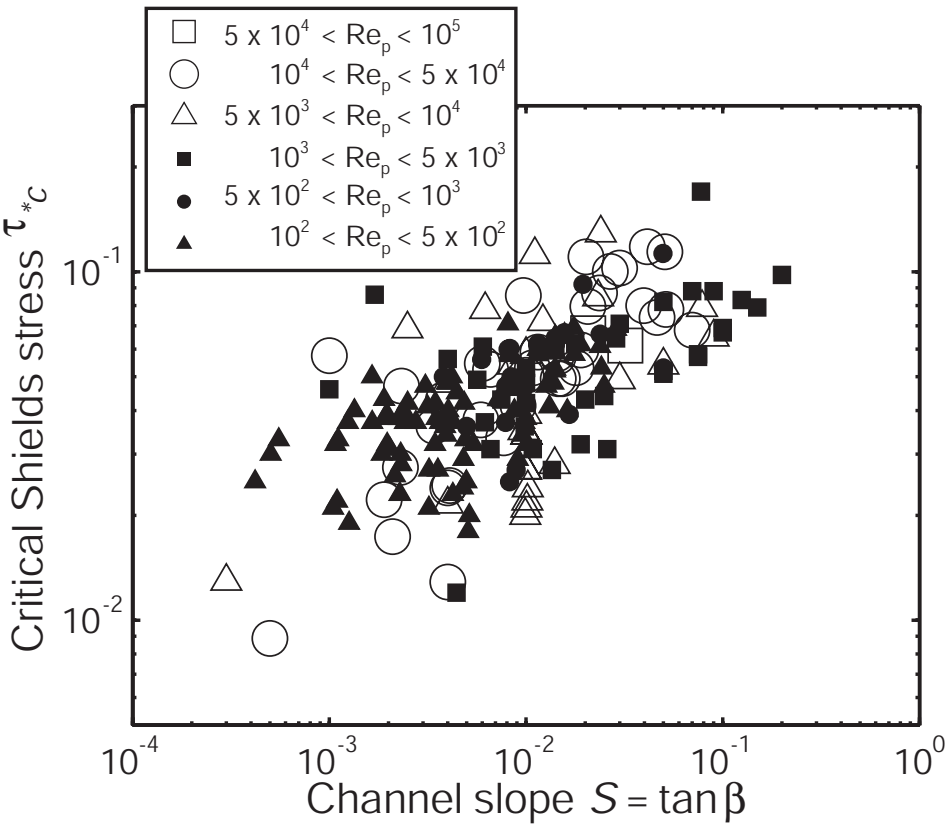

Figure 3. Incipient motion data from Figure 1 stratified according to particle Reynolds number Re_p.

$$\frac{\bar{u}(z)}{u_*} = \frac{1}{\kappa}\ln\left(\frac{z}{z_0}\right) \qquad (16)$$

where z is the height above the bed, κ is von Karman's constant of 0.41, and $z_0 = k_s/30$ for hydraulically rough flow [*Nikuradse*, 1933]. There is no total depth (h) dependency in equation (16), hence the local velocity is predicted to be independent of relative roughness k_s/h and channel slope for a given shear stress (Figure 4). For example, given a constant roughness height k_s and total shear stress, an increase in the flow depth is predicted to have no effect on the velocity at any location above the bed. This is the basis for the conclusion by many [e.g., *Yalin*, 1977] that incipient motion does not depend on the relative roughness.

Equation (16), however, is a poor predictor of the velocity around particles. Within the so-called *roughness layer*, the flow around sediment particles is strongly 3-D and influenced by wakes shed by grains [*Nowell and Church*, 1979; *Schmeeckle and Nelson*, 2003]. A unified theory does not yet exist for velocity profiles in the roughness layer, but observations in mountain streams have shown that the velocity profile can deviate strongly from logarithmic [e.g., *Byrd and Furbish*, 2000; *Wohl and Thompson*, 2000].

Some authors have suggested that, for the same bed shear stress, an increase in relative roughness causes a decrease in flow velocity around bed particles [e.g., *Ashida and Bayazit*, 1973; *Bayazit*, 1978; *Graf*, 1991; *Shvidchenko and Pender*, 2000; *Vollmer and Kleinhans*, 2007]. This hypothesis is partially supported by the experiments of

Chiew and Parker [1994]. They measured the conditions of incipient motion on variable slopes in a sealed duct and were thus able to vary slope while holding the relative roughness constant. Contrary to the open-channel experiments in Figure 1, *Chiew and Parker* [1994] showed that τ_{*_c} *decreased* with increasing channel slope due to the increased gravitational component in the downstream direction. These experiments, therefore, indicate that the observed increase in τ_{*_c} with increasing slope in open-channel flow is fundamentally due to the coincident increase in relative roughness (for the same boundary shear stress and particle size), although lack of aeration also might have been a factor.

There are several 1-D models for flow velocity within roughness elements, drawing largely on atmospheric boundary layer studies [e.g., *Raupach et al.,* 1991] or flow through vegetation [e.g., *Lightbody and Nepf*, 2006]. *Katul et al.* [2002] suggested a hyperbolic tangent function, but their relationship is only valid for $h > D$ because the inflection point at $z = D$ must be specified. *Nikora et al.* [2001; 2004] and *McLean and Nikora* [2006] have suggested constant, linear, and exponential velocity profiles within the roughness layer, based on different scaling arguments utilizing the double-averaged equations of motion. All of these models, however, predict a local velocity that is independent of relative roughness, which is contrary to available data [*Bayazit*, 1975; *Tsujimoto*, 1991]. Thus, applying these models to incipient particle motion would not result in the observed slope-dependent critical-Shields stress.

Relative roughness might affect velocity profiles by 1) reducing the stress borne by the fluid due to particle-induced form drag or 2) by changing the deformability of the fluid (i.e., its eddy viscosity) for a given bed stress. For example, the models of *Wiberg*

and Smith [1987b; 1991] and *Nelson et al.* [1991] considered both of these effects. These models showed that particle-induced form drag does affect local velocity profiles, and for a given total stress, form drag is a function of the bed roughness-length scale k_s as well as the concentration of roughness elements. Nonetheless, the models also suggest that for a given k_s, particle-induced form drag is not a function of flow depth, relative roughness or channel slope. We emphasize here that *flow resistance* is not equivalent to *particle form drag*. Flow resistance is a non-dimensional quantity that relates the depth-averaged flow velocity to the shear velocity, as in the Manning-Strickler and Darcy-Weisbach flow-resistance relations, and it necessarily is a function of (k_s / h) because the flow velocity is integrated over the total depth. Particle form drag, on the other hand, is a force due to pressure differentials about particles from wakes, and it scales with the local velocity around the particles [*Batchelor*, 1967], not the depth-averaged velocity. For simplicity, and because particle form drag appears to be independent of slope and k_s / h (for the same total shear stress), a particle-form-drag correction for the local flow velocity [e.g., *Wiberg and Smith*, 1991] is not attempted here.

The second way that relative roughness might affect the local flow velocity is through changes in fluid deformation (i.e., eddy viscosity) induced by mixing from wakes shed by particles. To explore this effect, we formulate a simple and plausible expression for the flow velocity within the roughness layer based on a mixing-length that is a function of bed roughness. The vertical structure of flow velocity in steady and uniform open-channel flow can be derived from an eddy viscosity approach [*Schlichting*, 1979] as

$$\tau(z) = \rho u_*^2\left(1-\frac{z}{h}\right) = \rho L^2\left(\frac{d\bar{u}}{dz}\right)^2 = \rho u_* L\frac{d\bar{u}}{dz} \qquad (17)$$

where L is the mixing length. This statement for the fluid shear stress uses the Boussinesq hypothesis that $\tau(z) = \rho\varepsilon\, d\bar{u}/dz$ and assumes that the eddy viscosity (ε) can be approximated from the product of local turbulent velocity and length scales (i.e., $u_* L$). The parameterization of the total stress as $\tau(z) = \rho u_*^2\left(1-\frac{z}{h}\right)$ is valid for an impermeable bed, but is an approximation near a sediment bed [*McLean and Nikora*, 2006].

Typically, the mixing length is set to

$$L = \kappa z\left(1-\frac{z}{h}\right), \qquad (18)$$

which, when combined with equation (17), yields the well-known logarithmic velocity profile given by equation (16). Inspection of equations (17) and (18) reveals that the depth dependencies (i.e., the term $(1-z/h)$) cancel when these equations are combined resulting in a self-similar velocity profile (equation 16) that is independent of relative roughness (Figure 4).

In the near-bed region, mixing instead should be dominated by wakes shed by the particles [*Lopez and Garcia*, 1996; *Nikora et al.*, 2001; *Defina and Bixio*, 2005]. Within the roughness layer it is appropriate to define the mixing length as

$$L = \alpha_1 k_s \,, \tag{19}$$

where α_1 is a constant of proportionality that is likely less than unity [*Schlichting*, 1979; *Wiberg and Smith*, 1987b; *Nelson et al.*, 1991; *Wiberg and Smith*, 1991]. Combining equation (17) and (19) and integrating, results in a quadratic velocity profile,

$$\frac{\bar{u}}{u_*} = \frac{z}{\alpha_1 k_s}\left(1 - \left(\frac{z}{2k_s}\frac{k_s}{h}\right)\right) \tag{20}$$

where the no-slip boundary condition $\bar{u}(z = 0) = 0$ has been applied. Note that applying a no slip condition at z_0 rather than z = 0 does not yield a significant difference in our model predictions. The coefficient was found to be α_1 = 0.12 by matching equations (16) and (20) at $z = k_s$ and assuming deep flow ($h >> k_s$). This value is similar to those proposed previously for equation (19) (e.g., 0.18: *Schlichting* [1979] and *Nelson et al.* [1991]; 0.41: *Wiberg and Smith* [1991]).

Equation (20) should hold only in the roughness layer and above this region a more appropriate velocity profile would be logarithmic. In addition, equation (20) might be invalid for $h < k_s$, because the dominant mixing length is likely smaller than k_s if particles are emergent from the flow. To our knowledge, no studies have measured the mixing length or the velocity profile in emergent gravel. For simplicity, we assume

that equation (20) is valid within the roughness layer ($z < k_s$) for all values of relative roughness (k_s / h).

By using a constant mixing length (i.e., one that does not vary linearly with $(1 - z/h)$), the local velocity about the grains (equation 20) is now predicted to depend on relative roughness k_s / h. For deep flow (small relative roughness), the quadratic profile is near linear within the roughness layer and matches the logarithmic profile at $z = k_s$ (Figure 4) This linear profile is consistent with the measurements of *Dittrich and Koll* [1997] and *Nikora et al.* [2001], the later of which are shown for the case k_s / h = 0.156 (Figure 4). The data do not support the logarithmic profile. For shallow flow, the quadratic profile predicts slower flow velocity than the logarithmic profile, especially near the top of the roughness layer. The logarithmic profile, on the other hand, is self-similar for all values of relative roughness, such that they plot on the same curve (Figure 4). Unfortunately, owing to the difficulty of measurements within the roughness layer, we know of no other data to test the model. The model is consistent, however, with the measurements of *Bayazit* [1975] that showed that flow velocity near the top of the roughness elements systematically decreases with increasing relative roughness.

Note that the change in local velocity as a function of relative roughness predicted by equation (20) will necessarily produce a change in particle form drag, since form drag depends on the local velocity [e.g., *Wiberg and Smith*, 1991]. Nonetheless, this is an indirect effect and the dependency of local-flow velocity on relative roughness appears to be due to changes in the eddy viscosity for a given bed stress, and not due to a reduction in stress due to increased form drag.

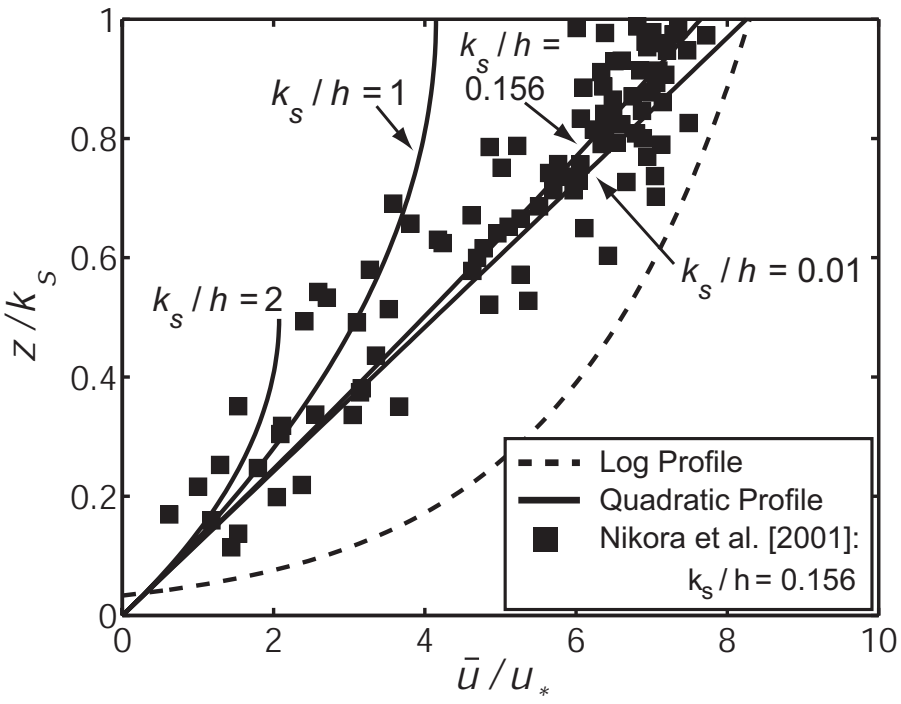

Figure 4. Velocity predictions for a logarithmic profile (equation 16) and the quadratic profile (equation 20) for different cases of relative roughness k_s / h. The height above the bed z is non-dimensionalized by the bed-roughness length scale k_s. The stream-wise velocity $\bar{u}$ is non-dimensionalized by the shear velocity u_*. The black squares are experimental measurements, which we have digitized from Figure 4b of *Nikora et al.* [2001]. In their original figure many data points overlap where $z / k_s > 0.5$, such that we have under sampled their data in this region. Note that the log profile is independent of k_s / h.

5.4.7. Turbulent Fluctuations

Many studies have shown that the local average velocity $\bar{u}$ is not the only relevant velocity scale in determining sediment mobility and, in addition, the fluctuations due to turbulence should be considered [e.g., *Grass*, 1970; *Jackson*, 1976; *Bayazit*, 1978; *Best*, 1992; *Chang*, 1998; *Sechet and Le Guennec*, 1999; *Papanicolaou et al.*, 2002; *Schmeeckle and Nelson*, 2003; *Zanke*, 2003; *Wu and Yang*, 2004; *Hofland et al.*, 2005; *Cheng*, 2006; *Vollmer and Kleinhans*, 2007], particularly in steep streams where the velocity profile is not logarithmic [*Furbish*, 1993; *Furbish*, 1998; *Furbish et al.*, 1998; *Byrd and Furbish*, 2000]. Of importance for bedload transport are outward interactions generated from wakes shed by roughness elements [*Nelson et al.*, 1995; *Papanicolaou et al.*, 2001] and downward-directed inrushes of high momentum fluid that contribute to the Reynolds stress (i.e., sweeps) [*Sutherland*, 1967; *Nakagawa et al.*, 1980; *Drake et al.*, 1988; *Best*, 1992]. The frequency of sweep events scale with the depth-averaged flow velocity and flow depth [*Rao et al.*, 1971; *Nezu and Nakagawa*, 1993; *Shvidchenko and Pender*, 2001; *Marquis and Roy*, 2006] (i.e., outer scaling), rather than the inner parameters of kinematic viscosity and shear velocity. In addition to turbulent fluctuations within the flow, pressure fluctuations within the pore fluid of the bed are important in inducing sediment motion [*Smart*, 2005; *Vollmer and Kleinhans*, 2007].

The intensity of turbulent fluctuations (i.e., σ_u / u_* where σ_u is the root-mean square of stream-wise velocity) varies with height above the bed and has a peak value near the bed in hydraulically smooth flow, or near the top of the roughness elements in hydraulically rough flow [*Raupach et al.*, 1991; *Nikora and Goring*, 2000]. This peak

value (i.e., $\sigma_{u,\max}/u_*$) has been called a "universal constant" [*Nezu and Nakagawa*, 1993] and typical values range from 2.2 to 2.8. Most studies, however, have focused on small relative roughness, i.e., $h >> k_s$ [*Kironoto and Graf*, 1994; *Song et al.*, 1994; *Wang and Dong*, 1996; *Nikora and Goring*, 2000; *Tachie et al.*, 2000; *Tachie et al.*, 2004; *Wu and Yang*, 2004] or hydraulically smooth beds [e.g. *Nezu and Rodi*, 1986]. We are aware of only four studies that have measured $\sigma_{u,\max}/u_*$ for a wide range of relative roughness [*Bayazit*, 1975; *Wang et al.*, 1993; *Dittrich and Koll*, 1997; *Carollo et al.*, 2005]. These studies show that $\sigma_{u,\max}/u_*$ is not a universal constant, but instead increases as depth increases relative to the roughness-length scale of the bed.

Figure 5 shows a compilation of $\sigma_{u,\max}/u_*$ for a wide range of relative roughness. Most of the data are from studies that were not designed for the purpose of assessing the effect of relative roughness on turbulence intensity. Instead, most workers showed vertical profiles σ_u/u_* for a limited range of relative roughness. We digitized these vertical profiles and extracted the peak near-bed value of σ_u/u_* for each experiment. The resultant data clearly show that the peak value in the turbulence intensity increases with decreasing relative roughness k_s/h. Figure 5 does not include data from the numerous studies that have measured $\sigma_{u,\max}/u_*$ for hydraulically smooth flow. Most data for smooth beds, however, range from about 2.2 to 2.8 (as indicated by dashed lines on Figure 5) [e.g., *Nezu and Rodi*, 1986]. Almost all of the compiled data for flow over rough beds indicate smaller $\sigma_{u,\max}/u_*$ than is typical for smooth-bed flows.

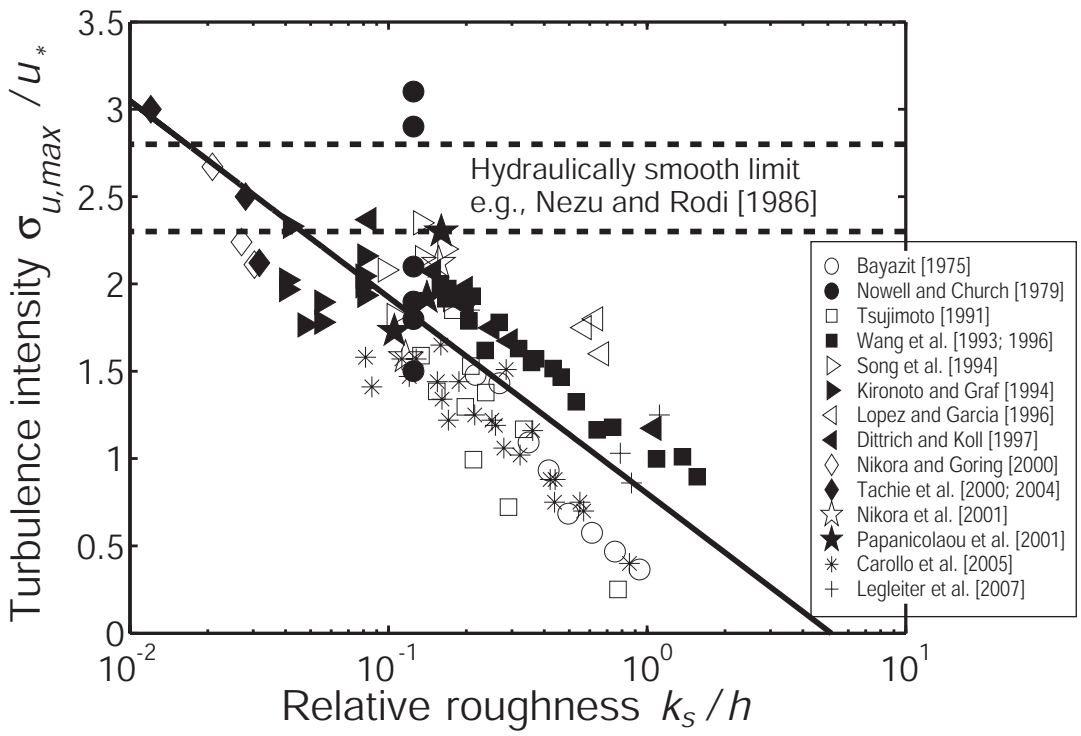

Figure 5. Near-bed peak turbulence intensity versus relative roughness. All points are data from previously published studies (see text for details). The two horizontal dashed lines represent the range in peak turbulent intensities for hydraulically smooth flow. The solid line is the model fit to the data with α_2 = 0.2 (equation 23).

The trend of increasing $\sigma_{u,\max}/u_*$ with decreasing k_s/h in Figure 5 is significant despite the fact that the data cover a wide range of roughness types including boulders and gravel in natural streams [*Nikora and Goring*, 2000; *Legleiter et al.*, 2007], and gravel, spheres, wire mesh, and square blocks in laboratory flumes. The differences in roughness type, as well as differences in the spatial concentration of roughness elements on the bed, are probably the main reasons for scatter in the data. For example, the experiments of *Nowell and Church* [1979] were designed to assess variable concentrations of roughness elements with the same roughness length-scale (Lego blocks). We made no attempt to account for the effect of roughness concentration, therefore the data of *Nowell and Church* [1979] plot as a vertical line on Figure 5, with increasing $\sigma_{u,\max}/u_*$ corresponding to lower areal roughness concentration. Their two experiments that have the largest values of $\sigma_{u,\max}/u_*$ (and are the most significant outliers on Figure 5) had roughness concentrations of only ~ 0.01 and 0.02. It is likely that the parameter k_s/h significantly overestimates the actual roughness in these experiments due to the extremely low roughness concentrations used. If a roughness concentration correction were made, these points would be shifted to the left on Figure 5 (i.e., smaller k_s/h) and would be more in line with the rest of the data.

To our knowledge, a unified model for the turbulence intensity as a function of relative roughness has yet to be proposed. We hypothesize that the reduction in turbulence intensity with increasing relative roughness is due to reduced macro-scale turbulent motions. For the same total shear stress, deeper flows are faster near the free surface, and therefore velocity fluctuations can be larger because the differential flow

velocity across the total depth is greater. Based on the evidence for scaling of turbulent sweeps to the outer-flow variables (discussed above), it seems plausible that turbulence intensity also should scale with the depth-averaged flow velocity *U*, which in turn is a function of relative roughness. We therefore propose that

$$\frac{\sigma_{u,\max}}{u_*} = \alpha_2 \frac{U}{u_*} \tag{21}$$

where α_2 is a constant of proportionality between the depth-averaged velocity and the peak near-bed turbulence intensity.

Many formulas have been proposed for the depth-averaged flow velocity of gravel-bed rivers and steep streams. One of the most widely used is that of *Bathurst* [1985],

$$\frac{U}{u_*} = 5.62 \log\left(\frac{h}{k_s}\right) + 4\,. \tag{22}$$

Combining equation (21) and (22) results in a semi-empirical model for the peak turbulence intensity

$$\frac{\sigma_{u,\max}}{u_*} = \alpha_2 \left[5.62 \log\left(\frac{h}{k_s}\right) + 4 \right], \tag{23}$$

where, based on a best fit with data in Figure 5, α_2 = 0.2. Thus, the peak turbulent fluctuations are typically 20% of the depth-averaged velocity, and decrease with increasing relative roughness.

5.4.8. Summary of Slope-Dependent Effects

In summary, there are several potential mechanisms for the observed reduction in sediment mobility with increasing slope and relative roughness. These are variations in drag from channel walls and morphologic structures on the bed, friction angles, particle emergence, air entrainment, lift and drag coefficients, and the structure of the local velocity and turbulent fluctuations. Drag from channel walls and morphologic structures, as well as friction angles, might vary with channel slope in some natural streams due to changes in channel and bed morphology, but the dependency on slope is most likely negligible in flume experiments. Since, both laboratory and field measurements show approximately the same trend in τ_{*c} with *S*, these factors alone cannot explain the data. Grain emergence and aeration are potentially important, but cannot explain the data for relatively low slopes. Lift and drag coefficients, unfortunately, are poorly known. The data that exist suggest that the drag coefficient increases with increasing slope due to backwater effects and an associated pressure differential, which would increase the mobility of particles on steeper slopes. This suggests, through a process of elimination, that the local flow velocity about the grains must decrease with increasing slope. Indeed, experimental studies have shown that, for the same bed shear stress, both the average local velocity and the magnitude of near-bed turbulent velocity fluctuations tend to decrease with increasing slope. These effects

appear to be due to variations in the vertical structure of mixing (i.e., the eddy viscosity) and large-scale turbulent motions as a result of changes in relative roughness.

5.5. Model Evaluation and Results

In order to explore the potential slope-dependent effects quantitatively, τ_{*cT} is calculated as a function of bed slope following equation (12). Equation (12) is solved using a simple iterative numerical scheme since bed slope appears on both sides of the equation. For a given total shear stress and channel slope, flow depth is solved from equation (11). The ratio of the lift force to the drag force is set to F_L/F_D = 0.85 [*Chepil*, 1958; *Wiberg and Smith*, 1987a]. Since much of the data in Figure 1 have been corrected for wall drag, we set τ_w = 0 in equation (12), which makes equations (12) and (13) equivalent (i.e., $\tau_{*cT} = \tau_{*cTR}$). The component of the total stress spent on drag from morphologic structures (τ_m) initially is set to zero for simplicity, since it is unlikely to contribute to a slope dependence as discussed in Section 5.4.2. The sensitivity of the model to morphologic drag is discussed in Section 5.7. The submerged specific density of sediment is set to r = 1.65 for siliceous material. The friction angle is initially set to 60˚ for the case of $D \cong k_s$ [*Wiberg and Smith*, 1987a]. The sensitivity to different friction angles and a heterogeneous grain-size distribution are considered in Section 5.6. Only coarse sediment is considered, so that viscous effects are neglected and C_D = 0.9 [*Nelson et al.*, 2001; *Schmeeckle et al.*, 2007]. Spherical particles are assumed, and the cross-sectional area of the particle that is exposed to the flow A_{xs} and the submerged volume of the particle V_{ps} are given in Appendix 1. First we discuss the baseline log-

profile model and then systematically include particle emergence, flow aeration, the quadratic velocity profile, and turbulent fluctuations.

5.5.1. Baseline Log-Profile Model

Initially, equation (12) is solved by neglecting all of the slope-dependent effects discussed above and therefore is similar to the model presented by *Wiberg and Smith* [1987a]. The logarithmic velocity profile (equation 16) was squared and integrated from $z_0 \le z \le D$ and combined with equation (12). As shown in Figure 6, the log-profile model predicts a relatively constant value of τ_{*cT} for low channel slopes that decreases rapidly at high channel slopes. This trend is expected from inspection of equation (12) – as the channel slope approaches the friction angle, τ_{*cT} tends to zero. This model does not match the data well.

5.5.2. Particle Emergence

Including particle emergence produces the exact same trend as the baseline log-profile model, except for channel slopes greater than about 0.05 where τ_{*cT} abruptly increases as particles emerge from the flow (Figure 6). Again, at very high slopes τ_{*cT} is forced to zero where the channel slope equals the friction angle. The dashed line in Figure 6 separates the regions of particle submergence ($D < h$) and emergence ($D > h$).

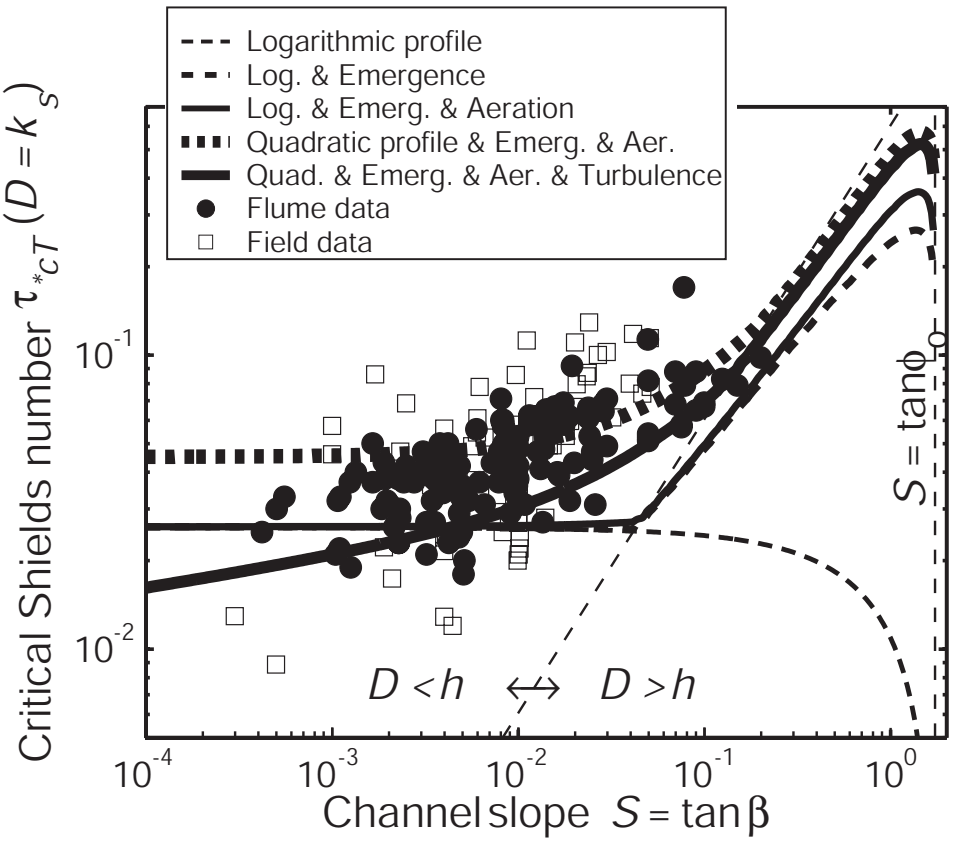

Figure 6. Model predictions and data for critical Shields stress as a function of channel slope. The effects considered include: 1) logarithmic velocity profile, 2) particle emergence, 3) flow aeration, 4) quadratic velocity profile, and 5) turbulent fluctuations. These are included cumulatively, such that the thick solid line represents all of the effects. The dashed diagonal line separates the fields of particle submergence ($D < h$) from emergence ($D > h$). The model predicts $\tau_{*cT} = 0$ where the bed-slope angle equals the friction angle, indicated by the vertical dashed line. Note that the predictions for $S >$ 0.57 should not be deemed reliable, as these slope angles (> 30 degrees) are larger than the typical angle of repose of loose sediment. Data shown are the same as Figure 1.

5.5.3. Flow Aeration

The effective density of the water-air mixture was calculated using equations (14) and (15). As mentioned above, equation (15) should provide a minimum estimate of aeration. Flow aeration has little affect for channel slopes less than 0.01 (Figure 6). In the region of $0.01 < S < 0.05$ flow aeration tends to offset the gravitational effects in the baseline log-profile model, resulting in a more constant value of τ_{*cT}. For channel slopes greater than 0.05, aeration causes a slightly greater τ_{*cT}, but the model prediction is dominated by the effect of emergence at these large slopes.

5.5.4. Quadratic Velocity Profile

The effects of wake mixing on the eddy viscosity is introduced in the model by using the quadratic velocity profile (equation 20), rather than the log profile (equation 16). By including the quadratic velocity profile, particles on all slopes are predicted to be less mobile and hence the Shields curve is shifted upwards. This is because the quadratic profile predicts lower velocities than the log profile at all channel slopes (Figure 4). Importantly, including the quadratic profile results in an increasing critical Shields stress with slope in the region of particle submergence. This also results in a smoother transition from fully submerged to partially emerged grains.

5.5.5. Turbulent fluctuations

Sediment is most likely to be entrained when turbulent fluctuations act to increase the local velocity around the grains above the average velocity. These down-

stream directed turbulent fluctuations, therefore, are included in the model by equating the local velocity $u(z)$ in equation (12) to an effective entrainment velocity, which is the sum of the local average velocity $\bar{u}(z)$ and the magnitude of turbulent excursions $\sigma_{u,\max}$ (i.e., $u(z) = \bar{u}(z) + \sigma_{u,\max}$). For simplicity, $\sigma_{u,\max}$ is assumed to be uniform about the exposed cross-sectional area of the particle A_{xs} and is given by equation (23) with α_2 = 0.2.

The model indicates that turbulent fluctuations affect incipient motion significantly. First, fluctuations increase the drag and lift forces on the particle, so that mobility is increased (i.e., τ_{*cT} is decreased) for all channel slopes (Figure 6). Second, the magnitude of the fluctuations are much larger for lower slopes (deeper flows), which results in a significant increase in τ_{*cT} with increasing channel slope. The result is a model that reproduces the trend and the magnitude of the data well.

5.5.6. Summary of Model Results

The baseline log-profile model does not predict the empirical trend of increasing τ_{*cT} with channel slope; in fact, it predicts an opposite trend. In light of this, the additional components considered here are a considerable improvement. Aeration has the least affect on the trend of the data. Particle emergence is significant, but only for slopes greater than 0.05. The most important effects considered are changes to the local velocity profile due to an eddy viscosity that incorporates wake mixing and changes to the intensity of velocity fluctuations due to the relative roughness dependency of macro-scale turbulence.

5.6. Mixed Particle Sizes

Thus far uniform-size sediment (or $D = k_s$) has been assumed. A more complete model must include heterogeneous particle sizes. Mixed particle sizes can lead to important dynamics in gravel and boulder-bedded streams, such as particle clustering and size-selective transport [*Paola et al.*, 1992; *Wilcock and McArdell*, 1993; *Church and Hassan*, 2002; *Yager et al.*, 2007]. Assessing these processes in a rigorous way is beyond the scope of this chapter. Here we take the simplistic approach of treating multiple grain sizes through the friction angle term in equation (12), which is dominantly a function of the particle size of interest D relative to the roughness length scale of the bed k_s [*Kirchner et al.*, 1990; *Johnston et al.*, 1998]. *Wiberg and Smith* [1987a] proposed the geometric relation

$$\phi_0 = \cos^{-1}\left[\frac{D/k_s + z_*}{D/k_s + 1}\right] \qquad (24)$$

based on the data of *Miller and Byrne* [1966], where k_s is the median particle size (i.e., $k_s = D_{50}$) and z_* is the "average level of the bottom of the almost moving grain" and was found empirically to be $z_* = -0.02$ for natural sand [*Wiberg and Smith*, 1987a].

Multiple Shields curves were generated for different friction angles from equations (12) and (24) (Figure 7). Particles are more difficult to move for larger friction angles, which results in an upward shift of the Shields curve. When D/k_s is unity, the friction angle given by equation (24) is predicted to be $\phi_0 \approx 60^\circ$, which is consistent with the previous calculations (i.e., Figure 6). More recent work on gravel-

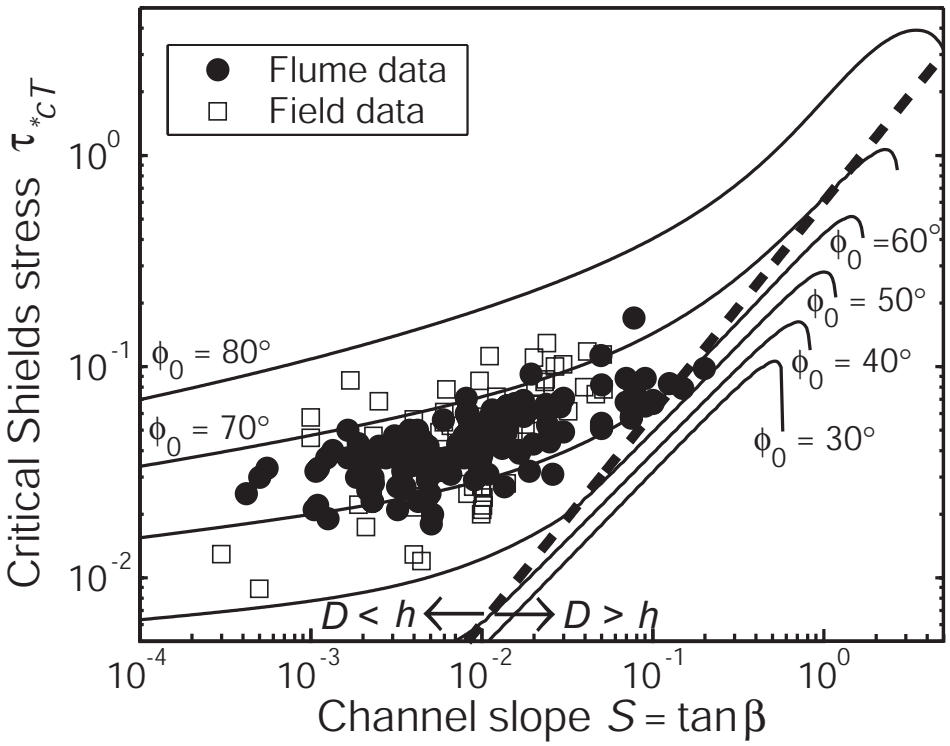

Figure 7. Model predications of the critical Shields stress versus slope for different values of the friction angle ϕ_0. The model includes particle emergence, flow aeration, the quadratic velocity profile, and turbulent fluctuations. The dashed diagonal line separates the fields of particle submergence ($D < h$) from emergence ($D > h$). Each model prediction tends to zero at large slopes where the bed-slope angle equals the friction angle. Data shown are the same as Figure 1.

beds have found $\phi_0 \approx 52^\circ$ for $D/k_s = 1$ [*Buffington et al.*, 1992; *Johnston et al.*, 1998]. It also has been shown that friction angles can vary substantially for the same value of D/k_s due to variable pocket geometries [*Kirchner et al.*, 1990]. Thus, it might be more appropriate to use a friction angle that is smaller than the mean angle predicted by equation (24). As shown in Figure 7, however, the data are consistent with friction angles ranging from about 60˚ to 70˚. This suggests that using a mean friction angle (e.g., equation 24) is reasonable. We have adopted equation (24) over other empirical power-law relations to be consistent with previous modeling work [*Wiberg and Smith,* 1987a].

To predict the sizes of grains that are most mobile for a given boundary shear stress, it is useful to normalize the critical shear stress by k_s, rather than D, because k_s is constant for a bed composed of multiple grain sizes [e.g., *Wiberg and Smith,* 1987a]. The curves for different friction angles in Figure 7 are interpreted to represent different relative particle sizes D/k_s following equation (24). Hence, large friction angles are interpreted to be for particles with small D/k_s and small friction angles are interpreted to be for particles with large D/k_s. Figure 8 shows that the theoretical Shields curves collapse when normalized by k_s (i.e., $(D/k_s)\tau_{*cT}$), which indicates that the critical shear stress necessary to mobilize different sediment sizes does not vary significantly (typically less than a factor of three). Moreover, the relative mobility of different sizes is a complex function of channel slope.

This is clearer in Figure 9 where the critical shear stress is plotted versus the relative particle size [c.f. *Wiberg and Smith,* 1987a]. Here the critical shear stress needed to move a given size D is normalized by the value needed to move the size

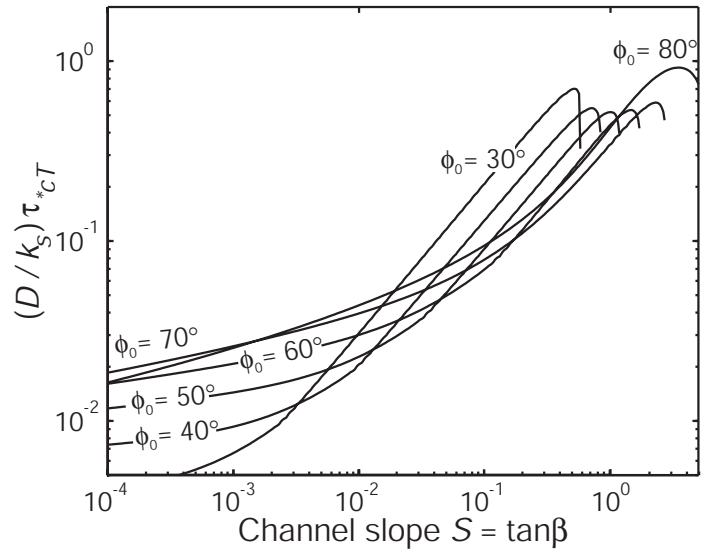

Figure 8. Same as Figure 7 except that the critical shear stress needed to move particle size D is normalized by k_s, which is constant for a bed of multiple particle sizes and represents here the median particle size on the bed. Thus, the curves indicate the relative mobility of different particle sizes under the same shear stress. The relationship between D, k_s, and ϕ_0 is given by equation (24).

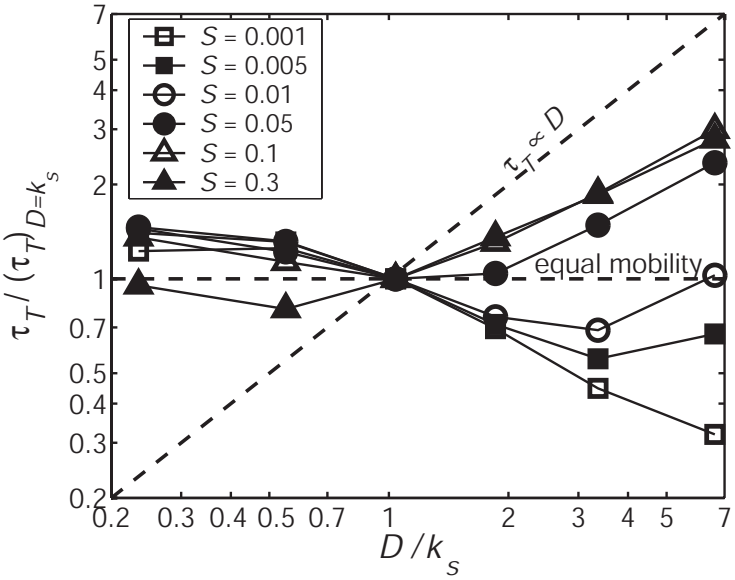

Figure 9. Total shear stress at incipient motion of particle size D normalized by the total shear stress necessary to move particle size $D = k_s$, versus the relative particle size D/k_s. Here, k_s represents the median particle size on the bed. The horizontal dashed line represents equal mobility. The diagonal dashed line represents size-selective transport given by the Shields stress, where the critical stress is proportional to the particle size.

$D = k_s$, where, following *Wiberg and Smith* [1987a], k_s is interpreted to be the median particle size. Thus, particle sizes that are more difficult to move than $D = k_s$ have values greater than unity and particles that are easier to move have values less than unity. A horizontal line represents equal mobility – where all particle sizes move at the same shear stress. For most channel slopes and particle sizes, the model predicts near equal mobility for the fine fraction $D < k_s$. The coarse fraction, on the other hand, is predicted to be the most mobile sediment on low slopes (S < 0.01), the least mobile sediment on steep slopes (S > 0.05), and approximately as mobile as the finer material on the moderate slopes in between. The latter finding is consistent with most studies, which have shown that sediment is nearly equally mobile, since many gravel-bed rivers studied have moderate slopes around 0.02 [e.g., *Parker*, 1990; *Parker et al.*, in press]. The large values of relative shear stress for the coarse fraction on steep slopes is also consistent with observations that boulders are relatively immobile in mountain streams [e.g., *Yager et al.*, 2007]. The reason for the systematic increase in relative shear stress with S for the coarser fraction is primarily because large particles become emergent from the flow before smaller particles, rendering them less mobile.

The force balance model described here provides a straightforward method of predicting relative mobility of a mixed bed. These predictions, however, should be treated with caution. For example, on very low slopes ($S < 10^{-2}$) the model predicts that coarse particles will move before finer particles (Figure 9). This is because the increased weight of larger particles is more than compensated for by smaller friction angles, which renders coarser particles more mobile. While this tendency has been documented before [*Solari and Parker*, 2000; *Brummer and Montgomery*, 2003], size-

selective mobility favoring finer sediment is typically considered the norm [e.g., *Parker*, 1990; *Buffington et al.*, 1992; *Paola et al.*, 1992; *Powell et al.*, 2001; *Ferguson*, 2003]. Others have found similar results as our model and argued that shifting of coarser particles could allow rapid entrainment of finer sediment [*Kirchner et al.*, 1990], or coarser particles might be partially buried by fines [*Buffington et al.*, 1992], rendering mixtures more equally mobile than simple models predict. We caution that changes to the empirical coefficients used to model aeration, wake mixing, and turbulent fluctuations would alter the overlap between the Shields curves in Figure 8, which could affect the predictions of size-selective mobility.

5.7. Discussion

5.7.1. Drag from Morphologic Structures

In the calculations above, the magnitude of stress spent on morphologic structures was set to zero (τ_m = 0) for simplicity. While it was argued in Section 5.4.2 that morphologic drag appears to be independent of channel-bed slope, it is probable that the magnitude of drag due to protruding particles, particle clusters and larger morphologic structures is non-negligible in flume experiments and natural streams [e.g., *Millar*, 1999]. We calculated the critical Shields stress as a function of slope using equation (12) with $\phi_0 = 60^\circ$ for constant values of the ratio of morphologic drag to the total stress (τ_m / τ_T). As expected, including a constant value of τ_m / τ_T (i.e., one that does not trend with channel slope) changes the magnitude of the critical Shields stress for a given slope (Figure 10). Increasing τ_m causes an increase in $\tau_{*_{cT}}$ because a smaller portion

of the total stress is available to move sediment. The model fits the data well if morphologic drag is set between 0 and 60% of the total driving stress. Larger portions of drag (e.g., 80%) result in an over-prediction of the data. This estimated range in morphologic drag is consistent with estimates by *Parker et al.* [in press] that morphologic form drag typically ranges from 21% to 57% of the total driving stress, based on a compilation of bankfull hydraulic measurements from gravel-bed rivers.

In order to make the model easier to apply, we have fit expressions to the theoretical curves in Figure 10 for τ_m / τ_T = 0%, 40%, and 60%. It was found that 4th-order polynomials approximate well the theoretical curves for $10^{-4} < S < 0.5$:

$$\tau_{*cT} = \exp\left[P_4 X^4 + P_3 X^3 + P_2 X^2 + P_1 X + P_0\right] \qquad (25)$$

where $X = 0.407 \ln(142S)$ after performing a centering and scaling algorithm to improve the least-squares fit. P_0, P_1, P_2, P_3 and P_4 are constants given by -3.57, 0.476, 0.199, 0.107, and 2.49 x 10^{-2} respectively for τ_m / τ_T = 0%; -3.14, 0.410, 0.142, 8.94 x 10^{-2}, and 2.59 x 10^{-2} respectively for τ_m / τ_T = 40%; and -2.8, 0.377, 0.121, 7.44 x 10^{-2}, and 2.02 x 10^{-2} respectively for τ_m / τ_T = 60%. The errors for these approximate curves are less than the thickness of the lines on Figure 10 within the regime $10^{-4} < S < 0.5$.

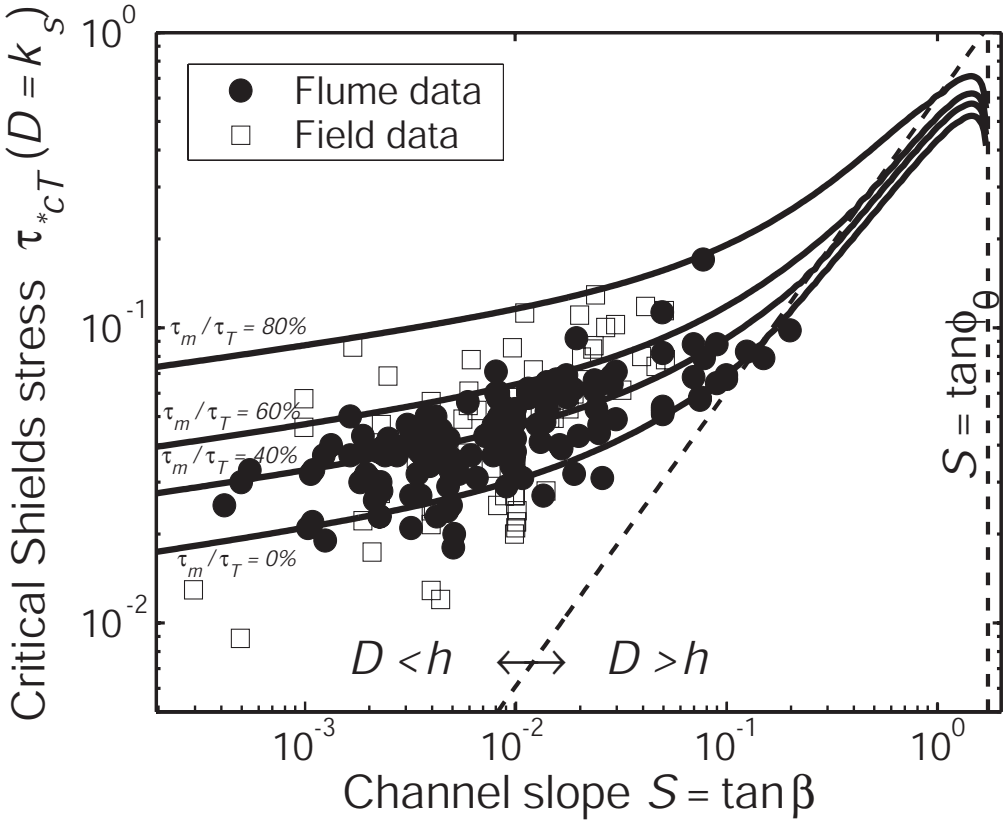

Figure 10. Model predications of the critical Shields stress versus slope for different values of the ratio of the stress borne by morphologic structures to the total stress τ_m / τ_T. The model includes particle emergence, flow aeration, the quadratic velocity profile, and turbulent fluctuations. The dashed diagonal line separates the fields of particle submergence ($D < h$) from emergence ($D > h$). Each model prediction tends to zero at large slopes where the bed-slope angle equals the friction angle. Data shown are the same as Figure 1.

5.7.2. Predicting Bed-Surface Grain Size

Many river restoration efforts attempt to adjust bed-surface particle size to improve habitat (e.g., for salmonid spawning) [*Kondolf and Wolman*, 1993]. Over long timescales, it is commonly assumed that particle sizes on the channel bed are adjusted to the hydraulic conditions, so that the bankfull Shields stress τ_{*bf} is approximately equal to the critical Shields stress τ_{*cT} [*Parker*, 1978; *Andrews*, 1983]. While oversimplified, such an assumption is powerful as it allows for a simple prediction of bed surface sediment size [e.g., *Buffington et al.*, 2004]. *Buffington and Montgomery* [1999] collected data from several stream reaches with different morphologies to test the assumption that $\tau_{*bf} \approx \tau_{*cT}$. They found that particle sizes were substantially finer than expected (i.e., $\tau_{*bf} > \tau_{*cT}$), which they attributed to morphologic form drag. This conclusion was supported by the fact that reaches with more woody debris had larger τ_{*bf}, as shown in Figure 11. Their data also show, however, that for a given channel morphology (with presumably similar values of morphologic drag), τ_{*bf} systematically increases with channel slope and systematically deviates from the assumed τ_{*cT} = 0.03 (Figure 11). The increase in τ_{*bf} with *S* is consistent with our model. Figure 11 shows the model predictions (equation 12) for different ratios of morphologic drag to the total stress. The model predictions are an improvement over assuming τ_{*cT} = 0.03, but still underestimate the data trend of increasing τ_{*bf} with *S*. This could be due to systematic variations in drag or friction angles within each morphologic division, among other assumptions inherent in such an analysis [*Buffington and Montgomery*, 2001; *Millar*

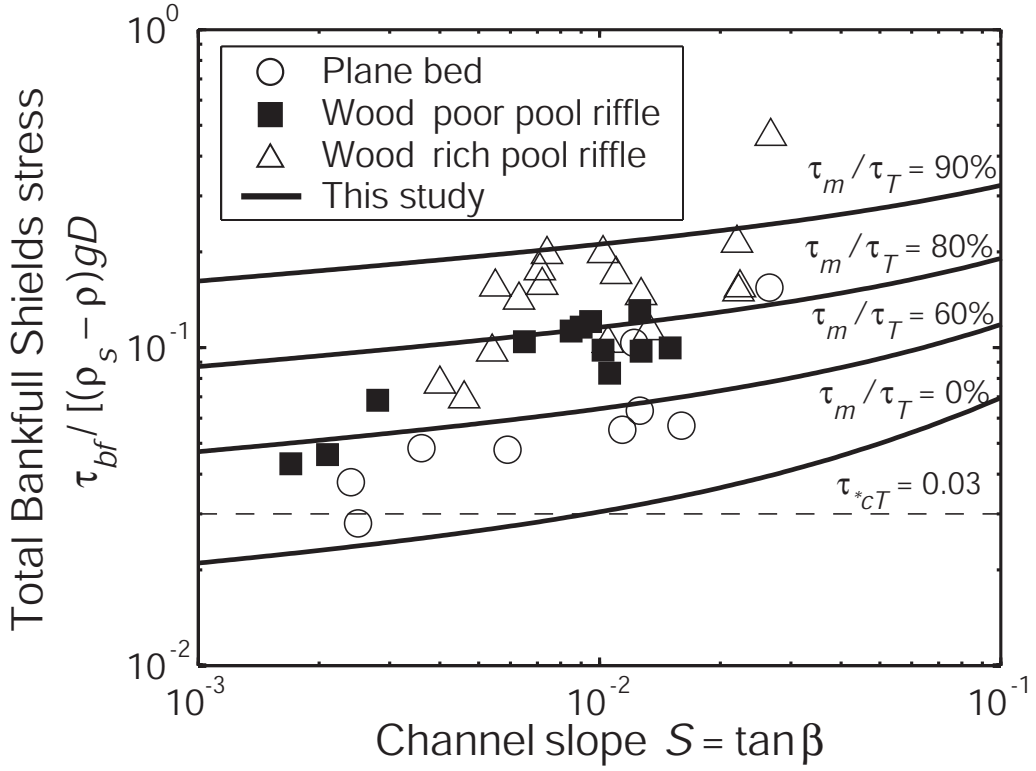

Figure 11. Field measurements of total bankfull Shields stress versus channel slope from *Buffington and Montgomery* [1999]. The data are stratified according to channel morphology. The dashed line represents the predicted relation where τ_{*cT} = 0.03, as assumed by *Buffington and Montgomery* [1999]. The solid lines are the expected relations using our model (equation 12) for different percentages of stress borne by morphologic structures divided by the total stress (τ_m / τ_T).

and Rennie, 2001; *Wilcock*, 2001]. The model predicts that the plane bed reaches have morphologic drag that constitutes zero to 60% of the total stress. In the wood-poor, pool-riffle reaches, morphologic drag is predicted to be about 60 to 80% of the total stress, and many of the wood-rich, pool-riffle reaches appear to have greater than 80% morphologic drag. These results are consistent with field measurements and analysis by *Buffington* [1998, Chapter 3].

Most rivers networks tend to have finer sediment on their beds in the downstream direction. This is typically attributed to abrasion of particles, selective transport of finer sediment, or a downstream reduction in shear stress. Some workers, however, have found that particle size increases in the downstream direction [*Solari and Parker*, 2000; *Brummer and Montgomery*, 2003]. Our study offers an explanation for this counter intuitive finding. If τ_{*cT} decreases downstream (because *S* decreases) more rapidly than the bankfull shear stress decreases, then the equilibrium particle size is predicted to increase downstream (if $\tau_{*bf} \approx \tau_{*cT}$). One then might expect to find downstream coarsening in steep headwater channels, since τ_{*cT} varies most strongly with slope for large slopes (Figure 6), which is consistent with the observations of *Brummer and Montgomery* [2003].

5.7.3. Implications for Low and High Gradient Channels

In lowland gravel-bed rivers, equation (12) indicates that τ_{*cT} can be a factor of two smaller than 0.03. In most natural settings, these low sloping rivers could have substantial concentrations of sand on the bed. The model of *Wilcock and Crowe* [2003], based on the experiments of *Wilcock et al.* [2001], shows that sand can cause a

reduction in τ_{*cT} from about 0.035 to 0.02 where the sand fraction increases from 10% to 30%. These workers also report a systematic reduction in channel slope with increasing sand content (from about 8×10^{-3} to 1.4×10^{-3}). Our model predicts a similar reduction in τ_{*cT} for this range in slopes due enhanced near-bed average velocities and turbulent fluctuations, without regard to sand content (Figure 6). More work is needed to sort out the potential overlapping influences of sand content and channel slope on incipient motion.

Most of the river network in hilly and mountainous landscapes is composed of small, steep channels, which are typically mantled by coarse sediment. The transport of boulders is considered a rate limiting process for bedrock erosion [*Seidl et al.*, 1994; *Sklar and Dietrich*, 2004; *Lamb et al.*, 2006] and has been shown to set the concavity of the longitudinal profile [*Sklar and Dietrich*, 2006]. It is common to assume that boulder transport on slopes > 0.1 occurs only by debris flows [*Stock and Dietrich*, 2003], or that boulders must break down in place. Moreover, stream-restoration researchers now place boulder clusters or other roughness elements in steep streams in an attempt to capture and store sediment to restore quasi-natural conditions [*Rosgen*, 1996; *Stallman et al.*, 2004]. These efforts are hampered because application of a constant τ_{*c} in mountain streams has had little success [e.g., *Zimmermann and Church*, 2001]. Our study allows for quantitative field estimation of boulder transport by fluvial processes. Equation (12) indicates that boulders become increasingly difficult to move by fluvial processes with increasing slope – but not impossible, as long as there is sufficient flow and boundary shear stress.

Also of note is the possibility that the peak in the critical Shields stress (Figure 10) identifies a zone of channel slopes in which sediment transport converges, which could be important for debris flow initiation. At very large slopes that approach the friction angle, sediment is highly mobile due to the large gravitational force pulling particles downslope. Particles that are transported in these steep zones by overland flow or raveling [e.g. *Imaizumi et al.*, 2006] might collect at lower slopes where particles are relatively immobile (i.e., for slopes of about $0.2 < S < \tan\phi_0$), which could eventually lead to failure initiating debris flows.

5.8. Conclusions

The critical Shields stress for incipient motion of sediment in open-channel flow increases with channel slope. This observation is contrary to standard theoretical models for incipient motion that predict increased mobility with increasing channel slope due to the added gravitational force in the downstream direction. Several processes might explain this discrepancy including variable drag caused by morphologic structures, wall drag, friction angles, grain emergence, flow aeration, changes to the vertical structure of flow velocity, and turbulent fluctuations. Increasing friction angles and drag due to changes in bed morphology do not appear to be the cause of the slope dependency, as is often assumed, because significant changes in bed morphology in controlled flume experiments seems unlikely. Moreover, data from flume experiments and natural streams are not significantly different, which suggests that other processes are responsible for the slope-dependent critical Shields stress. A

simple 1-D force-balance model indicates that the effect of aeration is small, and that grain emergence cannot explain the trend in the data for low slopes ($S < 0.1$). Through a process of elimination, it is concluded that the local velocity about the grains must decrease with increasing channel slope, for the same shear stress and particle size. A quadratic profile for the average local velocity is proposed based on a 1-D eddy viscosity model where mixing is dominated by wakes shed by particles. Inclusion of this profile in the force balance improves the model predictions of the trend in the data. To include the fluctuating component of local velocity due to turbulence, we hypothesize that the intensity of near-bed turbulent fluctuations are proportional to the depth-averaged flow velocity. A compilation of data supports this hypothesis and reveals the proportionality constant to be ~0.2. The combined effects of particle emergence, an eddy viscosity that incorporates wake mixing, and turbulent fluctuations in the model produce increasing τ_{*cT} with increasing slope that match the available data well. Collectively, these effects arise because of the coincident change in relative roughness with slope, since flow depth is inversely related to channel slope for a given bed-shear stress and particle size. Extension to multiple grain sizes indicates that the coarse fraction becomes increasingly less mobile on steeper slopes, primarily due to particle emergence. A slope-dependent critical Shields stress has broad implications as the assumption of constant τ_{*c} is the basis of many models used to predict such things as bedload transport, debris flow entrainment, bedrock erosion, downstream fining, and bed particle size.

5.9. Appendix 1 – Integrating Partial Spheres

The cross-sectional area of the particle that is exposed to the flow A_{xs} and the volume of the particle during partial emergence V_{ps} are calculated by integrating a partial sphere. Let $h^* = h/D$ and $z_0^* = z_0/D$. A_{xs} is given by

$$\frac{A_{xs}}{D^2} = \left[\left(h^* - \frac{1}{2}\right)\sqrt{h^* - h^{*2}} + \frac{1}{4}\arcsin(2h^* - 1) - \left(z_0^* - \frac{1}{2}\right)\sqrt{z_0^* - z_0^{*2}} - \frac{1}{4}\arcsin(2z_0^* - 1)\right] \text{ for } h^* < 1 \quad \text{(A1)}$$

and does not include the portion of the particle that is below z_o or above *h.* No account of shielding due to grain packing or burial are taken into account except through the term z_o. When a particle is fully submerged A_{xs} is given by

$$\frac{A_{xs}}{D^2} = \left[\frac{\pi}{8} - \left(z_0^* - \frac{1}{2}\right)\sqrt{z_0^* - z_0^{*2}} - \frac{1}{4}\arcsin(2z_0^* - 1)\right] \qquad \text{for} \quad h^* \geq 1 \qquad \text{(A2)}$$

The partially submerged volume of a particle V_{ps} is given by

$$\frac{V_{ps}}{D^3} = \pi h^{*2}\left(\frac{1}{2} - \frac{1}{3}h^*\right) \qquad \text{for} \quad h^* < 1 \qquad \text{(A3)}$$

For a fully submerged sphere ($h^* \geq 1$) $V_{ps} = V_p = 1/6\pi D^3$. More detail on these integrations can be found in *Yager et al.* [2007].

5.10. References

Aberle, J., and G.M. Smart (2003), The influence of roughness structure on flow resistance on steep slopes, *Journal of Hydraulic Research, 41* (3), 259-269.

Aguirre-Pe, J. (1975), Incipient erosion in high gradient open channel flow with artificial roughness elements, *Proceedings of the 16th Congress of the International Association of Hydraulic Research, San Paulo Brazil, 2*, 137-180.

Aguirre-Pe, J., and R. Fuentes (1991), Movement of big particles in steep, macro-rough streams, *Proceedings of the 24th Congress of the International Association of Hydraulic Research, Madrid, Spain, A*, 149-158.

Aguirre-Pe, J., M.L. Olivero, and A.T. Moncada (2003), Particle densimetric froude number for estimating sediment transport, *Journal of Hydraulic Engineering-Asce, June*, 428-437.

Aivazyan, O.M. (1987), Stabilized aeration on chutes, in *Hydrotechnical Construction*, pp. 713-722, Plenum Press, New York.

Andrews, E.D. (1983), Entrainment of gravel from naturally sorted riverbed material, *Geological Society of America Bulletin, 94*, 1225-1231.

Armanini, A., and C. Gregoretti (2005), Incipient sediment motion at high slopes in uniform flow conditions, *Water Resources Research, 41*, W12431.

Ashida, K., and M. Bayazit (1973), Initiation of motion and roughness of flows in steep channels., *Intl. Assoc. Hydraul. Res., Proc. 15th Congress, Istanbul, Turkey 1*, 475-484.

Ashworth, P.J., and R.I. Ferguson (1989), Size-selective entrainment of bed-load in gravel bed btreams, *Water Resources Research, 25* (4), 627-634.

Ashworth, P.J., R.I. Ferguson, P.E. Ashmore, C. Paola, D.M. Powell, and K.L. Prestegaard (1992), Measurements in a braided river chute and lobe: 2. Sorting of bed-load during entrainment, transport, and deposition, *Water Resources Research, 28* (7), 1887-1896.

Bartnick, W. (1991), Determination of the critical conditions of incipient motion of bed load in mountain rivers, in *Fluvial Hydraulics in Mountain Regions*, edited by A. Armanini, and G. Di Silvio, pp. 83-88, Springer-Verlag, Berlin.

Batchelor, G.K (1967), *An Introduction to Fluid Dynamics*, Cambridge University Press, Cambridge, 615 pp.

Bathurst, J.C. (1985), Flow resistance estimation in mountain rivers, *Journal of Hydraulic Engineering, 111* (4), 625-643.

Bathurst, J.C. (1987), Critical conditions for bed material movement in steep, boulder-bed streams, in *Erosion and Sedimentation in the Pacific Rim, Proceedings of the Corvallis Symposium, IAHS Publication no 165*, pp. 309-318.

Bathurst, J.C., H.H. Cao, and W.H. Graf (1984), *Hydraulics and sediment transport in a steep flume. Data from the EPFL study, report 64*, Inst. of Hydrol., Wallingford, Oxon, England.

Bathurst, J.C., W.H. Graf, and H.H. Cao (1987), Bed load discharge equations for steep mountain rivers, in *Sediment Transport in Gravel-bed Rivers*, edited by C.R. Thorne, J.C. Bathurst, and R.D. Hey, pp. 453-491, John Wiley & Sons.

Bathurst, J.C., R.M. Li, and D.B. Simons (1979), *Hydraulics of mountain rivers*, 229 pp., Engineering Research Center, Colorado State University, Fort Colins, CO.

Bayazit, M. (1975), Free surface flow in a channel of large relative roughness, *Journal of Hydraulic Research, 14* (2), 115-126.

Bayazit, M. (1978), Scour of bed material in very rough channels, *Journal of the Hydraulics Division, 104* (HY9), 1345-1349.

Best, J.L. (1992), On the entrainment of sediment and initiation of bed defects: insights from recent developments within turbulent boundary layer research, *Sedimentology, 39*, 797-811.

Bettess, R. (1984), Initiation of sediment transport in gravel streams, *Proceedings of the Institution of Civil Engineers, 77* (Technical Note 407), 79-88.

Braudrick, C.A., and G.E. Grant (2000), When do logs move in rivers?, *Water Resources Research, 36* (2), 571-583.

Brayshaw, A.C., L.E. Frostick, and I. Reid (1983), The Hydrodynamics of Particle Clusters and Sediment Entrainment in Coarse Alluvial Channels, *Sedimentology, 30* (1), 137-143.

Bridge, J.S., and S.J. Bennett (1992), A model for the entrainment and transport of sediment grains of mixed sizes, shapes, and densities, *Water Resources Research, 28* (2), 337-363.

Brummer, C.J., and D.R. Montgomery (2003), Downstream coarsening in headwater channels, *Water Resources Research, 39* (10), doi:10.1029/2003WR001981.\

Buffington, J.M. (1998), The use of streambed texture to interpret physical and biological conditions at watershed, reach, and subreach scales, Ph.D. dissertation, University of Washington, 147 pp.

Buffington, J.M., W.E. Dietrich, and J.W. Kirchner (1992), Friction angle measurements on a naturally formed gravel stream bed: implications for critical boundary shear stress, *Water Resources Research, 28* (2), 411-425.

Buffington, J.M., and D.R. Montgomery (1997), A systematic study of eight decades of incipient motion studies, with special reference to gravel-bedded rivers, *Water Resources Research, 33* (8), 1993-2029.

Buffington, J.M., and D.R. Montgomery (1999), Effect of hydraulic roughness on surface textures of gravel-bed rivers, *Water Resources Research, 35* (11), 3507-3521.

Buffington, J.M., and D.R. Montgomery (2001), Comment on "Effects of hydraulic roughness on surface textures of gravel-bed rivers" by John M. Buffington and David R. Montgomery - Reply, *Water Resources Research, 37* (5), 1529-1533.

Buffington, J.M., D.R. Montgomery, and H.M. Greenberg (2004), Basin-scale availability of salmonid spawning gravel as influenced by channel type and hydraulic roughness in mountain catchments, *Canadian Journal of Fisheries and Aquatic Sciences, 61* (11), 2085-2096.

Burr, D.M., J.P. Emery, R.D. Lorenz, G.C. Collins, and P.A. Carling (2006), Sediment transport by liquid surficial flow: Application to Titan, *Icarus, 181* (1), 235-242.

Byrd, T.C., and D.J. Furbish (2000), Magnitude of deviatoric terms in vertically averaged flow equations, *Earth Surface Processes and Landforms, 25*, 319-328.

Carling, P.A. (1983), Threshold of coarse sediment transport in broad and narrow natural streams, *Earth Surface Processes and Landforms, 8*, 1-18.

Carling, P.A., M. Hoffman, and A.S. Blatter (2002), Initial motion of boulders in bedrock channels, in *Ancient Floods, Modern Hazards: Principles and Applications of Paleoflood Hydrology*, American Geophysical Union, Washington DC.

Carollo, F.G., V. Ferro, and D. Termini (2005), Analyzing turbulence intensity in gravel bed channels, *Journal of Hydraulic Engineering, 131* (12), 1050-1061.

Chang, H.H. (1998), Riprap stability on steep slopes, *International Journal of Sediment Research, 13* (2), 40-49.

Chanson, H. (1994), Air-Water-Interface Area in Self-Aerated Flows, *Water Research*, *28* (4), 923-929.

Chanson, H. (2004), Drag reduction in skimming flow on stepped spillways by aeration, *Journal of Hydraulic Research*, *42* (3), 316-322.

Cheng, N.S. (2006), Influence of shear stress fluctuation on bed particle mobility, *Physics of Fluids*, *18* (9), doi:10.1063/1.2354434.

Chepil, W.S. (1958), The use of evenly spaced hemispheres to evaluate aerodynamic forces on soil surfaces, *Trans. AGU*, *39* (3), 397-404.

Chiew, Y., and G. Parker (1994), Incipient sediment motion on non-horizontal slopes, *Journal of Hydraulic Research*, *32* (5), 649-660.

Chiew, Y., and G. Parker (1995), Reply to "Incipient motion on non-horizontal slopes", *Journal of Hydraulic Research*, *33* (5), 728-730.

Christensen, B.A. (1995), Discussion of "Incipient motion on non-horizontal slopes", *Journal of Hydraulic Research*, *33* (5), 725-728.

Church, M., and M.A. Hassan (2002), Mobility of bed material in Harris Creek, *Water Resources Research*, *38* (11), doi:10.1029/2001WR000753.

Church, M., M.A. Hassan, and J.F. Wolcott (1998), Stabilizing self-organized structures in gravel-bed stream channels: Field and experimental observations, *Water Resources Research*, *34* (11), 3169-3179.

Cui, Y.T., and G. Parker (2005), Numerical model of sediment pulses and sediment-supply disturbances in mountain rivers, *Journal of Hydraulic Engineering-Asce*, *131* (8), 646-656.

Cui, Y.T., G. Parker, C. Braudrick, W.E. Dietrich, and B. Cluer (2006), Dam Removal Express Assessment Models (DREAM). Part 1: Model development and validation, *Journal of Hydraulic Research*, *44* (3), 291-307.

Dhamotharan, S., A. Wood, G. Parker, and H. Stefan (1980), Bedload transport in a model gravel stream, *Project Report 190*, St. Anthony Falls Laboratory, Minneapolis.

Defina, A., and A.C. Bixio (2005), Mean flow and turbulence in vegetated open channel flow, *Water Resources Research*, *41* (7), doi:10.1029/2004WR003475.

Diplas, P. (1987), Bedload Transport in Gravel-Bed Streams, *Journal of Hydraulic Engineering*, *113* (3), 277-292.

Dittrich, A., and K. Koll (1997), Velocity field and resistance of flow over rough surfaces with large and small relative roughness, *International Journal of Sediment Research, 12* (3), 21-33.

Drake, T.G., R.L. Shreve, W.E. Dietrich, P.J. Whiting, and L.B. Leopold (1988), Bedload transport of fine gravel observed by motion picture photography, *Journal of Fluid Mechanics, 192*, 193-217.

Einstein, H.A., and N.L. Barbarossa (1952), River channel roughness, *Transactions of the American Society of Civil Engineers*, *117*, 1121-1146.

Engelund, F., and J. Fredsoe (1976), A sediment transport model for straight alluvial channels, *Nord. Hydrol., 7*, 297-306.

Everts, C.H. (1973), Particle overpassing on flat granular boundaries, *J. Waterw. Harbors Coastal Eng. Div. Am. Soc. Civ. Eng., 99*, 425-439.

Ferguson, R.I. (1994), Critical discharge for entrainment of poorly sorted gravel, *Earth Surface Processes and Landforms*, *19*, 179-186.

Ferguson, R.I. (2003), Emergence of abrupt gravel to sand transitions along rivers through sorting processes, *Geology*, *31* (2), 159-162.

Fernandez Luque, R., and R. van Beek (1976), Erosion and transport of bed-load sediment, *J. Hydraul. Res., 14*, 127-144.

Flammer, G.H., J.P. Tullis, and E.S. Mason (1970), Free surface, velocity gradient flow past hemisphere, *Journal of the Hydraulics Division*, *7*, 1485-1502.

Furbish, D.J. (1993), Flow Structure in a Bouldery Mountain Stream with Complex Bed Topography, *Water Resources Research, 29* (7), 2249-2263.

Furbish, D.J. (1998), Irregular bed forms in steep, rough channels - 1. Stability anaysis, *Water Resources Research*, *34* (12), 3635-3648.

Furbish, D.J., S.D. Thorne, T.C. Byrd, J. Warburton, J.J. Cudney, and R.W. Handel (1998), Irregular bed forms in steep, rough channels - 2. Field observations, *Water Resources Research, 34* (12), 3649-3659.

Gessler, J. (1971), Beginning and ceasing of sediment motion, in *River Mechanics*, edited by H.W. Shen, Shen, H.W., Fort Collins.

Gilbert, G.K. (1914), The transportation of debris by running water, *U.S. Geol. Survey Prof. Pap., 86*, 263.

Graf, W.H. (1991), Flow resistance over a gravel bed: its consequences on initial sediment movement, in *Fluvial Hydraulics in Mountain Regions*, edited by A. Armanini, and G. Di Silvio, pp. 17-32, Springer-Verlag, Berlin.

Graf, W.H., and L. Suszka (1987), Sediment transport in steep channels, *Journal of Hydroscience and Hydraulic Engineering*, *5* (1), 11-26.

Graf, W.L. (1979), Rapids in canyon rivers, *Journal of Geology*, *87*, 533-551.

Grass, A.J. (1970), Initial instability of fine sand, *Journal of the Hydraulic Division of American Society of Civil Engineers*, *96* (619-632).

Hammond, F.D.C., A.D. Heathershaw, and D.N. Langhorne (1984), A Comparison between Shields Threshold Criterion and the Movement of Loosely Packed Gravel in a Tidal Channel, *Sedimentology*, *31* (1), 51-62.

Hassan, M.A., and M. Church (2000), Experiments on surface structure and partial sediment transport on a gravel bed, *Water Resources Research*, *36* (7), 1885-1895.

Hassan, M.A., and I. Reid (1990), The influence of microform bed roughness elements on flow and sediment transport in gravel bed rivers, *Earth Surface Processes and Landforms*, *15* (8), 739-750.

Ho, P.Y. (1939), *Abhangigkeit der geschiebebewegung von der kornform und der temperatur*, 43 pp.

Hofland, B., J.A. Battjes, and R. Booij (2005), Measurement of fluctuating pressures on coarse bed material, *Journal of Hydraulic Engineering-Asce*, *131* (9), 770-781.

Houjou, K., Shimizu, Y. and Ishii, C. (1990), Calculation of boundary shear stress in open channel flow, *Journal of Hydroscience and Hydraulic Engineering*, 8(2), 21-37.

Ikeda, S. (1982), Incipient Motion of Sand Particles on Side Slopes, *Journal of the Hydraulics Division-ASCE*, *108* (1), 95-114.

Imaizumi, F., R.C. Sidle, S. Tsuchiya, and O. Ohsaka (2006), Hydrogeomorphic processes in a steep debris flow initiation zone, *Geophysical Research Letters*, *33* (L10404), doi:1029/2006GL026250.

Jackson, R.G. (1976), Sedimentological and fluid-dynamic implications of turbulent bursting phenomenon in geophysical flows, *Journal of Fluid Mechanics*, *77* (3), 531-560.

Johnson, J.W. (1942), The importance of considering side-wall friction in bed-load investigations, *Civil Engineering*, *12*, 329-331.

Johnston, C.E., E.D. Andrews, and J. Pitlick (1998), In situ determination of particle friction ang les of fluvial gravels, *Water Resources Research*, *34* (8), 2017-2030.

Katul, G., P.L. Wiberg, J. Albertson, and G. Hornberger (2002), A mixing layer theory for flow resistance in shallow flows, *Water Resources Research*, *38* (11), doi: 10.1029/2001WR000817.

Kirchner, J.W., W.E. Dietrich, F. Iseya, and H. Ikeda (1990), The variability of critical shear stress, friction angle, and grain protrusion in water worked sediments, *Sedimentology*, *37*, 647-672.

Kironoto, B.A., and W.H. Graf (1994), Turbulence Characteristics in Rough Uniform Open-Channel Flow, *Proceedings of the Institution of Civil Engineers-Water Maritime and Energy*, *106* (4), 333-344.

Komar, P.D. (1979), Comparisons of the hydraulics of water flows in Martian Outflow Channels with flows of similar scale on Earth, *Icarus*, *37* (1), 156-181.

Komar, P.D. (1987), Selective Gravel Entrainment and the Empirical-Evaluation of Flow Competence, *Sedimentology*, *34* (6), 1165-1176.

Komar, P.D., and P.A. Carling (1991), Grain Sorting in Gravel-Bed Streams and the Choice of Particle Sizes for Flow-Competence Evaluations, *Sedimentology*, *38* (3), 489-502.

Kondolf, G.M., and M.G. Wolman (1993), The sizes of salmonid spawning gravels, *Water Resources Research*, *29* (7), 2275-2285.

Lamb, M.P., A.D. Howard, W.E. Dietrich, and J.T. Perron (2007), Formation of amphitheater-headed valleys by waterfall erosion after large-scale slumping on Hawaii, *Geological Society of America Bulletin*, *119*, 805-822, doi:10.1130/B25986.1

Lamb, M.P., A.D. Howard, J. Johnson, K.X. Whipple, W.E. Dietrich, and J.T. Perron (2006), Can springs cut canyons into rock?, *Journal of Geophysical Research*, *111* (E07002), doi:10.1029/2005JE002663.

Lawrence, D.S.L. (2000), Hydraulic resistance in overland flow during partical and marginal surface inundation: Experimental observations and modeling, *Water Resources Research*, *36* (8), 2381-2393.

Legleiter, C.J., T.L. Phelps, and E.E. Wohl (2007), Geostatistical analysis of the effects of stage and roughness on reach-scale patterns of velocity and turbulence intensity, *Geomorphology*, *83*, 322-345.

Lenzi, M.A., L. Mao, and F. Comiti (2006), When does bedload transport begin in steep boulder-bed streams?, *Hydrological Processes*, *20*, 3517-3533.

Lightbody, A.F., and H. Nepf (2006), Prediction of velocity profiles and longitudinal dispersion in emergent salt marsh vegetation, *Limnology and Oceanography*, *21* (1), 218-228.

Liu, T.-Y. (1935), Transportation of bottom load in an open channel, M.S. thesis, University of Iowa, Iowa City.

Lopez, F., and M.H. Garcia Turbulence structure in cobble-bed open-channel flow, in *Civil Engineering Studies, Univerisity of Illinois*, (1996), Urbana, Illinois.

Luque, R.F., and R. van Beek (1976), Erosion and transport of bed-load sediment, *Journal of Hydraulic Research*, *14* (2), 127-144.

Manga, M., and J.W. Kirchner (2000), Stress partitioning in streams by large woody debris, *Water Resources Research*, *36* (8), 2373-2379.

Marquis, G.A., and A.G. Roy (2006), Effect of flow depth and velocity on the scales of macroturbulent structures in gravel-bed rivers, *Geophysical Research Letters*, *33* (L24406), 10.1029/2006GL028420.

McLean, S.R., and V. Nikora (2006), Characteristics of turbulent unidirectional flow over rough beds: Double-averaging perspective with particular focus on sand dunes and gravel beds, *Water Resources Research*, *42* (W10409), doi:10.1029/2005WR004708.

Meyer-Peter, E., and R. Müller (1948), Formulas for bed-load transport, *Proceedings, 2nd Congress, International Association of Hydraulic Research, Stockholm*, 39-64.

Milhous, R.T. (1973), Movement of Individual Particles in a Gravel-Bottomed Stream, *Transactions-American Geophysical Union*, *54* (3), 139-139.

Millar, R.G. (1999), Grain and form resistance in gravel-bed rivers, *Journal of Hydraulic Research*, *37* (3), 303-312.

Millar, R.G., and C.D. Rennie (2001), Comment on "Effects of hydraulic roughness on surface textures of gravel-bed rivers" by John M. Buffington and David R. Montgomery, *Water Resources Research*, *37* (5), 1527-1528.

Miller, R.L., and R.J. Byrne (1966), The angle of repose for a single grain on a fixed rough bed, *Sedimentology*, *6*, 303-314.

Misri, R.L., R.J. Garde, and K.G.R. Raju (1984), Bed-load transport of coarse nonuniform sediment, *Journal of Hydraulic Engineering, 110* (3), 312-328.

Mizuyama, T. (1977), Bedload transport in steep channels, Ph.D. dissertation, Kyoto University, Kyoto, Japan.

Mueller, E.R., and J. Pitlick (2005), Morphologically based model of bed load transport capacity in a headwater stream, *Journal of Geophysical Research, 110*, F02016.

Mueller, E.R., J. Pitlick, and J. Nelson (2005), Variation in the reference Shields stress for bed load transport in gravel-bed streams and rivers, *Water Resources Research, 41*, doi: 10.1029/2004WRR003692.

Nakagawa, H., T. Tsjimoto, and Y. Hosokawa (1980), Statistical mechanics of bed-load transportation with 16 mm film analysis of behaviors of individual particles on a flat bed, *Third International Symposium on Stochastic Hydraulics, Tokyo, Japan*, 1-12.

Neill, C.R. (1967), Mean-velocity criterion for scour of coarse uniform bed-material, *Proceedings of the 12th Congress of the International Association for Hydraulic Research, 3*, 46-54.

Neill, C.R. (1968), Note on initial motion of coarse uniform bed material, *Journal of Hydraulic Research, 6* (2), 173-176.

Nelson, J., W.W. Emmett, and J.D. Smith (1991), Flow and sediment transport in rough channels, in *Proceedings of the 5th Interagency sedimentation conference*, pp. 55-62, Dept. of Energy.

Nelson, J.M., M.W. Schmeeckle, and R.L. Shreve (2001), Turbulence and particle entrainment, in *Bravel-Bed Rivers V*, edited by M.P. Mosley, pp. 221-240, New Zealand Hydrological Society, Wellington, New Zealand.

Nelson, J.M., R.L. Shreve, D.C. McLean, and T.G. Drake (1995), Role of near-bed turbulence structure in bed load transport and bed form mechanics, *Water Resources Research, 31* (8), 2071-2086.

Nezu, I., and H. Nakagawa (1993), *Turbulence in Open-Channel Flows*, 281 pp., A.A. Balkema, Rotterdam.

Nezu, I., and W. Rodi (1986), Open-channel flow measurements with a laser doppler anemometer, *Journal of Hydraulic Engineering, 112* (5), 335-355.

Nikora, V., and D. Goring (2000), Flow turbulence over fixed and weakly mobile gravel beds, *Journal of Hydraulic Engineering, 126* (9), 679-690.

Nikora, V., D. Goring, I. McEwan, and G. Griffiths (2001), Spatially averaged open-channel flow over rough bed, *Journal of Hydraulic Engineering*, *127* (2), 123-133.

Nikora, V., K. Koll, I. McEwan, S. McLean, and A. Dittrich (2004), Velocity distribution in the roughness layer of rough-bed flows, *Journal of Hydraulic Engineering*, *130* (10), 1036-1042.

Nikuradse, J. (1933), Stromungsgesetze in rauhen Rohren, *Forschg. Arb. Ing. Wes.*, *361*, 22.

Nowell, A.R.M., and M. Church (1979), Turbulent flow in a depth-limited boundary layer, *Journal of Geophysical Research*, *88* (C8), 4816-4824.

Olivero, M.L. Movimiento inciiente de particulas en flujo torrencial, (1984), pp. 169, University of Los Andes, Meridad, Venezuela.

Paintal, A.S. (1971), Concept of critical shear stress in loose boundary open channels, *Journal of Hydraulic Research*, *9*, 91-113.

Paola, C., G. Parker, R. Seal, S.K. Sinha, J.B. Southard, and P.R. Wilcock (1992), Downstream fining by selective deposition in a laboratory flume, *Science*, *258*, 1757-1760.

Papa, M., S. Egashira, and T. Itoh (2004), Critical conditions of bed sediment entrainment due to debris flow, *Natural Hazards and Earth System Sciences*, *4*, 469-474.

Papanicolaou, A.N., A. Bdour, and E. Wicklein (2004), One-dimensional hydrodynamic/sediment transport model applicable to steep mountain streams, *Journal of Hydraulic Research*, *42* (4), 357-375.

Papanicolaou, A.N., P. Diplas, C.L. Dancey, and M. Balakrishnan (2001), Surface roughness effects in near-bed turbulence: Implications to sediment entrainment, *Journal of Engineering Mechanics-Asce*, *127* (3), 211-218.

Papanicolaou, A.N., P. Diplas, N. Evaggelopoulos, and S. Fotopoulos (2002), Stochastic incipient motion criterion for spheres under various bed packing conditions, *Journal of Hydraulic Engineering-Asce*, *128* (4), 369-380.

Parker, G. (1978), Self-formed straight rivers with equilibrium banks and mobile bed. Part 2. The gravel river, *Journal of Fluid Mechanics*, *89* (1), 127-146.

Parker, G. (1990), Surface-Based Bedload Transport Relation for Gravel Rivers, *Journal of Hydraulic Research*, *28* (4), 417-436.

Parker, G., and P.C. Klingeman (1982), On Why Gravel Bed Streams Are Paved, *Water Resources Research, 18* (5), 1409-1423.

Parker, G., P.C. Klingman, and D.G. McLean (1982), Bedload and size distribution in paved gravel-bed streams, *ASCE Journal of Hydraulics, 108* (4), 544-571.

Parker, G., and A.W. Peterson (1980), Bar resistance of gravel-bed streams, *J. Hyd. Div., Proc. Am. Soc. Civ. Eng., 106*, 1559-1575.

Parker, G., P.R. Wilcock, C. Paola, W.E. Dietrich, and J. Pitlick (in press), Quasi-universal relations for bankfull hydraulic geometry of single-thread gravel-bed rivers, *Journal of Geophysical Research*.

Perron, J.T., M.P. Lamb, C.D. Koven, I. Fung, E. Yager, and M. Adamkovics (2007), Rainfall and sediment transport on Titan, *Journal of Geophysical Research*.

Picon, G.A. (1991), Estudio Experimental de Transporte Sedimentos en Rios de Montana, M.S. thesis, Merida, Venezuela.

Powell, D.M., I. Reid, and J.B. Laronne (2001), Evolution of bed load grain size distribution with increasing flow strength and the effect of flow duration on the caliber of bed load sediment yield in ephemeral gravel bed rivers, *Water Resources Research, 37* (5), 1463-1474.

Rao, K.N., R. Narasimha, and M.A.B. Narayanan (1971), The 'bursting' phenomenon in a turbulent boundary layer, *Journal of Fluid Mechanics, 48* (2), 339-352.

Raupach, M.R., R.A. Antonia, and S. Rajagopalan (1991), Rough-wall turbulent boundary layers, *Applied Mech. Rev., 44* (1), 1-25.

Rosgen, D.L. (1996), *Applied River Morphology*, Wildland Hydrology, Pagosa Springs, CO.

Schlichting, H. (1979), *Boundary-layer theory*, McGraw-Hill.

Schmeeckle, M.W., and J.M. Nelson (2003), Direct numerical simulation of bedload transport using a local, dynamic boundary condition, *Sedimentology, 50*, 279-301.

Schmeeckle, M.W., J.M. Nelson, and R.L. Shreve (2007), Forces on stationary particles in near-bed turbulent flows, *Journal of Geophysical Research, 112* (F02003), doi:10.1029/2006JF000536.

Schoklitsch, A. (1962), *Handbuch des Wasserbaues*, Springer-Verlag, Vienna.

Sechet, P., and B. Le Guennec (1999), Bursting phenomenon and incipient motion of solid particles in bed-load transport, *Journal of Hydraulic Research, 37* (5), 683-696.

Seidl, M. A., Dietrich, W. E., and Kirchner, J. W. (1994) Longitudinal profile development into bedrock: an analysis of Hawaiian channels, *Journal of Geology, 102*, 457–474.

Shen, H.W., and S. Wang (1985), Incipient sediment motion and riprap design, *Journal of Hydraulic Engineering, 111* (3), 520-538.

Shields, A. (1936), Awendung der Aehnlichkeitsmechanik und der Turbulenzforschung auf die Geschiebebewegung, *Mitt. Preuss. Versuchsanst. Wasserbau Schiffbau, 26*, 26.

Shvidchenko, A.B., and G. Pender (2000), Flume study of the effect of relative depth on the incipient motion of coarse uniform sediments, *Water Resources Research, 36* (2), 619-628.

Shvidchenko, A.B., and G. Pender (2001), Macroturbulent structure of open-channel flow over gravel beds, *Water Resources Research, 37* (3), 709-719.

Shvidchenko, A.B., G. Pender, and T.B. Hoey (2001), Critical shear stress for incipient motion of sand/gravel streambeds, *Water Resources Research, 37* (8), 2273-2283.

Sklar, L.S., and W.E. Dietrich (2004), A mechanistic model for river incision into bedrock by saltating bed load, *Water Resources Research, 40* (6).

Sklar, L.S., and W.E. Dietrich (2006), The role of sediment in controlling steady-state bedrock channel slope: implications of the saltation-abrasion incision model, *Geomorphology, 82* (1-2), 58-83.

Smart, G.M. (2005), A novel gravel entrainment investigation, in *River, Coastal, and Estuarine Morphodynamics, IAHR Symposium*, edited by G. Parker, and M. Garcia, pp. 65-69, Taylor and Francis, London.

Smith, J.D., and S.R. McLean (1977), Spatially averaged flow over a wavy surface, *Journal of Geophysical Research-Oceans, 8* (12), 1735-1746.

Solari, L., and G. Parker (2000), The curious case of mobility reversal in sediment mixtures, *Journal of Hydraulic Engineering, 126* (3), 185-197.

Song, T., U. Lemmin, and W.H. Graf (1994), Uniform flow in open channels with movable gravel bed, *Journal of Hydraulic Research, 32* (6), 861-876.

Stallman, J., C. Braudrick, D. Pedersen, Y. Cui, L. Sklar, B. Dietrich, and R. Real de Asua (2004), Geomorphic effects of boulder placement on gravel capture and retention in a regulated reach of the North Umpqua River, OR, *Eos Trans. AGU, 85* (47), Fall Meet. Suppl., Abstract H53B-1245.

Stock, J., and W.E. Dietrich (2003), Valley incision by debris flows: Evidence of a topographic signature, *Water Resources Research*, *39* (4).

Straub, L.G., and A.G. Anderson (1958), Experiments on self-aerated flow in open channels, *J. Hyd. Div., Proc. Am. Soc. Civ. Eng.*, *84* (HY7, paper 1890).

Straub, L.G., J.M. Killen, and O.P. Lamb (1954), Velocity Measurement of Air-Water Mixtures, *Transactions of the American Society of Civil Engineers*, *119*, 207-220.

Straub, L.G., and O.P. Lamb (1956), Studies of air entrainment on open-channel flows, *Am. Soc. Civ. Eng. Trans.*, *121*, 30-44.

Sutherland, A.J. (1967), Proposed mechanism for sediment entrainment by turbulent flows, *Journal of Geophysical Research, 72*, 6183-6194.

Tachie, M.F., D.J. Bergstrom, and R. Balachandar (2000), Rough wall turbulent boundary layers in shallow open channel flow, *Journal of Fluids Engineering, 122* (3), 533-541.

Tachie, M.F., D.J. Bergstrom, and R. Balachandar (2004), Roughness effects on the mixing properties in open channel turbulent boundary layers, *Journal of Fluids Engineering*, *126* (6), 1025-1032.

Torri, D., and J. Poesen (1988), Incipient motion conditions for single rock fragments in simulated rill flow, *Earth Surface Processes and Landforms, 13* (3), 225-237.

Tsujimoto, T. (1991), Bed-load transport in steep channels, in *Lecture Notes in Earth Science*, edited by S. Bhattacharji, G.M. Friedman, H.J. Neugebauer, and A. Seilacher, Springer-Verlag, Berlin.

U.S. Waterways Experimentation Station (USWES) (1935), *Study of river-bed material and their use with special reference to the Lower Mississippi River*, 161 pp., Vicksburg, Miss.

Valle, B.L., and G.B. Pasternack (2006), Air concentrations of submerged and unsubmerged hydraulic jumps in a bedrock step-pool channel, *Journal of Geophysical Research-Earth Surface, 111* (F3).

Vanoni, V.A., and N.H. Brooks (1957), Laboratory studies of the roughness and suspended load of alluvial streams, in *Calif. Inst. Technology Sedimentation*

Laboratory, Report E-68, pp. 121 (also US Army Corps of Eng., M.R.D. Sediment Series 11, 121 p.), California Institute of Technology, Pasadena, California.

Vollmer, S., and M. Kleinhans (2007), Predicting incipient motion, including the effect of turbulent pressure fluctuations in the bed, *Water Resources Research*, *43* (W05410), doi:10.1029/2006WR004919.

Wang, J., C.K. Chen, Z.N. Dong, and X. Zhenhuan (1993), The effects of bed roughness on the distribution of turbulent intensities in open-channel flow, *Journal of Hydraulic Research*, *31* (1), 89-98.

Wang, J.J., and Z.N. Dong (1996), Open-channel turbulent flow over non-uniform gravel beds, *Applied Scientific Research*, *56* (4), 243-254.

Wathen, S.J., R.I. Ferguson, T.B. Hoey, and A. Werritty (1995), Unequal Mobility of Gravel and Sand in Weakly Bimodal River Sediments, *Water Resources Research*, *31* (8), 2087-2096.

Wiberg, P.L., and J.D. Smith (1987a), Calculations of the critical shear stress for motion of uniform and heterogeneous sediments, *Water Resources Research*, *23*, 1471-1480.

Wiberg, P.L., and J.D. Smith (1987b), Initial motion of coarse sediment in streams of high gradient, *Erosion and Sedimentation in the Pacific Rim (Proceedings of the Corvallis Symposium)*, *IAHS Publication Number 165*, 299-308.

Wiberg, P.L., and J.D. Smith (1991), Velocity distribution and bed roughness in high gradient streams, *Water Resources Research*, *27*, 825-838.

Wiele, S.M., P.R. Wilcock, and P.E. Grams (2007), Reach-averaged sediment routing model of a canyon river, *Water Resources Research*, *43* (2).

Wilcock, P.R. (1987), Bed-load transport in mixed-size sediment, Ph.D. thesis, MIT, Cambridge.

Wilcock, P.R. (1993), Critical shear-stress of natural sediments, *Journal of Hydraulic Engineering*, *119* (4), 491-505.

Wilcock, P.R. (1998), Two-fraction model of initial sediment motion in gravel-bed rivers, *Science*, *280* (5362), 410-412.

Wilcock, P.R. (2001), Comment on "Effects of hydraulic roughness on surface textures of gravel-bed rivers" and "Effects of sediment supply on surface textures of gravel-bed rivers" by John M. Buffington and David R. Montgomery, *Water Resources Research*, *37* (5), 1525-1526.

Wilcock, P.R., and J.C. Crowe (2003), Surface-based transport model for mixed-size sediment, *Journal of Hydraulic Engineering, 129* (2), 120-128.

Wilcock, P.R., S.T. Kenworthy, and J.C. Crowe (2001), Experimental study of the transport of mixed sand and gravel, *Water Resources Research, 37* (12), 3349-3358.

Wilcock, P.R., and B.W. McArdell (1993), Surface-based fractional transport rates - mobilization thresholds and partial transport of a sand-gravel sediment, *Water Resources Research, 29* (4), 1297-1312.

Wilcock, P.R., and J.B. Southard (1988), Experimental-Study of Incipient Motion in Mixed-Size Sediment, *Water Resources Research, 24* (7), 1137-1151.

Wilcox, A.C., J.M. Nelson, and E.E. Wohl (2006), Flow resistance dynamics in step-pool channels: 2. Partitioning between grain, spill, and woody debris resistance, *Water Resources Research, 42* (5).

Wittler, R.J., and S.R. Abt (1995), Shields parameter in low submergence or steep flows, in *River, Coastal and Shoreline Protection: Erosion Control Using Riprap and Armourstone*, edited by C.R. Thorne, S.R. Abt, S.T. Barends, S.T. Maynord, and K.W. Pilarczyk, pp. 93-101, John Wiley & Sons, New York.

Wohl, E.E., and D.M. Thompson (2000), Velocity characteristics along a small step-pool channel, *Earth Surface Processes and Landforms, 25* (4), 353-367.

Wu, F.C., and K.H. Yang (2004), Entrainment probabilities of mixed-size sediment incorporating near-bed coherent flow structures, *Journal of Hydraulic Engineering-Asce, 130* (12), 1187-1197.

Yager, E.M., J.W. Kirchner, and W.E. Dietrich (2007), Calculating bed load transport in steep boulder bed channels, *Water Resources Research, 43* (7), doi: 10.1029/2006WR005432.

Yalin, M.S. (1977), *Mechanics of sediment transport*, 298 pp., Pergamon Press, Oxford.

Yalin, M.S., and E. Karahan (1979), Inception of Sediment Transport, *Journal of the Hydraulics Division-ASCE, 105* (11), 1433-1443.

Zanke, U.C.E. (2003), On the influence of turbulence on the initiation of sediment motion, *International Journal of Sediment Research, 18* (1), 17-31.

Zimmermann, A., and M. Church (2001), Channel morphology, gradient profiles and bed stresses during flood in a step-pool channel, *Geomorphology, 40* (3-4), 311-327.

Chapter 6

A Model for Fluvial Bedrock Incision by Impacting Suspended and Bedload Sediment

6.1. Introduction

River incision into bedrock is one of the fundamental drivers of landscape evolution and propagates climatic and tectonic signals throughout drainage networks. Incision into rock occurs relatively slowly and during large infrequent flood events making it difficult to investigate mechanistically. Instead, geomorphologists typically have relied on reach-scale rules to characterize river incision, for example, by setting the rate of erosion to be a function of boundary shear stress [*Howard and Kerby,* 1983; *Seidl and Dietrich,* 1992] or stream power [*Howard et al.*, 1994; *Seidl et al.*, 1994; *Whipple and Tucker,* 1999]. These models are limited in application, however, because they mask the physical mechanisms by which bedrock erosion occurs. More realistic model predictions require advances in our quantitative understanding of erosion processes [e.g., *Dietrich et al.*, 2003; *Whipple,* 2004].

One such model proposed by *Sklar and Dietrich* [2004] explicitly models the wear of bedrock by bedload particles (referred to as the *saltation-abrasion model* herein). Application of the saltation-abrasion model and related efforts have led to significant insights into the controls of bedrock river morphology including, channel slope [*Sklar and Dietrich*, 2006; *Gasparini et al.*, 2007], knickpoints [e.g., *Chatanantavet and Parker*, 2005; *Wobus et al., 2006*; *Crosby et al.*, 2007], slot canyons [*Carter and Anderson*, 2006; *Johnson and Whipple*, 2007], and channel width [*Finnegan et al.*, 2007; *Nelson and Seminara*, 2007; *Turowski et al.*, 2008]. The saltation-abrasion model is incomplete, however, because it neglects other important mechanisms for river-bed erosion such as cavitation, plucking of jointed rock and abrasion by suspended sediment [*Whipple et al.*, 2000]. Abrasion by suspended sediment in particular has been argued to be an important (or dominant) bedrock erosion mechanism in some natural streams [*Hancock et al.*, 1998; *Whipple et al.*, 2000; *Hartshorn et al.*, 2002] owing in part to the frequent occurrence of polished surfaces, flutes, potholes, and undulating canyon walls.

In this chapter, we investigate erosion by suspended particles by deriving a total-load erosion model, which expands on the saltation-abrasion model of *Sklar and Dietrich* [2004] to include suspended particles. Cavitation and plucking of jointed rock are not investigated here. In Section 6.2, the saltation-abrasion model is reviewed briefly and the assumption that the impact rate is zero at the onset of suspension is discussed. In Section 6.3, we propose that suspended particles do interact with the bed and that the impact rate scales with the product of the near-bed sediment concentration and the particle impact velocity. The near-bed sediment concentration is found by

partitioning a given sediment supply between the bed and suspended load. In Section 6.4, commonly used formulas are adopted to solve the model, including the Rouse concentration profile to describe the vertical distribution of suspended sediment. In Section 6.5, the total-load erosion model results are shown and compared to the saltation-abrasion model for different values of transport stage, sediment supply, particle size, and channel slope. Finally, the entrainment capacity, viscous damping of impacts, and implications for natural streams are discussed in Section 6.6.

6.2. Saltation-Abrasion Model

Sklar and Dietrich [2004], following the work of *Foley* [1980], *Beaumont et al.* [1992], *Tucker and Slingerland* [1994], and others, present a model for fluvial incision of bedrock by saltating sediment, which is briefly reviewed here. The saltation-abrasion model was formulated by neglecting abrasion by all modes of sediment transport except saltation. A planar bed, rectangular channel cross section, and uniform size sediment are assumed. The model is zero-dimensional and thus assumes that the net effects of spatial heterogeneity in hydraulics, rock strength, and sediment supply can be adequately represented in terms of a unit bed area.

The rate of vertical erosion E is defined as the product of the average volume of rock detached per particle-bedrock impact V_i, the rate of particle impacts per unit bed area per unit time I_r, and the fraction of exposed bedrock on the river bed F_e

$$E = V_i I_r F_e. \quad (1)$$

The volume of eroded bedrock per particle impact V_i is scaled by the kinetic energy of the particle impact

$$V_i = \frac{1}{2}\frac{V_p \rho_s w_i^2}{\varepsilon_v}, \tag{2}$$

where V_p, ρ_s, w_i and are the particle volume, density and impact velocity normal to the bed. A threshold kinetic energy needed to cause erosion is not included based on abrasion mill experiments [*Sklar and Dietrich*, 2001]. ε_v is the kinetic energy required to cause erosion of a unit volume of bedrock (i.e., units of energy per volume) and depends on the capacity of the rock to store energy elastically.

$$\varepsilon_v = k_v \frac{\sigma_T^2}{2Y}, \tag{3}$$

where σ_T is the tensile yield strength and Y is Young's modulus of elasticity of the bedrock. k_v is a dimensionless coefficient found to be of the order 10^6 [*Sklar and Dietrich*, 2006].

The rate of particle-bedrock impacts per unit bed area I_r is given by

$$I_r = \frac{q_b}{V_p L_b}, \tag{4}$$

where q_b is the volumetric sediment flux per unit channel width traveling as bedload and L_b is the saltation hop length. Note that q_b in this chapter is the same as q_b / ρ_s defined by *Sklar and Dietrich* [2004], since they defined q_b to be a mass flux rather than a volumetric flux.

Following the hypothesis of *Gilbert* [1877], the fraction of the river bed that is not covered with alluvium, and is therefore exposed bedrock, F_e is assumed to vary as

$$F_e = \left(1 - \frac{q_b}{q_{bc}}\right), \tag{5}$$

where q_{bc} is the volumetric bedload sediment-transport capacity per unit channel width [*Slingerland et al.*, 1997; *Sklar and Dietrich*, 2004]. This linear relationship has yet to be tested in nature, and others have argued that an exponential relationship is more appropriate [*Turowski et al.*, 2007]. Herein we use equation (5) to simplify later comparison of the saltation-abrasion model with the total-load erosion model. Equation (5) must be true in the end-member cases at steady state. Where the supply of sediment exceeds the transport capacity, sediment is deposited on the bed and the bedrock is protected from erosion. This is typically the case in alluvial, transport-limited rivers and many formulas exist to predict the sediment transport (and hence the transport capacity) under such conditions [e.g., *Fernandez Luque and van Beek*, 1976]. On the other hand, if the sediment supply is zero, the river bed will be free of cover. In this case, however, no erosion will occur because there are no particles to impact the bed.

Combining equations (1) – (5) yields the composite expression of the saltation-abrasion model

$$E = \frac{\rho_s q_b w_i^2 Y}{L_b k_v \sigma_T^2}\left(1 - \frac{q_b}{q_{bc}}\right). \qquad (6)$$

6.2.1. Particle Hop Length and the Transition to Suspension

Perhaps most important for the present study is evaluation of the saltation hop length L_b. *Sklar and Dietrich* [2004] compiled data from numerous experimental and theoretical studies on particle saltation [*Francis*, 1973; *Abbott and Francis*, 1977; *Wiberg and Smith*, 1985; *Sekine and Kikkawa*, 1992; *Lee and Hsu*, 1994; *Nino et al.*, 1994; *Hu and Hui*, 1996] and found the best-fit relationship to be

$$\frac{L_b}{D} = 8.0\left(\frac{\tau_*}{\tau_{*c}} - 1\right)^{0.88}, \qquad (7)$$

where D is the particle diameter and (τ_* / τ_{*c}) is the transport stage. τ_* is the non-dimensional bed stress or Shields stress given by

$$\tau_* = \frac{u_*^2}{RgD}, \qquad (8)$$

where R is the submerged specific density of the sediment ($R = (\rho_s - \rho_f)/\rho_f$), ρ_f is the density of the fluid, g is the acceleration due to gravity, and u_* is the bed shear velocity. τ_{*c} is the critical value of τ_* at the threshold of particle motion [*Shields*, 1936].

In the saltation-abrasion model, particle-hop length is assumed to be infinite for particles transported in suspension. A flow is typically considered competent to suspend sediment if

$$u_* / w_{st} \geq 1, \tag{9}$$

where w_{st} is the terminal settling velocity of the sediment [*Bagnold*, 1966]. Therefore, *Sklar and Dietrich* [2004] modified equation (7) to be

$$\frac{L_b}{D} = \frac{8.0\left(\tau_* / \tau_{*c} - 1\right)^{0.88}}{\sqrt{1 - (u_* / w_{st})^2}} \tag{10}$$

and the erosion rate (equation 6) is zero if $u_* / w_{st} \geq 1$.

The experimental particle trajectory data used to calibrate equation (10) does not extend into the regime $u_* / w_{st} \geq 1$, and thus the validity of equation (10) over equation (7) cannot be verified. We hypothesize that suspended sediment does contribute to bedrock erosion due to particle-bedrock impacts. In the next section, we develop this

hypothesis and present a model for bedrock erosion from suspended and bedload sediment.

6.3. Total-Load Erosion Model

Our model development follows the assumptions and limitations of previous work on erosion by bedload discussed above. In particular, our model is zero-dimensional and only considers incision into a flat bed by impacts of single-sized particles. The model is based on the concept that suspended sediment actually is not held in a fluid indefinitely. Instead, particles are continuously falling through the fluid due to gravitational settling and are advected towards the bed due to turbulence. Where $u_* / w_{st} \geq 1$, sediment travels both in suspension and bedload [*Bagnold*, 1966; *van Rijn*, 1984; *Nino et al.*, 2003]. Therefore, the incision model is developed to include impacts by both bedload and suspended particles (i.e., the total load) under a wide range of conditions, including $u_* / w_{st} \geq 1$.

6.3.1. Settling Flux

During conditions of suspended sediment transport (i.e., $u_* / w_{st} \geq 1$), particles do impact and interchange with the bed. Particles are entrained from the bed by coherent flow structures, which produce bursts of upward moving fluid [*Grass*, 1970; *Jackson*, 1976; *Sumer and Deigaard*, 1981; *Nelson et al.*, 1995; *Bennett et al.*, 1998]. As these structures dissipate, particles tend to settle towards the bed at a rate near their settling velocity in still water [e.g., *Sumer and Deigaard*, 1981; *Nino and Garcia*,

1996]. This gravitational settling results in a volumetric flux of sediment towards the bed per unit area given by

$$f_s = c_b w_s , \tag{11}$$

where c_b is the near-bed volumetric sediment concentration and w_s is the gravitational settling velocity of the sediment (which can be less than w_{st}). Despite this downwards sediment flux, an equilibrium concentration of particles can be attained because there is a dynamic balance between the upward and downward fluxes of particles [*Rouse*, 1937; *Smith and McLean*, 1977; *Parker*, 1978; *García and Parker*, 1991; *Bennett et al.*, 1998].

This concept is well illustrated in the experiments of *Einstein* [1968], in which a recirculating flume was used to create a steady, uniform flow over an open-framework and immobile gravel bed. The flow was highly turbulent and capable of suspending the silt that was introduced into the flume (u_* / w_{st} ranged from 74 to 7.2 x 10^3). Despite the fact that $u_* / w_{st} >> 1$, the *suspended* particles did indeed impact the bed, the turbid flows eventually clarified, and a steady state concentration profile was not attained. This was because the suspended silt settled through the gravel on the flume bed and the downward flux of sediment was not balanced by a commensurate entrainment flux from the bed.

6.3.2. Particle-Bed Impacts

Few experimental studies have traced the flow paths of individual suspended particles, which, along with the stochastic nature of such trajectories, makes it difficult to directly formulate an effective particle hop length for suspension. Since classic suspension theory is based in terms of sediment concentration [*Rouse,* 1937], it is useful to formulate the impact rate as a function of sediment concentration instead of hop length. Following the above arguments and equation (11), the rate of particle impacts per unit bed area can be expected on average to be proportional to the product of the near-bed sediment concentration and the particle velocity normal to the bed,

$$I_r = \frac{A_1 c_b w_i}{V_p}. \qquad (12)$$

The impact velocity normal to the bed (w_i) is used here as a measure of the particle velocity instead of the gravitational settling velocity (w_s, as in equation (11)) because w_s might not be normal to the bed and impacts also can occur because of turbulent fluctuations (discussed in Section 6.4.4). The coefficient $A_1 < 1$ accounts for the fact that some of the particles near the bed are advected upwards due to lift forces.

Equation (12) is not specific to suspension and also holds for bedload. For example, the downstream flux of bedload sediment can be written as

$$q_b = c_b U_b H_b, \qquad (13)$$

where U_b is the vertically averaged streamwise particle velocity and c_b is the vertically averaged sediment concentration within the bedload layer of height H_b. The average bedload velocity can be scaled as

$$U_b = \frac{L_b}{t_i} \approx \frac{A_2 w_s L_b}{H_b}, \tag{14}$$

where t_i is the timescale between bed impacts for an individual particle. $A_2 < 1$ accounts for the fact that the average fall velocity within the bedload layer might be less than the near-bed settling velocity, and that the total time between impacts should also include the particle ejection or rise time as well as the fall time. For example, *Sklar and Dietrich* [2004] suggest $A_2 \approx 1/3$. Combination of equations (4), (13) and (14) results in

$$I_r = \frac{A_2 c_b w_s}{V_p}, \tag{15}$$

which is the same as equation (12) provided that $A_2 w_s = A_1 w_i$.

6.3.3. Sediment Supply

In alluvial rivers with an unlimited supply of sediment on the bed and a steady-state concentration profile, the settling flux of sediment near the bed f_s is equal to the entrainment capacity of the flow (per unit bed area) f_e, which can be written as

$$f_e = \alpha w_s , \tag{16}$$

where α is a non-dimensional sediment entrainment parameter (which is a function of u_* / w_{st} [e.g., *García and Parker*, 1991]). Thus, where $f_e = f_s$, the near bed sediment concentration c_b can be determined directly from the hydraulics and sediment size because combination of equations (11) and (16) results in $\alpha = c_b$. This is not the case in bedrock rivers.

For supply-limited conditions typical of bedrock rivers, the concentration of particles in suspension (and therefore c_b) is not dependent on the entrainment capacity (i.e., $\alpha > c_b$) and instead is determined by the sediment supply from the bed, banks, and upstream. By continuity

$$q_s = \int_{H_b}^{H} cudz = c_b U H \chi , \tag{17}$$

where q_s is the volumetric flux of sediment per unit channel width traveling in suspension. c and u are the depth-dependent concentration and downstream flow velocity per unit channel width, averaged over turbulent fluctuations. U is the depth-averaged flow velocity in the downstream direction and H is the flow depth. z is the coordinate perpendicular to the river bed and $0 \le \chi \le 1$ is the integral that describes the vertical structure of velocity and concentration. In equation (17), it is assumed that the

average streamwise particle velocities are equal to the fluid velocities, as is typical for suspended sediment [e.g., *McLean*, 1992].

To evaluate the impact rate given by equation (12), the near-bed sediment concentration must be known. Here, we seek an expression for the near-bed concentration by partitioning the supplied sediment flux into bed and suspended load. To simplify matching the concentration profile between the bedload and the suspended sediment above, we assume that within the bedload layer ($z \le H_b$) sediment is well mixed [e.g., *McLean*, 1992] with a concentration of c_b (Fig. 1). Equations (13) and (17) can be summed and solved for c_b,

$$c_b = \frac{q}{UH\chi + U_b H_b}, \tag{18}$$

where q is the total volumetric flux of sediment traveling as both bed and suspended load per unit width, which is equivalent to the total sediment supply (per unit width) in the supply-limited conditions considered here. Thus, inclusion of suspended sediment (rather than considering only bedload) lowers the near-bed sediment concentration and therefore the rate of impacts for a given sediment supply. Equation (18), however, predicts a finite near-bed sediment concentration for all flow conditions.

6.3.4 Composite Expression for the Total-Load Erosion Model

Substituting equations (2), (3), (5), (12) and (18) into equation (1) yields the combined model for erosion by bed and suspended sediment:

$$E = \frac{A_1 \rho_s Y}{k_v \sigma_T^2} \frac{q w_i^3}{(UH\chi + U_b H_b)} \left(1 - \frac{q_b}{q_{bc}}\right), \tag{19}$$

where q_b is found from equations (13) and (18) to be

$$q_b = q\left(\frac{U_b H_b}{UH\chi + U_b H_b}\right). \tag{20}$$

6.4. Empirical Expressions and Calculation Procedure

Following *Sklar and Dietrich* [2004], the model is explored by holding some variables to constant values typical of a reference field site, the South Fork Eel River [*Seidl and Dietrich*, 1992; *Howard*, 1998]. As shown in Table 1, the characteristic sediment size and supply is set to D = 60 mm and q = 8.9 x 10^{-4} m^3/s (see *Sklar* [2003] for details) based on the average landscape lowering rate of 0.9 mm/yr [*Merritts and Bull*, 1989]. The representative discharge is 39.1 m^3/s, which has an exceedence probability of 0.013 and a transport stage of τ_* / τ_{*c} = 1.7 [*Sklar and Dietrich*, 2004]. Given this transport stage, the representative flow depth is found to be H = 0.95 m, assuming τ_{*c} = 0.03 (Table 1).

In order to better show the effects of suspension, we also consider 1-mm sand in addition to the 60-mm gravel. Note that the model is formulated in terms of single-sized particles that travel in both suspended load and bedload. A model incorporating multiple particle sizes interacting and impacting the bed at the same time is not

Table 1: Model Input and Output Values for Representative Field Case: South Fork Eel River, CA	
Channel Slope S	0.0053
Channel width W	18 m
Sediment supply q_s	8.9 x 10^{-4} m^2/s
Water discharge q_w	2.1 m^2/s
Flow velocity U	2.2 m/s
Flow depth H	0.95 m
Shear velocity u_*	0.22 m/s
Rock tensile strength σ_T	7 MPa
Young's Elastic Modulus Y	5.0 x 10^4 MPa
Rock resistance parameter k_v	1.0 x 10^6
Critical Shields stress τ_c^*	0.03
Sediment density ρ_s	2650 kg / m^3
Water density ρ_f	1000 kg / m^3
Kinematic viscosity of water ν	10^{-6} m^2/s
Sediment Size D	60 mm , 1 mm
Transport stage τ^* / τ_c^*	1.7 , 102
Particle fall height H_f	79 mm, 38 mm
Terminal settling velocity w_{st}	0.98 m/s, 0.13 m/s
Bedload velocity U_b	1.26 m/s, 2.2 m/s
Bedload concentration c_b	0.0089, 0.0151
Bedload layer height H_b	72.3 mm, 14.5 mm
Bedload transport capacity q_{bc}	1.0 x 10^{-3} m^2/s, 3.8 x 10^{-3} m^2/s
Erosion rate E	31 mm/yr, 10 mm/yr

attempted here. Thus, our calculations assume that the total load is composed either exclusively of 60-mm gravel or exclusively 1-mm sand. For the later case, the hydraulic and geometric conditions are set to the same representative values used for D = 60 mm, for purposes of comparison. In particular, with an equivalent representative discharge and flow depth, the transport stage for the 1-mm sand is found to be τ_* / τ_{*c} = 102 (Table 1). For simplicity, we use a constant value of τ_{*c} = 0.03 throughout, although a particle Reynolds number or relative roughness dependency could be explored in the future [*Buffington and Montgomery*, 1997; *Lamb et al.*, 2008].

To solve equation (19), expressions for the flow velocity, bedload transport capacity, bedload-layer height and velocity, sediment concentration, and impact velocity are needed. Due to the simplifying assumptions in developing the model (e.g., zero-dimensional, single-sized sediment, etc.), simple and commonly used formulas for these variables are employed here.

6.4.1. Flow Velocity

For turbulent boundary-layer flow in a channel, the downstream velocity can be calculated as

$$u = \frac{u_*}{\kappa} \ln\left(\frac{z}{z_0}\right) \qquad (21)$$

where z_0 is a function of the boundary roughness and κ is von Karman's constant (~ 0.41) (Fig. 1). The shear velocity is calculated from $u_* = \left(gH \sin\theta\right)^{1/2}$, where θ is the

channel-bed-slope angle. Strictly speaking, equation (21) is only applicable to the lower ~ 20% of the water column, and an adjustment to the eddy viscosity should be made for the upper portion of the flow [e.g., *Coles*, 1956; *Gelfenbaum and Smith*, 1986]. Modifications to the eddy viscosity should also be made due to stratification and form roughness [*Vanoni*, 1946; *McLean*, 1992; *Wright and Parker*, 2004]. For our purposes, we will assume that equation (21) is applicable throughout the water-column; however, it it could be replaced with a more complete expression if desired. The depth-averaged flow velocity U can be found by integrating equation (21)

$$U = \frac{1}{H}\int_{z_0}^{H} \frac{u_*}{\kappa} \ln\left(\frac{z}{z_0}\right) dz . \qquad (22)$$

For the following calculations we set $z_0 = nD/30$ with the empirical coefficient $n = 3$ [e.g., *Kamphius*, 1974]. In order to hold the hydraulic conditions constant for D = 60 mm and D = 1 m, we evaluate the roughness using D = 60 mm for both cases. This is done to simplify comparison. We suspect, however, that this might be an inaccurate parameterization of the flow roughness in natural bedrock streams where the bed is only partially covered with sediment. Furthermore, hydraulic roughness might be dominated by the banks, immobile boulders, or sculpted forms on the beds [*Finnegan et al.*, 2007; *Johnson and Whipple*, 2007; *Yager et al.*, 2007].

The resulting velocity profile for the representative conditions of the South Fork Eel River using equation (21) are shown in Figure 1. The depth-averaged velocity is calculated from equation (22) to be U = 2.2 m/s (Table 1).

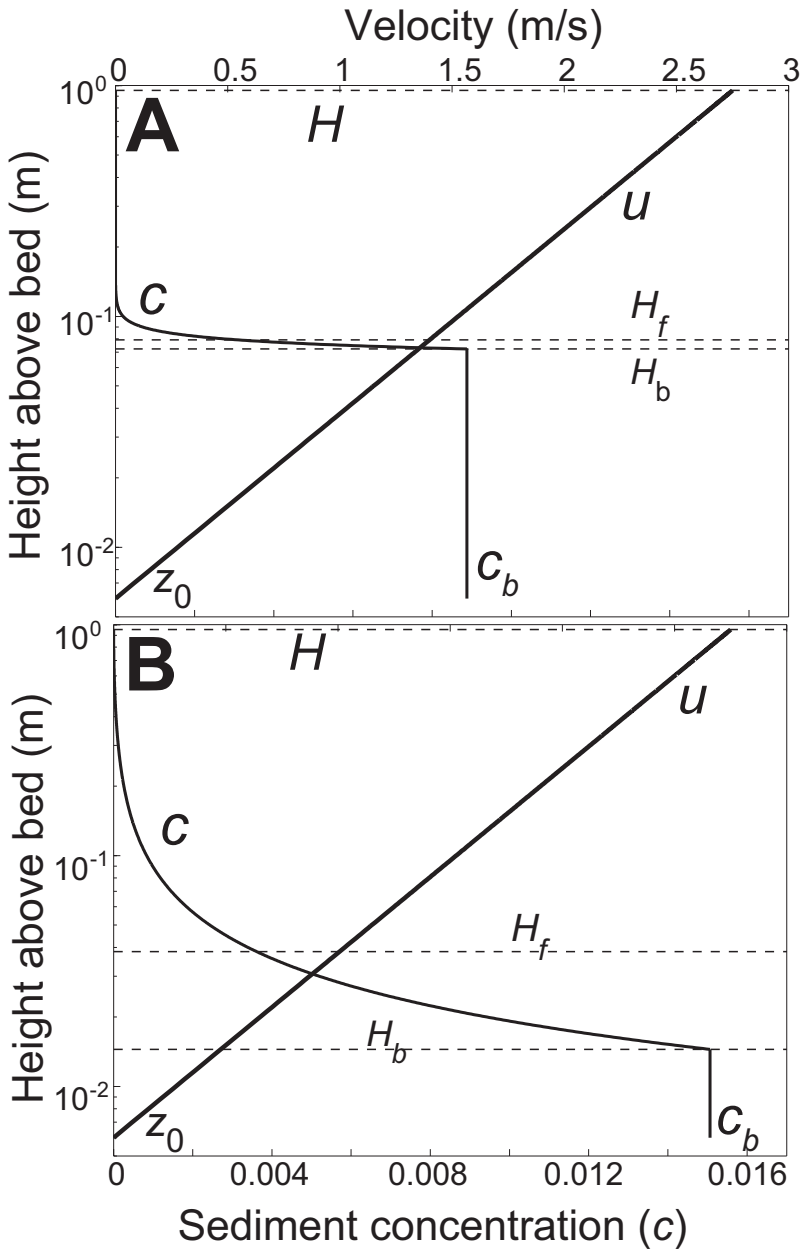

Figure 1. Schematic showing vertical profiles of sediment concentration c (equation 26) and velocity u (equation 21) for the conditions of the Eel River (Table 1), and for **A)** 60-mm gravel and **B)** 1-mm sand. Also shown are the calculated heights of the bedload layer H_b (equation 25), weighted-average particle-fall heights H_f (equation 32), flow depth H (Table 1), and the near-bed sediment concentration c_b (equation 18).

6.4.2. Bedload Transport Capacity, Layer Height, Concentration, and Velocity

Many equations exist for the bedload transport capacity. Here, we use the relation of *Fernandez Luque and van Beek* [1976]:

$$q_{bc} = 5.7\left(RgD^3\right)^{1/2}\left(\tau_* - \tau_{*c}\right)^{3/2}. \tag{23}$$

The sediment transport capacity for the two representative cases is found to be 1.0 x 10^{-3} m^2/s and 3.8 x 10^{-3} m^2/s for the 60-mm gravel and the 1-mm sand, respectively (Table 1).

The depth-averaged bedload velocity and layer height are given as empirical expressions by *Sklar and Dietrich* [2004] derived from several different bedload studies. The best fit relationships are

$$U_b = 1.56\left(RgD\right)^{1/2}\left(\frac{\tau_*}{\tau_{*c}} - 1\right)^{0.56} \tag{24}$$

and

$$H_b = 1.44D\left(\frac{\tau_*}{\tau_{*c}} - 1\right)^{0.50}. \tag{25}$$

The bedload velocities and layer heights for the two representative cases are found to be U_b = 1.26 m/s and H_b = 72.3 mm for the 60-mm gravel, and U_b = 2.6 m/s and H_b = 14.5 mm for the 1-mm sand (Table 1). For the 1-mm sand, equation (24) predicts a

bedload velocity that is greater than the depth averaged fluid velocity. The high transport stage for the sand (τ_* / τ_{*_c} = 102) is beyond the range of empirical data used to formulate equation (24). At large transport stages, particle velocities instead approach the fluid velocity [e.g., *Bennett et al.*, 1998]. To account for this effect, we set $U_b = U$ where equation (24) predicts $U_b > U$. Likewise, in rare cases with large transport stages, large channel slopes, and small flow depths, the empirical equation (25) predicts a bedload layer height (i.e., a saltation hop height) that is greater than the flow depth. In reality, under these conditions the bedload layer likely occupies the entire depth of flow. Therefore, where this occurs we set $H_b = H$. Using these expressions, the near-bed concentration of particles (equation (18)) is found to be 0.0089 and 0.0151 for the 60-mm gravel and the 1-mm sand, respectively (Table 1).

6.4.3. Vertical Structure of Suspended Load

In order to evaluate the erosion rate, the vertical structure of the suspended sediment load must be known. Here we use the most widely accepted expression for the vertical profile of suspended sediment – the *Rouse* [1936] equation

$$c = c_b \left[\frac{(1-\zeta_z)/\zeta_z}{(1-\zeta_b)/\zeta_b} \right]^P , \qquad (26)$$

where $\zeta_z = z/H$, $\zeta_b = H_b/H$, and $P = w_{st}/\beta\kappa u_*$ is the Rouse parameter (Fig. 1). To arrive at equation (26), Rouse balanced the entrainment and settling flux of suspended

sediment, and scaled the entrainment flux as a diffusive process using the well-known parabolic eddy viscosity of momentum for steady, uniform flow:

$$\nu_T = \beta u_* \kappa z (1 - z/H) . \tag{27}$$

The coefficient β is typically thought to be a constant of order unity and accounts for any differences between the diffusivity of momentum and sediment.

As discussed above for the logarithmic velocity profile, several authors have argued that the Rouse profile should not apply because equation (27) is only applicable to the lower 10 – 20% of the water column. Nonetheless, experimental data support use of the Rouse equation throughout the water column, with β ranging from approximately 0.5 to 3 [*Bennett et al.*, 1998; *Graf and Cellino*, 2002; *Nezu and Azuma*, 2004; *Wren et al.*, 2004; *Muste et al.*, 2005]. Due to the present uncertainty in the value of β, we simply assume that $\beta = 1$ in the following calculations.

To apply equation (26), the near-bed concentration (c_b) is calculated from equation (18), where the integral relating suspended-sediment flux to the bulk parameters of the flow (χ) can be found from equations (17), (21), and (26) as

$$\chi = \frac{1}{UH} \int_{H_b}^{H} \left[\frac{(1-\zeta_z)/\zeta_z}{(1-\zeta_b)/\zeta_b} \right]^{\frac{w_{st}}{\kappa u_*}} \frac{u_*}{\kappa} \ln\left(\frac{z}{z_0}\right) dz . \tag{28}$$

The resultant concentration profiles for the representative cases are shown in Figure 1. Due to the low value of the transport stage, most of the 60-mm gravel is contained

within the bedload layer. In contrast, a significant portion of the sediment extends above H_b for the 1-mm sand.

6.4.4. Particle Impact Velocity

For saltating sediment, *Sklar and Dietrich* [2004] used a scaling analysis combined with their empirical fits for L_b, U_b, and H_b to obtain an expression for the impact velocity,

$$w_i = 0.8(RgD)^{1/2}\left(\frac{\tau_*}{\tau_{*c}} - 1\right)^{0.18}\left(1 - \left(\frac{u_*}{w_{st}}\right)^2\right)^{1/2}. \qquad (29)$$

Equation (29) cannot be used in our model because the empirical data used to calibrate the equation does not extend into the suspension regime.

As an alternative approach, we consider particle impacts at the bed due to gravitational settling of particles and advection by turbulent eddies. First, we calculate the impact velocity due to gravitational settling directly from a momentum balance for a falling particle. It is important to calculate the settling velocity as a function of fall distance rather than assuming a terminal velocity because large particles might not have sufficient settling distance to reach terminal velocity upon impact. The component of the particle settling velocity normal to the bed can be calculated from a balance between the forces of gravity and drag as

$$w_s = w_{st}\cos\theta\sqrt{1-\exp\left(-\frac{3C_d\rho_f H_f}{2\rho_s D\cos\theta}\right)}, \tag{30}$$

where

$$w_{st} = \left(\frac{4}{3}\frac{RgD}{C_d}\right)^{1/2} \tag{31}$$

is the terminal settling velocity of the sediment (see Appendix 1). The drag coefficient C_d depends on the particle Reynolds number and grain shape, and we calculate C_d from the empirical formula of *Dietrich* [1982] for natural sediment (Corey Shape Factor = 0.8, Powers Roundness Scale = 3.5).

The particle velocity given by equation (30) depends on the distance over which a particle falls (H_f). In a combined bedload and suspension flow, particles are falling from all distances above the bed (z), from the top of the bedload layer to the depth of the flow ($H_b \le z \le H$). For uniform-size sediment, the average height from which particles fall should depend on the fraction of particles that are suspended to that elevation. Therefore, the shape of the steady-state concentration profile should reflect the relative heights that particles are suspended (and therefore their fall distances). To incorporate these effects, we propose an average fall distance that is weighted by the proportion of the total near-bed sediment c_b that is suspended to that height,

$$H_f = \frac{1}{c_b}\int_H^0 z\frac{dc}{dz}dz\,. \qquad (32)$$

Equation (32) produces expected results. For example, if all sediment is bedload, then equation (32) predicts that all particles fall from the top of the bedload layer, i.e. $H_f = H_b$, because we assume that sediment is uniformly mixed within the bedload layer, i.e. $\frac{dc}{dz} = 0$ for $z < H_b$. The calculated fall distances are shown on Figure 1 for the two representative cases. For the 60-mm gravel, H_f = 79.2 mm, which is only slightly greater than the bedload layer height (H_b = 72.3 mm) (Fig. 1). For the 1-mm sand, H_f = 38.4 mm and is greater than H_b = 14.5 mm, which is expected because the high transport stage for the sand results in more of the load carried above H_b.

In addition to gravity, turbulent fluctuations can advect particles away from the bed (resulting in zero impacts) and towards the bed (resulting in an increased impact rate). Rigorously characterizing the temporal and spatial variability in turbulent fluctuations is beyond the scope of this chapter. As a first-order approach, we assume that turbulent fluctuations follow a Gaussian distribution [e.g., *Bridge and Bennett*, 1992; *Nezu and Nakagawa*, 1993; *Cheng and Chiew*, 1999]. The probability density function (*P*) of velocity fluctuations (*w'*) is given by

$$P(w') = \frac{1}{\sqrt{2\pi}\sigma_w}\exp\left(-\frac{(w')^2}{2\sigma_w^2}\right) \qquad (33)$$

where $\sigma_w = \sqrt{\overline{w'^2}}$ is the standard deviation of velocity fluctuations perpendicular to the bed and the overbar denotes a time average. The standard deviation of these velocity fluctuations has been shown to be approximately equal to u_* in open-channel flow [*Nezu and Nakagawa*, 1993], which we employ here (i.e., $\sigma_w = u_*$).

In order to calculate the particle impact velocity, we assume that particles follow the fluid, so that equation (33) can be used to calculate the probability of fluctuations in *particle* velocity, as well as fluid velocity. Furthermore, we assume that inertial forces dominate near the bed so that particles impact the bed and are not swept laterally with the flow (see section 6.6 for discussion). With these assumptions, the average impact velocity can be found by summing the component of the gravitational settling velocity perpendicular to the bed with the turbulent-velocity fluctuations (which by definition are perpendicular to the bed), and integrating over all possible values of fluctuations as

$$w_i = \int_{-w_s}^{6\sigma_w} (w' + w_s) P dw', \qquad (34)$$

The upper limit of integration was chosen because it incorporates very near 100% of the positive fluctuations (Fig. 2). The lower limit, on the other hand, defines the condition $w' + w_s = 0$. Where $w' + w_s < 0$, particles are moving upwards and the impact velocity and impact rate are zero. Thus, despite the fact that the Gaussian distribution is symmetrical, the mean impact velocity can deviate from the gravitational settling velocity because the impact velocity must be non-negative (Fig. 2).

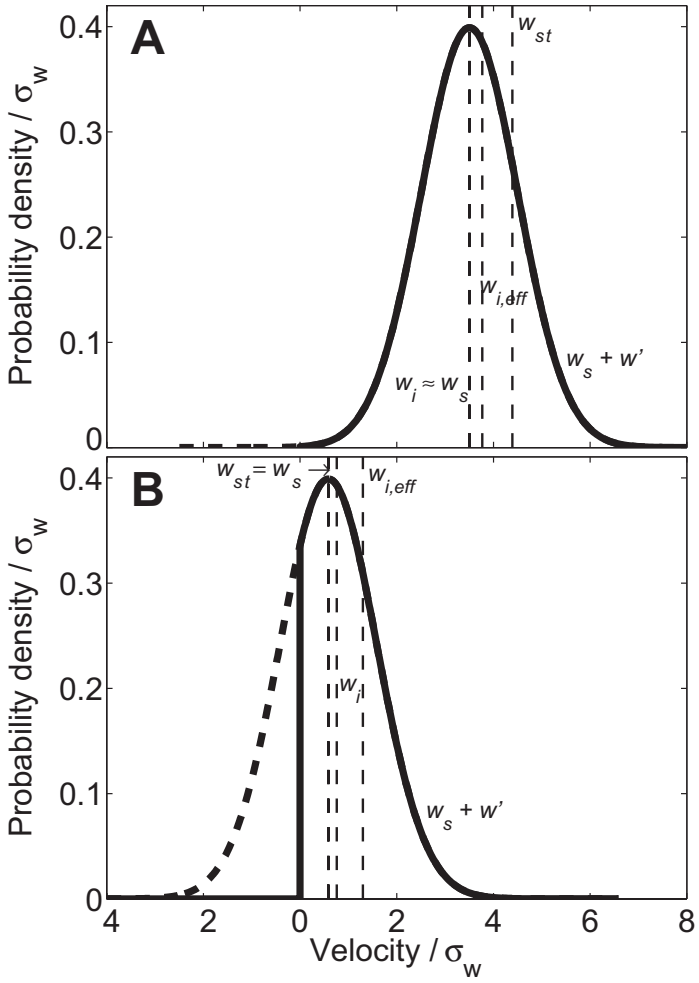

Figure 2. Probability density function for the particle velocity normalized by one standard deviation for **A**) 60-mm gravel and **B**) 1-mm sand. The density functions are centered about the gravitational settling velocity (w_s) and the distribution in velocity is due to turbulent fluctuations given by equation (33). The solid thick line shows the portion of the distribution that is integrated to calculate the average impact velocity (w_i) and the effective impact velocity ($w_{i,eff}$). The dashed thick line is the portion of the distribution that is not included in the integration because only non-negative velocities produce impacts.

The deviation of the impact velocity from the gravitational settling velocity is more important when considering that the erosion rate scales with the impact velocity cubed (equation 19). The erosion rate depends on the cube of the individual particle velocities (i.e., $w'+w_s$), however, and not the average impact velocity w_i. Thus to formulate an average impact velocity that scales with the erosion rate, we define the effective impact velocity by non-linear averaging, as

$$w_{i,eff} = \left[\int_{-w_s}^{6\sigma_w} (w'+w_s)^3 P dw' \right]^{1/3} . \qquad (35)$$

Similar to the turbulent fluctuations, the gravitational settling velocity also could be weighted to account for the cubic dependence of erosion rate on impact velocity, rather than using the velocity for the linearly averaged fall distance calculated in equation (32). We found, however, that accounting for this has a negligible effect on the results and therefore is neglected for simplicity.

Figure 2 shows the predicted probability density of impact velocities for the two representative cases. For the 60-mm gravel at τ_* / τ_{*c} = 1.7, the gravitational fall velocity is sufficiently large compared to the turbulent fluctuations, so that only the very tail of the distribution is within the regime $w'+w_s < 0$ (shown as a thick dashed line in Figure 2A). The result is that turbulent fluctuations tend to cancel, and therefore $w_i \approx w_s$. This notwithstanding, the minor asymmetry in the probability density function results in an average impact velocity that is slightly greater than that predicted from gravitational settling alone. As expected, this effect is enhanced for the

effective impact velocity $w_{i,eff}$ due to the cube of the velocity fluctuations (Fig. 2A). For the 60-mm gravel, both w_i and w_s are smaller than w_{st} because the fall distance is not sufficient for particles to reach terminal settling velocity.

Turbulence has a much stronger effect on the predicted impact velocities for the 1-mm sand owing to the large transport stage. Here the fall distance is sufficient that the gravitational fall velocity is equal to the terminal settling velocity (i.e., $w_s = w_{st}$) (Fig. 2B). The predicted average impact velocity is greater than the gravitational fall velocity because of turbulence. Figure 2B shows that a substantial portion of the probability distribution is within the regime $w'+w_s < 0$. Again, because impact velocities must be non-negative, the distribution is truncated at $w'+w_s = 0$ before integrating. This results in an asymmetric distribution and an average impact velocity and effective impact velocity that are much greater than the gravitational settling velocity (i.e., $w_{i,eff} > w_i > w_s$) (Fig. 2B).

Figure 3 illustrates the effect of transport stage on the different velocity formulations. The velocities shown are calculated for 60-mm particles falling from the top of the bedload layer (i.e., $H_f = H_b$). For the case of pure gravitational settling (w_s), the velocity increases as the bedload-layer height increases (equation 25) until a transport stage of about 10, beyond which particles are calculated to fall at the terminal velocity. The average impact velocity w_i and the effective impact velocity $w_{i,eff}$ are nearly equal to the gravitational settling velocity for low transport stages ($\tau_* / \tau_{*c} < 10$), which is expected since u_* is small. However, these velocities deviate significantly from the gravitational settling velocity where $w_s - u_* < 0$ because the distribution in

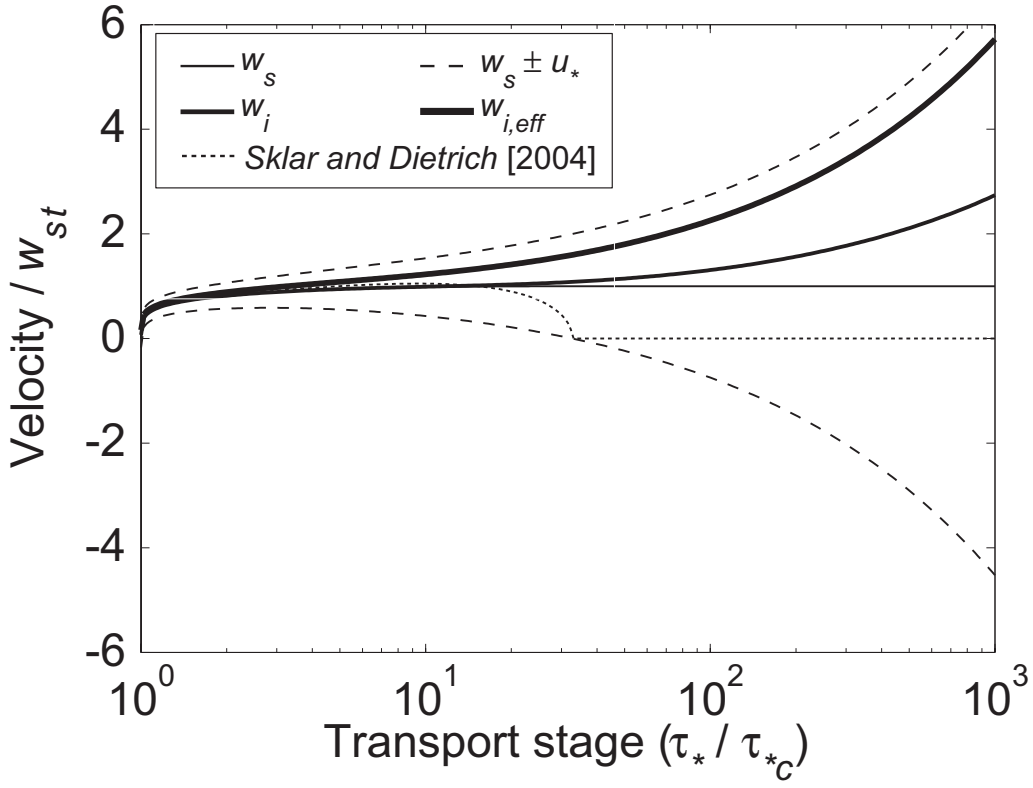

Figure 3. Calculated particle velocities relative to the terminal settling velocity (w_{st}) as a function of transport stage for 60-mm particles falling from the top of the bedload layer. Also shown by dashed lines is the settling velocity plus and minus one standard deviation due to turbulent fluctuations. The gravitational settling velocity (w_s) was calculated from equation (30) and approaches the terminal settling velocity at large transport stages. The calculated impact velocity (w_i) and effective impact velocity ($w_{i,eff}$) deviate from w_s at large transport stages where turbulence becomes significant. The impact velocity according to *Sklar and Dietrich* [2004] goes to zero at a transport stage of about 30. The plot would be slightly different, but qualitatively similar, for different particle sizes due to changes in the drag coefficient.

particle velocities becomes increasingly asymmetric. The result is that w_i and $w_{i,eff}$ are significantly greater than the terminal settling velocity for large transport stages. Note that all velocity measures calculated herein (i.e., w_s, w_i and $w_{i,eff}$) converge with the predictions of the empirical equation (29) at low transport stages, which is expected since this is the regime in which it was calibrated. Equation (29) predicts an impact velocity of zero at large transport stages (i.e., $u_* > w_{st}$), which contrasts with the velocity model proposed herein.

6.4.5. Bedrock Erosion by Total Load

Finally, to calculate the erosion rate, $w_{i,eff}$ replaces w_i in equation (19) resulting in

$$E = \frac{A_1 \rho_s Y}{k_v \sigma_T^2} \frac{q w_{i,eff}^3}{\left(UH\chi + U_b H_b\right)} \left(1 - \frac{q_b}{q_{bc}}\right) . \qquad (36)$$

Equation (36) can by non-dimensionalized as

$$E^* = \frac{E\sigma_T^2}{\rho_s Y (gD)^{3/2}} = \frac{A_1}{k_v} \left[\frac{q}{\left(UH\chi + U_b H_b\right)}\right] \left[\frac{w_{i,eff}}{(gD)^{1/2}}\right]^3 \left[1 - \frac{q_b}{q_{bc}}\right]. \qquad (37)$$

This reveals that E^* is a function of the three dimensionless quantities shown in brackets: 1) the normalized sediment supply or equivalently the near-bed sediment

concentration (see equation (18)), 2) the normalized effective impact velocity cubed, and 3) the relative sediment supply. By introducing the empirical expressions proposed in section 6.4, E^* can be shown to be a function of particle size, transport stage, relative sediment supply, and flow depth (or equivalently channel-bed slope for a given transport stage). The dependency on flow depth was not revealed in the saltation-abrasion model (equation 6). In the total-load model, it arises because both the near-bed sediment concentration and the gravitational fall velocity are sensitive to the vertical distribution of sediment in the water column, which in turn is a function of flow depth.

6.5. Model Results

Model results are shown for the two cases, where the total load is composed of either 60-mm gravel or 1-mm sand. The predicted erosion rates are given in millimeters per year; however, these rates are instantaneous and have not been multiplied by an appropriate intermittency factor for events that cause erosion. For the representative event of the South Fork Eel River, the instantaneous erosion rates for the gravel and sand are predicted to be 31 mm/yr and 10 mm/yr (Table 1), respectively. This yields an annual average erosion rate of 1.9 mm/yr and 0.6 mm/yr using an appropriate intermittency factor for the Eel River of 0.06 (see *Sklar* [2003] and *Sklar and Dietrich* [2004] for details). These predicted erosion rates seem reasonable given the average landscape lowering rate of 0.9 mm/yr [*Merritts and Bull*, 1989].

To explore model predictions over a wide range of parameter space, we vary sediment supply, flow depth, or channel slope for a given grain size and hold the other variables to constant values specified for the Eel River (Table 1). In addition to our

total-load erosion model, the predictions of the saltation-abrasion model are shown for comparison, and we set $A_1 = A_2 = 0.36$. The integrals in equations (22), (28), (32), (34) and (35) are solved numerically.

6.5.1. Effect of Transport Stage

Figure 4 shows the erosion rate as a function of transport stage and absolute sediment supply (q) and particle size (D) are held constant (Table 1). For a given grain size, the transport stage can be varied by changing either the channel slope or flow depth or both. The solid lines are the predictions for a constant slope ($S \equiv \tan\theta = 0.0053$; Table 1) and a varying transport stage due to flow depth. Alternately, the dashed lines are the predictions for a constant flow depth (H = 0.95 m) and a varying transport stage due to channel-bed slope.

For 60-mm gravel, the total-load model predicts zero erosion at transport stages $\tau_* / \tau_{*c} \leq 1.5$ because the transport capacity is less than the supply of sediment (Table 1), and the bed is therefore predicted to be covered with sediment. As transport stage increases, the rate of erosion increases as the bedrock becomes rapidly exposed. The rate of erosion initially peaks at $\tau_* / \tau_{*c} \approx 2.5$ with an erosion rate of ~70 mm/yr. For larger transport stages (but smaller than $\tau_* / \tau_{*c} \approx 50$) the models predict a decreasing erosion rate with transport stage. This is because for a constant sediment load, more sediment is held in the upper water column (i.e., χ and H_b increase in equation (18)), sediment is advected over the bed at a faster rate (i.e., U and U_b increase in equation

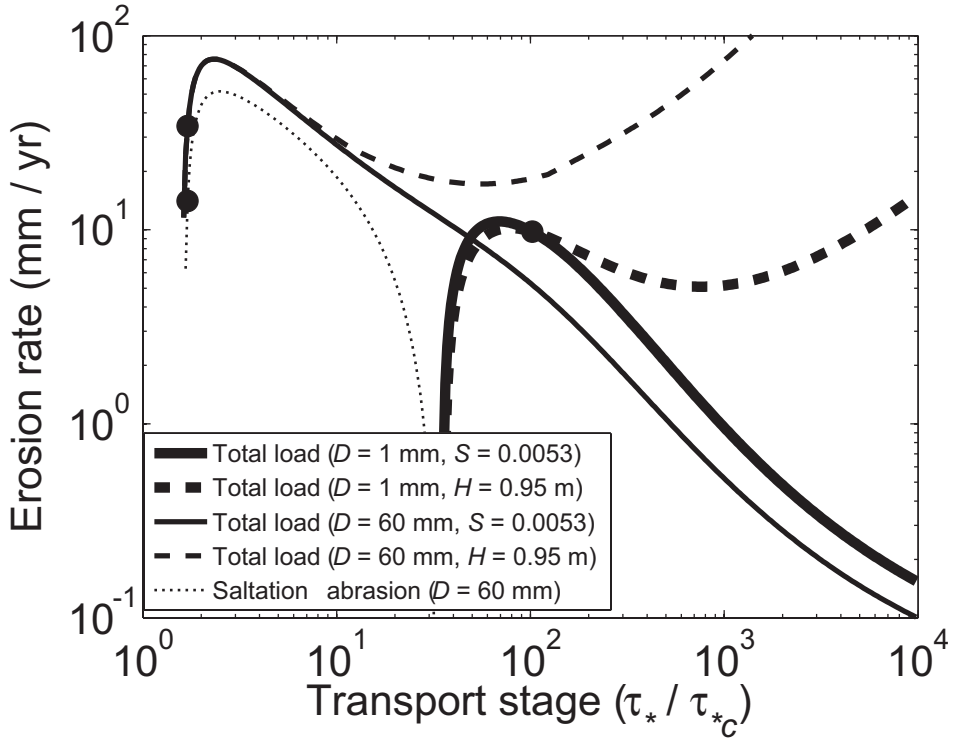

Figure 4. Log-log plot of erosion rate as a function of transport stage for 60-mm gravel and 1-mm sand. Two cases are shown for each particle size. For the first, shown by solid lines, the channel slope is S = 0.0053, and the flow depth varies with transport stage. For the second case, shown by dashed lines, the flow depth is H = 0.95 m, and the channel slope varies with transport stage. For all cases, the sediment supply is 8.9 x 10^{-4} m^2/s. The saltation-abrasion model is shown only for 60-mm gravel because it predicts near zero erosion for the 1-mm sand at all transport stages. The black circles are the conditions for the representative field case of the Eel River (Table 1).

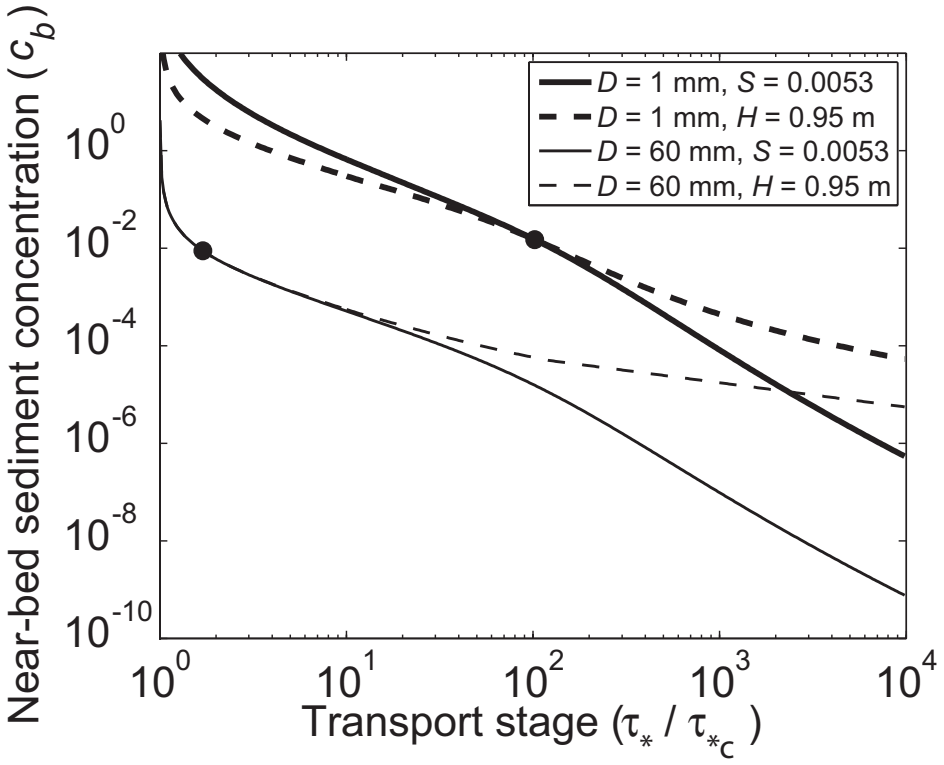

Figure 5. Log-log plot of near-bed sediment concentration as a function of transport stage for 60-mm gravel and the 1-mm sand. Two cases are shown for each particle size. For the first, shown by solid lines, the channel slope is S = 0.0053, and the flow depth varies with transport stage. For the second case, shown by dashed lines, the flow depth is H = 0.95 m, and the channel slope varies with transport stage. For all cases, the sediment supply is 8.9 x 10^{-4} m^2/s. The black circles are the conditions for the representative field case of the Eel River (Table 1).

(18)), and therefore the near-bed sediment concentration and the impact rate per unit bed area decrease with increasing transport stage.

Figure 5 illustrates the reduction in c_b as transport stage increases. The decrease in sediment concentration is more significant for the constant-slope case as compared to the constant-depth case. This is because an increased flow depth, in addition to transport stage, results in a reduction in near-bed sediment because a greater load can be transported in suspension in deeper flow (i.e., *H* increases equation (18)). In calculating the erosion rate, however, the reduction in c_b is offset by the increasing impact velocity with transport stage (Fig. 3). For the constant-depth case, the increased impact velocity more than compensates for the decrease in c_b at large transport stages (τ_* / τ_{*c} > ~50), resulting in an ever-increasing erosion rate with transport stage for steep slopes (S > ~0.15) (Fig. 4). Where slope is held constant the erosion rate decreases (but remains non-zero) with increasing transport stage.

Predictions for the 1-mm sand are qualitatively similar to the 60-mm gravel. The bed is predicted to be covered for τ_* / τ_{*c} < ~25 and the initial peak in erosion rate (~10 mm/yr) occurs at $\tau_* / \tau_{*c} \approx 100$. The magnitude of erosion is smaller for the sand as compared to the gravel because of its lower gravitational settling velocity. For the constant depth case, the erosion rate again increases with transport stage for large transport stages (τ_* / τ_{*c} > ~10^3) equivalent to *S* > ~0.05.

The saltation-abrasion model for the 60-mm gravel is qualitatively similar to the total-load model for small transport stages. The total-load model peaks at a slightly higher erosion rate because of the different formulation of the impact velocity (i.e.

equation (35) vs. (29)). The saltation-abrasion model differs from the total-load model at large transport stages because it forces the erosion rate to zero at $u_* / w_{st} = 1$, which corresponds to $\tau_* / \tau_{*c} \approx 35$. The saltation-abrasion model for 1-mm sand is not shown on Figure 4 because it predicts zero erosion for almost all transport stages because there is only a narrow range in which the bed is exposed and $u_* / w_{st} < 1$.

6.5.2. Effect of Sediment Supply

Figure 6 shows the model predictions of erosion rate as a function of relative sediment supply (q / q_{bc}) with constant values of transport stage, flow depth, and channel slope (Table 1). The saltation-abrasion model predicts a peak in erosion rate where the supply of sediment is one half the bedload-transport capacity. The erosion rate goes to zero where the sediment supply is zero because there are no particle impacts. At high relative supply, the erosion rate also goes to zero because of bed coverage. This upper limit is $q / q_{bc} = 1$ for the saltation-abrasion model because all of the supplied sediment is assumed to travel as bedload (i.e., $q = q_b$). The total-load model, however, indicates that erosion is possible where the supply exceeds the bedload capacity because some of the load is transported in suspension. Thus, the bedload flux (q_b) can be less than the bedload capacity, even though the total load (q) is not. This effect is more pronounced for the 1-mm sand than for the 60-mm gravel because a greater proportion of the sediment load is traveling in suspension (due to the higher transport stage). For the 1-mm sand, erosion persists until the supply is nearly double the bedload transport capacity (Fig. 6).

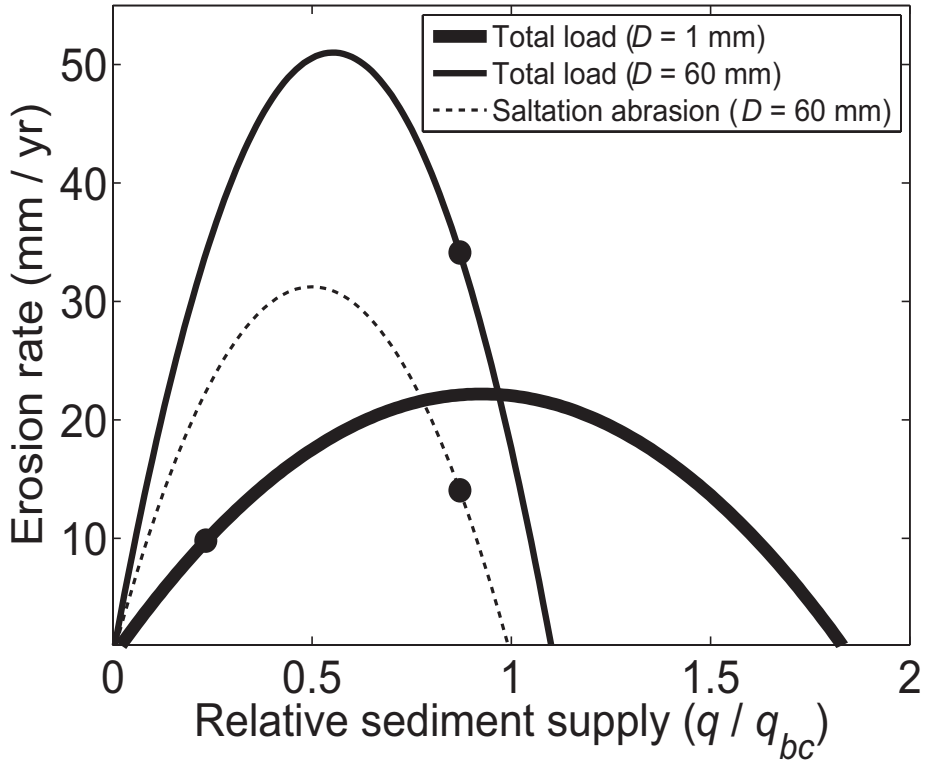

Figure 6. Erosion rate as a function of relative sediment supply for 60-mm gravel and 1-mm sand for the same hydraulic conditions (i.e., bed shear stress, flow depth, channel slope, and flow velocity (Table 1)). This corresponds to a transport stage of 1.7 and 102 for the gravel and sand, respectively. The saltation-abrasion model is shown only for 60-mm gravel because it predicts near zero erosion for the 1-mm sand at all transport stages. The black circles are the conditions for the representative field case of the Eel River (Table 1).

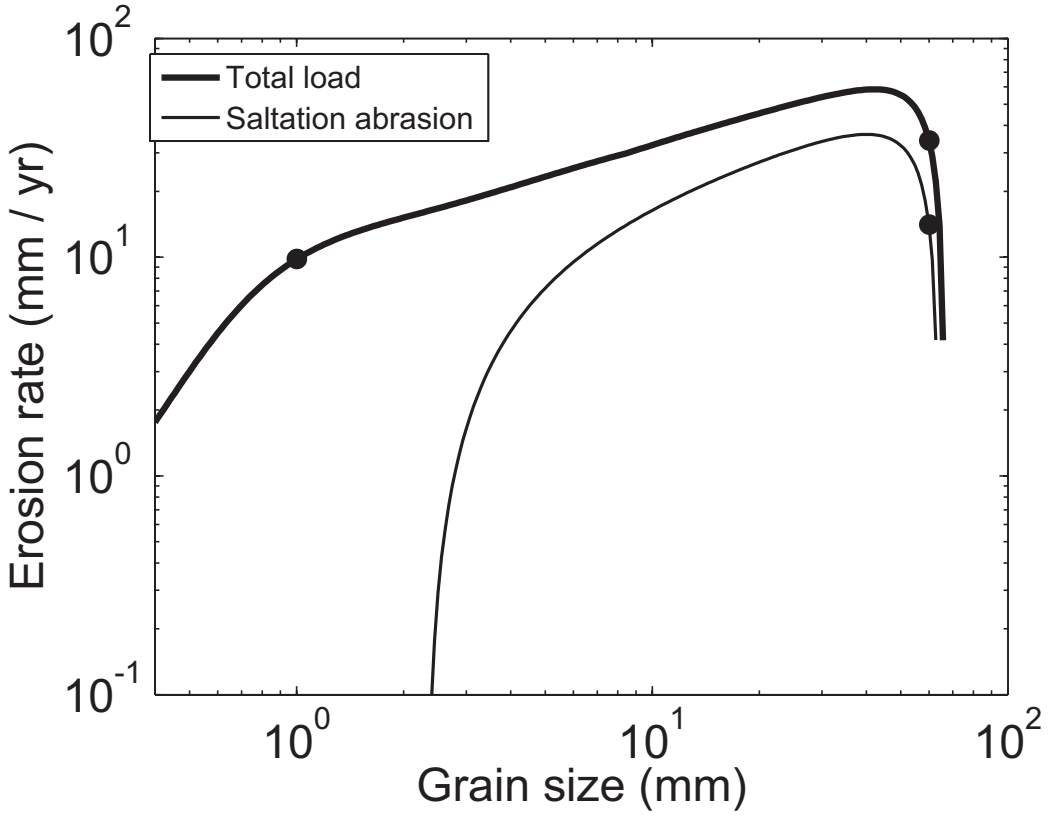

Figure 7. Log-log plot of erosion rate versus grain size for a constant flow depth (H = 0.95 m), channel slope (S = 0.0053) and sediment supply (8.9 x 10^{-4} m^2/s). The black circles are the conditions for the representative field case of the Eel River (Table 1).

6.5.3. Effect of Grain Size

Figure 7 shows erosion rate as a function of grain size, with a constant sediment supply, flow depth and channel slope (Table 1). For large grain sizes, the models predict zero erosion because the flow is not competent to transport these sizes, such that the bed is predicted to be covered with alluvium. Because of the dependence of erosion rate on gravitational settling velocity, the erosion rate decreases rapidly as grain size decreases. The saltation-abrasion model predicts zero erosion for sizes smaller than about 2 mm because $u_* / w_{st} > 1$. In contrast, the total-load model predicts a finite erosion rate for $u_* / w_{st} > 1$.

6.5.4. Effect of Flow Depth and Channel Slope

In contrast to the saltation-abrasion model, the total-load model is a function of flow depth, or channel slope for a given transport stage. Flow depth affects the erosion rate in two competing ways. First, the impact rate depends on the near-bed sediment concentration, which, among other things, is a function of flow depth. For the same bed shear-stress, particle size and sediment supply, a deeper flow on a smaller slope will have less sediment near the bed and a lower impact rate than a shallower flow on a steeper slope. On the other hand, for particles that do not attain terminal velocity, the particle impact velocity is larger in deeper flows because of the greater fall distance.

Figure 8 shows the erosion rate as a function of flow depth and channel slope, with a constant transport stage and sediment supply. For the 60-mm gravel, the erosion rate is nearly constant at low channel slopes, but decreases as slope increases. For this sediment size, the increased impact rate in shallower and steeper flows is more than

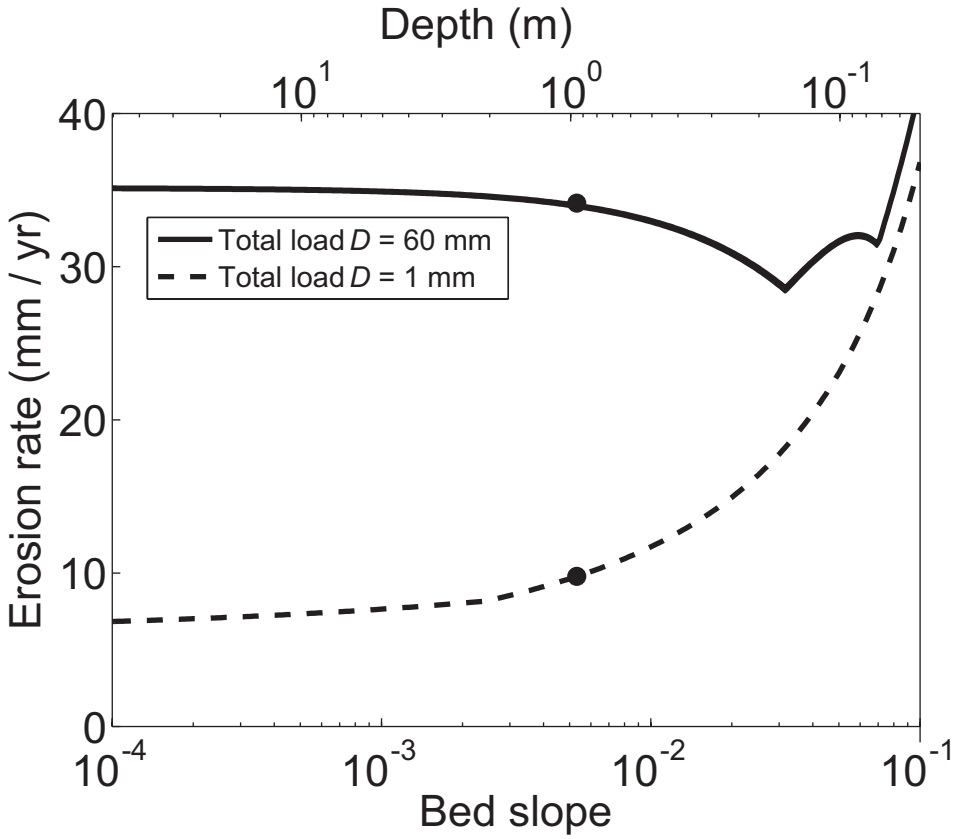

Figure 8. Erosion rate as a function of channel slope and flow depth for the 60-mm gravel (with a constant transport stage of 1.7) and the 1-mm sand (with a constant transport stage of 102) using a constant sediment supply (8.9×10^{-4} m^2/s). The saltation-abrasion model would plot as a horizontal line because it is not sensitive to the relative contributions of slope and flow depth in setting the transport stage. The black circles are the conditions for the representative field case of the Eel River (Table 1).

compensated for by the drop in impact velocity (due to the reduced fall distance), resulting in a decrease in erosion rate with increasing slope. In contrast, finer sediment rapidly reaches terminal velocity so that changes in flow depth have little effect on impact velocity. Thus, the erosion rate for 1-mm sand is predicted to increase with increasing slope due to the greater impact rate that results from the increased near-bed sediment concentration in steeper flows with smaller flow depths.

The abrupt increase in erosion rate for the 60-mm gravel at $S \approx 0.04$ and $H \approx 0.2\,\text{m}$ occurs where the bedload velocity given by equation (24) is predicted to be larger than the fluid velocity (equation 22), and therefore we set $U_b = U$ (see section 6.4.2). The jump in erosion rate is because the bedload velocity is predicted to increase with transport stage (regardless of flow depth), whereas U systematically decreases with increasing slope (and decreasing flow depth). This results in a heightened near-bed sediment concentration and erosion rate. The second jump in erosion rate at $S \approx 0.07$ and $H \approx 0.07\,\text{m}$ is where $H_b = H$, which again results in a heightened near-bed sediment concentration with increasing slope (and decreasing flow depth).

6.5.5. Contour Plots of Erosion Rate

To evaluate the total-load model over a wide range of parameter space, Figures 9-11 show contours of erosion rate versus transport stage and relative sediment supply. The saltation-abrasion model shows a peak erosion rate at a relative sediment supply of 0.5 and a transport stage of $\tau_* / \tau_{*c} \approx 15$ for both the 1-mm sand and the 60-mm gravel (Fig. 9). The peak erosion rate occurs at a slightly different transport stage for the two different sediment sizes because the relationship between transport stage and the onset

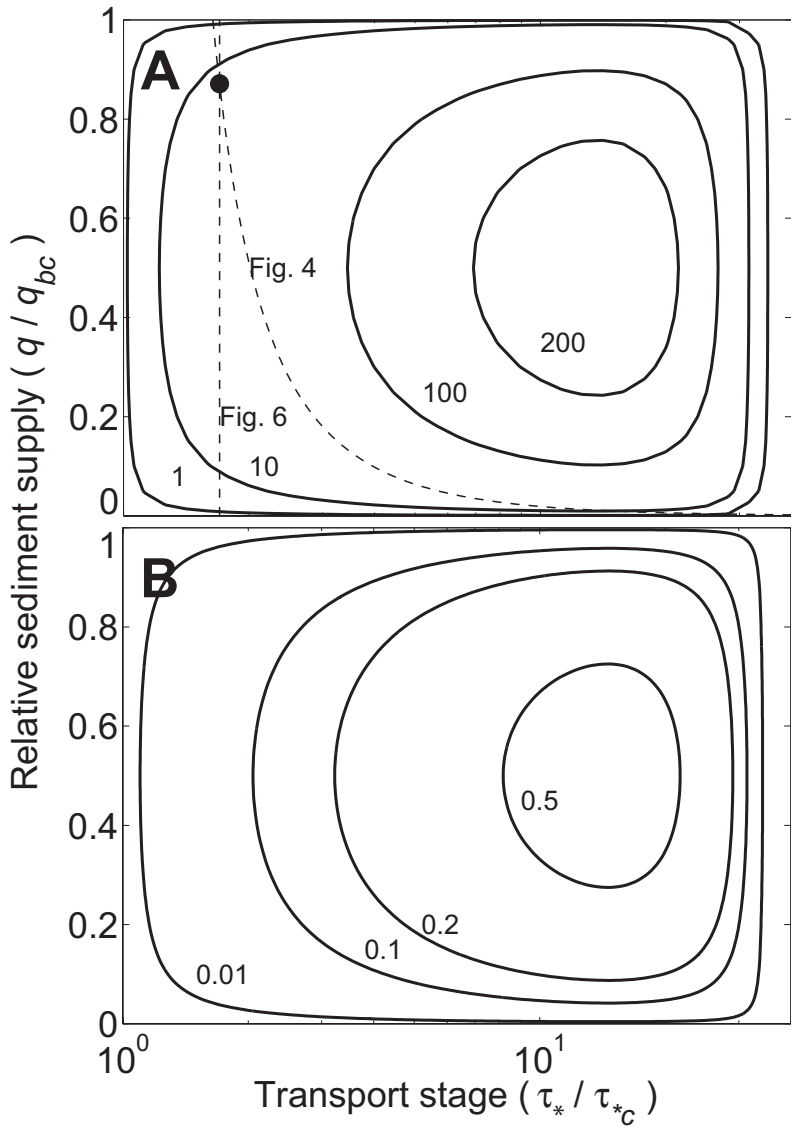

Figure 9. Contour plots of erosion rate in millimeters per year for the saltation-abrasion model versus transport stage and relative sediment supply for **A)** 60-mm gravel and **B**) 1-mm sand. The dashed lines are slices through parameter space that are shown on Figures 5 and 6. The black circles are the conditions for the representative field case of the Eel River (Table 1).

of suspension is a function of the drag coefficient, which is grain-size dependent [*Dietrich*, 1982]. The erosion rate goes to zero at high and low transport stages because of the onset of suspension and the threshold of motion, respectively. The erosion rate goes to zero at high and low relative sediment supply because of the effects of bedrock coverage and particle impact rate, respectively (see *Sklar and Dietrich* [2004] for a detailed discussion).

The contour plots of the total-load erosion model are strikingly different than the model that considers only bedload (Figs. 10 and 11). Figure 10 shows the erosion rate for a constant channel slope, so that transport stage is only a function of flow depth. Like the bedload model, the erosion rate increases with increasing transport stage because the impact velocity increases with increasing flow depth. The erosion rate, however, does not decline at large transport stages (for a given relative sediment supply). Instead, it increases because the heightened impact velocity due to turbulence. The dashed lines on Figure 10 show the 2-D parameter space represented in Figures 4 and 6. These show that an increase in transport stage results in a decrease in relative supply (q / q_{bc}), if the absolute sediment supply (q) is constant. This is the reason for the decrease in erosion rate at high transport stages in Figure 4. The contour plots, however, reveal that the erosion rate can increase indefinitely with increasing transport stage, as long as the absolute sediment supply also increases with transport stage. In such a case, the erosion rate does not have a maximum value (Fig. 10). Furthermore, at large transport stages ($\tau_* / \tau_{*c} > 100$), the erosion rate can be nonzero for sediment loads that are much larger than the bedload transport capacity.

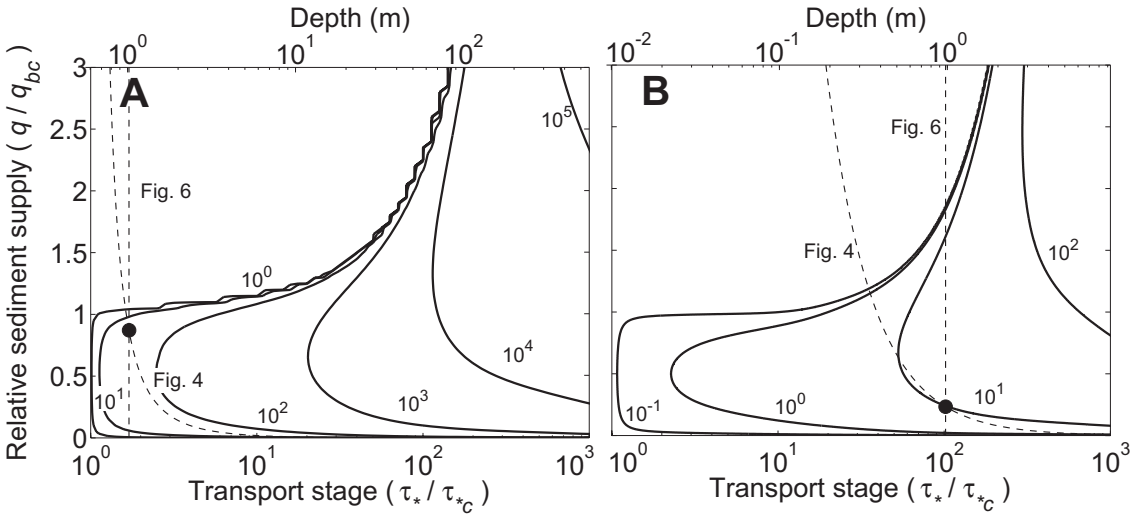

Figure 10. Contour plots of erosion rate in millimeters per year predicted by the total-load erosion model for **A)** 60-mm gravel and **B)** 1-mm sand. The dashed lines are slices through parameter space that are shown on Figures 4 and 6. The black circles are conditions for the field case of the Eel River (Table 1). The channel slope is held constant at S = 0.0053, so that transport stage is a function of flow depth. Note that three orders of magnitude in transport stage are explored here, versus only one in Figure 9. For the 60-mm gravel, the large transport stages shown correspond to unrealistic flow depths for the Eel River (see discussion in Section 6.3), but are shown for sake of comparison with the 1-mm sand.

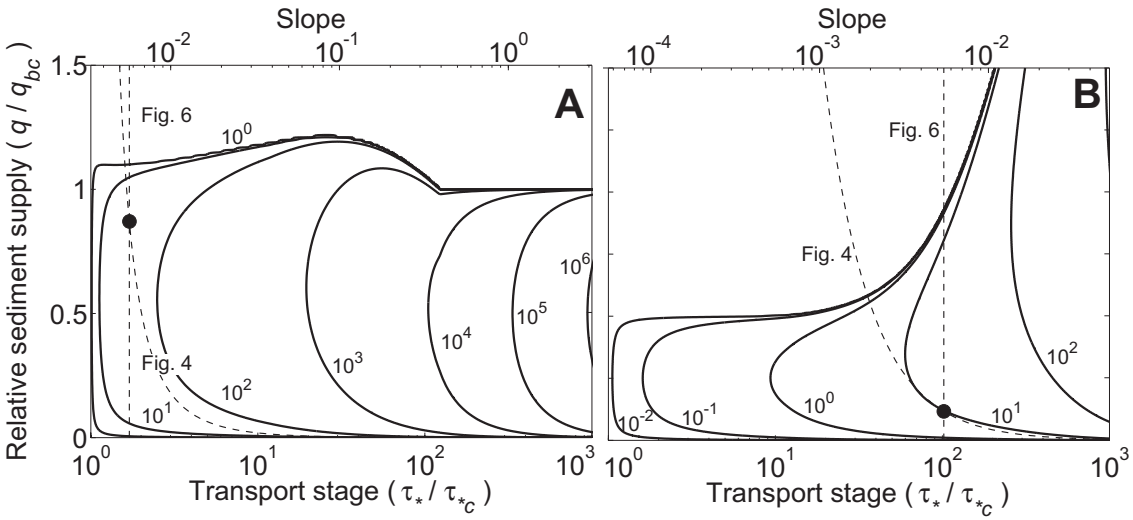

Figure 11. Contour plots of erosion rate in millimeters per year for the total-load erosion model for **A)** 60-mm gravel and **B)** 1-mm sand. The dashed lines are slices through parameter space that are shown on Figures 5 and 6. The black circles are conditions for the field case of the Eel River (Table 1). The flow depth is held constant at H = 0.95 m, so that the transport stage is a function of channel slope. The vertical axes differ for the 60-mm gravel and the 1-mm sand.

Figure 11 shows contour plots of erosion rate for the total-load model, but now the flow depth is held constant (rather than channel slope) at H = 0.95 m and therefore transport stage is only a function of slope. The predictions for the 1-mm sand (Fig. 11B) are qualitatively similar to the cases with constant channel slope (Fig. 10). However, as discussed in Section 6.5.1, the erosion rate is generally greater if depth is held constant, rather than slope, because the near-bed sediment concentration (and therefore impact rate) is a function of flow depth. This allows, for example, an ever increasing erosion rate with transport stage for large transport stages ($\tau_* / \tau_{*c} > \sim 50$), even if the absolute sediment supply is constant (Figs. 5, 11B). For the 60-mm gravel, the erosion rate is predicted to be zero for values of the relative sediment-supply greater than about unity (Fig. 11A). This is because, for the large slopes considered here, the bedload layer height predicted by equation (25) exceeds the flow depth, which results in zero flux of suspended sediment since the bedload layer occupies the entire water column.

6.6. Discussion

6.6.1. Entrainment Capacity for Total Load

Equation (36) contains a transport capacity for bedload q_{bc}, in which erosion is zero if $q_b > q_{bc}$ due to depositional cover. For flows with significant suspended sediment, the transport capacity of the total load is typically formulated in terms of a maximum near-bed sediment concentration instead of a maximum bedload flux [*Smith and McLean*, 1977; *Parker*, 1978; *García and Parker*, 1991]. This maximum sediment

concentration can be found by equating equations (11) and (16), i.e. $c_b = \alpha$, as discussed in Section 6.3.3. Under most model results shown, the near-bed sediment concentration did not exceed α, where α was calculated using the empirical model of *Garcia and Parker* [1991]. This, however, is not true for the 1-mm sand at small transport stages. Figure 12 shows the same model results as Figure 10B, except that the erosion rate is set to zero where $c_b > \alpha$. In this case, the bed is predicted to be covered with 1-mm sediment (and thus the erosion rate is zero) for $\tau_* / \tau_{*c} <$ ~10. This indicates a need for an accurate model of the maximum near-bed sediment concentration for both bedload and suspension conditions, and particularly the transition in between.

6.6.2. Viscous Damping of Impacts

Sklar and Dietrich [2004] assumed that there was not a threshold kinetic energy required to cause erosion in their model based on abrasion-mill experiments [*Sklar and Dietrich*, 2001], an assumption that we adopted in the total-load erosion model. Nonetheless, considering the fine particles addressed here, it is possible that some impacts might be viscously damped. Theoretical and experimental results suggest that particle-wall impacts can be viscously damped, and the degree to which is a function of the particle Stokes number [*Davies et al.*, 1986; *Lian et al.*, 1996; *Schmeeckle et al.*, 2001; *Joseph and Hunt*, 2004]. For spheres impacting a wall, the Stokes number can be written as,

$$St = \frac{\rho_s w_p D}{9 \rho_f \nu}, \tag{38}$$

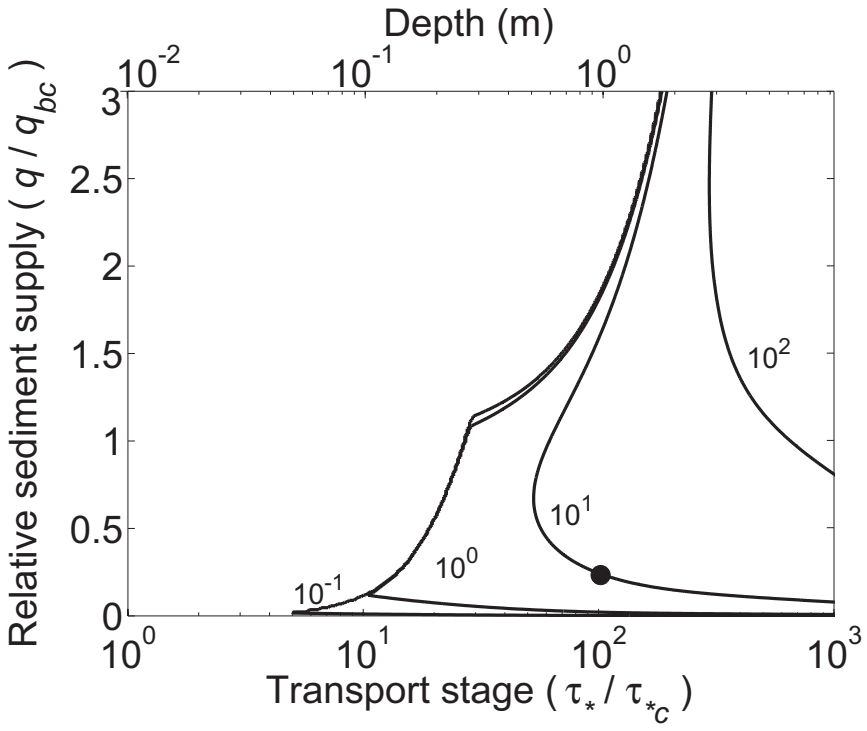

Figure 12. Contour plot of erosion rate in millimeters per year for the same model parameters as Figure 10B, except that erosion rate is set to zero where the near-bed sediment concentration exceeds the entrainment capacity of the flow (i.e., $c_b > \alpha$). The black circle represents the conditions for the field case of the Eel River (Table 1).

and is a measure of the particle inertia relative to the viscous force exerted on the particle from the fluid, where ν is the kinematic viscosity of the fluid (10^{-6} m^2/s) and w_p is the particle velocity. Both *Schmeeckle et al.* [2001] and *Joseph and Hunt* [2004] found that impacts from glass spheres were partially damped for $St <$ ~100, and completely damped for $St <$ ~ 30. *Schmeeckle et al.* [2001] also show that data are more scattered for natural sediment due to their nonspherical nature.

Figure 13A shows the results of the total-load erosion model for 1-mm sand, where the erosion rate was set to zero for particle impacts with $St < 30$ (where $w_p = w' + w_s$ in equation (25)). For this case, the 1-mm sand is predicted to cause no erosion for transport stages less than about 3. For larger transport stages the sand does erode the bed because the enhanced impact velocity due to turbulence increases the Stokes number to $St > 30$. Viscous damping apparently has no effect on the 60-mm gravel because the gravitational settling velocity is great enough that $St > 30$ for all transport stages.

Figure 13B shows the erosion model predictions compared to data from the abrasion mill experiments of *Sklar and Dietrich* [2001]. The experiments were performed by mechanically stirring sediment and water in a cylindrical basin with a bedrock floor. Particle size was varied whereas the total volume of sediment, which is equivalent to q in a closed system, was held constant. The saltation-abrasion model matches the data well for large particle sizes, but predicts zero erosion for the medium sand (D = 0.4 mm) because it was in suspension. The total-load erosion model, on the other hand, captures the measured finite erosion for the medium sand (Fig. 13B), but

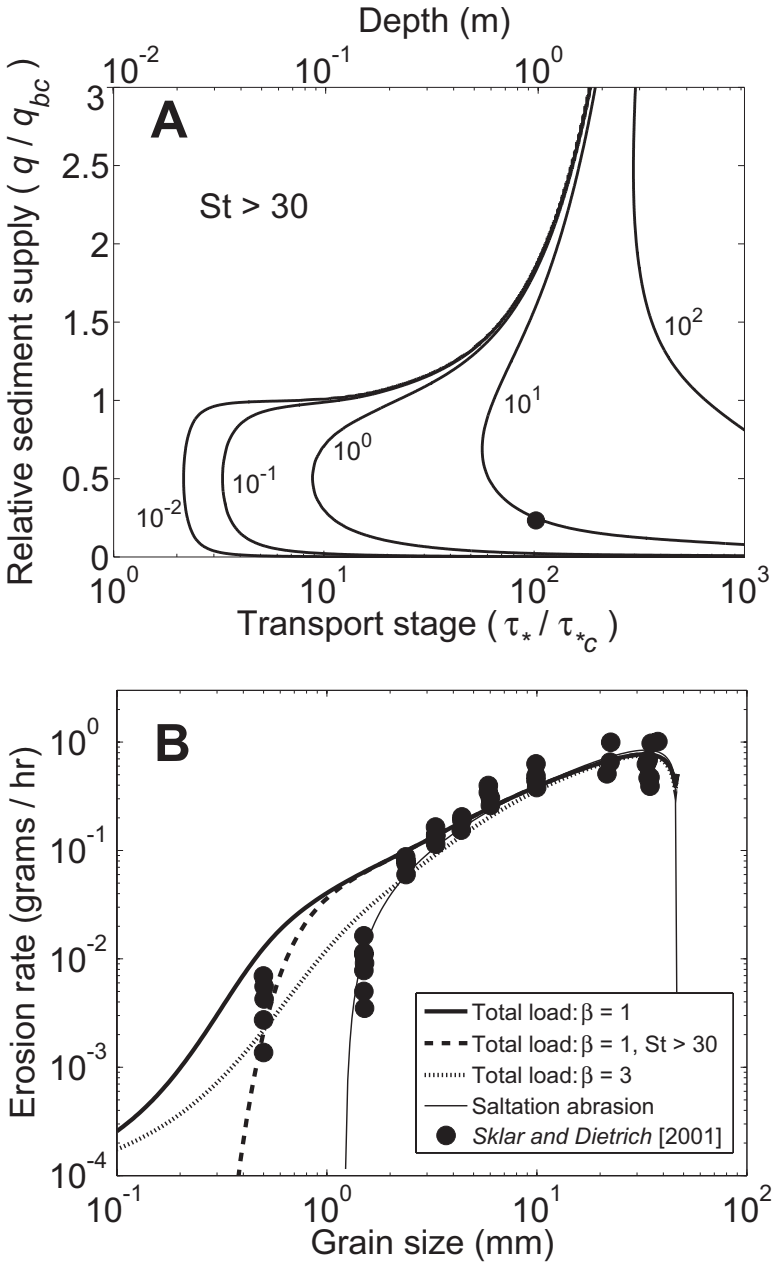

Figure 13. A) Contour plot of erosion rate in millimeters per year for the same model parameters as Figure 10B, except that the erosion rate is set to zero if particle impacts have a particle Stokes number less than 30. The black circle represents the conditions for the field case of the Eel River (Table 1). **B)** Comparison of the total-load erosion model and the saltation-abrasion model with the experimental abrasion-mill data of *Sklar and Dietrich* [2001]. To make these calculations $A_1 = 0.2$, $H = 0.5$ m, $k_v = 3 \times 10^{-5}$, $\sigma_T = 9$ MPa, $u_* = 0.15$ m/s, $q = 4.2 \times 10^{-4}$ m^2/s, and the cover term was neglected (see *Sklar and Dietrich* [2004] for more details).

over predicts the erosion rate. Although the fit seems better by including a Stokes number cutoff (Fig. 13B), it is nonetheless difficult to evaluate whether the data support this threshold. For example, *Sklar and Dietrich* [2004] reported that fine sand (D = 0.2 mm) did not produce wear above their detection limit (~10^{-3} g/hr), but this is also consistent with the predictions of the total-load erosion model both with or without the Stokes number cutoff. Furthermore, it is not obvious that the formulations used herein (i.e., the parabolic eddy viscosity: equation (27)) should hold for the abrasion mill where flow was driven by a propeller and strong secondary currents developed. The model fit, for example, is improved by setting $\beta = 3$ in equation (27) (Fig. 13B).

6.6.3. Implications for Natural Streams

The total-load erosion model differs significantly from the saltation-abrasion model for high transport stages and high relative sediment-supply rates. The large transport stages explored for the 60-mm gravel (e.g., $\tau_* / \tau_{*c} >> 1$) most likely occur during relatively large floods or in steep mountain terrain. For example, the bed-shear stress for the Bonneville flood of the western United States has been estimated to be 2500 Pa [*O'Connor*, 1993]. We calculate that this flood was competent to suspend 150-mm cobbles (i.e., u_* / w_{st} = 1, using the w_{st} relation of *Dietrich* [1982] for natural sediment), which is consistent with Bonneville flood deposits [*O'Connor*, 1993]. During this event, 60-mm gravel was at a transport stage of τ_* / τ_{*c} = 85, and 1-mm sand was at τ_* / τ_{*c} = 5.2 x 10^3. In mountain terrains, such large bed stresses can be achieved more readily. For example, during Typhoon Bilis in 2000, which has a

recurrence interval of about 20 years, the reach averaged bed stress of the LiWu River in Taiwan was about 2300 Pa [*Hartshorn et al*., 2002], making this more frequent event nearly as competent as the Bonneville flood in suspending gravel. In fact, the maximum across-channel erosion rates during Typhoon Bilis occurred several meters above the channel thalweg, suggesting that erosion by suspended particles outpaced bedload erosion in the channel thalweg [*Hartshorn et al*., 2002].

The total-load erosion model is also important to consider fine sediment, which can be at large transport stages during more regular flow events. For the characteristic event on the Eel River, the 1-mm sand is calculated to have a transport stage of τ_* / τ_{*c} = 102. For these conditions the saltation-abrasion model predicts no erosion, whereas the total-load model predicts an instantaneous erosion rate of approximately 10 mm/yr. The erosion rate due to sand is smaller than that predicted for gravel (for the same sediment supply), but it is nonetheless significant (Table 1). The total-load model might be particularly important for rivers where the load is dominated by sand, for example due to granite or sandstone lithologies.

Deciphering between the relative roles of sand and gravel in fluvial erosion is beyond the scope of this chapter. A significant limitation of the model is that it only considers sediment of a single size. It is clear from evaluation of the contour plots (Figs. 10 and 11), that there are regimes in parameter space where erosion from sand can be greater than that from gravel, but this depends on the relative supply of each. Since finer particles often dominate the load of a river, it seems possible that erosion from sand might be as or more important than erosion from gravel. Incorporating multiple particle sizes and particularly bimodal distributions of sediment into the model,

however, is not trivial. For example, it has been shown that the addition of sand into a gravel bed can lead to non-linear increases in the transport capacity of both sizes [*Wilcock et al.*, 2001; *Wilcock and Crowe*, 2003]. Extending the erosion model to multiple particle sizes would require reassessment of several formulas used herein to account for mixture and bimodal effects (over a bedrock bed) including the bedload transport capacity, the hydraulic roughness of the bed, the bedload velocity and the bedload layer height. Experimental and field measurements are needed to guide future theoretical work.

The total-load erosion model is most sensitive to the prediction of impact velocity, and this is also a topic that deserves future study. For example, our characterization of particle fluctuations that result in impacts as a Gaussian distribution is undoubtedly oversimplified. The degree to which particles detach from the fluid near the boundary likely depends on the relative particle response time compared to the fluid turbulence timescale (i.e. a particle Stokes number) [e.g., *Crowe et al.*, 1996]. In addition, local turbulent fluctuations can be intense, especially above a non-uniform bed. The model does not incorporate changes in hydraulic roughness or turbulence due to sediment cover or bedforms. Erosion of protruding pieces of bedrock is likely to be much more efficient than erosion into a flat bed (as assumed herein), because the impact velocity should scale with the mean flow rather than turbulence intensity or the gravitational settling velocity [e.g., *Anderson*, 1986]. Furthermore, erosion by suspended sediment could be substantial over bedforms such as flutes or potholes, where there is a significant advective component of the impact velocity by the mean

flow or vortices [*Alexander*, 1932; *Tinkler*, 1997; *Whipple et al.*, 2000; *Johnson and Whipple*, 2007].

Where it differs from the saltation-abrasion model, the total-load erosion model should have significant implications for predicting river channel morphology. For example, variations of the saltation-abrasion model have been used to model knickpoint migration in bedrock rivers [e.g., *Chatanantavet and Parker*, 2005; *Gasparini et al.*, 2007; *Crosby et al.*, 2007], and the total-load model is likely to make different predictions owing to the large transport stages that typify these steepened reaches. It has been suggested, for example, that hanging valleys might form because, based on the saltation-abrasion model, steepened reaches have lower erosion rates due to increased particle hop lengths and decreased impact rates [*Wobus et al.*, 2006; *Crosby et al.*, 2007]. The total-load erosion model, however, suggests the opposite: erosion rates increase with increasing channel slope and transport stage (at least for large transport stages, e.g., Fig. 4) because of the advection of suspended particles towards the bed by turbulent eddies.

Although the total-load erosion model offers insight into channel dynamics, we caution against using it (or other fluvial-abrasion models) for quantitative estimates in steep reaches with large roughness to depth ratios (i.e., k_s / H). In these cases, descriptions of flow resistance [e.g., *Bathurst*, 1985], sediment transport capacity [*Yager et al.*, 2007] and incipient sediment motion [*Lamb et al.*, 2008] are likely to be different. Moreover, at near vertical slopes, other processes such as plunge pool erosion [e.g., *Lamb et al.*, 2007] are probably more important than fluvial abrasion.

6.7. Conclusions

We have developed a mechanistic model for fluvial bedrock incision by suspended and bedload sediment. Particles are considered to impact the bed due to gravitational settling and advection by turbulent eddies, the later of which dominates at high transport stages. The model predicts that the erosion rate is a function of three dimensionless quantities for a given grain size: transport stage, relative sediment supply, and channel slope. Inclusion of suspension is important for high transport stages (i.e., large floods, steep slopes, or small particle sizes) and high relative sediment-supply rates. For a given ratio of sediment supply to transport capacity, the erosion rate is predicted to increase with transport stage because of the heightened impact velocity due to turbulent fluctuations, and does not taper to zero as predicted in the saltation-abrasion model. For most cases, erosion rates increase more rapidly with transport stage by increasing slope and fixing depth, rather than the opposite. This depth (or slope) dependency on erosion rate arises because both the near-bed sediment concentration and the particle fall velocity are sensitive to the vertical distribution of sediment in the water column. The total-load erosion model predicts that erosion can be substantial where the sediment supply exceeds the bedload transport capacity because a portion of the load is carried in suspension.

6.8. Appendix 1 – Fall Velocity

The acceleration of a falling particle can be calculated from the difference between the gravitational acceleration of the particle and deceleration due to drag

$$\frac{dw}{dt} = C_1 - C_2 w^2, \tag{A1}$$

where w is velocity in the vertical dimension, g is the acceleration due to gravity and C_1 and C_2 are given by

$$C_1 = \frac{(\rho_s - \rho_f)}{\rho_s} g \tag{A2}$$

$$C_2 = \frac{1}{2} C_d \frac{\rho_f}{\rho_s} \frac{A_x}{V_p}, \tag{A3}$$

where C_d is a drag coefficient, ρ_f is the density of the fluid that the particle is falling through, ρ_s is the particle density, A_x is the cross sectional area of the particle perpendicular to fall velocity, and V_p is the volume of the particle. We are interested in the acceleration over a certain fall distance rather than over a certain fall time. Equation (A1) can be written in terms of vertical distance z (positive downward) by substituting $dt = dz / w$, which yields

$$w\frac{dw}{dz} + C_2 w^2 = C_1 \tag{A4}$$

In order to solve equation (A4) analytically, we assume that C_2, and therefore C_d, is not a function of *z*. In reality C_d should vary as particles accelerate and the particle Reynolds number increases. Using a simple numerical integration, we found that accounting for a variable drag coefficient typically has less than a 10%-effect on settling velocity. We therefore assume that C_d is a constant for a given particle size and solve the non-linear ordinary differential equation as

$$w = \sqrt{\frac{C_1}{C_2}\left(1 - \exp\left(-2C_2 z\right)\right)}\,. \tag{A5}$$

where the boundary condition $w(z = 0) = 0$ has been applied. Substituting equations (A2) and (A3) into equation (A5), assuming spherical particles (i.e. $V_p / A_x = 2D/3$), defining the fall distance as $z = H_f / \cos\theta$, and taking the component normal to the bed results in equation (30).

6.9. Appendix 2 – Notation

A_x	Cross-sectional area of a sediment particle (L^2)
c	Volumetric sediment concentration (-)
c_b	Near-bed volumetric sediment concentration (-)
C_d	Drag coefficient (-)
D	Sediment diameter (L)
E	Rate of vertical erosion (LT^{-1})
I_r	Impact rate per unit bed area ($L^{-2}T^{-1}$)
F_e	Fraction of exposed bedrock (-)
g	Acceleration due to gravity (LT^{-2})
H	Depth of flow (L)
H_b	Thickness of the bedload layer (L)
H_f	Particle fall distance (L)
L_b	Particle saltation hop length (L)
n	Roughness coefficient (-)
P	Rouse parameter (-)
q	Volumetric sediment supply per unit channel width (L^2T^{-1})
q_b	Volumetric bedload flux per unit channel width (L^2T^{-1})
q_{bc}	Volumetric bedload-transport capacity per unit channel width (L^2T^{-1})
q_s	Volumetric suspended-load flux per unit channel width (L^2T^{-1})
q_w	Volumetric water discharge per unit channel width (L^2T^{-1})
R	Submerged specific density of sediment (-)
S	Channel-bed slope (-)
St	Particle Stokes number (-)
t_i	Time between particle impacts (T)
u	Stream-wise flow velocity (LT^{-1})
U	Depth-averaged stream-wise flow velocity (LT^{-1})
U_b	Depth-averaged stream-wise bedload velocity (LT^{-1})
u_*	Shear velocity (LT^{-1})
V_i	Volume of eroded rock per impact (L^3)
V_p	Volume of a particle (L^3)
W	Channel width (L)
w	Vertical velocity (LT^{-1})
w_{st}	Terminal settling velocity of a particle (LT^{-1})
w_i	Impact velocity of a particle at the bedrock interface (LT^{-1})
$w_{i,eff}$	Effective impact velocity (LT^{-1})
w_p	Particle velocity (LT^{-1})

w_s Velocity of a falling particle normal to the bed (LT^{-1})
w' Velocity fluctuations perpendicular to the bed (LT^{-1})
Y Young's modulus of elasticity ($ML^{-1}T^{-2}$)
z Height above the bed (L)
z_0 Flow roughness parameter (L)
ε_v Energy to erode a unit volume of bedrock ($ML^{-1}T^{-2}$)
σ_T Rock tensile strength ($ML^{-1}T^{-2}$)
σ_w Standard deviation in vertical velocity fluctuations (LT^{-1})
α Sediment entrainment parameter (-)
β Proportionality constant relating the diffusivity of momentum and sediment (-)
k_v Empirical rock erodibility coefficient (-)
κ von Karman's constant (-)
ζ_z Relative height above the bed (-)
ζ_b Relative height of the bedload layer (-)
ν Kinematic viscosity of the fluid (L^2T^{-1})
ν_T Turbulent eddy viscosity (L^2T^{-1})
ρ_s Density of sediment (ML^{-3})
ρ_f Density of fluid (ML^{-3})
τ_* Shields stress (-)
τ_{*c} Critical Shields stress for incipient sediment motion (-)
χ Integral relating the flux of suspended sediment to c_b, H and U (-)

6.10. References

Abbott, J.E., and J.R.D. Francis (1977), Saltation and Suspension Trajectories of Solid Grains in a Water Stream, *Philos. Trans. R. Soc. London, Ser. A, 284* (1321), 225-254.

Alexander, H.S. (1932), Pothole erosion, *J. Geol., 40* (4), 305-337.

Anderson, R.S. (1986), Erosion profiles due to particles entrained by wind: Application of an eolian sediment-transport model, *Geol. Soc. Am. Bull., 97*, 1270-1278.

Bagnold, R.A. (1966), *An Approach to the Sediment Transport Problem from General Physics*, U.S. Geological Survey, Washington, D. C.

Baker, V.R. (1982), *The Channels of Mars*, University of Texas Press, Austin.

Bathurst, J.C. (1985), Flow Resistance Estimation in Mountain Rivers, *J. Hydraul. Eng., 111* (4), 625-643.

Beaumont, C., P. Fullsack, and J. Hamilton (1992), Erosional control of active compressional orogens, in *Thrust Tectonics*, edited by K. R. McClay, pp. 1 –18, Chapman and Hall, New York.

Bennett, S.J., J.S. Bridge, and J.L. Best (1998), Fluid and sediment dynamics of upper stage plane beds, *J. Geophys. Res., 103* (C1), 1239-1274.

Bridge, J.S., and S.J. Bennett (1992), A model for the entrainment and transport of sediment grains of mixed sizes, shapes, and densities, *Water Resour. Res., 28* (2), 337-363.

Buffington, J. M., and D. R. Montgomery (1997), A systematic analysis of eight decades of incipient motion studies, with special reference to gravel-bedded rivers, *Water Resour. Res.*, 33, 1993– 2029.

Carter, C.L., and Anderson, R.S. (2006), Fluvial erosion of physically modeled abrasion-dominated slot canyons, *Geomorphology, 81*, 89-113.

Chatanantavet, P., and G. Parker (2005), Modeling the bedrock evolution of western Kaua'i, Hawai'i, by a physically-based incision model based on abrasion, in *River, Coastal, and Estuarine Morphodynamics, IAHR Symposium*, edited by G. Parker, and M. Garcia, pp. 99-110, London, Taylor and Francis.

Cheng, N.S., and Y.M. Chiew (1999), Analysis of initiation of sediment suspension from bed load, *J. Hydraul. Eng., 125* (8), 855-861.

Coles, D.F. (1956), The law of the wake in turbulent boundary layer, *J. Fluid. Mech.*, *1*, 191-226.

Crosby, B.T., K.X. Whipple, N.M. Gasparini, and C.W. Wobus (2007), Formation of fluvial hanging valleys: Theory and simulation, *J. Geophys. Res.*, *112* (F3), doi: 10.1029/2006JF000566.

Crowe, C.T., T.R. Trout, and J.N. Chung (1996), Numerical models for two-phase flows, *Annual Review of Fluid Mechanics*, *28*, 11-43.

Davies, R., J. Serayssol, and E. Hinch (1986), The elastohydrodynamical collision of two spheres, *J. Fluid Mech.*, *163*, 479-497.

Dietrich, W.E. (1982), Settling Velocity of Natural Particles, *Water Resour. Res.*, *18* (6), 1615-1626.

Dietrich, W.E., D. Bellugi, L. Sklar, J.D. Stock, A.M. Heimsath, and J.J. Roering (2003), Geomorphic transport laws for predicting landscape form and dynamics, in *Prediction in Geomorphology*, edited by P. Wilcock, and R. Iverson, pp. DOI: 10.1029/135GM09.

Einstein, H.A. (1968), Deposition of suspended particles in a gravel bed, *J. Hydraul. Eng.*, *94* (5), 1197-1205.

Einstein, H.A., and N. Chien (1955), Effects of heavy sediment concentration near the bed on velocity and sediment distribution, in *MRD Sediment Series 8*, University of California, Berkeley.

Fernandez Luque, F.R., and R. van Beek (1976), Erosion and transport of bed-load sediment, *J. Hydraul. Res.*, *14*, 127-144.

Finnegan, N.J., Sklar, L.S., and T.K. Fuller (2007), Interplay of sediment supply, river incision, and channel morphology revealed by the transient evolution of an experimental bedrock channel, *J. Geophys. Res.*, *112*, p. 1-17, doi:10.1029/2006JF000569.

Foley, M.G. (1980), Bedrock incision by streams, *Geol. Soc. Am. Bull.*, *91*, 2189-2213.

Francis, J.R.D. (1973), Experiments on motion of solitary grains along bed of a water-stream, *Proc. R. Soc. London, Ser. A*, *332* (1591), 443-471.

García, M.H., and G. Parker (1991), Entrainment of bed sediment into suspension, *J. Hydraul. Eng.*, *117* (4), 414-435.

Gasparini, N.M., K.X. Whipple, and R.L. Bras (2007), Predictions of steady state and transient landscape morphology using sediment-flux-dependent river incision models, *J. Geophys. Res.*, *112* (F3), doi: 10.1029/2006JF000567.

Gelfenbaum, G., and J.D. Smith (1986), Experimental evaluation of a generalized suspended-sediment transport theory, in *Shelf Sands and Sandstones*, edited by R.J. Knight, and S.R. McLean, pp. 133-144, Mem. Can. Soc. Petrol. Geol.

Gilbert, G.K. (1877), *Report on the Geology of the Henry Mountains: Geographical and Geological Survey of the Rocky Mountain Region*, 166 pp., U.S. Gov. Print. Off., Washington, D.C.

Graf, W.H., and M. Cellino (2002), Suspension in open channels; experimental study, *J. Hydraul. Res.*, *40* (4), 435-447.

Grass, A.J. (1970), Initial instability of fine bed sands, *J. Hydrau. Eng.*, *96*, 619-632.

Hancock, G.S., R.S. Anderson, and K.X. Whipple (1998), Beyond Power: Bedrock River Incision Process and Form, in *Rivers Over Rock*, edited by K.J. Tinkler, and E.E. Wohl, pp. 35-60, American Geophyscial Union.

Hartshorn, K., N. Hovius, W.B. Dade, and R.L. Slingerland (2002), Climate-driven bedrock incision in an active mountain belt, *Science*, *297* (5589), 2036-2038.

Howard, A.D. (1998), Long profile development of bedrock channels: Interaction of weathering, mass wasting, bed erosion, and sediment transport, in *Rivers Over Rock: Fluvial Processes in Bedrock Channels*, edited by K.J. Tinkler, and E.E. Wohl, pp. 237-260, AGU, Washington, D.C.

Howard, A.D., W.E. Dietrich, and M.A. Seidl (1994), Modelling fluvial erosion on regional and continental scales, *J. Geophys. Res.*, *99*, 13971-13986.

Howard, A.D., and G. Kerby (1983), Channel Changes in Badlands, *Geol. Soc. Am. Bull.*, *94* (6), 739-752.

Hu, C.H., and Y.J. Hui (1996), Bed-load transport: 1. Mechanical characteristics, *J. Hydraul. Eng.*, *122* (5), 245-254.

Jackson, R.G. (1976), Sedimentological and fluid-dynamic implications of turbulent bursting phenomenon in geophysical flows, *J. Fluid Mech.*, *77* (3), 531-560.

Johnson, J.P. and K.X. Whipple (2007), Feedbacks between erosion and sediment transport in experimental bedrock channels, *Earth Surf. Processes Landforms*, *32*, 1048-1062, doi:10.1002/esp.1471.

Joseph, G.G., and M.L. Hunt (2004), Oblique particle-wall collisions in a liquid, *J. Fluid Mech., 510,* 71-93.

Kamphius, J.W. (1974), Determination of sand roughness for fixed beds, *J. Hydraul. Res., 12* (2), 193-203.

Lamb, M.P., W.E. Dietrich, and J.G. Venditti (2008), Is the critical Shields number for incipient sediment motion dependent on channel-bed slope?, *J. Geophys. Res.*, in press.

Lamb, M.P., A.D. Howard, W.E. Dietrich, and J.T. Perron (2007), Formation of amphitheater-headed valleys by waterfall erosion after large-scale slumping on Hawaii, *Geol. Soc. Am. Bull.*, 119, 805-822, doi:10.1130/B25986.1.

Lee, H.Y., and I.S. Hsu (1994), Investigation of Saltating Particle Motions, *J. Hydraul. Eng., 120* (7), 831-845.

Lian, G., M. Adams, and C. Thornton (1996), Sediment suspension with rippled bed, *J. Fluid Mech., 311,* 141-152.

Malde, H.E. (1968), The catastrophic late Pleistocene Bonneville Flood in the Snake River Plain, Idaho, *U.S. Geological Survey Professional Paper, 596*, 1-52.

McLean, S.R. (1992), On the calculation of suspended-load for noncohesive sediments, *J. Geophys. Res., 97* (C4), 5759-5770.

Merritts, D., and W. B. Bull (1989), Interpreting Quaternary uplift rates at the Mendocino triple junction, northern California, from uplifted marine terraces, *Geology,* 17, 1020–1024.

Muste, M., K. Yu, I. Fujita, and R. Ettema (2005), Two-phase versus mixed-flow perspective on suspended sediment transport in turbulent channel flows, *Water Resour. Res., 41*, doi: 10.1029/2004/WR003595.

Nakagawa, H., and I. Nezu (1977), Prediction of Contributions to Reynolds Stress from Bursting Events in Open-Channel Flows, *J. Fluid Mech., 80* (APR4), 99-128.

Nelson, J.M., R.L. Shreve, D.C. McLean, and T.G. Drake (1995), Role of near-bed turbulence structure in bed load transport and bed form mechanics, *Water Resour. Res., 31* (8), 2071-2086.

Nelson, P.A. and G Seminara (2007), Sediment Supply and the Prediction of Bedrock Channel Cross Section Evolution, *Eos Trans. AGU, 88*(52), Fall Meet. Suppl., Abstract H44B-04.

Nezu, I., and R. Azuma (2004), Turbulence characteristics and interaction between particles and fluid in particle-laden open channel flows, *J. Hydraul. Eng.*, *130* (10), 988-1000.

Nezu, I., and H. Nakagawa (1993), *Turbulence in Open-Channel Flows*, 281 pp., A.A. Balkema, Rotterdam.

Nino, Y., M. Garcia, and L. Ayala (1994), Gravel Saltation: 1. Experiments, *Water Resour. Res.*, *30* (6), 1907-1914.

Nino, Y., and M.H. Garcia (1996), Experiments on particle-turbulence interactions in the near-wall region of an open channel flow: Implications for sediment transport, *J. Fluid Mech.*, *326*, 285-319.

Nino, Y., F. Lopez, and M. Garcia (2003), Threshold for particle entrainment into suspension, *Sedimentology*, *50* (2), 247-263.

O'Connor, J.E. (1993), *Hydrology, Hydraulics and Geomorphology of the Bonneville Flood*, Geological Society of America, Boulder, CO.

Parker, G. (1978), Self-formed straight rivers with equilibrium banks and mobile bed: 1. Sand-silt river, *J. Fluid Mech.*, *89*, 109-125.

Parker, G. (1991), Selective sorting and abrasion of river gravel. II: Applications, *J. Hydraul. Eng.*, *117* (2), 150-171.

Rouse, H.R. (1937), Modern conceptions of the mechanics of turbulence, *Trans. Am. Soc. Civ. Eng.*, *102*, 463-543.

Schmeeckle, M.W., J.M. Nelson, J. Pitlick, and J.P. Bennet (2001), Interparticle collision of natural sediment grains in water, *Water Resour. Res.*, *37* (9), 2377-2391.

Seidl, M.A., and W.E. Dietrich (1992), The problem of channel erosion into bedrock, in *Functional Geomorphology*, edited by K.H. Schmidt, and J. de Ploey, pp. 101-124.

Seidl, M.A., W.E. Dietrich, and J.W. Kirchner (1994), Longitudinal profile development into bedrock: an analysis of Hawaiian channels, *J. Geol.*, *102*, 457–474.

Sekine, M., and H. Kikkawa (1992), Mechanics of Saltating Grains .2, *J. Hydraul. Eng.*, *118* (4), 536-558.

Shields, A. (1936), Anwendung der Aehnlichkeitsmechanik und der Turbulenzforschung auf die Geschiebebewegung, *Mitt. Preuss. Versuchsanst. Wasserbau Schiffbau*, *26*, 26.

Sklar, L.S. (2003), *The influence of sediment supply, grain size, and rock strength on rates of river incision into bedrock*, Ph.D. Thesis, 342 pp., University of California, Berkeley.

Sklar, L.S., and W.E. Dietrich (2001), Sediment and rock strength controls on river incision into bedrock, *Geology*, *29* (12), 1087-1090.

Sklar, L.S., and W.E. Dietrich (2004), A mechanistic model for river incision into bedrock by saltating bed load, *Water Resour. Res.*, *40* (6).

Sklar, L.S., and W.E. Dietrich (2006), The role of sediment in controlling steady-state bedrock channel slope: Implications of the saltation-abrasion incision model, *Geomorphology*, *82* (1-2), 58-83.

Slingerland, R., S. D. Willett, and H. L. Hennessey (1997), A new fluvial bedrock incision model based on the work-energy principle, *Eos Trans. AGU*, *78*(46), Fall Meet. Suppl., Abstract H42F-12.

Smith, J.D., and S.R. McLean (1977), Spatially averaged flow over a wavy surface, *J. Geophys. Res.*, *8* (12), 1735-1746.

Sumer, B.M., and R. Deigaard (1981), Particle Motions near the Bottom in Turbulent-Flow in an Open Channel .2, *J. Fluid Mech.*, *109* (AUG), 311-337.

Tinkler, K.J. (1997), Rockbed wear at a flow convergence zone in Fifteen Mile Creek, Niagara Peninsula, Ontario, *J. Geol.*, *105*, 263-274.

Tucker, G. E., and R. L. Slingerland (1994), Erosional dynamics, flexural isostasy, and long-lived escarpments: A numerical modeling study, *J. Geophys. Res.*, *99*, 12,229– 12,243.

Turowski, J.M., Hovius, N., Meng-Long, H., Lague, D., and C. Men-Chiang (2008), Distribution of erosion across bedrock channels, *Earth Surf. Processes Landforms*, *33*, 353-362, doi:10.10002/esp.1559.

Turowski, J.M., Lague, D., and N. Hovius, N., (2007), Cover effect in bedroick abrasion: A new derivation and its implications for the modeling of bedrock channel morphology, *J. Geophys. Res.*, 112, 1-16, doi:10.1029/2006JF000697.

van Rijn, L.C. (1984), Sediment Transport: 2. Suspended-Load Transport, *J. Hydraul. Eng.*, *110* (11), 1613-1641.

Vanoni, V.A. (1946), Transportation of Suspended Sediment by Water, *Transactions of the American Society of Civil Engineers*, *111*, 67-102.

Whipple, K.X. (2004), Bedrock rivers and the geomorphology of active orogens, *Annual Review of Earth and Planetary Sciences*, *32*, 151-185.

Whipple, K.X., G.S. Hancock, and R.S. Anderson (2000), River incision into bedrock: Mechanics and relative efficacy of plucking, abrasion, and cavitation, *Geol. Soc. Am. Bull.*, *112* (3), 490-503.

Whipple, K.X., and G.E. Tucker (1999), Dynamics of the stream-power river incision model: Implications for height limits of mountain ranges, landscape response timescales, and research needs, *J. Geophys. Res.*, *104* (B8), 17661-17674.

Wiberg, P.L., and J.D. Smith (1985), A Theoretical-Model for Saltating Grains in Water, *J. Geophys. Res.*, *90* (NC4), 7341-7354.

Wilcock, P.R., and J.C. Crowe (2003), Surface-based transport model for mixed-size sediment, *J. Hydraul. Eng.*, *129* (2), 120-128.

Wilcock, P.R., S.T. Kenworthy, and J.C. Crowe (2001), Experimental study of the transport of mixed sand and gravel, *Water Resour. Res.*, *37* (12), 3349-3358.

Wobus, C.W., B.T. Crosby, and K.X. Whipple (2006), Hanging valleys in fluvial systems: Controls on occurrence and implications for landscape evolution, *J. Geophys. Res.*, *111* (F2), doi:10.1029/2005JF000406.

Wren, D.G., S.J. Bennet, B.D. Barkdoll, and R.A. Kuhnle (2004), Distribution of velocity, turbulence, and suspended sediment over low-relief antidunes, *J. Hydraul. Res.*, *43* (1), 3-11.

Wright, S., and G. Parker (2004), Flow resistance and suspended load in sand-bed rivers: Simplified stratification model, *J. Hydraul. Eng.*, *130* (8), 796-805.

Yager, E.M., J.W. Kirchner, and W.E. Dietrich (2007), Calculating bed load transport in steep boulder bed channels, *Water Resour. Res.*, *43* (7), doi:10.1029/2006WR005432.